

Higher order finite elements and the fictitious domain concept for wave propagation analysis

Dissertation

zur Erlangung des akademischen Grades

**Doktoringenieur
(Dr.-Ing.)**

von Dipl.-Ing. Sascha Duczek

geb. am 05.10.1984 in Berlin

genehmigt durch die Fakultät für Maschinenbau
der Otto-von-Guericke-Universität Magdeburg

Gutachter: Prof. Dr.-Ing. habil. Dr. h. c. Ulrich Gabbert

Prof. Dr.-Ing. habil. Alexander Düster

Assoc.-Prof. DI. Dr. Michael Krommer

Promotionskolloquium am 10.09.2014

Preface

Die vorliegende Arbeit entstand während meiner Tätigkeit als wissenschaftlicher Mitarbeiter am Lehrstuhl für numerische Mechanik der Fakultät für Maschinenbau der Otto-von-Guericke-Universität Magdeburg. Während dieser Zeit realisiert man sehr schnell, dass eine Doktorarbeit nur selten die Leistung einer einzelnen Person ist. Die Arbeit hat stark von den Erkenntnissen, der Beratung und der Unterstützung vieler Kollegen profitiert. Deshalb ist es mir auch eine besondere Freude, diese gesondert zu erwähnen.

An erster Stelle möchte ich mich bei meinen Doktorvater, Herrn Prof. Dr.-Ing. habil. Dr. h. c. Ulrich Gabbert, für die großzügige Unterstützung und wissenschaftliche Betreuung dieser Arbeit bedanken. Sein stetes Interesse und seine große Bereitschaft zu fachlichen und auch überfachlichen Diskussionen haben wesentlich zum Gelingen der Arbeit beigetragen. Ferner sorgte er immer für ein angenehmes Arbeitsklima auf dem die Arbeit gedeihen konnte. Nicht zuletzt werde ich mich immer sehr gern an die gemeinsamen Besuche der Bördelandhalle und darauf folgenden Gespräche über den Handball erinnern.

Herrn Prof. Dr.-Ing. habil. Alexander Düster danke ich ebenfalls für die Übernahme eines Koreferates und darüber hinaus auch für die bereitwillige Unterstützung, die seit meiner Diplomarbeitszeit besteht. Schon damals gab er mir, ohne mich zu kennen, immer wieder wertvolle Hinweise zum Thema p -FEM und hat somit maßgeblich dazu beigetragen, dass ich mich von diesem Thema bis zum heutigen Zeitpunkt nicht mehr lösen konnte - und natürlich auch nicht wollte. In so manchen verweifelten Stunden haben mir sein Rat und seine Dissertation beigestanden.

Mein weiterer Dank gilt Herrn Assoc.-Prof. DI. Dr. Michael Krommer für die bereitwillige Übernahme des Koreferates. Über das rege Interesse und die vielen Hinweise und Anregungen habe ich mich sehr gefreut. Der wissenschaftliche Austausch auf vielen Konferenzen war stets von großem Respekt und Freundlichkeit geprägt. Auch die sozialen Zusammenkünfte werden in guter Erinnerung bleiben.

Des Weiteren möchte ich allen Kollegen für die zu allen Zeiten angenehme Arbeitsatmosphäre danken. Dabei möchte ich insbesondere Herrn Dr.-Ing. Christian Willberg für die zahlreichen Diskussionen, wichtigen Hinweise und natürlich auch das Korrekturlesen der vorliegenden Arbeit danken. Ohne ihn wäre meine Arbeitszeit an der OvGU doch um einiges langweiliger gewesen und natürlich hätte ich dann auch keinen Trainingspartner mehr für den morgendlichen Sport gehabt. Auch Dr.-Ing. Zair Ahmad und Dr.-Ing. Juan Miguel Vivar Perez bin ich zu großem Dank verpflichtet für die zahlreichen Anmerkungen und fachlichen Gespräche, die in einem beträchtlichen Maße zum Gelingen der Doktorarbeit beigetragen haben.

Die kollegiale und vor allem freundschaftliche Zusammenarbeit, die durch unzählige Film- und Cocktailabendene abgerundet wurde, werde ich nie vergessen. Besonders hervorzuheben ist dabei Dipl.-Ing. Steffen Liefold, den ich mehrmals pro Tag von der Arbeit ablenken konnte ohne auch nur ein Murren zu hören. Trotz dieser „Belästigung“ hatte er immer ein offenes Ohr für meine Probleme und hat mir immer bereitwillig mit Rat und Tat zur Seite gestanden, wenn es darum ging meine Ideen visuell zu verwirklichen. Auch die unzähligen Aktivitäten nach der Arbeit, seien es Videoabend oder Grillen im Nordpark, werden in meiner Erinnerung nie verblassen. Dafür ist ihm mein ewige Dankbarkeit gewiss. Da wir zufällig auch am gleichen Tag, wenn auch nicht im gleichen Jahr, geboren wurden konnten wir unsere Geburtstage immer gemeinsam feiern. Auch das werde ich zutiefst vermissen. Selbstverständlich bleibt auch mein Büronachbar Dipl.-Ing. Fabian Duvigneau nicht unerwähnt, der mich die letzten zwei Jahre dieser Arbeit immer wieder freundlich motiviert hat. Unsere Nachbesprechungen werden für immer in meinem Gedächtnis bleiben. Auch werde ich die Sätze „Nun sei doch nicht so!“ und „Was stimmt denn mit dir nicht!“ durchaus vermissen. Das wir stets einen freundlichen, von Respekt geprägten Umgang miteinander hätten wäre sicherlich eine große Untertreibung. Da wir beide zu etwas direkteren Anreden neigen, haben wir es auch nicht gescheut dem anderen die Wahrheit direkt ins Gesicht zu sagen.

Natürlich habe ich bei weitem noch nicht alle Menschen, die zum Gelingen dieser Arbeit beigetragen haben aufgezählt. Das tut mir auch im Herzen weh, nur würde dies den Rahmen dieser einleitenden Worte sprengen. Es sei allen Kollegen und Freunden, die jetzt nicht genannt wurden versichert, dass ich für deren Hilfe trotzdem sehr dankbar bin und die Unterstützung auch zu schätzen weiß. Zu erwähnen seien in diesem Zusammenhang noch Herr Dr.-Ing. Seyed Hosseini und Dipl.-Math.techn. Mathias Würkner.

Schließlich möchte ich mich ganz herzlich bei meinen Eltern Rosemarie und Wilhelm, sowie meinem Bruder André und dessen Frau Petra für die große Geduld und Rücksichtnahme, welche mir bei der Anfertigung dieser Arbeit entgegengebracht wurde, bedanken. Natürlich vergesse ich auch nicht meinen kleinen Neffen, Bennett Alexander, der es immer wieder aufs Neue verstanden hat, mich abzulenken und zu erfreuen (auch wenn er am Anfang meistens auf der Flucht vor seinem Onkel war). Zuletzt möchte ich mich noch bei der wichtigsten Person, meiner Partnerin Christine, für das große Verständnis bedanken, dass sie mir immer wieder entgegengebracht hat. Sie hatte es sicherlich nicht immer leicht mit mir, besonders während der letzten Wochen vor Abgabe der vorliegenden Arbeit.

Magdeburg, September 2014

Sascha Duczek

- Douglas Adams -

The Ultimate Hitchhiker's Guide to the Galaxy: The Restaurant at the End of the Universe

“In cases of major discrepancy it's always reality that's got it wrong.”

Ehrenerklärung

Ich versichere hiermit, dass ich die vorliegende Arbeit ohne unzulässige Hilfe Dritter und ohne Benutzung anderer als der angegebenen Hilfsmittel angefertigt habe. Die Hilfe eines kommerziellen Promotionsberaters habe ich nicht in Anspruch genommen. Dritte haben von mir weder unmittelbar noch mittelbar geldwerte Leistungen für Arbeiten erhalten, die im Zusammenhang mit dem Inhalt der vorgelegten Dissertation stehen. Verwendete fremde und eigene Quellen sind als solche kenntlich gemacht.

Ich habe insbesondere nicht wissentlich:

- Ergebnisse erfunden oder widersprüchliche Ergebnisse verschwiegen,
- statistische Verfahren absichtlich missbraucht, um Daten in ungerechtfertigter Weise zu interpretieren,
- fremde Ergebnisse oder Veröffentlichungen plagiiert,
- fremde Forschungsergebnisse verzerrt wiedergegeben.

Mir ist bekannt, dass Verstöße gegen das Urheberrecht Unterlassungs- und Schadensersatzansprüche des Urhebers sowie eine strafrechtliche Ahndung durch die Strafverfolgungsbehörden begründen kann.

Ich erkläre mich damit einverstanden, dass die Dissertation gegebenenfalls mit Mitteln der elektronischen Datenverarbeitung auf Plagiate überprüft werden kann.

Die Arbeit wurde bisher weder im Inland noch im Ausland in gleicher oder ähnlicher Form als Dissertation eingereicht und ist als Ganzes auch noch nicht veröffentlicht.

Sascha Duczek
Magdeburg, 06.05.2014

Contents

List of Symbols	VIII
Abstract	XXIII
Kurzzusammenfassung	XXIV
1 Introduction	1
1.1 SHM - General principles and current research activities	1
1.2 Numerical methods for wave propagation analysis	9
1.3 Working hypotheses and outline	15
2 Lamb waves	18
2.1 Governing equations of elastic wave propagation	18
2.1.1 Navier's equation for an isotropic body	18
2.1.2 Helmholtz decomposition for isotropic media	19
2.1.3 Rayleigh-Lamb wave equation	20
2.2 Application of ultrasonic guided waves to SHM problems	25
3 Piezoelectricity	28
3.1 The piezoelectric effect	28
3.2 Constitutive equations of piezoelectricity	32
4 Higher Order Finite Element Method	35
4.1 Higher order finite elements for electro-mechanically coupled problems	36
4.1.1 Weak form of equilibrium	37
4.2 Matrix of shape functions	43
4.3 Transient analysis for structures including piezoelectric elements	46
4.3.1 Dynamic equations of a piezoelectric body	46
4.3.2 Central difference method	47
4.3.3 Newmark algorithm	48
4.4 Representation of the geometry - Mapping	50
4.4.1 Blending function method	51
4.4.2 Sub-parametric mapping concept	52
4.5 Implementation of boundary conditions	53
4.5.1 Dirichlet boundary conditions	53
4.5.2 Neumann boundary conditions	55
4.6 Diagonalization of the mass matrix	56
4.6.1 Nodal quadrature technique	57
4.6.2 Row-sum technique	57
4.6.3 HRZ-lumping technique	58

5	Higher Order Fictitious Domain Method	59
5.1	Basic concept of the FCM/SCM for smart structure applications	60
5.2	Representation of the geometry - Adaptive integration	67
5.2.1	Gauß quadrature	68
5.2.2	Adaptive quadrature scheme	70
5.2.3	Improved adaptive integration concepts	73
5.2.4	Vector integration and hp -spectral quadrature algorithm	75
6	Shape Functions	76
6.1	One-dimensional shape functions	77
6.1.1	One-dimensional shape functions: FEM	77
6.1.2	One-dimensional shape functions: SEM	79
6.1.3	One-dimensional shape functions: p -FEM	81
6.1.4	One-dimensional shape functions: Fourier- p -FEM	83
6.1.5	Generation of one-dimensional hierarchic shape functions	85
6.2	Multi-dimensional shape functions	86
6.3	Comparison of different one-dimensional Ansatz functions	87
6.3.1	Hierarchic vs. non-hierarchic shape functions	87
6.3.2	Critical time-step and condition number	91
6.4	C_0 -continuity	94
7	Convergence Studies	100
7.1	Model set-up	100
7.2	Convergence behavior of the SEM	105
7.2.1	h -Refinement in x_1 -direction	106
7.2.2	p -Refinement in x_2 -direction	110
7.3	Convergence behavior of the p -FEM	111
7.3.1	h -Refinement in x_1 -direction	112
7.3.2	p -Refinement in x_2 -direction	115
7.4	Convergence behavior of the Fourier- p -FEM	117
7.4.1	h -Refinement in x_1 -direction	120
7.4.2	p -Refinement in x_2 -direction	120
7.5	Comparison of different higher order finite element approaches	121
7.5.1	h -Refinement in x_1 -direction	122
7.6	Influence of the time-step width Δt	125
7.7	Influence of the chosen signal processing method: CWT	126
7.8	Convergence disturbance	128
7.8.1	Numerical model	128
7.8.2	Modal analysis of a single finite element	133
7.8.3	Frequency dependency of the elemental eigenfrequency effect	135
7.8.4	Modal analysis of a group of finite elements	137
8	Numerical Results	140
8.1	Modal analysis of a piezoelectric disc	140
8.2	2D perforated plate	147
8.3	2D porous plate	153
8.4	2D plate: A_1 -mode	156

8.5	3D plate with a conical hole	158
8.6	Validation - Aluminum plate with sensor network	164
9	Bandgaps	168
9.1	Bandgap structures	170
9.1.1	Fibonacci lattice	170
9.1.2	Square hole arrangement	171
9.2	Simulation results	171
9.2.1	Fibonacci lattice	172
9.2.2	Square hole arrangement	174
10	Conclusion & Outlook	180
A	Piezoelectric constitutive matrices	184
B	3D shape functions: p-FEM	187
C	Ansatz spaces for higher order finite elements	191
C.1	The trunk space for 2D quadrilateral finite elements	191
C.2	The tensor product space for 2D quadrilateral finite elements	192
C.3	The trunk space for 3D hexahedral finite elements	192
C.4	The tensor product space for 3D hexahedral finite elements	193
D	Numerical Quadrature - points and weights	195
D.1	Gauß-Legendre quadrature	195
D.2	Gauß-Lobatto quadrature	197
	References	199

List of Symbols

Please note that, originally, only waves propagating in isotropic plates of constant thickness are called Lamb waves. Only in these cases Lamb waves are decoupled from shear horizontal waves (Love waves). Nonetheless, there is a tendency in the available literature to also use this terminology for waves travelling in anisotropic composite plates despite the fact that Lamb and Love waves are coupled in such media. In the thesis at hand, however, the term ultrasonic guided wave is preferred.

Regarding the notation it is to say that for the convenience of representation, the spatial coordinates x , y and z are freely interchanged with x_1 , x_2 and x_3 , respectively. The superscript (e) denotes variables associated with a single finite element while the superscript (c) marks variables corresponding to a single cell.

Acronyms

A_i :	i -th anti-symmetric Lamb wave mode
AFC:	Active fiber composite
BEM:	Boundary element method
BBS:	Baseline signal stretch
CAD:	Computer aided design
CDM:	Central difference method
CFRP:	Carbon fiber reinforced plastic
CGL:	Chebyshev-Gauß-Lobatto nodal distribution
CT:	Computer tomography
CWT:	Continuous wavelet transform
DoF:	Degrees-of-freedom
DIC:	Digital image correlation
FC:	Finite cell
FCM:	Finite cell method
FE:	Finite element
FEA:	Finite element analysis
FEM:	Finite element method
FFT:	Fast Fourier transform
Fourier- p -FEM:	Fourier- p -version of the finite element method
FSDT:	First order shear deformation theory
GFRP:	Glass fiber reinforced plastic
GLL:	Gauß-Lobatto-Legendre nodal distribution
GW:	Guided waves
h -FEM:	h -version of the finite element method
HO -FEM:	Higher order finite element method
HRZ:	Hinton-Rock-Zienkiewicz mass-lumping technique
IGA:	Isogeometric analysis

IGE:	Isogeometric element
LISA:	Local interaction simulation approach
LSDV:	Laser scanning Doppler vibrometry
MAC:	Modal assurance criterion
MFC:	Micro fiber composite
MSLM:	Mass-spring lattice model
NURBS:	Non-uniform rational B-splines
OBS:	Optimal baseline selection
p -FEM:	p -version of the finite element method
PZT:	Lead-zirconate-titanate
RAM:	Random access memory
RC:	Reinforced concrete
RVE:	Representative volume element
S_i :	i -th symmetric Lamb wave mode
SAFE:	Semi-analytical finite element method
SC:	Spectral cell
SCM:	Spectral cell method
SE:	Spectral element
SEM:	Spectral element method
SHM:	Structural health monitoring
WFE:	Wave finite element

Mathematical operators

Symbol	Meaning
div	Divergence operator
$\det(\mathbf{A})$	Determinant of matrix \mathbf{A}
$H(u(t))$	Hilbert transform of the displacement signal $u(t)$
$\partial(\cdot)/\partial x_1 =$ $(\cdot)_{,x} = (\cdot)_{,1}$	Partial derivative of (\cdot) with respect to x_1
$\partial(\cdot)/\partial x_2 =$ $(\cdot)_{,y} = (\cdot)_{,2}$	Partial derivative of (\cdot) with respect to x_2
$\partial(\cdot)/\partial x_3 =$ $(\cdot)_{,z} = (\cdot)_{,3}$	Partial derivative of (\cdot) with respect to x_3
$\partial(\cdot)/\partial t = (\dot{\cdot})$	Partial derivative of (\cdot) with respect to t
$ \cdot $	Absolute value
$\ \cdot\ $	Norm
$\max(p_\xi, p_\eta, p_\zeta)$	Maximum of the polynomial degrees p_ξ , p_η , and p_ζ
$\min(p_\xi, p_\eta, p_\zeta)$	Minimum of the polynomial degrees p_ξ , p_η , and p_ζ
∇	Nabla operator
Δ	Laplace operator
δ	Variational operator

Chapter 1

Symbol	Meaning
A_{S_1}	Amplitude of S_1 -mode
A_{S_2}	Amplitude of S_2 -mode
b_e	Characteristic finite element size
\mathbf{F}^c	Load vector of the finite cell method
\mathbf{F}^e	Load vector of the finite element method
f_0	Center frequency of the excitation signal for the guided ultrasonic waves
f_1	Vibration frequency (shaker excitation)
h	Characteristic finite element size
k	Wavenumber
\mathbf{K}^c	Stiffness matrix of a finite cell
\mathbf{K}^e	Stiffness matrix of a finite element
\mathbf{M}^c	Mass matrix of a finite cell
\mathbf{M}^e	Mass matrix of a finite element
n	Integral number
p	Polynomial degree
χ	Number of nodes/modes per wavelength

Chapter 2

Symbol	Meaning
A	Unknown of the displacement Ansatz
B	Unknown of the displacement Ansatz
b	Half plate thickness
C	Unknown of the displacement Ansatz
c_g	Group velocity
c_L	Longitudinal wave velocity
c_p	Phase velocity
c_T	Transversal wave velocity
D	Unknown of the displacement Ansatz
d	Plate thickness
E	Young's modulus
\mathbf{e}_i	Unit vector in the direction of the i -th coordinate axis
f	Frequency
\mathbf{f}_b	Body force (per unit volume)
\mathbf{H}	Vector potential (Helmholtz decomposition)
i	Imaginary unit $\sqrt{-1}$
k	Wavenumber
t	Time
\mathbf{u}	Displacement vector

Symbol	Meaning
\mathbf{x}	Location vector $\{x_1, x_2, x_3\}$
α	Abbreviation $\omega^2/c_L^2 - k^2$
β	Abbreviation $\omega^2/c_T^2 - k^2$
δ_{ij}	Kronecker delta
$\boldsymbol{\delta}$	Identity tensor
$\boldsymbol{\varepsilon}$	Strain tensor
$\tilde{\lambda}$	First Lamé constant
λ	Wavelength
$\tilde{\mu}$	Second Lamé constant
ν	Poisson's ratio
ρ	Mass density
$\boldsymbol{\sigma}$	Stress tensor
ϕ	Scalar potential (Helmholtz decomposition)
ω	Circular frequency $\omega = 2\pi f$

Chapter 3

Symbol	Meaning
\mathbf{C}	Matrix of elastic coefficients
\mathbf{D}	Dielectric displacement vector
\mathbf{d}	Matrix of dielectric constants
\mathbf{E}	Electrical field
E	Electrical field strength
E_c	Coercive electrical field strength
E_{max}	Maximum electrical field strength
\mathbf{e}	Matrix of piezoelectric coupling constants
\mathbf{f}_b	Body force (per unit volume)
G	Gibb's free energy
H	Electrical enthalpy
\mathbf{L}_u	Mechanical differential operator matrix
\mathbf{L}_φ	Electrical differential operator matrix
\mathbf{n}	Unit normal vector
Q	Electric surface charge
\bar{Q}	Prescribed electric surface charge
q_b	Electric body charge
\mathbf{S}	Compliance matrix
T	Temperature
\mathbf{t}	Traction vector
$\bar{\mathbf{t}}$	Prescribed traction vector
T_c	Curie temperature
\mathbf{T}_n	Stress transformation matrix
\mathbf{u}	Displacement vector

Symbol	Meaning
Γ	Domain boundary
$\Gamma_{D,u}$	Domain boundary where mechanical Dirichlet boundary conditions are prescribed
$\Gamma_{D,\varphi}$	Domain boundary where electrical Dirichlet boundary conditions are prescribed
$\Gamma_{N,u}$	Domain boundary where mechanical Neumann boundary conditions are prescribed
$\Gamma_{N,\varphi}$	Domain boundary where electrical Neumann boundary conditions are prescribed
$\boldsymbol{\varepsilon}$	Strain tensor
$\boldsymbol{\kappa}$	Matrix of dielectric constants (permittivity)
$\boldsymbol{\kappa}^{(\boldsymbol{\sigma})}$	Matrix of dielectric constants for a constant mechanical stress state
ρ	Mass density
$\boldsymbol{\sigma}$	Stress tensor
φ	Electric potential
$\hat{\varphi}$	Prescribed electric potential

Chapter 4

Symbol	Meaning
\mathbf{A}	Assembly operator
b_e	Element width
$\tilde{B}(\xi)$	Linear blending function (-)
$\hat{B}(\xi)$	Linear blending function (+)
\mathbf{B}_u	Strain-displacement matrix
\mathbf{B}_φ	Electric field-electric potential matrix
\mathbf{C}	Matrix of elastic coefficients
\mathcal{C}	Constraint equation
c	Diagonal scaling factor for the HRZ lumping technique
\mathbf{D}	Dielectric displacement vector
\mathcal{D}	Metric tensor
d	Dimension of the problem
\mathbf{e}	Matrix of piezoelectric coupling constants
\mathbf{e}_i	Difference between a curved and a linear edge in the context of the blending function method
E_i	Edges of the reference element $i = 1, \dots, 12$
\mathbf{E}_i	Parametric description of the edge geometry $i = 1, \dots, 12$
\mathbf{F}	System load vector
f	Frequency
\mathbf{f}^*	Modified system load vector
\mathbf{f}_b	Body force per unit volume
F_i	Faces of the reference element $i = 1, \dots, 6$
\mathbf{F}_i	Parametric description of the face geometry $i = 1, \dots, 6$

Symbol	Meaning
\mathbf{f}_i	Difference between a curved and a bi-linear face in the context of the blending function method
F_L	Lagrange multiplier function
F_N	Nitsche function
F_p	Penalty function
\mathbf{F}_p	Mechanical point/concentrated force vector (FEM)
\mathbf{F}_q	Point/concentrated charge load (FEM)
\mathbf{f}_{surf}	Vector of surface loads (FEM)
\mathbf{f}_{uu}	Mechanical load vector (FEM)
$\mathbf{f}_{\varphi\varphi}$	Electrical load/charge vector (FEM)
h_e	Element height
\mathbf{J}	Jacobian matrix
\mathbf{K}	System stiffness matrix (FEM)
$\bar{\mathbf{K}}_{\text{piezo}}$	Effective dynamic system stiffness matrix for a piezoelectric body (Newmark)
\mathbf{K}^*	Modified system stiffness matrix (FEM)
\mathbf{K}_{uu}	Mechanical stiffness matrix (FEM)
$\mathbf{K}_{u\varphi}$	Direct piezoelectric coupling matrix (FEM)
$\mathbf{K}_{\varphi\varphi}$	Dielectric stiffness matrix (FEM)
\mathbf{L}_u	Mechanical differential operator matrix
$l e_n(\xi)$	n-th order Legendre polynomial
\mathbf{L}_φ	Electrical differential operator matrix
\mathbf{M}	System mass matrix
m	Total mass
$m^{(e)}$	Total mass of a single element
\mathbf{M}_{uu}	Consistent mass matrix (FEM)
$\mathbf{M}_{uu}^{\text{diag}}$	Diagonalized (lumped) mass matrix (FEM)
\mathbf{n}	Unit normal vector
n_{dof}	Number of degrees-of-freedom
n_{node}	Number of nodes
$N_i^{\text{type},3D}$	Three-dimensional shape function
N_i	Corner nodes of the reference element $i = 1, \dots, 8$
N^{int}	Internal shape function
N^{E_i}	Edge shape function $i = 1, \dots, 12$
N^{F_i}	Face shape function $i = 1, \dots, 6$
N^{N_i}	Nodal shape function $i = 1, \dots, 8$
n_e	Number of finite elements
\mathbf{N}_u	Matrix of shape functions on the element level (mechanical)
n_u	Number of mechanical point/concentrated loads
\mathbf{N}_φ	Matrix of shape functions on the element level (electrical)
n_φ	Number of point/concentrated charge loads
p	Polynomial degree
p_ξ	Polynomial degree in the local ξ coordinate
p_η	Polynomial degree in the local η coordinate
p_ζ	Polynomial degree in the local ζ coordinate

Symbol	Meaning
Q	Electric surface charge
\bar{Q}	Prescribed electric surface charge
$\mathbf{Q}^{(e)}(\boldsymbol{\xi})$	Elemental mapping function
q_b	Electric body charge
\mathbf{R}_{uu}	Damping matrix
\mathbf{t}	Traction vector
$\bar{\mathbf{t}}$	Prescribed traction vector
t	Time
\mathbf{U}	Global displacement vector (FEM)
\mathbf{u}	Displacement vector
$\bar{\mathbf{u}}$	Prescribed displacement vector
\mathbf{u}_e	Vector of mechanical degrees-of-freedom for a single finite element
$w_i^{(n)}$	Integration weights for a n-point Gaussian quadrature rule
\mathbf{x}	Global coordinates (x_1, x_2, x_3)
\mathbf{X}_i	Nodal coordinates $i = 1, \dots, 8$
α	Mass-proportional damping coefficient
β	Stiffness-proportional damping coefficient
β_p	Penalty parameter (penalty method)
β_N	Second Newmark parameter
β_S	Stabilization parameter (Nitsche's method)
Γ	Domain boundary
$\Gamma_{D,u}$	Domain boundary where mechanical Dirichlet boundary conditions are prescribed
$\Gamma_{D,\varphi}$	Domain boundary where electrical Dirichlet boundary conditions are prescribed
$\Gamma_{N,u}$	Domain boundary where mechanical Neumann boundary conditions are prescribed
$\Gamma_{N,\varphi}$	Domain boundary where electrical Neumann boundary conditions are prescribed
γ	Scaling factor of the electrical material properties
γ_N	First Newmark parameter
δ_{ij}	Kronecker delta
Δt	Time-step width
$\delta \mathbf{u}$	Virtual displacement
$\delta \Pi_c$	Constraint virtual work
$\delta \varphi$	Virtual electric potential
$\delta \chi_u$	Virtual mechanical work
$\delta \chi_\varphi$	Virtual electric work
$\boldsymbol{\kappa}$	Matrix of dielectric constants (permittivity)
$\boldsymbol{\lambda}$	Vector of Lagrange multiplier
$\boldsymbol{\xi}$	Local coordinates (ξ, η, ζ)
$\xi_i^{(n)}$	Integration points for a n-point Gaussian quadrature rule
$\Pi_{c,L}$	Constraint potential based on the Lagrange multiplier method
$\Pi_{c,N}$	Constraint potential based on Nitsche's method

Symbol	Meaning
$\Pi_{c,P}$	Constraint potential based on the penalty method
ρ	Mass density
$\varrho(\mathbf{A})$	Spectral radius of matrix \mathbf{A}
$\boldsymbol{\sigma}$	Stress tensor
Φ	Global electric potential vector (FEM)
φ	Electric potential
$\bar{\varphi}$	Prescribed electric potential
$\boldsymbol{\varphi}_e$	Vector of electrical degrees-of-freedom for a single finite element
Ω	Physical domain
Ω_e	Finite element domain
ω	Circular frequency $\omega = 2\pi f$
ω_{max}	Maximum circular frequency
$\mathbf{1}$	Identity (unit) matrix

Chapter 5

Symbol	Meaning
\mathbf{A}	Assembly operator
\mathbf{B}_u	Strain-displacement matrix
\mathbf{B}_φ	Electric field-electric potential matrix
\mathbf{C}	Matrix of elastic coefficients
d	Dimension of the problem
\mathbf{e}	Matrix of piezoelectric coupling constants
$h_{x_1}, h_{x_2}, h_{x_3}$	Finite cell dimensions
h_ξ, h_η, h_ζ	Integration sub-cell dimensions
k	Sub-cell refinement level
\mathbf{K}_{uu}	Mechanical stiffness matrix (FCM)
$\mathbf{K}_{u\varphi}$	Direct piezoelectric coupling matrix (FCM)
$\mathbf{K}_{\varphi\varphi}$	Dielectric stiffness matrix (FCM)
\mathbf{f}_b	Body force (per unit volume)
\mathbf{f}_{uu}	Vector of surface loads (FCM)
$\mathbf{f}_{\varphi\varphi}$	Electrical load/charge vector (FCM)
\mathbf{J}	Jacobian matrix
$\mathbf{J}^{(c)}$	Jacobian matrix of a single finite cell
$\mathbf{J}^{(sc)}$	Jacobian matrix of a single sub-cell
\mathbf{L}_u	Mechanical differential operator matrix
\mathbf{L}_φ	Electrical differential operator matrix
\mathbf{M}_{uu}	Consistent mass matrix (FCM)
n	Number of integration points
n_c	Number of finite cells
n_{sc}	Number of integration sub-cells
N_i	Corner nodes of the reference element $i = 1, \dots, 8$
N^{N_i}	Nodal shape function $i = 1, \dots, 8$

Symbol	Meaning
\mathbf{N}_u	Matrix of shape functions on the element level for the mechanical degrees-of-freedom
\mathbf{N}_φ	Matrix of shape functions on the element level for the electrical degrees-of-freedom
p	Polynomial degree
p_ξ	Polynomial degree in the local ξ coordinate
p_η	Polynomial degree in the local η coordinate
p_ζ	Polynomial degree in the local ζ coordinate
Q	Electric surface charge
\bar{Q}	Prescribed electric surface charge
q_b	Electric body charge
$\mathbf{Q}^{(e)}(\boldsymbol{\xi})$	Elemental mapping function
\mathbf{r}	Sub-cell coordinates (r, s, t)
\mathbf{t}	Traction vector
$\bar{\mathbf{t}}$	Prescribed traction vector
\mathbf{u}	Displacement vector
$\bar{\mathbf{u}}$	Prescribed displacement vector
\mathbf{u}_c	Vector of mechanical degrees-of-freedom for a single finite cell
\mathbf{U}	Global displacement vector (FCM)
$w_i^{(n)}$	Integration weights for a n-point Gaussian quadrature rule
\mathbf{x}	Global coordinates (x_1, x_2, x_3)
\mathbf{X}_i	Nodal coordinates $i = 1, \dots, 8$
$\alpha(\mathbf{x})$	Indicator function
Γ	Domain boundary
$\Gamma_{D,u}$	Domain boundary where mechanical Dirichlet boundary conditions are prescribed
$\Gamma_{D,\varphi}$	Domain boundary where electrical Dirichlet boundary conditions are prescribed
$\Gamma_{N,u}$	Domain boundary where mechanical Neumann boundary conditions are prescribed
$\Gamma_{N,\varphi}$	Domain boundary where electrical Neumann boundary conditions are prescribed
Γ_c	Finite cell boundary
Γ_{em}	Boundary of the embedding domain
Γ_I	Interface between physical and fictitious domain
$\delta\mathbf{u}$	Virtual displacement
$\delta\varphi$	Virtual electric potential
$\delta\chi_u$	Virtual mechanical work
$\delta\chi_\varphi$	Virtual electric work
$\boldsymbol{\kappa}$	Matrix of dielectric constants (permittivity)
$\tilde{\lambda}$	First Lamé constant
$\tilde{\mu}$	Second Lamé constant
$\boldsymbol{\xi}$	Local coordinates (ξ, η, ζ)
$\xi_i^{(n)}$	Integration points for a n-point Gaussian quadrature rule

Symbol	Meaning
ρ	Mass density
φ	Electric potential
$\bar{\varphi}$	Prescribed electric potential
φ_c	Vector of electrical degrees-of-freedom for a single finite cell
Φ	Global electric potential vector (FCM)
Ω	Physical domain
Ω_c	Finite cell domain
Ω_{em}	Embedding domain
Ω_{fict}	Fictitious domain
<i>phys</i>	Superscript or subscript indicating variables defined in the physical domain
<i>fict</i>	Superscript or subscript indicating variables defined in the fictitious domain
<i>em</i>	Superscript or subscript indicating variables defined in the whole domain
<i>sc</i>	Superscript or subscript indicating variables defined in the sub-cell domain
<i>I</i>	Superscript or subscript indicating variables defined on the interface between the fictitious and the physical domain

Chapter 6

Symbol	Meaning
E	Young's modulus
E_i	Edges of the reference element $i = 1, \dots, 12$
f	Frequency
\mathbf{F}	System load vector (FEM)
F_i	Faces of the reference element $i = 1, \dots, 6$
\mathbf{f}_{uu}	Vector of surface loads (FEM)
\mathbf{K}	System stiffness matrix (FEM)
\mathbf{K}_{uu}	Mechanical stiffness matrix (FEM)
$la_n(\xi)$	n-th order Lagrange polynomial
$le_n(\xi)$	n-th order Legendre polynomial
\mathbf{LM}	Topology/location matrix (FEM)
$lo_n(\xi)$	n-th order Lobatto polynomial
\mathbf{M}	System mass matrix (FEM)
\mathbf{M}_{uu}	Consistent mass matrix (FEM)
N_i	Corner nodes of the reference element $i = 1, \dots, 8$
N_i^{type}	One-dimensional shape function
$N_i^{\text{type},3D}$	Three-dimensional shape function
n_{dof}	Number of degrees-of-freedom for a single element
n_e	Number of finite elements

Symbol	Meaning
n_l	Number of digits lost due to round-off errors
N^{int}	Internal shape function
N^{E_i}	Edge shape function $i = 1, \dots, 12$
N^{F_i}	Face shape function $i = 1, \dots, 6$
N^{N_i}	Nodal shape function $i = 1, \dots, 8$
n_{sys}	Number of degrees-of-freedom for the whole model
p	Polynomial degree
p_ξ	Polynomial degree in the local ξ coordinate
p_η	Polynomial degree in the local η coordinate
p_ζ	Polynomial degree in the local ζ coordinate
$q_i^{(e)}$	Edge orientation flag (C_0 -continuity)
$\mathbf{q}_i^{(f)}$	Vector of face orientation flags (C_0 -continuity)
S	Mapping matrix
x	Global coordinates (x_1, x_2, x_3)
X_i	Nodal coordinates $i = 1, \dots, n_{dof}$ (SEM)
δ_{ij}	Kronecker delta
Δt	Time-step width
κ	Condition number
λ_{max}	Largest eigenvalue of a matrix
λ_{min}	Smallest eigenvalue of a matrix
ν	Poisson's ratio
ρ	Mass density
$\varrho(\mathbf{A})$	Spectral radius of matrix A
ξ	Local coordinates (ξ, η, ζ)
ω	Circular frequency $\omega = 2\pi f$
ω_{max}	Maximum circular frequency

Chapter 7

Symbol	Meaning
A	Amplitude
A_u	Area
a	Scale (CWT)
b	Position (CWT)
b_e	Element width
C	Wavelet coefficient
c_g	Group velocity
c_L	Longitudinal wave velocity
c_p	Phase velocity
c_T	Transversal wave velocity
E	Young's modulus
$e(t)$	Envelope of the Hilbert-transform

Symbol	Meaning
E_{rel}	Relative error
$F(t)$	Time-dependent signal
\hat{F}	Amplitude of a time-dependent signal
f	Frequency
f_c	Center frequency of a Hann-window modulated sine-burst
f_r	Resonance frequency
$H(f(t))$	Hilbert transform of the function f
\mathbf{K}_{uu}	Mechanical stiffness matrix (FEM)
\mathbf{M}_{uu}	Consistent mass matrix (FEM)
n	Number of cycles of a Hann-window modulated sine-burst
n_{dof}	Number of degrees-of-freedom
$\text{nnz}(\mathbf{A})$	Number of non-zero element of matrix \mathbf{A}
p	Polynomial degree
p_{x_1}	Polynomial degree in the global x_1 coordinate
p_{x_2}	Polynomial degree in the global x_2 coordinate
p_{x_3}	Polynomial degree in the global x_3 coordinate
p_ξ	Polynomial degree in the local ξ coordinate
p_η	Polynomial degree in the local η coordinate
p_ζ	Polynomial degree in the local ζ coordinate
T	Time of oscillation
t	Time
t_c	Time-of-flight
t_{cpu}	Computational time
\mathbf{u}	Displacement vector
$\hat{\mathbf{v}}$	Mode shape
\mathbf{x}	Global coordinates (x_1, x_2, x_3)
Δt	Time-step width
λ	First Lamè constant
λ_{A_0}	Wavelength of the fundamental anti-symmetric Lamb mode
λ_{S_0}	Wavelength of the fundamental symmetric Lamb mode
μ	Second Lamè constant
ν	Poisson's ratio
ρ	Mass density
χ_{A_0}	Number of nodes/modes per fundamental anti-symmetric wavelength
χ_{S_0}	Number of nodes/modes per fundamental symmetric wavelength
$\boldsymbol{\xi}$	Local coordinates (ξ, η, ζ)
Ψ	Mother wavelet
Ω	Eigenvalue
ω	Circular frequency $\omega = 2\pi f$

Chapter 8

Symbol	Meaning
A	Amplitude
b_e	Element width
\mathbf{C}	Matrix of elastic coefficients
c_g	Group velocity
c_p	Phase velocity
d	Plate thickness
\mathbf{d}	Matrix of dielectric constants
\mathbf{e}	Matrix of piezoelectric coupling constants
E_{rel}	Relative error
$F(t)$	Time-dependent signal
\hat{F}	Amplitude of a time-dependent signal
f	Frequency
f_c	Center frequency of a Hann-window modulated sine-burst
\mathbf{f}_{uu}	Vector of surface loads
$\mathbf{f}_{\varphi\varphi}$	Electrical load/charge vector
h	Beam/plate thickness
k	Sub-cell refinement level
\mathbf{K}_{uu}	Mechanical stiffness matrix
$\mathbf{K}_{u\varphi}$	Direct piezoelectric coupling matrix
$\mathbf{K}_{\varphi\varphi}$	Dielectric stiffness matrix
\mathbf{K}^*	Modified system stiffness matrix
\mathbf{M}_{uu}	Consistent mass matrix
MAC	Value of the modal assurance criterion
n	Number of cycles of a Hann-window modulated sine-burst
n_c	Number of finite cells
n_{dof}	Number of degrees-of-freedom
n_f	Eigenfrequency number
n_{sample}	Number of sampling points
p	Polynomial degree
p_{x_1}	Polynomial degree in the global x_1 coordinate
p_{x_2}	Polynomial degree in the global x_2 coordinate
p_{x_3}	Polynomial degree in the global x_3 coordinate
p_ξ	Polynomial degree in the local ξ coordinate
p_η	Polynomial degree in the local η coordinate
p_ζ	Polynomial degree in the local ζ coordinate
t	Time
t	Plate thickness
\mathbf{u}	Displacement vector
\mathbf{U}	Global displacement vector (FEM/FCM)
\mathbf{x}	Global coordinates (x_1, x_2, x_3)
Δt	Time-step width
γ	Fiber angle

Symbol	Meaning
κ_0	Vacuum permittivity
$\boldsymbol{\kappa}$	Matrix of dielectric constants (permittivity)
λ_{A_i}	Wavelength of the i -th anti-symmetric Lamb mode
λ_{S_i}	Wavelength of the i -th symmetric Lamb mode
ρ	Mass density
ν	Poisson's ratio
φ	Electric potential
φ_{norm}	Normalized electric potential
Φ	Mode shape
Φ	Global electric potential vector (FEM/FCM)
χ_{A_0}	Number of nodes/modes per fundamental anti-symmetric wavelength
χ_{S_0}	Number of nodes/modes per fundamental symmetric wavelength
$\boldsymbol{\xi}$	Local coordinates (ξ, η, ζ)
ω	Circular frequency $\omega = 2\pi f$
ω	Eigenvalue

Chapter 9

Symbol	Meaning
b_e	Finite element size
\mathbf{C}	Matrix of elastic coefficients
d_a	Thickness of material A
d_b	Thickness of material B
d_h	Hole diameter
d_l	Lattice spacing
$F(t)$	Time-dependent excitation force
f	Frequency
f_c	Center frequency of a Hann-window modulated sine-burst
L	Plate thickness
l_f	Distance between the Fibonacci array and the excitation point
L	Plate thickness of the Fibonacci array model
L_p	Plate length of the Fibonacci array model
l_p	Plate length of the square hole arrangement model
l_{p_b}	Distance between the Fibonacci array and the second measurement point
l_{P_b}	Distance between the square hole arrangement array and the second measurement point
l_{p_i}	Distance between the Fibonacci array and the first measurement point
l_{P_i}	Distance between the square hole arrangement array and the first measurement point
l_1	Distance between the beginning of the square hole arrangement array and excitation point

Symbol	Meaning
l_2	Distance between the end of the Fibonacci array and excitation point
N	Number of Fibonacci cells
n	Number of cycles of a Hann-window modulated sine-burst
p	Polynomial degree
r_{bi}	Transmitted spectrum
S_i	i -th Fibonacci sequence
t	Time
t_p	Plate thickness of the square hole arrangement model
\mathbf{u}_b	Displacement vector at point P_b
\mathcal{U}_b	Fourier transform of the displacement vector at point P_b
\mathbf{u}_i	Displacement vector at point P_i
\mathcal{U}_i	Fourier transform of the displacement vector at point P_i
w_p	Plate width of the square hole arrangement model
λ	Wavelength
ρ	Mass density

Abstract

The focus of the present thesis is on further developing and improving numerical methods based on higher order polynomials as Ansatz functions. The research into this field is strongly motivated by structural health monitoring (SHM) activities. In the context of SHM applications, especially accurate results for ultrasonic guided wave propagation problems are of utmost importance. Such numerical simulations are computationally demanding, because online monitoring systems operate in a high frequency-short and wavelength regime. The efficiency of commercial software packages, on the other hand, is limited when a fine spatial as well as temporal discretization is required. This is true especially in the context of multi-physics applications. Therefore, higher order finite element methods (*HO-FEMs*) and fictitious domain methods are promoted. Generally speaking, these higher order methods significantly decrease the computational effort and are therefore a viable means to address the shortcomings of available software tools, commonly based on the *h*-version of the finite element method (*h-FEM*).

To provide a holistic simulation approach, the state-of-the-art of numerical simulation methods is extended in several aspects. In a first step, higher order finite element (*HO-FE*) and fictitious domain approaches are extended to smart structure applications, especially piezoelectricity. Second, the concept of the finite cell method (FCM) is applied to wave propagation analysis. By introducing spectral Ansatz functions and an appropriate mass-lumping technique for cut cells (cells intersected by a physical boundary), the so-called spectral cell method (SCM) combines the high convergence rates of *HO-FEMs*, the automated mesh generation of fictitious domain methods and computational time (CPU time) savings of explicit time-stepping methods. The SCM is consequently seen as a viable tool to provide a deeper insight into wave propagation phenomena.

The proposed methods are verified and validated using several numerical benchmark problems and experimental data. The results indicate the superior efficiency and high accuracy of the SCM, probably making it the method of choice for wave propagation analysis in thin-walled structures.

Kurzzusammenfassung

Der Schwerpunkt der vorliegenden Dissertation liegt auf numerischen Berechnungsmethoden, die höherwertige Ansatzfunktionen verwenden. Motiviert werden diese Entwicklungen durch Forschungsarbeiten zum Thema „Structural Health Monitoring“ (SHM). Für den gezielten Entwurf solcher Überwachungssysteme ist das detaillierte Verständnis von Wellenausbreitungsvorgängen unerlässlich. Da die angesprochenen Systeme üblicherweise im hohen kHz-Bereich arbeiten, liegen die zu beobachtenden Wellenlängen im mm-Bereich. Das hat zur Folge, dass zur Berechnung elastischer Ultraschallwellen sowohl eine feine zeitliche als auch räumliche Auflösung benötigt wird. Bei solchen Konstellationen stoßen kommerzielle Berechnungsprogramme, hinsichtlich der Speicheranforderungen und Genauigkeit, schnell an ihre Grenzen. Deshalb müssen neuartige Methoden entwickelt werden, um effizientere und hochauflösendere Simulationen sicherzustellen. Aus diesem Grund stehen die Finite-Elemente-Methode (FEM) und die Finite-Zellen-Methode (FCM) im Fokus der vorliegenden Arbeit. Für die Formulierung beider Methoden wird auf höherwertige Ansatzfunktionen zurückgegriffen; mittels dieser Ansätze können die Defizite von kommerziellen Berechnungsprogrammen, die zumeist auf der h -Version der FEM beruhen, umgangen werden.

Da es der Anspruch dieser Arbeit ist, einen allgemein gültigen Berechnungsansatz für beliebig komplexe Strukturen mit integrierten SHM-Systemen zu liefern, wird der aktuelle Stand der Technik in mehreren Aspekten erweitert. Ansätze zur Berechnung von Strukturen, die elektro-mechanisch gekoppelte Eigenschaften aufweisen, werden sowohl für die höherwertige FEM, als auch für die FCM umgesetzt. Mit dieser Erweiterung können nun auch Modelle für piezoelektrische Wandler in die Berechnung einbezogen werden. In einem zweiten Schritt wird die FCM erstmalig zur Simulation von elastischen Ultraschallwellen angewandt. In diesem Zusammenhang wird der Einsatz von spektralen Ansatzfunktionen in Verbindung mit einer geeigneten Methode zur Diagonalisierung der Massenmatrix von geschnittenen Zellen (Zellen die vom Rand des physikalischen Gebietes geteilt werden) vorgeschlagen. Durch diese Maßnahmen kann die Effizienz transienter Analysen im Vergleich zu herkömmlichen Verfahren enorm gesteigert werden. In Analogie zur Unterscheidung zwischen der FEM und der Spektralen-Elemente-Methode (SEM) wird die entwickelte Methodik als Spektrale-Zellen-Methode (SCM) bezeichnet. Die SCM vereint somit die hohen Konvergenzraten von höherwertigen FE-Formulierungen, mit der automatisierten Diskretisierung von fiktiven Gebietsmethoden und mit der Rechenzeiterparnis, die durch die Benutzung von expliziten Zeitintegratoren erzielt werden kann.

Die angesprochenen Vorteile machen die SCM zu einem vielversprechenden Berechnungswerkzeug für die detaillierte Untersuchung von Wellenausbreitungsvorgängen. Die entwickelten Methoden werden mit Hilfe von mehreren numerischen Beispielen und experimentellen Daten verifiziert und validiert. Die erzielten Ergebnisse untermauern die Aussage, dass die SCM ein weitverbreitetes Verfahren zur Berechnung von geführten Wellen in dünnwandigen Strukturen werden kann.

Chapter 1

Introduction

The first chapter introduces the topic of Structural Health Monitoring (SHM) and provides a comprehensive overview on current research activities dealing with both online monitoring systems and the state-of-the-art in numerical wave propagation analysis. The latter subject is also an essential aspect of the further content of the thesis at hand.

1.1 SHM - General principles and current research activities

SHM objectives The primary objectives of every SHM system are the continuous monitoring of safety-relevant component parts during service and the identification of anomalies or damages such as cracks, delaminations and debondings in structures. In this context, the term continuous can also be understood in the way of taking measurements periodically throughout the operation-time. One proposal to achieve these objectives is to equip engineering structures such as airplanes, as depicted in Fig. 1.1, with a network of transducers in a way that is inspired by the human nervous system [1].



Figure 1.1: Analogy of a SHM network and the human nervous system.

In the applications considered in the present thesis, sensors and actuators are piezoelectric transducers, but in real-life applications they can also be pressure, temperature or moisture sensors, depending on defect/anomaly to be identified. An online monitoring system should be devised such that - based on a structure similar to the nervous system - it is able to report on the “health” state of the structure during service time. This includes tasks such as the detection and the localisation of damages as well as the prediction of their severity. This approach can therefore either be used to increase the service-life of a structure or to maximize the utilization of the material. The current practice, however, is to inspect the structural integrity based on scheduled maintenance [2] activities. These inspections are executed using standard non-destructive testing techniques, such as visual inspection and/or ultrasound techniques [3]. Since such an approach is both time-consuming and dependent on well-trained personnel, there is a high potential for saving costs and avoiding errors. Therefore, a transition from scheduled to condition based maintenance should take place, as also demanded by high-tech industries [4]. Accordingly, the main motivation driving the need for a successful application of SHM systems is the prospect of a significant reduction of inspection costs without introducing safety risks [5, 6]. One possible way to achieve the aforementioned goals - design and successfully apply a SHM system - could be to transfer and to extend already existing techniques, known from the condition monitoring of machines, to safety-relevant parts.

Wave-based SHM Over the years, many dynamics-based SHM techniques have been developed - and valuable reviews of the state-of-the-art can be found in [5, 7]. Among the dynamics-based techniques, guided wave (GW) inspections provide a good compromise in terms of the sensitivity to defects and the extent of the area that can be monitored. GWs show the ability to travel relatively long distances within the structure with little attenuation compared to bulk waves [8–11].

In isotropic, homogeneous plates of constant thickness these ultrasonic guided waves are referred to as Lamb waves, named after their discoverer Horace Lamb [12]. Despite their complex characteristics, such as the occurrence of at least two different modes for each frequency and the highly dispersive behavior [13], they are still a common choice for the online monitoring of structures [14–18]. The majority of today’s research is devoted to studying GW-based approaches to SHM as it has matured to an accepted technology for damage detection purposes [5, 6, 10, 11, 19, 20].

Mode conversion As mentioned before (Paragraph Wave-based SHM), Lamb waves can propagate in different modes. One characteristic feature is their ability to convert into each other [15]. This mode conversion is a key aspect of the damage quantification process using Lamb waves, defined as the phenomenon in which energy is transferred from one wave mode to another. This partial energy transfer results in an altered particle motion of the wave mode; the out-of-plane displacement component can be amplified compared to the incident mode for instance [10]. A launched S_0 mode partially converts to an A_0 upon arrival at the defect location, or vice versa [15, 21]. We have to keep in mind, however, that only asymmetric perturbations with respect to the middle plane of the structure can cause this phenomenon [15].

Damage detection Much of the literature considers excitation configurations relying on the first (fundamental) symmetric (S_0) or anti-symmetric (A_0) for the interrogation of the structural state. The applied frequency range is commonly below the cut-off frequency of the second anti-symmetric (A_1) mode [5, 6, 10].

A more recent approach, however, uses so-called “non-linear” acoustics. Here, higher order modes are employed to detect damages. One popular method is to exploit the second order harmonics to indicate defects within the structure. The prerequisite is that the different modes have a matching phase and group velocity, to ensure that enough energy can be transferred from the fundamental to the second order harmonic wave. The basic idea is to launch a single frequency ultrasonic wave. After propagating a certain distance in the material, the wave is composed of the original component and of a new component with double frequency (second order harmonic). Li *et al.* [22] apply the S_1 - S_2 -mode pair to detect thermal fatigue in composite structures. These materials are widely used in aerospace applications, where they are consequently subjected to frequent variations in temperature. As a consequence, material degradation can be induced and damages may accumulate. This change of the original structure is observed by monitoring the change in the non-linear acoustic parameter. This parameter is essentially the ratio A_{S_2}/A_{S_1} , where A_{S_1} denotes the amplitude of the S_1 -mode (fundamental wave) and A_{S_2} represents the amplitude of the S_2 -mode (second order harmonic wave). In this case it is assumed that the distributed micro-cracks (micro-structural defects) or lattice anomalies are the main source of non-linearity. Preull *et al.* [23–25] emphasize that the normalized acoustic non-linearity measured with Lamb waves is directly related to the fatigue damage. They thereby assess that non-linear techniques can quantitatively detect and characterize plasticity driven material damage prior to the formation of micro-cracks.

Aymerich and Staszewski employ a different method for impact damage detection by way of non-linear acoustics [26]. Their technique is based on the following methodology: First, an ultrasonic wave is introduced at an arbitrary point A . Simultaneously, the structure is also excited modally (with an eigenfrequency - f_1) at point B . If the structure is intact, the frequency spectrum will contain only the frequency components f_0 the guided wave has been excited with. On the other hand, if the structure is damaged, the high frequency wave will be modulated by the low frequency vibration. The formation of frequency sidebands ($f_0 \pm n f_1$) is therefore observed. The intensity of the modulation is strongly related to the crack size [27]. Moreover, it has to be mentioned that all effects depend on the amplitude of the modal/vibration excitation. Despite the fact that various theoretical explanations are given in literature, it seems that these non-linear effects are not well understood [27].

Damage localization Features such as mode conversion, transmission and reflection are the basis for damage localization algorithms. Defects in structures can be found by employing various methods, of which the most important ones are mentioned in the following. One approach is to use a triangulation method [28, 29]. Another scheme is based on tomography techniques [30–34] and time reversal methods [35]. A more complex analysis is required if artificial neural networks are to be applied for damage detection purposes [36–38]. Extensive data sets are needed in order to teach the algorithm how to determine the existence of damages. However, if the teaching data sets do not cover the conditions encountered in real-life applications, such methods will be unable to detect damages reliably and therefore may fail. In reference [39] a migration based technique is used, also

accounting for the differences in wave speed, depending on the propagation angle. This approach is an extension to the well-known time-of-arrival triangulation techniques that are often used for isotropic or quasi-isotropic materials.

Wave propagation in heterogeneous materials The propagation of ultrasonic guided waves in real-life structures is highly influenced by many factors - including, but not limited to material properties (micro-structure of the material, anisotropy class, etc.) and ambient conditions such as temperature, moisture, and corrosion among others. As this is a very complex topic, only a few of the many parameters are illustrated in Fig. 1.2. In recent years, the focus of the research activities shifted from relatively simple homogenous, isotropic materials to more complex composite and sandwich plates [40–42]. The different branches of engineering and industry show a clear tendency to rely on such materials. The basic advantage of composites is their higher strength relative to mass in comparison to other materials. Moreover, they exhibit a higher corrosion stability. At the same time, composites are more sensitive to impact actions [43, 44], which can cause damages in the form of cracks or delaminations [45–47]. It is especially the low velocity impacts that are of interest, as they often result in barely visible damages that are hardly detectable using conventional visual testing techniques. Such damages are critical and could potentially result in destruction of the component part. Since a special focus is placed on thin-walled, lightweight structures which are typically made of carbon or glass fiber reinforced plastic (CFRP, GFRP) and sandwich panels, one has to deal with highly heterogeneous materials. Moreover, the material anisotropy has to be taken into account which further complicates the damage detection process [39, 48–50].

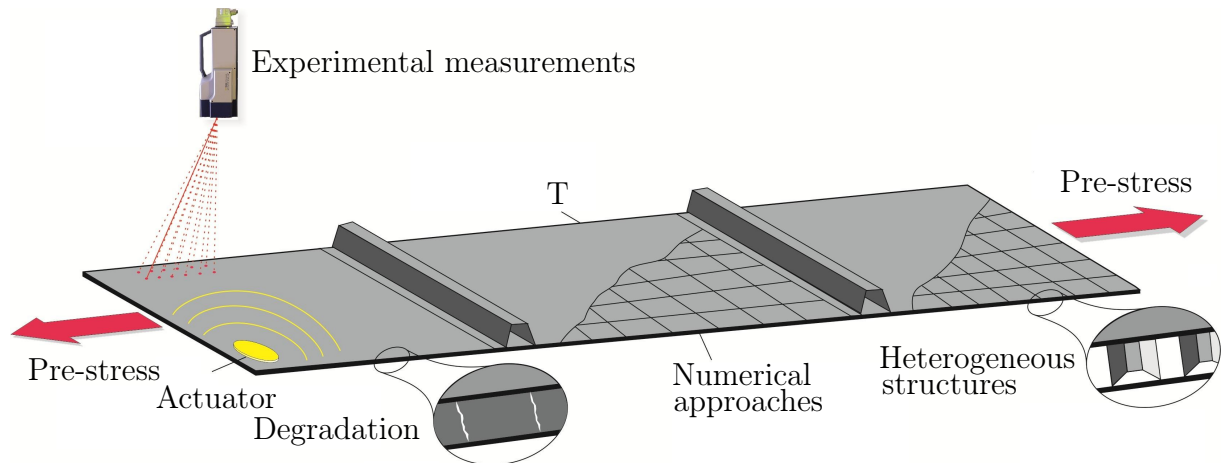


Figure 1.2: Current research topics in SHM.

These kinds of materials pose significant difficulties for most numerical methods, as the micro-structures of such heterogeneous materials need to be accurately resolved in order to capture phenomena such as transmission, interaction, scattering and conversion of the different wave modes [51, 52]. Structural elements like stringers or rivets pose additional problems as they cause further wave scattering and render the wave signal very hard to interpret.

Influence of ambient conditions on SHM concepts Pre-stressing, temperature variations [18, 53, 54] and different moisture contents are among the possible parameters that may additionally influence the wave propagation in real-life structures. It is especially the last point that is critical for high-tech materials typically used in the off-shore wind energy and aeronautical industries. Several of these influencing factors have already been addressed in extensive research campaigns. The first important topic in the context of ambient conditions that needs to be discussed further is the dependency of the material properties on the moisture content.

Moisture The effect of moisture absorption on the Lamb wave propagation in viscoelastic composite materials has been studied by Schubert and Herrmann [55]. They stress the fact that a SHM system is subjected to changes in the ambient conditions and material degradations, entailing the necessity to incorporate measures to distinguish between these changes and real structural damages. All investigations in reference [55] are based on a higher order plate theory (not to be confused with higher order shape functions for the finite element method). They compared experimental results with different moisture contents to determine its effect on the wave propagation. Schubert and Herrmann observed changes in the wave velocity and damping characteristics. If a baseline approach is used for damage detection, these effects need to be included in the model. The experimental methodology was as follows: (i) The carbon fiber reinforced plastic plate was stored for 25 days in a climate chamber at $70^{\circ}C$ and 80% humidity. (ii) Thereafter, the new material properties were recorded. Generally speaking, they found that the wave velocity decreases and that the damping increases due to the described conditioning process. The bonding layer is also influenced by the procedure as the energy transfer from the piezoelectric transducer to the host structure is decreased (degradation of the adhesive layer).

Temperature Several researchers have recently conducted studies on the effect of the ambient temperature on the propagation of elastic guided waves [53, 54, 56–58]. Clarke [56], for example, employs a baseline subtraction approach to account for temperature variations. His aim is to develop temperature stable piezoelectric sensors for a mono-modal excitation of Lamb wave modes. Lu and Michaels [54] also propose an approach to detect structural damages in the presence of unmeasured temperature changes. They assume that the primary effect of temperature on the recorded signals is a dilatation or compression of the time signal caused by the velocity change and the thermal expansion of the structure under observation. As a secondary effect the distortion of the wave form can be noticed. An attempt to apply the proposed strategy will require baseline measurements at various temperatures, reflecting the service-conditions. Naturally, the probability of detection of structural damages increases with a finer temperature resolution of the baseline data. The basic idea of the proposed method is to find the best match between a time trace in the baseline data set and the measured time signal. The mean square deviation of the two signals and the maximum residual amplitude of the differential signal are recommended as suitable error indicators. In a second step, the time axis of the previously recorded baseline data is adjusted to the experimental results by stretching or compressing it. This procedure serves as a means to compensate the temperature variation and thus to ensure that the damage detection methodology can be executed. The physically reasonable assumption here, is that the mean squared error between two signals is related to the amount of

damage, given that there are no other changes. In further literature the described method is referred to as a combination of optimal baseline selection (OBS) and baseline signal stretch (BSS). Croxford *et al.* [53], Moll [58, 59] and Schubert [57] employ the same methodology to account for changes in the ambient temperature. Moll has successfully applied this procedure to aluminum and glass fiber reinforced plastic plates. To identify structural damages he utilizes a novelty detection algorithm. Note however, that Lu and Michaels use diffuse ultrasonic waves excited by an impulse excitation and generated by multiple reflections [54]. The discussed approach requires an comprehensive baseline data set. Therefore, the continuous acquisition of data for temperature compensation methods is described by Putkis and Croxford [60].

Corrosion Corrosion, induced by the ambient conditions, is a different kind of flaw that can be monitored using ultrasonic guided waves. Miller *et al.* [61] monitor the corrosion of reinforced concrete (RC). Today, corrosion is one of the primary durability concerns for RC. The fact that this process of chemical degradation eventually causes delamination or separation of the steel rebar from the concrete affects the propagating waves as well as the measured signal strength. However, determining the current state of health of the RC appears to be a difficult task, because of two opposing effects: (i) Due to the corrosion, the surface roughness increases - leading to a reduction in signal strength. (ii) At the same time, the signal strength is increased by a separation of the steel bar and the surrounding concrete. Miller *et al.* [61] suggest to make use of the fact that the wave velocity varies with the applied stress. The time-of-flight should consequently depend on the stress level in the rod. As the stress level also changes with the quality of the bonding between steel bar and concrete, the health of the system can be assessed.

In civil engineering SHM systems are already in use. A famous example is the on-line monitoring system implemented on the Tsing Ma Bridge in China. It has been successfully applied since the bridge's construction in May 1997 [62].

Steps for the development of a robust SHM-System The ultimate goal of SHM is to create an autonomous online monitoring system that is able to locate damages within the structure as well as to determine their size and if possible to predict the remaining lifetime of the assembly. Different steps need to be completed in order to reach these goals. The workflow is as follows:

0. **Numerical simulations** (related issues are: designing a SHM system; optimal placement of transducers; physical understanding of important wave propagation phenomena),
1. **Data acquisition** (related issues are: energy efficiency of the transducers; the wireless transmission of measured data; data storage),
2. **Signal processing** (related issues are: feature extraction to facilitate damage detection under varying ambient conditions),
3. **Numerical simulations** (related issues are: assessing the severity of the damage; assessing the remaining service lifetime).

The zeroth step was included although it is not necessarily related to SHM itself. Nonetheless, it is an important approach to enhance the understanding of wave propagation phenomena and the wave interaction with defects. It can consequently be seen as prerequisite that facilitates a fast and effective development of online monitoring systems. Without verified and thoroughly validated numerical simulation tools only experimental tests will provide reliable information. Thus, an efficient virtual engineering software is needed to try to reduce the development costs of SHM systems.

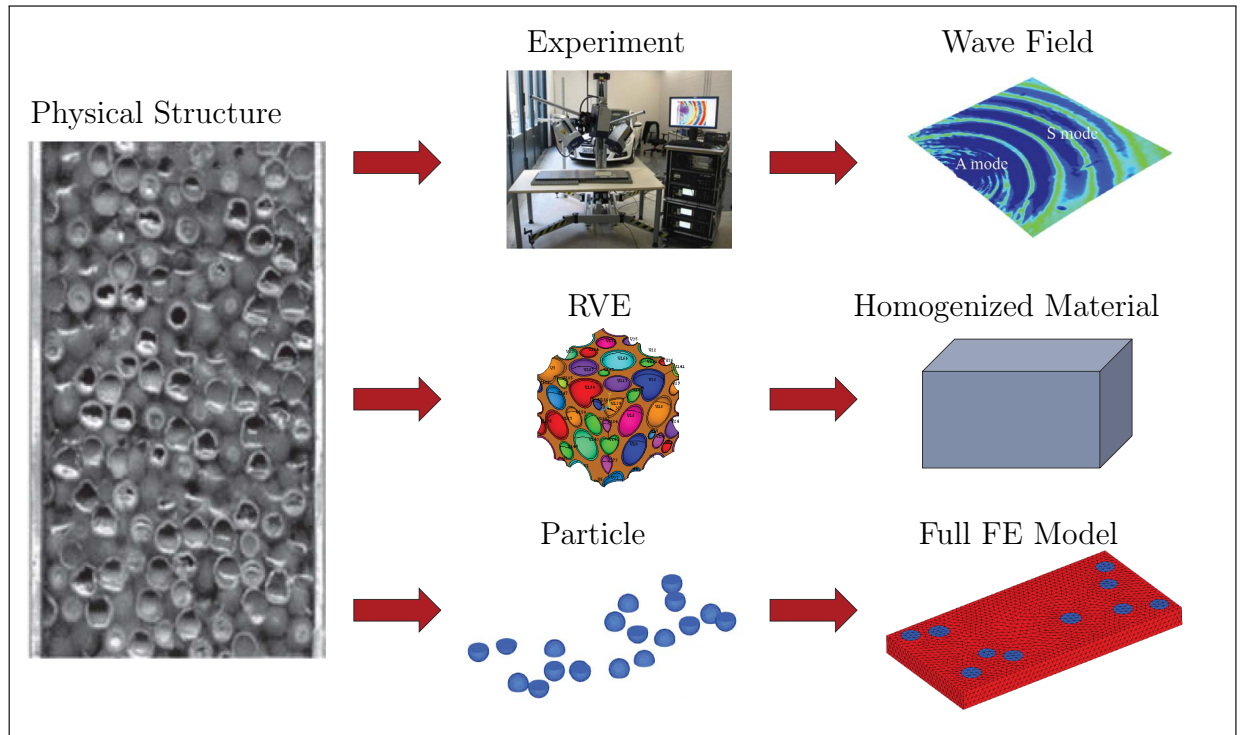


Figure 1.3: Experimental and numerical investigation of heterogeneous materials for SHM purposes.

The main objective of the present thesis, however, is to develop a numerical simulation tool for the analysis of guided ultrasonic waves. Fig. 1.3 illustrates different approaches to tackle this task. Furthermore, experimental measurements are required in order to validate the methodologies. Numerical methods - with a special focus on wave propagation analysis - are extensively discussed in Section 1.2. Experimental techniques are not in the scope of the current work and are therefore only briefly mentioned at this point. Measurement results can be obtained, for example, by using a Laser Scanning Doppler Vibrometer (LSDV). The full wave field information can be recorded by employing a three-dimensional LSDV [6]. Thereafter, the measurements can be used to visualize the damage interaction and the propagation of GWs. Lasers offer the advantages of a high spatial resolution and contactless measurements [63–65], which is why they often come into use. Other possibilities would include water and/or air-coupled ultrasound measurements [66, 67] or speckle interferometry [68]. No coupling medium is required for these approaches either.

The experimental data can then be used to validate existing numerical approaches. One way to simulate heterogeneous materials is to determine the effective material properties. In the case of a sandwich materials the core layer can be homogenized, for example. This procedure will facilitate the finite element (FE) discretization process, but has the drawback that it is only applicable in a low frequency range. For higher frequencies, the interactions of the waves with the core material or with the micro-structure are not resolved at all, which causes significant errors in the course of a respective simulation [41, 42].

A full scale model of the structure is needed to circumvent this problem. Here, the core layer is geometrically resolved. This methodology provides very accurate simulations, but, on the other hand, may result in prohibitively large computational costs [40]. Accordingly, different techniques are called for to solve wave propagation problems in heterogeneous media. Various numerical methods that are suitable for wave propagation analysis are discussed in detail in Section 1.2.

Damage repair Since one of the main goals of SHM systems is to increase the service-lifetime of safety-relevant component parts, repair techniques need to be addressed as well. For the sake of completeness, a few approaches are briefly introduced at this point. Ahn *et al.* [69] investigated one-sided patch repairs as one possible option to prolong the service-life of a damaged structure. Pavlopoulou *et al.* [19] studied life cycle health monitoring as a means to avoid extended periods of inspections, to reduce maintenance costs and to rule out unexpected catastrophic failures. They successfully applied pattern recognition algorithms for damage classification [70, 71]. An experimental and numerical evaluation of the performance of externally bonded and scarf type bonded patches for the repair of aerospace structures made of composite materials is provided in references [20, 71, 72]. The authors deployed different online monitoring techniques, such as digital image correlation (DIC) and guided wave propagation (excited and received by piezoelectric transducers), to assess the damage detection capabilities of their signal processing approach. They point out that the proposed methods can successfully be applied for online monitoring purposes. Furthermore, the authors recommend the second repair approach as it provides a higher join efficiency.

Miscellaneous research activities concerned with geometrically non-linear analysis are pursued and should also be mentioned briefly. In [73] Abedinnasab and Hussein investigate the wave propagation in a geometrically non-linear rod and beam model. They observe amplitude dependent shifts in frequency, phase and group velocity in the dispersion spectrum. This can further complicate all efforts directed at developing SHM systems.

The cited scientific works clearly show that there is a steadily growing research interest in SHM activities. Although a lot of progress was made in the last decades, there is still not enough secured knowledge about basic problems related to online monitoring of structures using ultrasonic guided waves. Since the present thesis aims to provide one step to gain a deeper understanding of the underlying physics by using advanced numerical models for the simulation of elastic guided waves in thin-walled structures, the next section features a comprehensive review of the state-of-the-art in wave propagation analysis using numerical methods.

1.2 Numerical methods for wave propagation analysis

The current section sets out to provide an answer to the question “Why are higher order finite element methods (*HO*-FEMs) indispensable for wave propagation analysis?”. Furthermore, potential research areas are discussed - resulting in the motivation for the thesis at hand.

Generally speaking, wave propagation problems require extremely accurate solutions [74]. The reason for this is that the numerical dispersion error produced by the method tends to distort the basic appearance of the time domain solution. The term *dispersion error* refers to the fact that higher frequency components of an FE solution exhibit a phase lead, that is to say they propagate faster than they theoretically should. Accordingly, a phase shift in the signal can be observed. This phase shift can, for example, cause destructive interferences where constructive ones are expected and vice versa [74].

The computationally highly demanding task of simulating the propagation of ultrasonic guided waves is most commonly solved using explicit structural dynamics solvers. To accurately resolve the wave front of ultrasonic guided waves, a fine temporal [75] as well as spatial [76, 77] discretization is needed. Despite these rigorous requirements, the *h*-version of the finite element method (*h*-FEM) is often applied for wave propagation analysis. This can be attributed to the wide-spread distribution of commercial FE software that typically features only low order FEs ($p \leq 3$). In an article by Willberg *et al.* [78] it was demonstrated, however, that conventional linear FEs based on a displacement formulation are not suitable to solve the wave equation accurately enough and that they quickly reach their limits - in terms of computational effort and memory storage requirements - if ultrasonic guided wave propagation problems are considered. Moreover, one has to keep in mind that certain restrictions have to be imposed on the aspect ratio and angle between element edges of low order FEs. A value of approximately 1 and 90° is recommended, respectively. This also implies that - if possible - all elements should be of similar size [79]. These measures are very important, since it has been conclusively demonstrated that meshing is an issue when studying wave scattering problems. This is especially true for weak scatterers, for large variations in the element sizes can cause wave scattering and beam steering due to a mismatch of the mechanical impedance [79].

Analytical and semi-analytical methods To determine the point-wise response of geometrically simple structures and to calculate dispersion diagrams, analytical or semi-analytical methods are an appropriate choice [15, 21, 80–83]. These approaches also allow for an examination of the physical damping on the dispersion curves [84]. However, it is challenging - if at all possible - to provide an analytical description of the wave propagation in structures containing failures, such as delaminations, cracks or other defects. Hence, it is hardly possible to describe the wave propagation in complex three-dimensional structures without further modifications to these methods.

An idea to circumvent the limitations of purely analytical methods to simple geometries is given by Ahmad and Gabbert [15] and Vivar-Perez *et al.* [85]. They propose to couple FE models and analytical solutions. Ahmad and Gabbert use the semi-analytical finite element method (SAFE) to compute the wave propagation in the unperturbed part of the plate-like structure and model the boundary and the damages of the part explicitly using conventional linear FEs. They found that mode conversion between symmetric and anti-symmetric Lamb wave modes does only occur when the perturbation of the structure is

asymmetric with respect to its middle plane. Vivar-Perez *et al.* follow a different approach [86]. The analytical models developed in reference [87] are coupled with a higher order finite element (*HO-FE*) approach, namely the spectral element method (SEM) based on a Chebyshev-Gauß-Lobatto (CGL) grid. This scheme is used to discretize a piezoelectric transducer with spectral elements (SEs) and to couple it to a homogeneous plate that is analytically described. The results are very promising in terms of computational costs compared to modeling the whole structure by means of the FEM. For dispersion analysis Mazotti *et al.* [88, 89] employed a coupled SAFE-BEM (boundary element method) approach, investigating the phenomenon of leaky guided waves propagating in beams with arbitrary cross-section. Unbounded media can easily be modelled by using the BEM [89]. Another approach to solving the wave equation is to be seen in wave finite elements (WFE). According to Ahmad [21], this method is more flexible than the SAFE-method, but it holds the disadvantage that the structure to be investigated has to be periodic. Another problem is to be seen in the ill-conditioned system matrices that are likely to occur [90]. The idea behind the WFE is to use wave modes (eigenmodes) as a representation basis for describing the kinematic variables - that is the displacements and external as well as internal forces - of the structure [90, 91]. To this end, the given structure is assumed to be described numerically by a set of identical substructures. The wave modes are then calculated using a FE model of such a typical substructure, reflecting the cross-sectional dynamical behavior. The original system is obtained by connecting the numerical models along the principal axis. Note that the FE discretization has to be fine enough to predict a sufficient number of highly oscillating wave shapes. This approach results in a significant decrease in computational-time for calculating the forced response of a system. It has been successfully applied to beam-like structures, fluid filled pipes and Reissner-Mindlin plates [90]. Modelling junctions between two waveguides follows the same procedure as detailed for the SAFE method. The junction is explicitly modelled deploying conventional FE schemes and then coupled to the WFE formulation of the different waveguides.

An extension of semi-analytical finite element methods has been published by Gopalakrishnan *et al.* [92–94]. This approach can be thought of as a FEM formulated in the frequency domain. While linear wave analysis of simple geometries is shown to be solved very efficiently even for the higher order modes, non-linear effects such as the contact between debonded surfaces and delaminations can hardly be treated because the problem is solved in frequency domain; the fast Fourier transform (FFT) is only viable for linear systems. Moreover, if transient time-domain solutions are required, there is a significant increase in calculation time [95].

Miscellaneous numerical methods The local interaction simulation approach (LISA) [96–99], the mass-spring lattice model (MSLM) [100] and cellular automata [101] are also numerical tools that are employed to simulate Lamb wave propagation problems. Complex geometries and boundary conditions pose difficulties - which are not insurmountable - for those methods. The FEM, however, generally offers a broader variety of applications and is not limited to special assumptions, such as e.g. material parameters or geometrical regularities.

Higher order shell elements From our point of view, higher order FEMs constitute viable options to circumvent the difficulties that are related to the approaches discussed in the

previous paragraphs. As mentioned before using *HO*-FE formulations is very advantageous regarding the computational efficiency and accuracy. To overcome the low convergence rate of conventional *h*-version FEs the focus of research has shifted to the implementation of higher order shape functions. Since thin-walled structures play an important role in advanced lightweight designs (candidate for SHM applications), an obvious approach would be to deploy finite shell elements or continuum shell elements. These elements are based on a dimensionally reduced theory (Kirchhoff, Reissner-Mindlin). They offer numerical advantages for the investigation of thin-walled designs. Finite shell elements based on the SEM have been recently developed by Ostachowicz *et al.* [102–107] and Fritzen *et al.* [108–110]. Ostachowicz *et al.* [106] use the SEM to simulate the Lamb wave propagation in composite plates for aeronautical applications. Their finite shell element is based on the first order shear deformation theory (FSDT). Its applicability and efficiency for SHM has been shown in various publications by this research group [14, 102, 104, 111]. Because of the assumptions used to derive a shell theory, both symmetric and anti-symmetric Lamb wave modes can only be described in a certain frequency range [106]; vibrations over the thickness of the plate cannot be resolved. Additional drawbacks are that multi-layered materials and complex three-dimensional stress states cannot be resolved at welded-joints or rivets, for example. Consequently, numerical tools based on higher order finite shell elements are inappropriate to cover all phenomena arising from wave propagation problems.

Higher order continuum/solid elements Accordingly, we are convinced that the implementation of a fully three-dimensional discretization technique is favorable in order to resolve all effects in detail. To this end, the literature proposes a wide variety of higher order shape functions. The main focus of the present thesis is on the SEM [106, 112–114] and hierarchical higher order FEMs (hierarchical *HO*-FEMs) [115–120]. Lagrange polynomials through non-equidistant points (Gauß-Lobatto-Legendre or Chebyshev-Gauß-Lobatto nodal distributions) are a common choice as Ansatz functions in the framework of the SEM, while the normalized integrals of the Legendre polynomials are typical for the hierarchical version of the *HO*-FEM, in this particular case termed the *p*-version of the FEM (*p*-FEM). Another promising approach applies non-uniform rational B-splines (NURBS) as shape functions and is known under the name isogeometric analysis (IGA) [121–126]. The properties of this method, in the context of ultrasonic guided wave propagation, are discussed in reference [125]. Heretofore, the SEM has been used almost exclusively for high frequency wave propagation problems - and the other two mentioned approaches were mainly employed to solve static problems including non-linear analyses, plasticity etc. or eigenvalue problems [127–129]. Applications of the *p*-version of the FEM to complex geometries, such as femur bones and arteries, for example, are described in [130]. The application of *HO*-FEMs to geometrically and physically non-linear analyses is demonstrated in [131–134]. Several articles have also dealt with fluid-structure interaction [135–138] based on an implicit time-integration scheme. The wide variety of examples can be seen as a proof for the versatility of *HO*-FEMs. The robustness against geometric distortions and high aspect ratios is also clearly highlighted in the cited references [116].

Spectral element method The literature on the SEM, applied to wave propagation analysis, is very rich in contrast to the other mentioned *HO*-FE approaches. The versatility of the SEM has been shown by Seriani and Su [139, 140]. They solved the acoustic wave equation for complex media (seismic wave propagation in the earth's mantle) using a SEM

poly-grid approach. Highly accurate algorithms are needed to study wave propagation phenomena in media with variable physical properties in the domain of interest. When dealing with continuous variations of physical properties, auxiliary grids can be introduced to avoid the necessity of using a fine global grid. The simulation of wave propagation phenomena in heterogeneous media can be readily conducted using this novel technique. This approach bears similarities to the methodology adopted by the finite cell method (FCM, cf. Chapter 5) and related fictitious domain methods. In a different study, Seriani and Priolo found that the SEM shows more accurate results compared to low order FEs [141]. Peng *et al.* drew on three-dimensional continuum SEs to investigate the effect of adhesive on the wave propagation and to show the excellent properties of the SEM for damage detection in laminates and beams [113, 142–144]. Komatitsch *et al.* [145–147] employ the SEM to model seismic wave propagation problems. A fully three-dimensional earth model is used to simulate global wave propagations. The influence of the rotation, self-gravitation and the oceans is taken into account, whereas the oceans are modeled as an equivalent load. Ha [148–150] used the SEM to study the influence of the adhesive layer between a piezoelectric transducer and the host structure. For this purpose he developed a hybrid SE with linear shape functions in the out-of-plane direction as well as spectral shape functions of arbitrary order in the in-plane direction.

The widely accepted use of the SEM to solve dynamic problems - documented in the paragraph above - is due to the fact that the global mass matrix is diagonal (mass-lumping is readily available and easy to implement). Dauksher and Emery [151, 152] demonstrated that a row-summing procedure provides accurate solutions when SEs are employed. This row-summing technique is only performed on the global mass matrix. Nonetheless, the solution characteristics are relatively unaffected by the diagonalized mass matrix, but the numerical costs can be drastically reduced by means of an explicit time-integration algorithm. In the case of a diagonal mass matrix, only matrix-vector operations are needed in each time-step to solve the equations of motion. Dauksher's and Emery's results are based on Lagrange polynomials defined on a CGL nodal distribution. The authors of references [151, 152] opt for a deployment of row-summed mass matrix SEs in conjunction with a central difference method (CDM) for time-stepping as a means to solve the wave equation. In reference [153] they have demonstrated that the spectral approach can achieve nearly zero dispersion for a wide range of spatial and temporal discretizations. Moreover, Dauksher and Emery infer from their studies that the same conclusions can be drawn for both elastic and scalar (acoustic) waves. Another possibility to diagonalize the mass matrix is to use the same points that were employed to define the shape functions for the SEM as points for a Gaussian quadrature. Here, SEs based on a Gauß-Lobatto-Legendre (GLL) grid in conjunction with the well-known GLL-quadrature rule offer this elegant way to diagonalize the mass matrix [78]. The numerical dispersion error is reduced significantly and, as a rule of thumb, 4 nodes per wavelength are recommended for the spatial resolution using the polynomial degree $p = 4$. If we want to investigate longer wave propagation periods, however, higher polynomial orders are needed to avoid error accumulation and numerical anisotropy [154, 155]. Sridhar *et al.* [156] also employed Chebyshev SEs. They confirmed that the error decreases with $O[(1/p)^p]$ and that the SEM therefore also shows an exponential convergence. Furthermore, it is demonstrated that aspect ratios of 500 do not induce shear locking and that Chebyshev polynomials are a suitable choice for non-periodic problems.

p-version of finite element method and isogeometric analysis Apart from the SEM also the p -version of the FEM and IGA are, in principle, viable options to solve wave propagation problems. One important work that investigates the reliability of these higher order FE schemes in the context of wave propagation analysis was recently published [78]. Willberg *et al.* [78] derive a guideline on how to choose the optimal polynomial degrees and the corresponding FE size to reduce the numerical costs. In this article the authors deal with three different *HO*-FE approaches, namely the SEM [106], the p -version of the FEM [115, 120] and the IGA [123]. It is shown that using *HO*-FEMs can entail significant savings concerning memory storage requirements and numerical costs - in comparison to commercially available FEM software packages. The cited publication is one of very few articles using the p -version of the FEM and IGA for ultrasonic guided wave propagation analysis. On the other hand, the p -version of the FEM and the IGA are often used for static or eigenvalue problems [127–129] but as mentioned before rarely for wave propagation analysis. This can be attributed to the fact that, at least to our knowledge, there is no viable algorithm to lump the mass matrix. Thus, one should consider implicit time-stepping algorithms like the Newmark method. If the mass matrix is fully populated there is a linear system of equations to be solved in every time-step. This is the only reason why so far only Willberg and co-workers [78] utilized the p -FEM and the IGA for solving the elastic wave equation. In their paper, they demonstrated that the convergence characteristics of all higher order C_0 -continuous FE schemes are very similar. *HO*-FEMs are therefore a viable choice in the context of wave propagation analysis.

Numerical dispersion error After we discussed the benefits of higher order FEMs for wave propagation analysis, an important and frequently raised question has to be addressed: “How to control the numerical dispersion error?”. The previous paragraphs already contain a few hints, but a more thorough review will be given at this point. In their seminal works [157, 158] Ihlenburg and Babuška presented error estimates for solving the wave equation. They concluded that it is generally not possible to eliminate the phase error in two- and three-dimensional analyses. However, a suitable discretization, depending on the wavenumber, can still lead to considerable error reductions. Furthermore, they state that the choice of the shape functions is irrelevant regarding the dispersive characteristics of the numerical solution. Again, the importance of higher order shape functions is highlighted. It is found that *HO*-FEs exhibit an increased accuracy compared to low order FEs for the same number of degrees-of-freedom. In contrast to the frequently claimed 10 nodes per wavelength to obtain accurate results, Ihlenburg and Babuška [157] show that at least 25 nodes per wavelength are necessary to reduce the phase error to less than 1% for linear FEs. According to their research, it is recommended to use square normalized meshes, i.e. meshes with $kh^2 = \text{const.}$, where k depicts the wavenumber and h the FE size. Using that type of discretization the dispersive effects are negligible. For large k , weaker conditions are introduced because the number of degrees-of-freedom tends to get prohibitively large very fast. The most significant improvements in accuracy are reached by passing the standard h -version (with $p = 1$) to approximation order $p = 2$ or $p = 3$. Komatitsch and Tromp [146], however, recommend a polynomial degree of $p = 4/5$ since it provides the best trade-off between accuracy and integration stability from their point of view. According to their research they concluded that there is a theoretical limit of the number of nodes per minimum wavelength of π for an increasing polynomial degree. Here,

the accuracy remains almost unchanged even for long propagation times. Also Ainsworth and Wajid [159] find π as a theoretical limit for the number of nodes per wavelength if the polynomial degree is increased accordingly. For practical applications, however, 4.5 nodes per wavelength deploying a polynomial degree of $p = 8$ are recommended [146].

Jensen [74], Christon [160] and Ainsworth and Wajid [159, 161] additionally comment on the influence of the mass matrix on the numerical results. Jensen [74] employs the SEM and concludes that mass-lumping by Gauß-Lobatto-Legendre quadrature does not introduce additional errors. Christon [160] studies the dependence of the dispersive error on the wave propagation direction, mesh aspect ratio and wavenumber. He shows that a so-called higher order mass matrix - a linear combination of lumped and consistent mass matrices - may improve the dispersion characteristics of both reduced and fully integrated FEs. Ainsworth and Wajid [159, 161] also utilized a weighted average of the consistent and diagonalized mass matrices. They demonstrate that the optimal blending parameter for FEs of order p is given by the ratio $1 : p$. Compared to the pure schemes, two additional orders of accuracy can be gained. An efficient implementation of the higher order mass matrix can be achieved by nonstandard integration rules. An explicit construction of the nodes and weights is given in reference [161].

Concluding remarks on higher order methods The previous paragraphs clearly demonstrate that *HO*-FEMs are a viable option for wave propagation analysis in complex structures. These methods can help to solve several practice-oriented problems, which can be attributed to the fact that their derivation is not based on any assumptions in order to simplify the underlying physics. Non-linear analyses, both physically and geometrically, can be conducted without any difficulties. Moreover, arbitrary constitutive equations can be included. From our point of view, the conclusion of the previous paragraphs could be that *HO*-FEMs are a universally applicable tool in the context of wave propagation problems.

In the framework of *HO*-FEMs only SEs are thoroughly researched in the context of wave propagation analysis. In the present thesis, other higher order basis functions will also be employed to solve wave propagation problems. The results will then be compared with the results of the established SEM. Here, we take a special interest in hierarchical basis functions such as the normalized integrals of the Legendre polynomials (p -version of FEM) and trigonometric functions (p -Fourier-FEM). Hierarchical basis functions offer two distinct advantages over nodal basis functions: (i) they can employ the so-called trunk space formulation, and (ii) all shape functions of polynomial degree $p - 1$ are contained in the set of basis functions for the polynomial order p [115, 120]. But the impact of these features on the efficiency and the accuracy of wave propagation solutions has to be investigated. On the other hand, there is the drawback that no lumping technique is known for a set of hierarchical shape functions - which is why it is of interest to compare the different higher order approaches. The conclusion of this analysis will point the reader to an effective numerical tool with respect to wave propagation problems.

Fictitious domain concept However, we feel that despite their favorable numerical properties, the aforementioned methods cannot be recommended without restrictions. Considering heterogeneous materials with complex “micro”-structures, such as sandwich panels with a honeycomb or foam core, the user still faces the problem of mesh generation. It is

widely known that generating conforming FE grids from complex CAD (computer aided design) based geometrical models is rather expensive in terms of computational input and also quite difficult to accomplish fully automated, if at all possible. Normally, the generated mesh has to be adjusted manually by the user.

We therefore propose to apply the concept of the fictitious domain/immersed boundary methods to wave propagation analysis in the context of SHM applications. Since immersed boundary methods do not demand body-fitted meshes [129], but divide the domain in a regular grid of Cartesian cells, the geometric complexity is irrelevant as long as it can be analytically described or if voxel models and STL*-data are available. Therefore, a holistic design approach offers undreamt of possibilities. That is to say, that the desired hexahedral meshes can be generated on the basis of computed tomography scans [162]. Thus, the mesh generation procedure requires no user interaction - and it can be fully automated. Consequently, to circumvent the time consuming discretization, we suggest the FCM as a means to solve Lamb wave propagation problems. The FCM is essentially a combination of conventional fictitious domain approaches and *HO*-FE schemes. The high convergence rates as well as the simple discretization procedure are transferred to the FCM [162].

The FCM was first proposed by Parvizian *et al.* [162] and then successfully applied to different classes of problems [129, 163–166] such as the homogenization of cellular and foamed materials [164], geometrically non-linear problems [163, 167], elasto-plasticity problems [168, 169], optimization problems [170], multi-material problems [171] and multi-physics problems [172, 173]. The simple yet effective idea behind this method is to extend the partial differential equation beyond the physical domain of computation up to the boundaries of an embedding domain, which can be discretized without any difficulties. Therefore, we can replace the FE mesh by a structured grid of cells embedding the whole domain. In doing so, we shift the manual effort of discretizing any bounded domain to the numerical costs of an adaptive integration scheme that is able to capture the influence of the geometrical boundaries. The general idea can be traced back to classical fictitious domain or immersed boundary methods [174, 175].

The extension of the FCM to wave propagation analysis and the introduction of spectral shape functions has been recently proposed by Duczek *et al.* [176–178]. They coined the term *spectral cell method* (SCM) in accordance with the SEM. Their results highlight the promising capabilities of both the FCM and the SCM for the simulation of ultrasonic guided waves.

1.3 Working hypotheses and outline

To account for the complexity of wave propagation problems in SHM applications, we try to put the following hypothesis into practice:

HO-FEs and the fictitious domain concept offer significant advantages for wave propagation problems, especially concerning the investigation of complex structures or heterogeneous materials. By introducing these advanced numerical methods to wave propagation analysis we will provide an efficient numerical tool to facilitate a holistic simulation approach.

*STL: surface tessellation language. STL files describe the surface geometry of a three-dimensional object.

The current state-of-the-art is therefore extended by five novel aspects:

1. Guidelines concerning the performance of different hierarchical and non-hierarchical shape functions are compiled to illustrate their applicability to wave propagation problems.
2. The finite cell method is extended by spectral shape functions and the term *spectral cell method* is accordingly introduced.
3. The coupling between electrical and mechanical properties is taken into account. The finite/spectral cell method is therefore extended to multi-physics simulations.
4. The properties (convergence behavior e.g.) of the finite/spectral cell method are assessed in the context of wave propagation analysis.
5. Explicit time-integration techniques are introduced in order to improve the applicability of the spectral cell method to wave propagation problems. This is achieved by devising a suitable mass-lumping technique that is able to handle finite cells (FCs) that are intersected by the physical boundary (cut cells).

Outline Chapter 2 provides a brief introduction to ultrasonic guided waves and their characteristic features.

Turning to electro-mechanically coupled field problems, **Chapter 3** offers the fundamentals of piezoelectricity and provides the governing equations needed for the derivation of FE and fictitious domain approaches.

Chapter 4 deals with a detailed derivation of *HO*-FEMs - which are independent of a special class of higher order approximation basis - for smart structure applications.

Based on the FEM formulation **Chapter 5** provides a concise introduction to the FCM for electro-mechanically coupled field problems. Again, the formulation is derived regardless of the choice of a special family of Ansatz functions.

Specific shape functions are only described in **Chapter 6**. Four different basis functions are discussed and compared: First, Lagrange polynomials based on an equidistant nodal distribution are presented. These shape functions are known from standard *h*-type FE approaches. Second, Lagrange polynomials defined on a Gauß-Lobatto-Legendre grid are considered giving rise to the SEM and the SCM. Thereafter, hierarchic basis functions are discussed. To this end, the third set of shape functions is based on the normalized integrals of the Legendre polynomials, well-known from the *p*-version of the FEM/FCM. Fourth, trigonometric functions are introduced. The corresponding numerical scheme is named the Fourier-*p*-FEM/FCM.

Convergence studies assessing the accuracy and sensitivity of the *HO*-FEMs are conducted in **Chapter 7**. Here, it is shown that the solution behavior of the different basis functions is similar and merely depends on the polynomial degree of the family of Ansatz functions.

Chapter 8 demonstrates the validity, versatility and efficiency of both the *HO*-FEMs and the fictitious domain methods. To this end, a range of numerical benchmark problems is studied.

A more complex model is treated in **Chapter 9**. The phenomenon of bandgaps and stopbands is discussed. The simulation results are validated by three-dimensional measurements, based on the use of a LSDV. The investigations focus on a Fibonacci lattice and a plate with periodically aligned holes. These examples both demonstrate the capabilities of the higher order fictitious domain methods and validate their results.

Chapter 10 closes the thesis with a concise summary and important conclusions that can be drawn from the present thesis.

Chapter 2

Lamb waves

There are many textbooks that focus on the propagation of elastic waves in solid media [1, 10, 13, 52, 179–181]. In the present work, we take a special interest in guided elastic waves. One important representative of this class of waves are Lamb waves. They propagate in plate- and shell-like structures with free surfaces. The term was coined in order to honor its discoverer Horace Lamb, who was the first to provide a mathematical description in his seminal work “On Waves in an Elastic Plate” [12]. The first comprehensive book on this subject was published by Viktorov [13] and is now regarded as the standard text on Lamb wave propagation.

The present chapter aims to lay out a theoretical background on Lamb waves in order to enable the reader to interpret the simulated and measured time signals. To this end, the Rayleigh-Lamb dispersion equations are first derived, followed by a detailed discussion of their implications. The derivation of the basic equations closely follows the approach taken by Raghavan and Cesnik [8].

2.1 Governing equations of elastic wave propagation

2.1.1 Navier’s equation for an isotropic body

The derivation of the Navier’s equation starts with the three-dimensional equations of motion for an elastic solid

$$\nabla \cdot \boldsymbol{\sigma} + \mathbf{f}_b - \rho \ddot{\mathbf{u}} = \mathbf{0}. \quad (2.1)$$

$\boldsymbol{\sigma}$ is the stress tensor, ρ denotes the mass density of the body, \mathbf{f}_b stands for the body force per unit volume and $\ddot{\mathbf{u}}$ is the acceleration of the particle under consideration. Linear elastic, isotropic constitutive equations are assumed - for the sake of simplicity. Accordingly, the material law is expressed as

$$\boldsymbol{\sigma} = \tilde{\lambda} \mathbf{tr} \boldsymbol{\varepsilon} \boldsymbol{\delta} + 2\tilde{\mu} \boldsymbol{\varepsilon}, \quad (2.2)$$

with $\tilde{\lambda}$ and $\tilde{\mu}$ representing the Lamé coefficients for an isotropic body, $\boldsymbol{\delta}$ is the identity tensor and \mathbf{tr} is the trace operator. $\boldsymbol{\varepsilon}$ and $\boldsymbol{\sigma}$ denote the strain and the stress tensors, respectively. Provided that only small deformations are assumed, the kinematical relations (strain-displacement relation) are given as follows

$$\boldsymbol{\varepsilon} = \frac{1}{2} \left[\nabla \mathbf{u} + (\nabla \mathbf{u})^T \right]. \quad (2.3)$$

If we combine Eqs. (2.1), (2.2), and (2.3), we obtain Navier’s wave equation for a three-dimensional isotropic body

$$\left(\tilde{\lambda} + \tilde{\mu} \right) \nabla \nabla \cdot \mathbf{u} + \mu \Delta \mathbf{u} + \mathbf{f}_b = \rho \ddot{\mathbf{u}}, \quad (2.4)$$

where ∇ is the Nabla operator defined as

$$\nabla = \left\{ \frac{\partial}{\partial x_1} \quad \frac{\partial}{\partial x_2} \quad \frac{\partial}{\partial x_3} \right\}^T = \frac{\partial}{\partial x_i} \mathbf{e}_i. \quad (2.5)$$

Here, \mathbf{e}_i is the unit normal vector in the i -th local direction and the Laplace operator Δ is given by

$$\Delta = \nabla^2 = \frac{\partial^2}{\partial x_1^2} + \frac{\partial^2}{\partial x_2^2} + \frac{\partial^2}{\partial x_3^2}. \quad (2.6)$$

2.1.2 Helmholtz decomposition for isotropic media

In order to derive the equations describing the propagation of Lamb waves, it is helpful to decompose the displacement field into a scalar potential ϕ and a vector potential \mathbf{H} . They are also known as potentials of longitudinal and shear waves, respectively [13]. Thus, the particle displacement vector \mathbf{u} can be written in the form

$$\mathbf{u} = \nabla\phi + \nabla \times \mathbf{H}. \quad (2.7)$$

Additionally, we impose

$$\nabla \cdot \mathbf{H} = 0 \quad (2.8)$$

in order to guarantee the uniqueness of the solution [8]. Due to the fact that there are four unknowns and equally four equations, the Helmholtz decomposition for a given displacement field is always possible and unique. If we then substitute Eq. (2.7) into Navier's equation - cf. Eq. (2.4) without external forces - we obtain

$$\nabla \left[\left(\tilde{\lambda} + 2\tilde{\mu} \right) \Delta\phi - \rho\ddot{\phi} \right] + \nabla \times \left[\tilde{\mu}\Delta\mathbf{H} - \rho\ddot{\mathbf{H}} \right] = 0. \quad (2.9)$$

Normally, the influence of the body forces \mathbf{f}_b (such as gravity) on the wave propagation is negligible, which is why the corresponding term in Eq. (2.9) can be canceled. Consequently, the following explanations will only focus on the free propagation of waves. Since the potentials ϕ and \mathbf{H} are independent, Eq. (2.9) can only hold if the following two conditions are simultaneously satisfied

$$\left(\tilde{\lambda} + 2\tilde{\mu} \right) \Delta\phi - \rho\ddot{\phi} = 0, \quad (2.10)$$

$$\tilde{\mu}\Delta\mathbf{H} - \rho\ddot{\mathbf{H}} = 0. \quad (2.11)$$

We introduce the longitudinal wave velocity c_L and the transverse wave velocity c_T

$$c_L = \sqrt{\left(\tilde{\lambda} + 2\tilde{\mu} \right) / \rho}, \quad (2.12)$$

$$c_T = \sqrt{\tilde{\mu} / \rho}, \quad (2.13)$$

to re-write Eqs. (2.10) and (2.11) in the following form

$$\Delta\phi = \frac{1}{c_L^2} \ddot{\phi}, \quad (2.14)$$

$$\Delta\mathbf{H} = \frac{1}{c_T^2} \ddot{\mathbf{H}}. \quad (2.15)$$

Navier's equation is now decomposed into a scalar wave equation Eq. (2.14) and a vector wave equation Eq. (2.15) which can be treated individually.

2.1.3 Rayleigh-Lamb wave equation

Through multiple reflections on the plate's lower and upper surfaces, and through constructive and destructive interferences, pressure waves (also labeled primary or P-waves) and shear waves (also labeled secondary or S-waves) give rise to Lamb waves, which consist of a pattern of standing waves in the x_3 - (thickness)-direction (Lamb wave modes) behaving like travelling waves in the x_1 -direction [10].

An infinite plate in the in-plane directions with a thickness of $d = 2b$ is regarded. Its geometry is depicted in Fig. 2.1. Because harmonic waves in the x_1 - x_3 -plane are relevant here, it is assumed that the wave field is independent of the x_2 -direction. In other words, all derivatives with respect to x_2 vanish ($\partial(\cdot)/\partial x_2 = 0$). For that reason, we do not take shear horizontal modes into consideration.

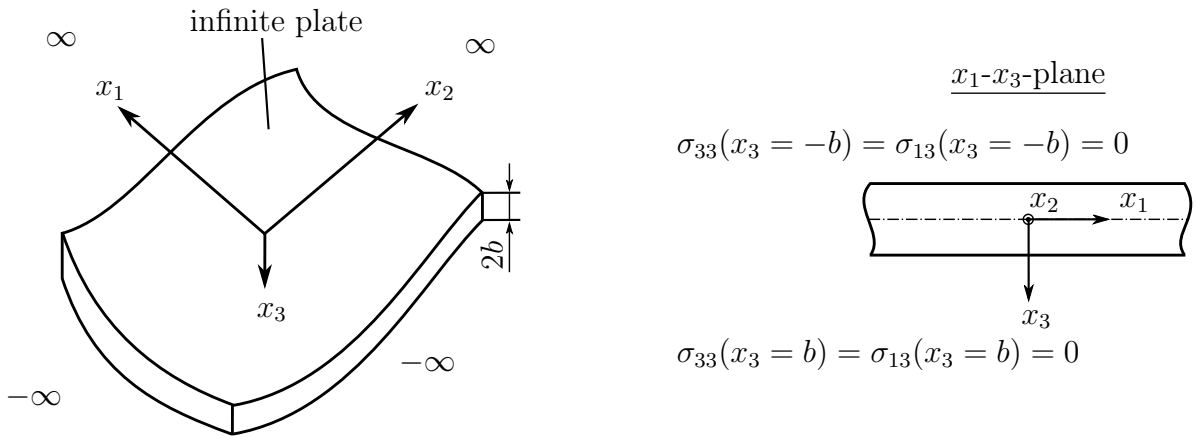


Figure 2.1: Infinite plate with free surfaces and Neumann boundary conditions.

Accordingly, the displacements are constraint to the x_1 - x_3 -plane ($u_2 = 0$ - plane strain assumption). Under those assumptions a two-dimensional problem can be considered [10], which is why the following statements concern only shear (represented by the potential H_{x_2}) and pressure waves (represented by the potential ϕ) as well as their combination. Eqs. (2.14) and (2.15) accordingly take the following form

$$\Delta\phi = \frac{1}{c_L^2}\ddot{\phi}, \quad (2.16)$$

$$\Delta H_{x_2} = \frac{1}{c_T^2}\ddot{H}_{x_2}. \quad (2.17)$$

Initially, those two equations are uncoupled. The coupling is only introduced due to the surface traction-free boundary conditions. As a consequence of this, all Lamb wave modes show a dispersive behavior [10], that is to say the wave velocity depends on the frequency of the travelling wave. We choose an Ansatz of the form

$$\phi(x_1, x_3, t) = f(x_3)e^{i(kx_1 - \omega t)}, \quad (2.18)$$

$$H_{x_2}(x_1, x_3, t) = h_{x_2}(x_3)e^{i(kx_1 - \omega t)} \quad (2.19)$$

to solve the governing equations - Eqs. (2.16) and (2.17). In doing so, we can derive equations that describe the propagation of Lamb waves. Here, t denotes the time, k represents the wavenumber, and ω is the circular frequency. The suggested approach yields plane waves in the x_1 - x_3 -plane propagating along the positive x_1 -direction. By combining Eqs. (2.16) and (2.17) with Eqs. (2.18) and (2.19) we obtain

$$\frac{d^2 f}{dx_3^2} + \left(\frac{\omega^2}{c_L^2} - k^2 \right) f = 0, \quad (2.20)$$

$$\frac{d^2 h_{x_2}}{dx_3^2} + \left(\frac{\omega^2}{c_T^2} - k^2 \right) h_{x_2} = 0. \quad (2.21)$$

Introducing the abbreviations α and β

$$\alpha = \frac{\omega^2}{c_L^2} - k^2, \quad (2.22)$$

$$\beta = \frac{\omega^2}{c_T^2} - k^2 \quad (2.23)$$

the solutions to Eqs. (2.20) and (2.21) can be determined. The wave field can now be evaluated by the following functions

$$f(x_3) = A \sin(\alpha x_3) + B \cos(\alpha x_3), \quad (2.24)$$

$$h_{x_2}(x_3) = C \sin(\beta x_3) + D \cos(\beta x_3). \quad (2.25)$$

The unknowns A , B , C and D can be determined depending on the enforced boundary conditions, cf. Fig. 2.1. The dispersion relations for Lamb waves can be obtained by using these solutions and taking the boundary conditions into account, cf. Fig. 2.1. There are two possible results (cf. Fig. 2.2) corresponding to symmetric and anti-symmetric movements with respect to the center plane of the plate:

1. Symmetric modes:

$$\begin{bmatrix} -(k^2 - \beta^2) \cos(\alpha b) & 2ik\beta \cos(\beta b) \\ -2ik\alpha \sin(\alpha b) & (k^2 - \beta^2) \sin(\beta b) \end{bmatrix} \cdot \begin{Bmatrix} B \\ C \end{Bmatrix} = \begin{Bmatrix} 0 \\ 0 \end{Bmatrix} \quad (2.26)$$

Nontrivial solutions exist if and only if

$$\det \begin{bmatrix} -(k^2 - \beta^2) \cos(\alpha b) & 2ik\beta \cos(\beta b) \\ -2ik\alpha \sin(\alpha b) & (k^2 - \beta^2) \sin(\beta b) \end{bmatrix} = 0 \quad (2.27)$$

holds. The solution to Eq. (2.27) is the dispersion relation for symmetric Lamb wave modes

$$\frac{\tan(\beta b)}{\tan(\alpha b)} = \frac{-4\alpha\beta k^2}{(k^2 - \beta^2)^2}. \quad (2.28)$$

2. Anti-symmetric modes:

$$\begin{bmatrix} -(k^2 - \beta^2) \sin(\alpha b) & -2ik\beta \sin(\beta b) \\ 2ik\alpha \cos(\alpha b) & (k^2 - \beta^2) \cos(\beta b) \end{bmatrix} \cdot \begin{Bmatrix} A \\ D \end{Bmatrix} = \begin{Bmatrix} 0 \\ 0 \end{Bmatrix} \quad (2.29)$$

Nontrivial solutions exist if and only if

$$\det \begin{bmatrix} -(k^2 - \beta^2) \sin(\alpha b) & -2ik\beta \sin(\beta b) \\ 2ik\alpha \cos(\alpha b) & (k^2 - \beta^2) \cos(\beta b) \end{bmatrix} = 0 \quad (2.30)$$

holds. The solution to Eq. (2.30) is the dispersion relation for anti-symmetric Lamb wave modes

$$\frac{\tan(\beta b)}{\tan(\alpha b)} = \frac{-(k^2 - \beta^2)^2}{4\alpha\beta k^2}. \quad (2.31)$$

The terms *symmetric* and *anti-symmetric* refer to the u_3 displacement component (cf. Figs. 2.2 and 2.3). The out-of-plane displacement is symmetric with respect to the mid-plane for symmetric modes (S_i) and asymmetric for anti-symmetric modes (A_i). The displacement field at higher frequencies (cf. Fig. 2.3) clearly demonstrates the need to employ methods with a higher resolution in order to be able to accurately capture the complex displacement field through the thickness of the plate.

For a given isotropic material Eqs. (2.28) and (2.31) have to be solved numerically in order to explicitly obtain a relation between the circular frequency ω and the wavenumber k . Having determined the wavenumber k as a function of ω , one is able to calculate the phase velocity c_p by

$$c_p = \frac{\omega}{k} = \lambda \cdot f. \quad (2.32)$$

Whereas the group velocity c_g is defined as a differential relation between the circular frequency ω and the wavenumber k

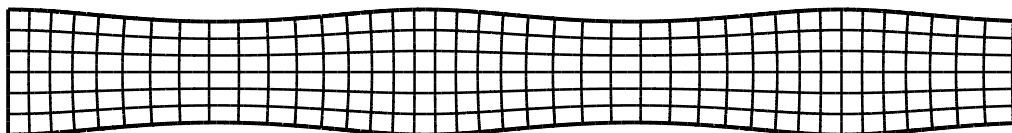
$$c_g = \frac{d\omega}{dk}. \quad (2.33)$$

Since k can be expressed as a function of c_p and ω the group velocity may be also expressed as [181, 182]

$$c_g = c_p^2 \left(c_p - \omega \frac{dc_p}{d\omega} \right)^{-1}. \quad (2.34)$$

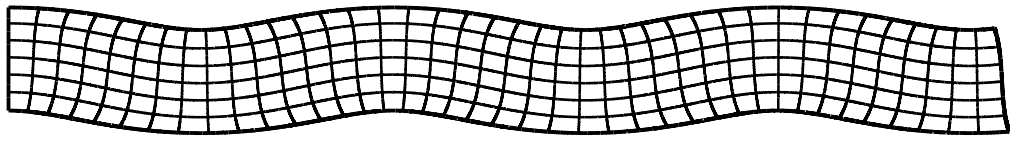
Table 2.1: Material data for aluminum.

Young's modulus (E)	Poisson's ratio (ν)	Mass density (ρ)	Longitudinal speed (c_L)	Transversal speed (c_T)
$7 \times 10^{10} \text{ N/m}^2$	0.33	2700 kg/m^3	6197 m/s	3121 m/s



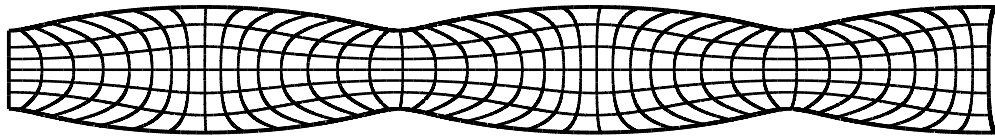
(a) S_0 -mode with a phase velocity of $c_p = 5.248 \text{ km/s}$

Figure 2.2: Lamb wave modes encountered in an aluminium plate (material data: Tab. 2.1) at $fd = 1.25 \text{ MHzmm}$.

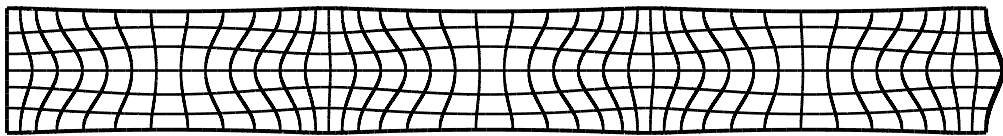


(b) A_0 -mode with a phase velocity of $c_p = 2.464$ km/s

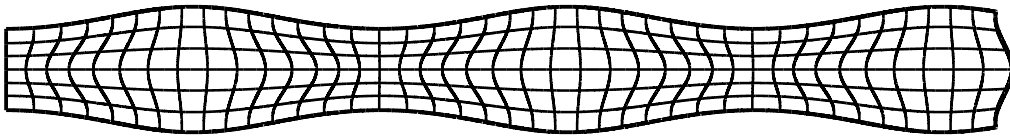
Figure 2.2: Lamb wave modes encountered in an aluminium plate (material data: Tab. 2.1) at $fd = 1.25$ MHzmm.



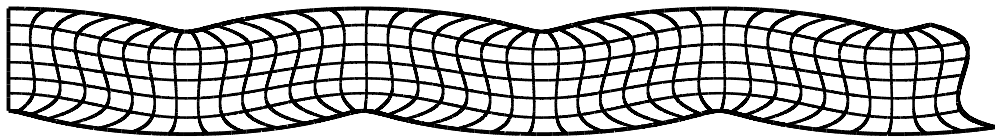
(a) S_0 -mode with a phase velocity of $c_p = 3.034$ km/s



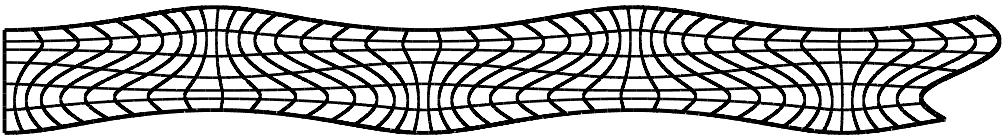
(b) S_1 -mode with a phase velocity of $c_p = 6.144$ km/s



(c) S_2 -mode with a phase velocity of $c_p = 14.39$ km/s



(d) A_1 -mode with a phase velocity of $c_p = 2.844$ km/s



(e) A_2 -mode with a phase velocity of $c_p = 5.028$ km/s

Figure 2.3: Lamb wave modes encountered in an aluminium plate (material data: Tab. 2.1) at $fd = 3.8$ MHzmm.

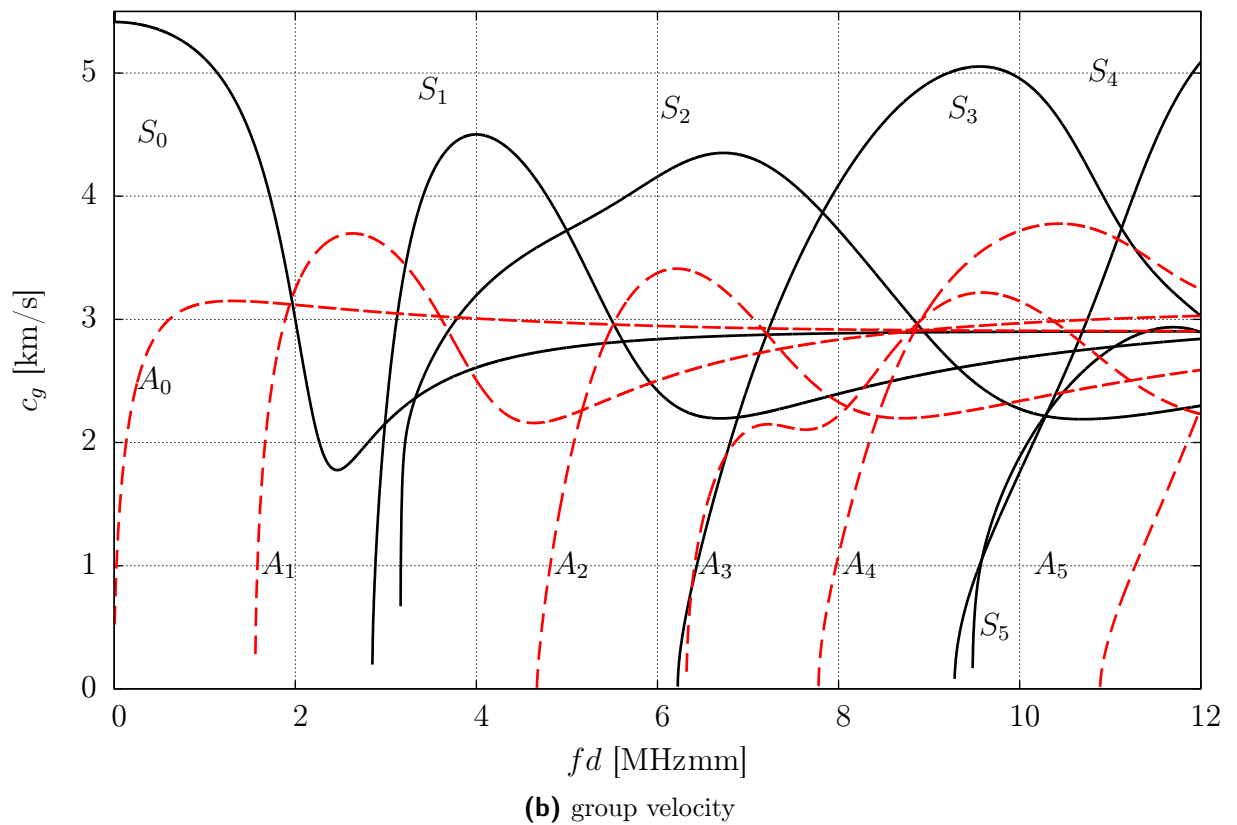
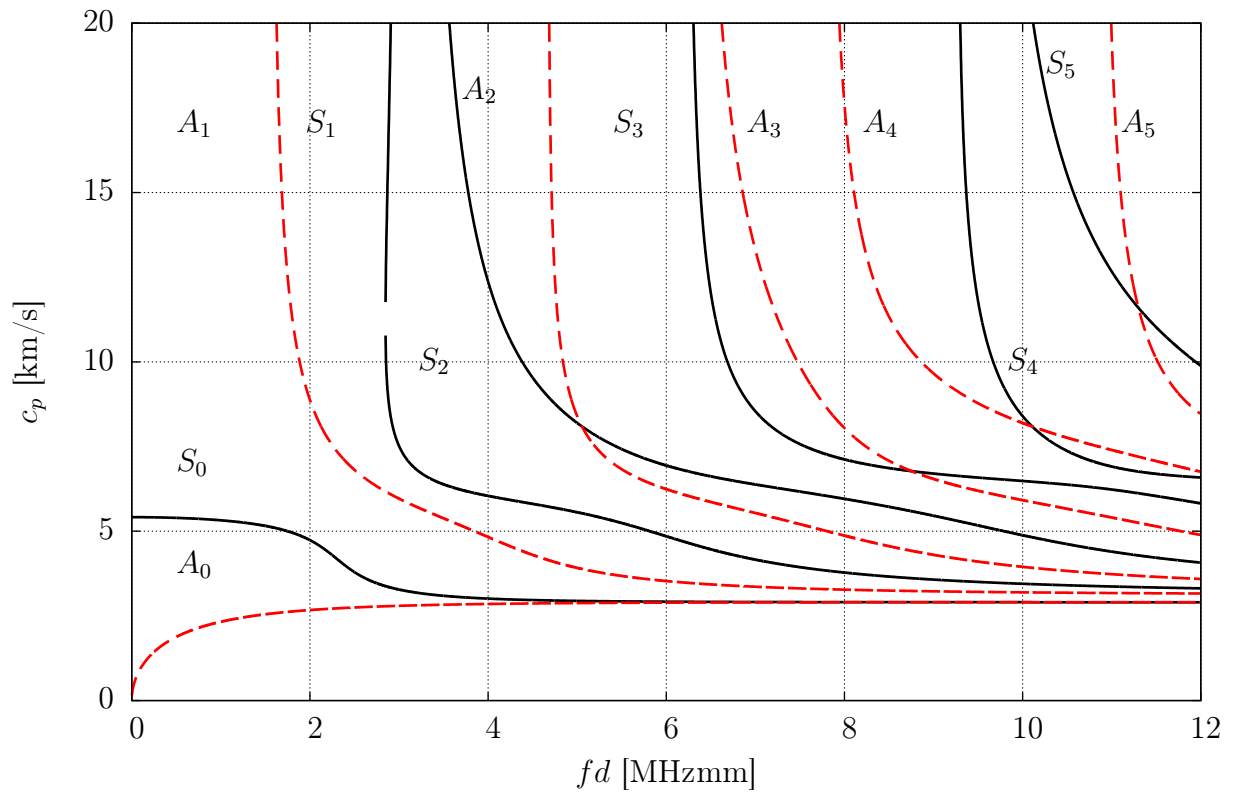


Figure 2.4: Phase and group velocity dispersion curves for an aluminium plate (material data: Tab. 2.1); dashed lines denote the anti-symmetric (A_i) and solid lines the symmetric modes (S_i).

This is a very convenient relation between the phase and group velocities. From this, it is easy to see that, for non-dispersive waves, the group and phase velocities coincide. The corresponding dispersion diagrams for a plate consisting of an aluminium alloy are plotted in Fig. 2.4.

We obtain the displacement field (visualized in Figs. 2.2 and 2.3) by substituting Eqs. (2.24) and (2.25) into Eqs. (2.18) and (2.19) and then into the Helmholtz decomposition (cf. Eq. (2.7)). The results are given as

$$u_{x_1} = [ik(A \sin(\alpha x_3) + B \cos(\alpha x_3)) + \beta(C \sin(\beta x_3) - D \cos(\beta x_3))] e^{i(kx_1 - \omega t)}, \quad (2.35)$$

$$u_{x_3} = [\alpha(A \cos(\alpha x_3) - B \sin(\alpha x_3)) - ik(C \sin(\beta x_3) + D \cos(\beta x_3))] e^{i(kx_1 - \omega t)}. \quad (2.36)$$

Two cases are to be distinguished:

1. $A = D = 0$ corresponds to the symmetric Lamb wave modes,
2. $B = C = 0$ corresponds to the anti-symmetric Lamb wave modes.

In order to determine the values of the unknown constants, the boundary conditions have to be taken into account. Additionally, C can be substituted by B using Eq. (2.28) and D can be expressed by A with the help of Eq. (2.31).

Despite their disadvantages (dispersion, multi-modal behavior), Lamb waves are nonetheless a widely accepted means for SHM applications [5, 87, 125, 182, 183].

2.2 Application of ultrasonic guided waves to structural health monitoring problems

SHM is an area of research that shows a steadily growing level of awareness. The increasing technical and scientific interest is founded on the fact that classical maintenance approaches are very time consuming and costly. Standard non-destructive testing methods should be replaced by SHM approaches, especially in the field of aircraft-related applications (with a growing demand for lightweight structures). Thus, it could become common practice to only carry out immediately necessary maintenance work, while it is still common nowadays to have scheduled maintenance intervals [2, 4]. Hence, the life-cycle costs can be significantly reduced by incorporating SHM systems into the structure during the design process. In general, online monitoring technologies that are installed on structures have the potential to ensure increased safety and reliability. In the course of developing suitable systems for the application to thin-walled structures, which are an integral part of lightweight structures, monitoring the propagation of ultrasonic waves ought to shed light on the “health” condition of the assembly.

Generally, there are two main approaches [52, 184] towards SHM as illustrated in Fig. 2.5:

- *active SHM*

Active SHM approaches are concerned with directly assessing the state of structural health [185–187]. It is their intrinsic purpose to discover the presence and extent of structural damage. Ultrasonic guided waves are excited intentionally in order to measure the response of the structure. Depending on the damages within the specimen reflection, diffraction and mode conversion behavior can be observed in the

measured signal. Such information is closely related to the position and to the type of the defect. Advanced signal processing techniques are applied to extract the essential data from the signal. In that respect, active SHM is similar to traditional NDT, only that SHM takes the concept to another level, because permanently installed actuators and sensors permit a continuous online monitoring program.

- *passive SHM*

Passive SHM approaches have two main aspects [188, 189]. The first one being the measurement of various operational parameters to draw conclusions about the state of structural health. Secondly, a passive method could also be established to monitor the ultrasonic wave propagation caused by an unknown event. For example, a network of piezoelectric sensors could serve the purpose to localize and determine the nature of a detected event.

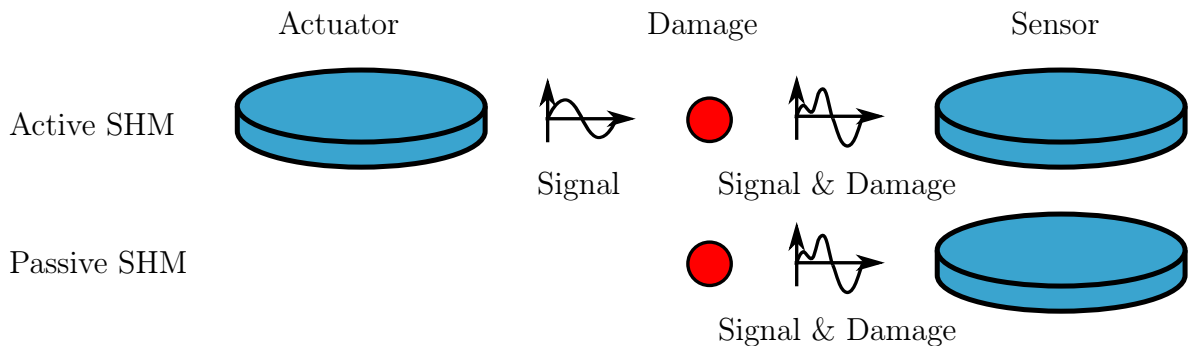
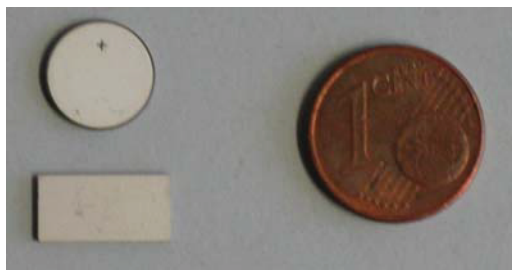
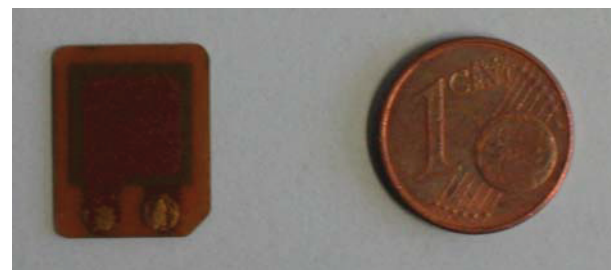


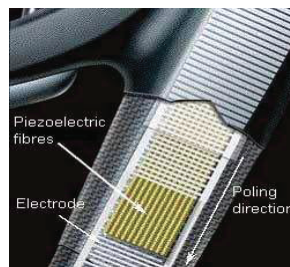
Figure 2.5: Damage detection in active and passive SHM systems [21].



(a) Piezoceramic transducer

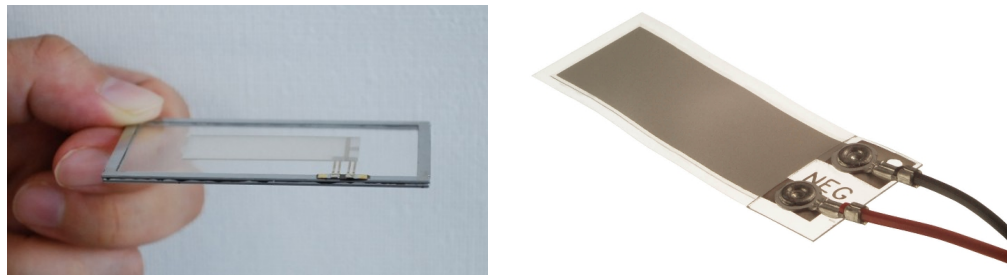


(b) Piezoceramic composite

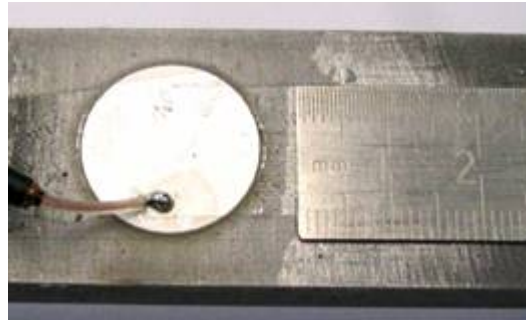


(c) Piezoelectric fiber

Figure 2.6: Examples of different types of piezoelectric transducers [125, 190, 191].



(d) Piezoelectric thin layer



(e) Surface-bonded transducer

Figure 2.6: Examples of different types of piezoelectric transducers [125, 190, 191].

Using Lamb waves - or in general guided waves - is an advantageous option since they are able to propagate for long distances in thin-walled structures with very little amplitude loss [10, 192, 193]. Hence, the number of necessary sensors can be notably reduced in comparison to approaches based on bulk waves, for example.

In active SHM systems, ultrasonic guided waves need to be excited and monitored - and piezoelectric transducers can be seen as an appropriate means to do so. Piezoelectric patches are bonded to the structure (cf. Fig. 2.6), allowing the excitation and sensing of these guided waves, relying on the inverse and the direct piezoelectric effect as explained in Chapter 3. Due to the fact that they can be integrated into a structure fairly easily and due to the low costs, these sensors and actuators belong to the most widespread types [194, 195]. As shown in Fig. 2.6 piezoelectric transducers are available in various versions. The application and modeling of composite type transducers (cf. Figs. 2.6b and 2.6c), either micro fiber or active fiber composites (MFC/AFC), are discussed in [196–198]. The benefits of thin wafer transducers (cf. Fig. 2.6d) are dealt with in [10, 194]. A review on the state-of-the-art in modeling piezoelectric transducers is given by Benjeddou in reference [199].

Chapter 3

Piezoelectricity

Piezoelectric materials are a special group among the so-called multi-functional materials. They are also commonly referred to as *smart materials*. This is because they have an inherent capability to transform electrical energy into mechanical energy and vice versa, which can be used to actively influence the structural behavior of a component part. Hence, they provide a means to design active structures. In the present thesis, we use patch transducers made of piezoelectric material both as sensors and as actuators, to monitor or to excite ultrasonic guided waves.

The present chapter describes the mechanisms of the direct and the converse piezoelectric effect. However, the influence of temperature [200] and magnetism will be neglected throughout this thesis. Although it has been shown that the thermal field can have significant influence on the elastic, dielectric and electro-mechanical constants, we assume negligible temperature changes as well as short periods of time in which the piezoelectric transducer comes to use. Therefore, the constitutive equations of the linear theory of piezoelectricity are applicable. For a more detailed review of piezoelectricity, the interested reader should refer to standard textbooks on that matter [201–203] and the literature cited therein.

Note that the equations are usually given in cartesian coordinates and the Voigt-notation is assumed throughout the present thesis.

3.1 The piezoelectric effect

The piezoelectric effect was first discovered in 1880 by Jacques and Pierre Curie [204]. When subjected to a mechanical deformation, a piezoelectric material generates an electric polarization and vice versa. The first effect is called the direct piezoelectric effect and serves as a basis for all sensor applications. The latter effect, the ability to generate an external force proportional to the applied charge, is accordingly called the converse (inverse) piezoelectric effect. Essentially, the piezoelectric effect can be described as a transfer between mechanical and electrical energy [205]. In order to understand the described behavior we have to take a closer look at the crystallographic structure of ferroelectric materials, especially ceramics.

The crystal lattice of ferroelectrics has a center of symmetry in a temperature range above the so called Curie temperature (T_c) [206]. In this state, the unit cell does not generate a dipole moment. As long as the ambient temperature is below the Curie temperature, however, a phase change can be observed. The unit cell accordingly represents a natural dipole since the crystallographic structure loses its center of symmetry. The ability to be

polarized is the prerequisite for the occurrence of a piezoelectric effect and characteristic of the group of ferroelectric crystals [207]. Materials that can be polarized by applying an external electrical field are generally referred to as dielectric materials. A dielectric material which is not polarized on the macro-scale is composed of various polarized domains (regions with uniform polarization - Weiss domains) on a micro-scale. A global polarization can thus be introduced when the material is subjected to an external electric field causing a dipole reorientation [205]. If the globally polarized material is loaded with external forces, its lattice will be distorted and the material will respond with an electrical charge. Within a certain range of the applied external load and the variation of the electrical dipole moment (electrical charge) a linear and reversible relation can be assumed [208]. For the non-linear case it is referred to [209] for example.

The dipole reorientation process does not induce perfectly aligned polarizations throughout the material, since there is only a certain amount of allowed directions within each domain [205]. This remanent polarization ($\approx 90\%$ of the spontaneous polarization*) causes the permanent piezoelectric properties of the ferroelectric material (cf. Fig. 3.2) [207]. Fig. 3.1 schematically illustrates the change of the strain in the material with respect to the applied electric field.

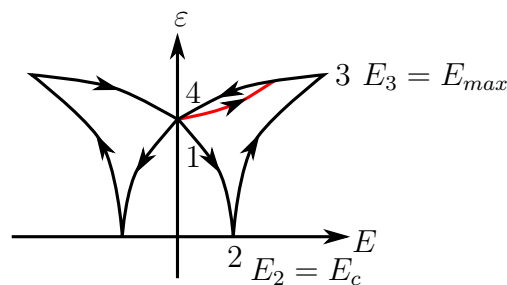


Figure 3.1: Butterfly curve.

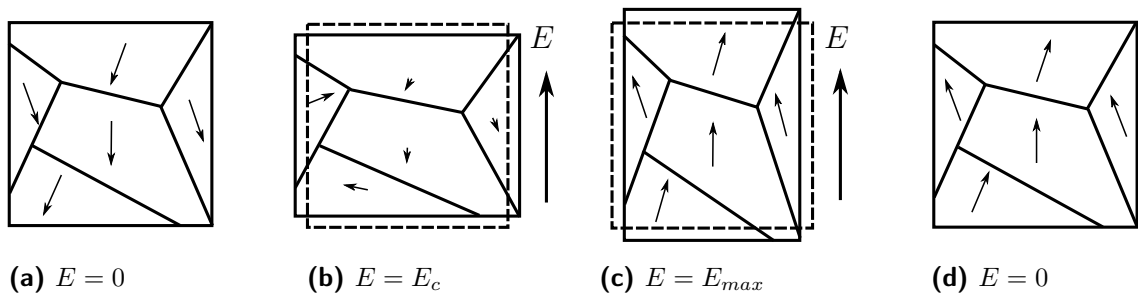


Figure 3.2: Domain reorientation (the dashed line denotes the original size of the domain).

The process of the domain reorientation is schematically shown in Fig. 3.2. An initial polarization of the material along the negative direction can be seen in Fig. 3.2(a). An electric field is applied during the second step, acting in the positive direction, cf. Fig. 3.2(b). Thus, the crystal will shrink with an increasing external electric field. At the coercive field (E_c) the strain reaches a minimum. This is the moment in which the polarization starts to align with the direction of the applied electrical field. At field strengths higher than the coercive field the crystal starts to expand (cf. Fig. 3.2(c)) as the global polarization

*maximal attainable polarization of a single crystal

has been partially reversed. Upon reaching the maximum field strength E_{max} the domains are almost perfectly aligned with the outer electrical field. When the field is decreased again, no reversal of the polarization direction will have taken place. When reaching a zero electric field, the strain will be zero as well: a similar situation to the initial setting, except for the fact that the polarization is now reversed, cf. Fig. 3.2(d).

Here, barium titanate ($BaTiO_3$) can serve as an example of a typical piezoceramic. $BaTiO_3$ changes its lattice structure from a cubic to tetragonal one below the Curie temperature (cf. Fig. 3.3) of $T_c \approx 120^\circ\text{C}$ [207]. The unit cells of a compound with a perovskite structure are depicted in Fig. 3.3.

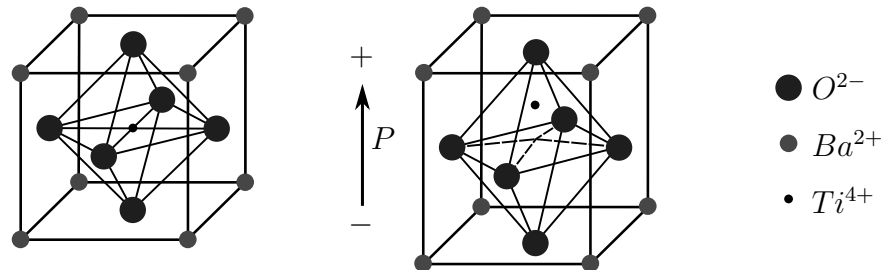


Figure 3.3: Cubic ($T > T_c$) and tetragonal ($T < T_c$) unit cells of a perovskite structure.

Due to its excellent properties, most of the commercially available applications employ lead zirconate titanate based ceramics (PZT). They promise an efficient electro-mechanical energy conversion and high Curie temperatures. Disadvantageous, however, is the vulnerability to a brittle fracture [210].

Because of the polarization, piezoceramic materials exhibit non-linearities which can only be neglected by operating with small maximal values of the electric field, cf. Fig. 3.1. Hysteresis effects have to be accounted for, if the field amplitude is increased too much. Since most technological applications considered in the present thesis drive the piezoelectric material within the linear range, the linear constitutive equations are sufficient to accurately describe its behavior.

In order to describe the coupled electro-mechanical field problem, we need to take the following equations into account: (i) the balance of linear momentum (mechanical equilibrium equations; cf. Eq. (3.1)), (ii) Boltzmann's axiom (consequence of the balance of moment of momentum; Eq. (3.2)), and (iii) Gauß's law (electric equilibrium equations; Eq. (3.3))

$$\nabla \cdot \boldsymbol{\sigma} + \mathbf{f}_b - \rho \ddot{\mathbf{u}} = \mathbf{0}, \quad (3.1)$$

$$\sigma_{ij} = \sigma_{ji}, \quad (3.2)$$

$$\nabla \cdot \mathbf{D} - q_b = 0. \quad (3.3)$$

$\boldsymbol{\sigma}$ describes the mechanical stress tensor commonly given in matrix notation also known as Voigt-notation ($\{\sigma_{11} \sigma_{22} \sigma_{33} \tau_{12} \tau_{23} \tau_{31}\}^T$). ρ denotes the mass density of the material, $\mathbf{f}_b = \{f_{b1} f_{b2} f_{b3}\}^T$ are body forces per unit volume applied to the body, $\ddot{\mathbf{u}} = \{\ddot{u}_1 \ddot{u}_2 \ddot{u}_3\}^T$ is the acceleration field, q_b stands for the electric body charge and $\mathbf{D} = \{D_1 D_2 D_3\}^T$ represents the dielectric displacement vector. Those equilibrium equations are the foundation of the FE approach discussed in detail in Chapter 4. In addition to the given equations boundary conditions, both mechanical and electrical, are required to solve electro-mechanical

problems. The mechanical Dirichlet and Neumann boundary conditions are specified in the following manner:

$$\bar{\mathbf{u}} - \mathbf{u} = \mathbf{0} \quad \text{on } \Gamma_{D,u}, \quad (3.4)$$

$$\bar{\mathbf{t}} - \mathbf{t} = \mathbf{0} \quad \text{on } \Gamma_{N,u}, \quad (3.5)$$

$$\mathbf{t} = \mathbf{T}_n^T \boldsymbol{\sigma} = \boldsymbol{\sigma} \mathbf{n}. \quad (3.6)$$

Eq. (3.5) demands an equality of the prescribed traction vector $\bar{\mathbf{t}}$ and the boundary stress/traction vector \mathbf{t} . \mathbf{t} is obtained by a multiplication of the stress tensor at the specified point with the outward normal vector \mathbf{n} of the surface Γ at that point. Equally, the rotation of the stress tensor can be achieved via a transformation matrix \mathbf{T}_n (transformation matrix of stresses for a rotation in the direction of \mathbf{n}) containing the directional cosines. The electrical Dirichlet and Neumann boundary conditions can be stated as follows:

$$\bar{\varphi} - \varphi = 0 \quad \text{on } \Gamma_{D,\varphi}, \quad (3.7)$$

$$\bar{Q} + Q = 0 \quad \text{on } \Gamma_{N,\varphi}, \quad (3.8)$$

$$Q = \mathbf{D}^T \mathbf{n}. \quad (3.9)$$

Here, Eq. (3.8) again demands an equality of the applied electric surface charge \bar{Q} and the electric charge Q generated within the material at the boundary of the regarded domain. The electric charge at the surface is computed using a similar approach to the one in Eq. (3.6).

In order to complete the set of equations necessary for a FE implementation, we need a relation between the mechanical strains $\boldsymbol{\varepsilon}$ and displacements \mathbf{u} (cf. Eq. (3.10)), the so-called strain-displacement relation - as well as a relation between the electric field \mathbf{E} and the electric potential φ (cf. Eq. (3.11))

$$\boldsymbol{\varepsilon} = \mathbf{L}_u \mathbf{u}, \quad (3.10)$$

$$\mathbf{E} = -\mathbf{L}_\varphi \varphi. \quad (3.11)$$

At this point the equations are given in matrix notation. \mathbf{L}_u and \mathbf{L}_φ constitute the mechanical and electrical differential (matrix) operators, respectively. The two linear differential operators are given in Eqs. (3.12) and (3.13), respectively, as

$$\mathbf{L}_u = \begin{bmatrix} \frac{\partial}{\partial x_1} & 0 & 0 & \frac{\partial}{\partial x_2} & 0 & \frac{\partial}{\partial x_3} \\ 0 & \frac{\partial}{\partial x_2} & 0 & \frac{\partial}{\partial x_1} & \frac{\partial}{\partial x_3} & 0 \\ 0 & 0 & \frac{\partial}{\partial x_3} & 0 & \frac{\partial}{\partial x_2} & \frac{\partial}{\partial x_1} \end{bmatrix}^T, \quad (3.12)$$

$$\mathbf{L}_\varphi = \begin{bmatrix} \frac{\partial}{\partial x_1} & \frac{\partial}{\partial x_2} & \frac{\partial}{\partial x_3} \end{bmatrix}^T. \quad (3.13)$$

The three-dimensional electro-elastic problem now consists in finding the mechanical displacements and electric potential that satisfy the governing equations above, complemented by adequate initial and boundary conditions.

3.2 Constitutive equations of piezoelectricity

The constitutive relations for the linearly coupled electro-mechanical system are derived from thermodynamic considerations. We consider a linear system to be a system in which the variables of two different phenomena are linearly coupled. In other words, energy is converted between these two phenomena when the physical state variables are changed [201], in our case between mechanical and electrical energy. Generally speaking, the thermodynamic potential reaches a stationary value in equilibrium state. Concerning a piezoelectric material, the most general description would allow for a coupling of mechanical, electrical and thermal variables [207]. Since the influence of temperature plays only a minor role in the intended applications, it will be neglected [200]. Likewise, phenomena caused by magnetism are excluded from the current considerations. Thus, we can derive the constitutive equations using the electric Gibbs energy H [201]

$$H = \frac{1}{2}\boldsymbol{\varepsilon}^T \mathbf{C} \boldsymbol{\varepsilon} - \boldsymbol{\varepsilon}^T \mathbf{e} \mathbf{E} - \frac{1}{2} \mathbf{E}^T \boldsymbol{\kappa} \mathbf{E}. \quad (3.14)$$

This particular formulation is helpful if $\boldsymbol{\varepsilon}$ and \mathbf{E} are chosen as independent variables. In the case that the mechanical stresses $\boldsymbol{\sigma}$ and the electric displacements \mathbf{D} are chosen as independent variables, the Gibbs free energy G [201]

$$G = -\frac{1}{2}\boldsymbol{\sigma}^T \mathbf{S}^E \boldsymbol{\sigma} - \boldsymbol{\sigma}^T \mathbf{d} \mathbf{E} - \frac{1}{2} \mathbf{E}^T \boldsymbol{\kappa}^{(\boldsymbol{\sigma})} \mathbf{E} \quad (3.15)$$

is the starting point for the derivation of the constitutive laws. These equations correspond to derivatives of the specific energy function with respect to certain variables depending on the choice of independent variables. We now obtain the piezoelectric relations by deriving Eq. (3.14) with respect to the mechanical strains $\boldsymbol{\varepsilon}$ and electric field \mathbf{E} , respectively [201], as

$$\boldsymbol{\sigma} = \frac{\partial H}{\partial \boldsymbol{\varepsilon}} = \mathbf{C} \boldsymbol{\varepsilon} - \mathbf{e}^T \mathbf{E}, \quad (3.16)$$

$$\mathbf{D} = -\frac{\partial H}{\partial \mathbf{E}} = \mathbf{e} \boldsymbol{\varepsilon} + \boldsymbol{\kappa} \mathbf{E}. \quad (3.17)$$

A different but also frequently used form is obtained by deriving Eq. (3.15) with respect to the mechanical stresses $\boldsymbol{\sigma}$ and with respect to the electric displacements \mathbf{D} , respectively [201], as

$$\boldsymbol{\varepsilon} = -\frac{\partial G}{\partial \boldsymbol{\sigma}} = \mathbf{S}^E \boldsymbol{\sigma} + \mathbf{d}^T \mathbf{E}, \quad (3.18)$$

$$\mathbf{D} = -\frac{\partial G}{\partial \mathbf{E}} = \mathbf{d} \boldsymbol{\sigma} + \boldsymbol{\kappa}^{(\boldsymbol{\sigma})} \mathbf{E}. \quad (3.19)$$

Here, \mathbf{e} is the matrix of piezoelectric coupling constants, relating the mechanical stresses $\boldsymbol{\sigma}$ to the electric field \mathbf{E} when constant mechanical strains $\boldsymbol{\varepsilon}$ are present within the regarded body. \mathbf{C} denotes Hooke's matrix of elastic coefficients for a constant electric field. In scrutinizing Eq. (3.17) we see that \mathbf{e} also relates the electric displacements \mathbf{D} with the mechanical strains under a constant electric field (short-circuited electrodes) condition. $\boldsymbol{\kappa}$ symbolizes the matrix of dielectric constants (permittivity) for a constant mechanical strain state. \mathbf{S}^E is the compliance matrix at constant electrical field and \mathbf{d} denotes the

matrix of piezoelectric coupling constants relating the mechanical strains $\boldsymbol{\varepsilon}$ to the electric field \mathbf{E} when constant mechanical stresses $\boldsymbol{\sigma}$ are present within the regarded body. $\boldsymbol{\kappa}^{(\sigma)}$ denotes the matrix of dielectric constants for a constant mechanical stress state. We provide both versions of the constitutive equations as they are rather helpful when deriving the two-dimensional laws. Eqs. (3.16) and (3.17) are preferable when a plane strain state is considered, whereas Eqs. (3.18) and (3.19) are utilized to derive the plane stress laws. In the corresponding equations, the strains or stresses can be canceled out directly. Note that the constitutive (material) matrices are not independent from each other. The following relations between different material matrices hold

$$\mathbf{S}^E = \mathbf{C}^{-1}, \quad (3.20)$$

$$\mathbf{d} = \mathbf{e}\mathbf{S}^E, \quad (3.21)$$

$$\boldsymbol{\kappa}^{(\sigma)} = \mathbf{e}\mathbf{S}^E\mathbf{e}^T + \boldsymbol{\kappa}. \quad (3.22)$$

The structures of the constitutive matrices for the two-dimensional as well as the three-dimensional cases assuming transversally isotropic material properties are given in Appendix A. For a piezoelectric actuator, Eq. (3.16) is the starting point for derivation of the mathematical formulae. Otherwise, Eq. (3.17) can be deployed to derive sensor applications [207].

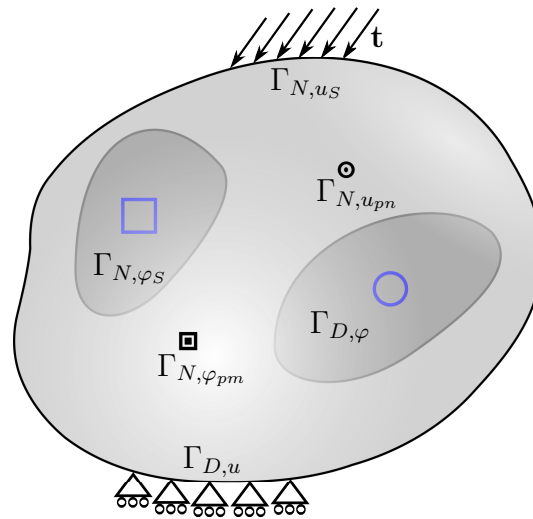


Figure 3.4: Boundary conditions of a piezoelectric body. A square denotes a prescribed surface charge while a circle represents prescribed electric potential. A circle with a dot inside stands for a point load and a square with a square inside marks the position of a concentrated electric charge.

The boundary conditions can be divided into essential/Dirichlet boundary conditions specifying the primary variables (displacements, electric potential) and natural/Neumann boundary conditions specifying the secondary variables (mechanical force, electric charge). Four distinct subregions of the boundary Γ can be distinguished; Two of them are defined by natural boundary conditions and the other two by essential boundary conditions. The essential boundary conditions are the prescribed displacement field on $\Gamma_{D,u}$ and the electric potential on $\Gamma_{D,\varphi}$. The natural boundary conditions are the external mechanical forces

applied to $\Gamma_{N,u}$ (the Neumann boundary is divided into two parts: surface loads acting on Γ_{N,u_S} and point loads at n different points $\Gamma_{N,u_{pn}}$) and the external charges applied to $\Gamma_{N,\varphi}$ (the Neumann boundary is divided into two parts: surface charges on Γ_{N,φ_S} and concentrated electric charges at m different points $\Gamma_{N,\varphi_{pm}}$), cf. Fig. 3.4.

Note that the boundaries $\Gamma_{N,u}$ and $\Gamma_{D,u}$ are disjoint. The same statement also holds for $\Gamma_{N,\varphi}$ and $\Gamma_{D,\varphi}$

$$\Gamma_{N,u} \cap \Gamma_{D,u} = \emptyset, \quad \Gamma_{N,u} \cup \Gamma_{D,u} = \Gamma, \quad (3.23)$$

$$\Gamma_{N,\varphi} \cap \Gamma_{D,\varphi} = \emptyset, \quad \Gamma_{N,\varphi} \cup \Gamma_{D,\varphi} = \Gamma. \quad (3.24)$$

By accounting for the electro-mechanical coupling, we are now able to address multi-field problems. In the following chapter, we accordingly derive the weak form of the governing equations and develop the FE formulation for piezoelectric bodies.

Chapter 4

Higher Order Finite Element Method

The FEM is one of the most widely used numerical tools to approximately solve partial differential equations arising in many problems related to different engineering disciplines. It is an efficient and universal approach to analyze a wide variety of field problems, including temperature, fluid flow and structural analyses. Investigations are possible for static and dynamic (time-dependent) processes. Both the geometry and the material laws are not restricted in any way. The general idea behind the FEM is to divide the physical domain of a complex structure into various sub-domains called finite elements (FEs) [119, 211–213]. The sought-after solution is then approximated on each sub-domain by means of simple and only locally defined functions (shape functions) to represent the distribution of the unknown field variables. Thus, the governing differential equations are solved in a weighted-integral sense based on the weak formulation of the problem. Due to its applicability to many problems of practical interest, it is a very successful and established numerical tool to solve partial differential equations.

The FEM, however, only predicts the behavior of a model with a certain, limited accuracy. Assuming that the mathematical description of the physical problem is accurate enough, the performance of the FE simulations mainly depend on the discretization of the model and the modeling assumptions. In the present thesis, the main objective is to develop a robust numerical tool for wave propagation analysis in complex structures. We therefore propose to employ a three-dimensional FE formulation based on hexahedral elements. This kind of FE framework does not rely on any assumptions. Consequently, the primary possibility to reduce the error is to adjust the discretization of the structure. The three most commonly used approaches to increase the accuracy of FE simulations are: (i) to deploy a h -refinement (the FE size is successively reduced), (ii) to deploy a p -refinement (the polynomial degree of the shape function is successively increased), or (iii) to deploy a combination of both, called hp -refinement (both the FE size and the polynomial degree of the shape functions are adjusted). By utilizing a p -type method, the accuracy of the solution can be improved rapidly without the need to change geometrical parameters of the discretization (re-meshing) [115, 120]. Section 1.2 contains a detailed explanation of the numerical advantages of higher order p -type approaches - all FEMs using higher order polynomial shape functions (polynomial degree $p \geq 3$) are referred to as a p -type approach - over conventional h -version FEs, such as - for instance - a fast convergence. In recent years, the academic community hence showed an increased interest in HO -FEs. They promise high, possibly even exponential, convergence rates as well as robustness regarding distortion and locking phenomena.

In the present chapter, we explain the basic principles of HO -FEMs, regardless of their functional basis. As mentioned before, unlike in the h -version of the FEM, convergence

is not obtained by a mesh refinement procedure. In p -type approaches, the discretization is accordingly left unchanged while convergence is reached by a local or global increase in the polynomial degree. Even an anisotropic approximation of the field variables is possible [116, 214, 215]. That is to say, different polynomial degrees for the local element variables (local coordinates) of the Ansatz functions can be chosen. As only a few elements are used to describe the geometry, special methods are needed to approximate the geometry of the structure accurately (Section 4.4). Even though the speed and the capacity of computers are steadily increasing efficient strategies are nonetheless far from becoming obsolete. They are still beneficial for efforts to simulate more realistic problems, such as in coupled field analyses. Furthermore, we will show that, due to the possibility to exploit anisotropic Ansatz spaces, the need for dimensionally reduced FEs (beam element, shell element e.g.) vanishes [116, 150, 215]. Thus, an efficient discretization strategy that allows complex structures to be consistently meshed with only one type of FEs (solid/continuum elements) can be established [116, 215]. Every structure can be, therefore, simulated in a three-dimensional framework based on the equilibrium equations of a continuous body. We will develop the fundamentals of such a computational framework based on higher order hexahedral FEs in the following sections. As already pointed out, we see piezoelectrically-induced wave propagation in thin-walled structures as an important area of application. The derivation of the weak form of the governing equations is therefore based on Eqs. (3.1) and (3.3) where electro-mechanical coupling terms are accounted for. However, the derivation is independent of the chosen set of shape functions and consequently generally applicable for all *HO*-FEMs.

Different kinds of Ansatz functions are not introduced until Chapter 6. Depending on the functions that are used to approximate the independent field variables we can distinguish between the FEM (Lagrange polynomials based on a equidistant grid, cf. Section 6.1.1), the SEM (Lagrange polynomials based on a GLL grid, cf. Section 6.1.2), the p -version of the FEM (normalized integrals of the Legendre polynomials, cf. Section 6.1.3) and the Fourier- p -version of the FEM (trigonometric shape functions, cf. Section 6.1.4). By comparing the properties of these higher order approaches in Chapter 7, we provide a recommendation for the appropriate choice for wave propagation analysis.

4.1 Higher order finite elements for electro-mechanically coupled problems

The current section deals with the formulation of FEs for electro-mechanically coupled systems. We compile the most important equations and derive the system matrices. Thus, the static and dynamic behavior of structures containing active piezoelectric materials can be evaluated. The fact that the derivation is based on the theory of linear piezoelectricity (cf. Chapter 3) allows only small deformations and rotations, as well as a low electric field, respectively. The formulation of FEs augmented with piezoelectric properties follows the approach taken in [124, 207, 216–219]. The numerical problems that are used for the verification process have already been published in reference [220].

4.1.1 Weak form of equilibrium

The point of departure for the formulation of FEs with both electrical and mechanical degrees-of-freedom are the equilibrium equations for a piezoelectric body: Eqs. (3.1) and (3.3). We apply the principle of virtual work in order to derive the weak form of the governing equations. The governing equations are accordingly multiplied by weighting functions [199, 221]. For multi-physics applications involving piezoelectric materials, the test functions are the virtual displacements $\delta \mathbf{u}$ and the virtual electric potential $\delta \varphi$. It is assumed that $\delta \mathbf{u}$ and $\delta \varphi$ are admissible, meaning that they vanish at the boundaries ($\Gamma_{N,u}$ and $\Gamma_{N,\varphi}$) where \mathbf{u} and φ fulfill the Dirichlet boundary conditions. Therefore, the variational formulation takes the following form

$$\delta \chi_u = \int_{\Omega} \delta \mathbf{u}^T (\mathbf{L}_u^T \boldsymbol{\sigma} + \mathbf{f}_b - \rho \ddot{\mathbf{u}}) d\Omega = 0, \quad (4.1)$$

$$\delta \chi_{\varphi} = \int_{\Omega} \delta \varphi^T (\mathbf{L}_{\varphi}^T \mathbf{D} - q_b) d\Omega = 0. \quad (4.2)$$

Eqs. (4.1) and (4.2) are equivalent to the differential equations also referred to as strong form. Rearranging the expressions for the virtual work yields

$$\delta \chi_u = \int_{\Omega} \delta \mathbf{u}^T (\mathbf{L}_u^T \boldsymbol{\sigma}) d\Omega + \int_{\Omega} \delta \mathbf{u}^T \mathbf{f}_b d\Omega - \int_{\Omega} \delta \mathbf{u}^T \rho \ddot{\mathbf{u}} d\Omega, \quad (4.3)$$

$$\delta \chi_{\varphi} = \int_{\Omega} \delta \varphi (\mathbf{L}_{\varphi}^T \mathbf{D}) d\Omega - \int_{\Omega} \delta \varphi^T q_b d\Omega. \quad (4.4)$$

In the next step, we recast the first term in each of the two equations above using Gauß's theorem (divergence theorem) in conjunction with a multi-dimensional integration by parts, resulting in

$$\begin{aligned} \int_{\Omega} \delta \mathbf{u}^T (\mathbf{L}_u^T \boldsymbol{\sigma}) d\Omega &= \int_{\Gamma_u} \delta \mathbf{u}^T \boldsymbol{\sigma} \mathbf{n} d\Gamma - \int_{\Omega} (\mathbf{L}_u \delta \mathbf{u})^T \boldsymbol{\sigma} d\Omega, \\ &= \int_{\Gamma_{D,u}} \delta \mathbf{u}^T \boldsymbol{\sigma} \mathbf{n} d\Gamma + \int_{\Gamma_{N,u}} \delta \mathbf{u}^T \boldsymbol{\sigma} \mathbf{n} d\Gamma - \int_{\Omega} (\mathbf{L}_u \delta \mathbf{u})^T \boldsymbol{\sigma} d\Omega, \end{aligned} \quad (4.5)$$

$$\begin{aligned} \int_{\Omega} \delta \varphi^T (\mathbf{L}_{\varphi}^T \mathbf{D}) d\Omega &= \int_{\Gamma_{\varphi}} \delta \varphi^T \mathbf{D} \mathbf{n} d\Gamma - \int_{\Omega} (\mathbf{L}_{\varphi} \delta \varphi)^T \mathbf{D} d\Omega, \\ &= \int_{\Gamma_{D,\varphi}} \delta \varphi^T \mathbf{D} \mathbf{n} d\Gamma + \int_{\Gamma_{N,\varphi}} \delta \varphi^T \mathbf{D} \mathbf{n} d\Gamma - \int_{\Omega} (\mathbf{L}_{\varphi} \delta \varphi)^T \mathbf{D} d\Omega. \end{aligned} \quad (4.6)$$

We then substitute Eqs. (4.5) and (4.6) into the principle of virtual displacements and into the principle of virtual electric potential, respectively. The definitions of $\bar{\mathbf{t}}$ and \bar{Q} (cf. Eqs. (3.6) and (3.9)) are also taken into account. Keeping in mind that

$$\bar{\mathbf{u}} - \mathbf{u} = \mathbf{0} \text{ on } \Gamma_{D,u} \quad (\delta \mathbf{u} = \mathbf{0} \text{ on } \Gamma_{D,u}) \quad (4.7)$$

and

$$\bar{\varphi} - \varphi = 0 \text{ on } \Gamma_{D,\varphi} \quad (\delta\varphi = 0 \text{ on } \Gamma_{D,\varphi}) \quad (4.8)$$

has to be fulfilled, we arrive at

$$\delta\chi_u = - \int_{\Omega} (\mathbf{L}_u \delta \mathbf{u})^T \boldsymbol{\sigma} d\Omega + \int_{\Omega} \delta \mathbf{u}^T \mathbf{f}_b d\Omega - \int_{\Omega} \delta \mathbf{u}^T \rho \ddot{\mathbf{u}} d\Omega + \int_{\Gamma_{N,u}} \delta \mathbf{u}^T \bar{\mathbf{t}} d\Gamma, \quad (4.9)$$

$$\delta\chi_{\varphi} = - \int_{\Omega} (\mathbf{L}_{\varphi} \delta \varphi)^T \mathbf{D} d\Omega - \int_{\Omega} \delta \varphi^T q_b d\Omega - \int_{\Gamma_{N,\varphi}} \delta \varphi^T \bar{Q} d\Gamma. \quad (4.10)$$

Substituting the constitutive equations Eqs. (3.16) and (3.17) into Eqs. (4.9) and (4.10) leads to the electric potential-based variational principle

$$\begin{aligned} \delta\chi_u = & - \int_{\Omega} (\mathbf{L}_u \delta \mathbf{u})^T \mathbf{C} (\mathbf{L}_u \mathbf{u}) d\Omega - \int_{\Omega} (\mathbf{L}_u \delta \mathbf{u})^T \mathbf{e}^T (\mathbf{L}_{\varphi} \varphi) d\Omega + \int_{\Omega} \delta \mathbf{u}^T \mathbf{f}_b d\Omega \\ & - \int_{\Omega} \delta \mathbf{u}^T \rho \ddot{\mathbf{u}} d\Omega + \int_{\Gamma_{N,u}} \delta \mathbf{u}^T \bar{\mathbf{t}} d\Gamma, \end{aligned} \quad (4.11)$$

$$\begin{aligned} \delta\chi_{\varphi} = & - \int_{\Omega} (\mathbf{L}_{\varphi} \delta \varphi)^T \mathbf{e} (\mathbf{L}_u \mathbf{u}) d\Omega + \int_{\Omega} (\mathbf{L}_{\varphi} \delta \varphi)^T \boldsymbol{\kappa} (\mathbf{L}_{\varphi} \varphi) d\Omega \\ & - \int_{\Omega} \delta \varphi^T q_b d\Omega - \int_{\Gamma_{N,\varphi}} \delta \varphi^T \bar{Q} d\Gamma. \end{aligned} \quad (4.12)$$

The equations above are also the starting point for the derivation of FE formulations employing \mathbf{u} and φ as independent variables. Keeping in mind that the domain Ω is discretized into n_e FEs,

$$\Omega = \bigcup_{e=1}^{n_e} \Omega_e \quad (4.13)$$

where Ω_e is the domain represented by a single FE with the boundary Γ_e , the independent field variables can be expressed by means of the matrix of shape functions ($\mathbf{N}_u, \mathbf{N}_{\varphi}$) and degrees-of-freedom (unknowns) connected to an element (\mathbf{u}_e, φ_e). It is possible, in principle, to use different shape functions for both the displacement field and the electric potential. The independent variables on the element level are therefore given as

$$\mathbf{u} = \mathbf{N}_u \mathbf{u}_e, \quad (4.14)$$

$$\varphi = \mathbf{N}_{\varphi} \varphi_e. \quad (4.15)$$

In the present thesis, however, the components of both shape function matrices corresponding to the same node/mode are identical. Due to the fact that the variational formulation contains only first derivatives, C_0 -continuous shape functions are sufficient. Different types of basis functions are not introduced and discussed until Chapter 6. Substituting

Eqs. (4.14) and (4.15) into the principle of virtual work given for a single FE yields

$$\begin{aligned} \delta\chi_u^e = & - \int_{\Omega_e} (\mathbf{L}_u \mathbf{N}_u \delta \mathbf{u}_e)^T \mathbf{C} (\mathbf{L}_u \mathbf{N}_u \mathbf{u}_e) d\Omega - \int_{\Omega_e} (\mathbf{L}_u \mathbf{N}_u \delta \mathbf{u}_e)^T \mathbf{e}^T (\mathbf{L}_\varphi \mathbf{N}_\varphi \varphi_e) d\Omega \\ & + \int_{\Omega_e} (\mathbf{N}_u \delta \mathbf{u}_e)^T \mathbf{f}_b d\Omega - \int_{\Omega_e} (\mathbf{N}_u \delta \mathbf{u}_e)^T \rho (\mathbf{N}_u \ddot{\mathbf{u}}_e) d\Omega + \int_{\Gamma_{e,N,u}} (\mathbf{N}_u \delta \mathbf{u}_e)^T \bar{\mathbf{t}} d\Gamma, \end{aligned} \quad (4.16)$$

$$\begin{aligned} \delta\chi_\varphi^e = & - \int_{\Omega_e} (\mathbf{L}_\varphi \mathbf{N}_\varphi \delta \varphi_e)^T \mathbf{e} (\mathbf{L}_u \mathbf{N}_u \mathbf{u}_e) d\Omega + \int_{\Omega_e} (\mathbf{L}_\varphi \mathbf{N}_\varphi \delta \varphi_e)^T \boldsymbol{\kappa} (\mathbf{L}_\varphi \mathbf{N}_\varphi \varphi_e) d\Omega \\ & - \int_{\Omega_e} \delta (\mathbf{N}_\varphi \delta \varphi_e)^T q_b d\Omega - \int_{\Gamma_{N,\varphi}} (\mathbf{N}_\varphi \delta \varphi_e)^T \bar{Q} d\Gamma. \end{aligned} \quad (4.17)$$

In the next step, we apply the differential operators - Eqs. (3.12) and (3.13) - to the shape function matrices. The symbolic notation \mathbf{B}_u and \mathbf{B}_φ is accordingly introduced as

$$\mathbf{B}_u = \mathbf{L}_u \mathbf{N}_u, \quad (4.18)$$

$$\mathbf{B}_\varphi = \mathbf{L}_\varphi \mathbf{N}_\varphi. \quad (4.19)$$

Using these abbreviations, Eqs. (4.16) and (4.17) read

$$\begin{aligned} \delta\chi_u^e = & - \int_{\Omega_e} \delta \mathbf{u}_e^T \mathbf{B}_u^T \mathbf{C} \mathbf{B}_u \mathbf{u}_e d\Omega - \int_{\Omega_e} \delta \mathbf{u}_e^T \mathbf{B}_u^T \mathbf{e}^T \mathbf{B}_\varphi \varphi_e d\Omega + \int_{\Omega_e} \delta \mathbf{u}_e^T \mathbf{N}_u^T \mathbf{f}_b d\Omega \\ & - \int_{\Omega_e} \delta \mathbf{u}_e^T \mathbf{N}_u^T \rho \mathbf{N}_u \ddot{\mathbf{u}}_e d\Omega + \int_{\Gamma_{N,u}} \delta \mathbf{u}_e^T \mathbf{N}_u^T \bar{\mathbf{t}} d\Gamma, \end{aligned} \quad (4.20)$$

$$\begin{aligned} \delta\chi_\varphi^e = & - \int_{\Omega_e} \delta \varphi_e^T \mathbf{B}_\varphi^T \mathbf{e} \mathbf{B}_u \mathbf{u}_e d\Omega + \int_{\Omega_e} \delta \varphi_e^T \mathbf{B}_\varphi^T \boldsymbol{\kappa} \mathbf{B}_\varphi \varphi_e d\Omega \\ & - \int_{\Omega_e} \delta \varphi_e^T \mathbf{N}_\varphi^T q_b d\Omega - \int_{\Gamma_{e,N,\varphi}} \delta \varphi_e^T \mathbf{N}_\varphi^T \bar{Q} d\Gamma. \end{aligned} \quad (4.21)$$

The final step in the derivation of the FE formulation of a piezoelectric body is to factor out the virtual displacements and the electric potential as

$$\begin{aligned} \delta\chi_u^e = & \delta \mathbf{u}_e^T \left[\int_{\Omega_e} \mathbf{B}_u^T \mathbf{C} \mathbf{B}_u d\Omega \mathbf{u}_e + \int_{\Omega_e} \mathbf{B}_u^T \mathbf{e}^T \mathbf{B}_\varphi d\Omega \varphi_e - \int_{\Omega_e} \mathbf{N}_u^T \mathbf{f}_b d\Omega \right. \\ & \left. + \int_{\Omega_e} \mathbf{N}_u^T \rho \mathbf{N}_u d\Omega \ddot{\mathbf{u}}_e - \int_{\Gamma_{N,u}} \mathbf{N}_u^T \bar{\mathbf{t}} d\Gamma \right] = 0, \end{aligned} \quad (4.22)$$

$$\begin{aligned} \delta\chi_\varphi^e = & \delta \varphi_e^T \left[\int_{\Omega_e} \mathbf{B}_\varphi^T \mathbf{e} \mathbf{B}_u d\Omega \mathbf{u}_e - \int_{\Omega_e} \mathbf{B}_\varphi^T \boldsymbol{\kappa} \mathbf{B}_\varphi d\Omega \varphi_e \right. \\ & \left. + \int_{\Omega_e} \mathbf{N}_\varphi^T q_b d\Omega + \int_{\Gamma_{e,N,\varphi}} \mathbf{N}_\varphi^T \bar{Q} d\Gamma \right] = 0. \end{aligned} \quad (4.23)$$

We obtain the equations of motion on the element level by utilizing the fundamental lemma of variational calculus. As the variations $\delta \mathbf{u}$ and $\delta \varphi$ are arbitrary, Eqs. (4.22) and (4.23) can only hold if the terms within the square brackets are identical zero. Thus, the semi-discrete system of differential equations describing the motion of a piezoelectric FE is given as

$$\mathbf{0} = \mathbf{K}_{uu}^{(e)} \mathbf{u}_e + \mathbf{K}_{u\varphi}^{(e)} \varphi_e + \mathbf{M}_{uu}^{(e)} \ddot{\mathbf{u}}_e - \mathbf{f}_{uu}^{(e)}, \quad (4.24)$$

$$\mathbf{0} = \mathbf{K}_{\varphi u}^{(e)} \mathbf{u}_e - \mathbf{K}_{\varphi\varphi}^{(e)} \varphi_e - \mathbf{f}_{\varphi\varphi}^{(e)}. \quad (4.25)$$

The following notation has been introduced:

$$\text{Element mass matrix:} \quad \mathbf{M}_{uu}^{(e)} = \int_{\Omega_e} \rho \mathbf{N}_u^T \mathbf{N}_u d\Omega, \quad (4.26)$$

$$\text{Mechanical element stiffness matrix:} \quad \mathbf{K}_{uu}^{(e)} = \int_{\Omega_e} \mathbf{B}_u^T \mathbf{C} \mathbf{B}_u d\Omega, \quad (4.27)$$

$$\text{Direct piezoelectric element coupling matrix:} \quad \mathbf{K}_{u\varphi}^{(e)} = \int_{\Omega_e} \mathbf{B}_u^T \mathbf{e}^T \mathbf{B}_\varphi d\Omega, \quad (4.28)$$

$$\text{Inverse piezoelectric element coupling matrix:} \quad \mathbf{K}_{\varphi u}^{(e)} = \int_{\Omega_e} \mathbf{B}_\varphi^T \mathbf{e} \mathbf{B}_u d\Omega = \mathbf{K}_{u\varphi}^{(e)T}, \quad (4.29)$$

$$\text{Dielectric element stiffness matrix:} \quad \mathbf{K}_{\varphi\varphi}^{(e)} = \int_{\Omega_e} \mathbf{B}_\varphi^T \boldsymbol{\kappa} \mathbf{B}_\varphi d\Omega, \quad (4.30)$$

$$\text{External mechanical element force vector:} \quad \mathbf{f}_{uu}^{(e)} = \int_{\Omega_e} \mathbf{N}_u^T \mathbf{f}_b d\Omega + \int_{\Gamma_{e,N,u}} \mathbf{N}_u^T \bar{\mathbf{t}} d\Gamma, \quad (4.31)$$

$$\text{Electric element charge vector:} \quad \mathbf{f}_{\varphi\varphi}^{(e)} = - \int_{\Omega_e} \mathbf{N}_\varphi^T q_b d\Omega - \int_{\Gamma_{e,N,\varphi}} \mathbf{N}_\varphi^T \bar{Q} d\Gamma. \quad (4.32)$$

After the assembly of the individual element matrices and element vectors, the well-known system of equations for the motion of a piezoelectric body (regardless of the initial and the boundary conditions) is expressed as

$$\underbrace{\begin{bmatrix} \mathbf{M}_{uu} & \mathbf{0} \\ \mathbf{0} & \mathbf{0} \end{bmatrix}}_{\mathbf{M}} \underbrace{\begin{Bmatrix} \ddot{\mathbf{U}} \\ \ddot{\Phi} \end{Bmatrix}}_{\mathbf{F}} + \underbrace{\begin{bmatrix} \mathbf{K}_{uu} & \mathbf{K}_{u\varphi} \\ \mathbf{K}_{u\varphi}^T & -\mathbf{K}_{\varphi\varphi} \end{bmatrix}}_{\mathbf{K}} \underbrace{\begin{Bmatrix} \mathbf{U} \\ \Phi \end{Bmatrix}}_{\mathbf{F}} = \underbrace{\begin{Bmatrix} \mathbf{f}_{uu} \\ \mathbf{f}_{\varphi\varphi} \end{Bmatrix}}_{\mathbf{F}} \quad (4.33)$$

where

$$\mathbf{K}_{uu} = \mathbf{A} \sum_{e=1}^{n_e} \mathbf{K}_{uu}^{(e)}, \quad (4.34)$$

$$\mathbf{K}_{\varphi\varphi} = \mathbf{A} \sum_{e=1}^{n_e} \mathbf{K}_{\varphi\varphi}^{(e)}, \quad (4.35)$$

$$\mathbf{K}_{u\varphi} = \mathbf{A} \sum_{e=1}^{n_e} \mathbf{K}_{u\varphi}^{(e)}, \quad (4.36)$$

$$\mathbf{M}_{uu} = \mathbf{A} \sum_{e=1}^{n_e} \mathbf{M}_{uu}^{(e)}, \quad (4.37)$$

$$\mathbf{f}_{uu} = \mathbf{A} \sum_{e=1}^{n_e} \mathbf{f}_{uu}^{(e)}, \quad (4.38)$$

$$\mathbf{f}_{\varphi\varphi} = \mathbf{A} \sum_{e=1}^{n_e} \mathbf{f}_{\varphi\varphi}^{(e)}, \quad (4.39)$$

$$\mathbf{U} = \mathbf{A} \sum_{e=1}^{n_e} \mathbf{u}_e, \quad (4.40)$$

$$\Phi = \mathbf{A} \sum_{e=1}^{n_e} \varphi_e. \quad (4.41)$$

In this context \mathbf{A} denotes the assembly operator.

Implementation of admissible loads

Generally speaking, the excitation by concentrated forces \mathbf{F}_p is inadmissible in structural mechanics. A traction \mathbf{t} , acting on the surface $\Gamma_{N,u}$ of the structure, is therefore usually preferred (cf. Fig. 4.1 - observe the symmetric boundary conditions). Accordingly, a consistent load is applied without introducing a singularity if and only if distributed forces are deployed. A point force can accordingly be substituted by a distributed load using the following formula

$$\mathbf{F}_p(\mathbf{t}) = \int_{\Gamma_{N,u}} \mathbf{t} d\Gamma. \quad (4.42)$$

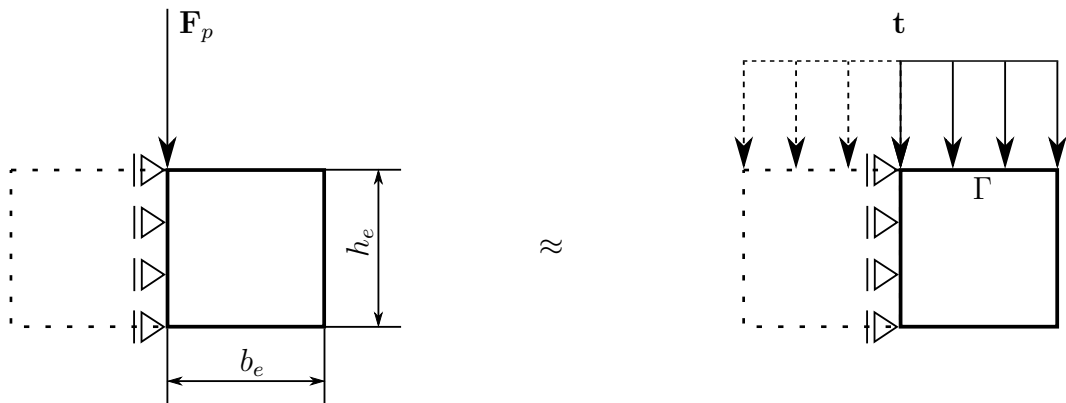


Figure 4.1: Concentrated point force \mathbf{F}_p modelled as energetically equivalent constant traction \mathbf{t} . According to Saint-Venant's principle, both loads exert an equivalent impact on the displacement field in a sufficient distance from the area where the loads are applied.

Instead of modeling the distributed load as constant (cf. Fig. 4.1) other distributions of the loading function are possible too. However, if the application of a concentrated load or electric charge is inevitable, additional terms have to be introduced to Eqs. (4.31) and (4.32). The contribution of n_u concentrated point forces to the mechanical element force vector is given by

$$\mathbf{f}_{uuF_i}^{(e)} = \sum_{j=1}^{n_u} \mathbf{N}_u^T \mathbf{F}_{pj} \quad (4.43)$$

and the contribution of n_φ concentrated electrical charges to the element charge vector is expressed by

$$\mathbf{f}_{\varphi\varphi F_{q_j}}^{(e)} = \sum_{j=1}^{n_\varphi} \mathbf{N}_\varphi^T \mathbf{F}_{q_j}. \quad (4.44)$$

Structural damping

Depending on the application, structural damping might also play an important role in the analysis. The effects caused by damping are often modeled employing a velocity proportional Ansatz (viscous damping). To this end, we usually employ the Rayleigh hypothesis [222]

$$\mathbf{R}_{uu} = \alpha \mathbf{M}_{uu} + \beta \mathbf{K}_{uu}. \quad (4.45)$$

Consequently, the equation of motion takes the following form

$$\begin{bmatrix} \mathbf{M}_{uu} & \mathbf{0} \\ \mathbf{0} & \mathbf{0} \end{bmatrix} \begin{Bmatrix} \ddot{\mathbf{U}} \\ \ddot{\mathbf{\Phi}} \end{Bmatrix} + \begin{bmatrix} \mathbf{R}_{uu} & \mathbf{0} \\ \mathbf{0} & \mathbf{0} \end{bmatrix} \begin{Bmatrix} \dot{\mathbf{U}} \\ \dot{\mathbf{\Phi}} \end{Bmatrix} + \begin{bmatrix} \mathbf{K}_{uu} & \mathbf{K}_{u\varphi} \\ \mathbf{K}_{\varphi u} & -\mathbf{K}_{\varphi\varphi} \end{bmatrix} \begin{Bmatrix} \mathbf{U} \\ \mathbf{\Phi} \end{Bmatrix} = \begin{Bmatrix} \mathbf{f}_{uu} \\ \mathbf{f}_{\varphi\varphi} \end{Bmatrix}. \quad (4.46)$$

Numerical implementation

The numerical implementation of FEs with piezoelectric characteristics, however, poses a problem that should be taken into account. Due to the differences of several orders of magnitude in the absolute values of the mechanical and electrical material properties (given in SI units) the stiffness matrix \mathbf{K} suffers from ill-conditioning. The components of \mathbf{K} need to be modified accordingly by introducing a scaling factor γ . We can consequently transform the independent variables as

$$\tilde{\mathbf{\Phi}} = \gamma^{-1} \mathbf{\Phi}. \quad (4.47)$$

The development of the ‘‘scaled’’ version of the FE relations for a piezoelectric body starts with Eqs. (4.22) and (4.23). By substituting Eq. (4.47) into these variational equations we obtain the following system of equations

$$\mathbf{0} = \begin{Bmatrix} \delta \mathbf{U} \\ \gamma \delta \tilde{\mathbf{\Phi}} \end{Bmatrix}^T \left(\begin{bmatrix} \mathbf{K}_{uu} & \mathbf{K}_{u\varphi} \\ \mathbf{K}_{\varphi u} & -\mathbf{K}_{\varphi\varphi} \end{bmatrix} \begin{Bmatrix} \mathbf{U} \\ \gamma \tilde{\mathbf{\Phi}} \end{Bmatrix} - \begin{Bmatrix} \mathbf{f}_{uu} \\ \mathbf{f}_{\varphi\varphi} \end{Bmatrix} + \begin{bmatrix} \mathbf{M}_{uu} & \mathbf{0} \\ \mathbf{0} & \mathbf{0} \end{bmatrix} \begin{Bmatrix} \ddot{\mathbf{U}} \\ \gamma \ddot{\tilde{\mathbf{\Phi}}} \end{Bmatrix} \right). \quad (4.48)$$

After simplifying Eq. 4.48, the final result of the scaled system of equations reads

$$\begin{bmatrix} \mathbf{M}_{uu} & \mathbf{0} \\ \mathbf{0} & \mathbf{0} \end{bmatrix} \begin{Bmatrix} \ddot{\mathbf{U}} \\ \gamma \ddot{\tilde{\mathbf{\Phi}}} \end{Bmatrix} + \begin{bmatrix} \mathbf{K}_{uu} & \gamma \mathbf{K}_{u\varphi} \\ \gamma \mathbf{K}_{\varphi u} & -\gamma^2 \mathbf{K}_{\varphi\varphi} \end{bmatrix} \begin{Bmatrix} \mathbf{U} \\ \tilde{\mathbf{\Phi}} \end{Bmatrix} = \begin{Bmatrix} \mathbf{f}_{uu} \\ \gamma \mathbf{f}_{\varphi\varphi} \end{Bmatrix}. \quad (4.49)$$

For typical applications, we recommend $\gamma = 10^{10}$ as an appropriate value. This improves the condition number of the stiffness matrix by several orders of magnitude and thus avoids the negative effects of round-off errors. For the sake of clarity and an improved readability the tilde over the electric potential $\tilde{\Phi}$ is omitted in the further course of the thesis.

4.2 Matrix of shape functions

In the previous section, we introduced the matrix of shape functions for the approximation of the displacement field \mathbf{N}_u (cf. Eq. (4.14)) and the matrix of shape function for the electric potential \mathbf{N}_φ (cf. Eq. (4.15)). Generally speaking, the shape functions can be classified into four individual groups:

1. Shape functions corresponding to degrees-of-freedom associated with the corner nodes of a hexahedral FE.
2. Shape functions corresponding to degrees-of-freedom associated with the edges of a hexahedral FE.
3. Shape functions corresponding to degrees-of-freedom associated with the faces of a hexahedral FE.
4. Shape functions corresponding to degrees-of-freedom associated with the interior of a hexahedral FE.

Fig. 4.2 shows the reference element that serves as a basis for the following definitions. Here, the local node, edge and face numbers are specified [116].

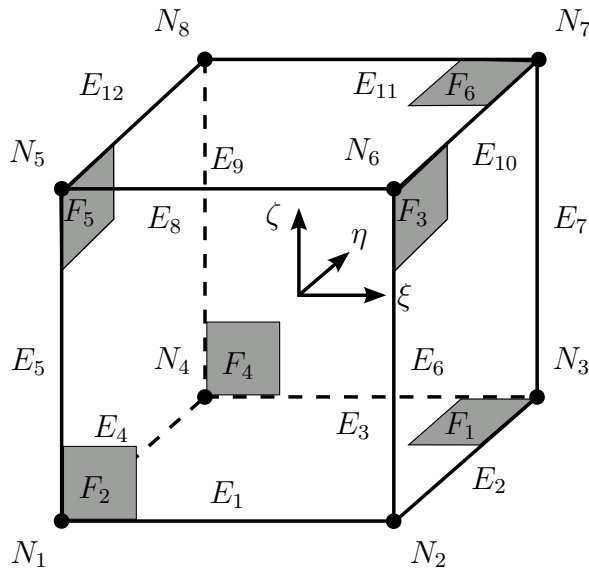


Figure 4.2: Hexahedral reference element ($-1 \leq \xi \leq 1$, $-1 \leq \eta \leq 1$, $-1 \leq \zeta \leq 1$) with definitions of the local coordinate system and node/edge/face numbers.

We can consequently also separate \mathbf{N}_u and \mathbf{N}_φ into four sub-matrices

$$\mathbf{N}_u = [\mathbf{N}_u^N \ \mathbf{N}_u^E \ \mathbf{N}_u^F \ \mathbf{N}_u^{int}], \quad (4.50)$$

$$\mathbf{N}_\varphi = [\mathbf{N}_\varphi^N \ \mathbf{N}_\varphi^E \ \mathbf{N}_\varphi^F \ \mathbf{N}_\varphi^{int}]. \quad (4.51)$$

The “nodal” modes

$$\mathbf{N}_u^N = \begin{bmatrix} N_{u(1,1,1)}^{N_1} & 0 & 0 & \cdots & N_{u(1,1,1)}^{N_8} & 0 & 0 \\ 0 & N_{u(1,1,1)}^{N_1} & 0 & \cdots & 0 & N_{u(1,1,1)}^{N_8} & 0 \\ 0 & 0 & N_{u(1,1,1)}^{N_1} & \cdots & 0 & 0 & N_{u(1,1,1)}^{N_8} \end{bmatrix}, \quad (4.52)$$

$$\mathbf{N}_\varphi^N = [N_{\varphi(1,1,1)}^{N_1} \ \cdots \ N_{\varphi(1,1,1)}^{N_8}] \quad (4.53)$$

are the standard trilinear shape functions well-known from the eight-node iso-parametric brick element [212]. The “edge” modes

$$\mathbf{N}_u^E = [\mathbf{N}_u^{E_1} \ \mathbf{N}_u^{E_2} \ \mathbf{N}_u^{E_3} \ \cdots \ \mathbf{N}_u^{E_{12}}], \quad (4.54)$$

$$\mathbf{N}_\varphi^E = [\mathbf{N}_\varphi^{E_1} \ \mathbf{N}_\varphi^{E_2} \ \mathbf{N}_\varphi^{E_3} \ \cdots \ \mathbf{N}_\varphi^{E_{12}}] \quad (4.55)$$

are defined individually for each edge. The modes associated with edge 1 (E_1) connecting the nodes 1 and 2 are

$$\mathbf{N}_u^{E_1} = \begin{bmatrix} N_{u(2,1,1)}^{E_1} & 0 & 0 & \cdots & N_{u(p_\xi,1,1)}^{E_1} & 0 & 0 \\ 0 & N_{u(2,1,1)}^{E_1} & 0 & \cdots & 0 & N_{u(p_\xi,1,1)}^{E_1} & 0 \\ 0 & 0 & N_{u(2,1,1)}^{E_1} & \cdots & 0 & 0 & N_{u(p_\xi,1,1)}^{E_1} \end{bmatrix}, \quad (4.56)$$

$$\mathbf{N}_\varphi^{E_1} = [N_{\varphi(2,1,1)}^{E_1} \ \cdots \ N_{\varphi(p_\xi,1,1)}^{E_1}]. \quad (4.57)$$

In Eq. (4.56) all shape functions corresponding to edge E_1 for a polynomial degree up to p_ξ are assembled. Analogous expressions can be obtained for the remaining “edge” modes. The “face” modes are defined separately for each face as well

$$\mathbf{N}_u^F = [\mathbf{N}_u^{F_1} \ \mathbf{N}_u^{F_2} \ \mathbf{N}_u^{F_3} \ \cdots \ \mathbf{N}_u^{F_6}], \quad (4.58)$$

$$\mathbf{N}_\varphi^F = [\mathbf{N}_\varphi^{F_1} \ \mathbf{N}_\varphi^{F_2} \ \mathbf{N}_\varphi^{F_3} \ \cdots \ \mathbf{N}_\varphi^{F_6}]. \quad (4.59)$$

Utilizing the tensor product space (cf. Section 6.2) the $(p_\xi - 1)(p_\eta - 1)$ “face” modes are arranged in

$$\mathbf{N}_u^{F_1} = \begin{bmatrix} N_{u(1,2,2)}^{F_1} & 0 & 0 & \cdots & N_{u(1,p_\eta,p_\zeta)}^{F_1} & 0 & 0 \\ 0 & N_{u(1,2,2)}^{F_1} & 0 & \cdots & 0 & N_{u(1,p_\eta,p_\zeta)}^{F_1} & 0 \\ 0 & 0 & N_{u(1,2,2)}^{F_1} & \cdots & 0 & 0 & N_{u(1,p_\eta,p_\zeta)}^{F_1} \end{bmatrix}, \quad (4.60)$$

$$\mathbf{N}_\varphi^{F_1} = [N_{\varphi(1,2,2)}^{F_1} \ \cdots \ N_{\varphi(1,p_\eta,p_\zeta)}^{F_1}]. \quad (4.61)$$

The definition of the remaining “face” modes follows an analogous pattern. The matrix of the internal modes takes the following form

$$\mathbf{N}_u^{int} = \begin{bmatrix} N_{u(2,2,2)}^{int} & 0 & 0 & \cdots & N_{u(p_\xi,p_\eta,p_\zeta)}^{int} & 0 & 0 \\ 0 & N_{u(2,2,2)}^{int} & 0 & \cdots & 0 & N_{u(p_\xi,p_\eta,p_\zeta)}^{int} & 0 \\ 0 & 0 & N_{u(2,2,2)}^{int} & \cdots & 0 & 0 & N_{u(p_\xi,p_\eta,p_\zeta)}^{int} \end{bmatrix}, \quad (4.62)$$

$$\mathbf{N}_\varphi^{int} = [N_{\varphi(2,2,2)}^{int} \ \cdots \ N_{\varphi(p_\xi,p_\eta,p_\zeta)}^{int}]. \quad (4.63)$$

In $\mathbf{N}_{u/\varphi}^{int}$ the $(p_\xi - 1)(p_\eta - 1)(p_\zeta - 1)$ internal shape functions are assembled. We can now implement FEs using anisotropic Ansatz spaces without any difficulties. This is done by adjusting the size of the matrices so that they coincide with the number of shape functions related to the anisotropic definition of the polynomial degree template.

Since the numbering of the shape functions is somewhat arbitrary, there are endless possibilities to compile numbering conventions. Two meaningful approaches are either to order the shape functions according to their polynomial degree or to assign to the n_{int} internal shape functions the highest degree-of-freedom numbers. The latter approach means that the shape functions are ordered in such a way that the n_{int} internal shape functions are assembled to form a single block which is located at the $3n_{int}$ last columns of the matrix, cf. Eq. (4.50). The first approach provides the opportunity to directly take advantage of the hierarchic structure of the resulting element stiffness matrix - and the latter simplifies the process of condensation of all internal degrees-of-freedom [116]. The differential operator matrix applied to the matrix of shape functions is consequently given as

$$\mathbf{B}_u(\mathbf{x}) = \mathbf{L}_u \mathbf{N}_u(\mathbf{x}) = [\mathbf{B}_u^1 \mathbf{B}_u^2 \cdots \mathbf{B}_u^{n_{dof}}], \quad (4.64)$$

$$\mathbf{B}_\varphi(\mathbf{x}) = \mathbf{L}_\varphi \mathbf{N}_\varphi(\mathbf{x}) = [\mathbf{B}_\varphi^1 \mathbf{B}_\varphi^2 \cdots \mathbf{B}_\varphi^{n_{dof}}]. \quad (4.65)$$

The differential operator matrix is applied to each shape function. Numbering all shape functions consecutively, in such a way that $i = 1, 2, \dots, n_{dof}$ denotes the number of every mode $N_i^{\text{type},3D}$ (type can be “nodal”, “edge”, “face” or “internal”), $\mathbf{B}_u^i/\mathbf{B}_\varphi^i$ are given as

$$\mathbf{B}_u^i = \begin{bmatrix} \frac{\partial N_i^{\text{type},3D}}{\partial x_1} & 0 & 0 & \frac{\partial N_i^{\text{type},3D}}{\partial x_2} & 0 & \frac{\partial N_i^{\text{type},3D}}{\partial x_3} \\ 0 & \frac{\partial N_i^{\text{type},3D}}{\partial x_2} & 0 & \frac{\partial N_i^{\text{type},3D}}{\partial x_1} & \frac{\partial N_i^{\text{type},3D}}{\partial x_3} & 0 \\ 0 & 0 & \frac{\partial N_i^{\text{type},3D}}{\partial x_3} & 0 & \frac{\partial N_i^{\text{type},3D}}{\partial x_2} & \frac{\partial N_i^{\text{type},3D}}{\partial x_1} \end{bmatrix}^T, \quad (4.66)$$

$$\mathbf{B}_\varphi^i = \left[\frac{\partial N_i^{\text{type},3D}}{\partial x_1} \quad \frac{\partial N_i^{\text{type},3D}}{\partial x_2} \quad \frac{\partial N_i^{\text{type},3D}}{\partial x_3} \right]^T. \quad (4.67)$$

Due to the fact that the shape functions are normally defined on a reference element with its local coordinates ξ , η and ζ (cf. Fig. 4.2) the computation of the derivatives in Eq. (4.66) necessitates the application of the chain rule

$$\frac{\partial N_i^{\text{type},3D}}{\partial \mathbf{x}} = \begin{Bmatrix} \frac{\partial N_i^{\text{type},3D}}{\partial x_1} \\ \frac{\partial N_i^{\text{type},3D}}{\partial x_2} \\ \frac{\partial N_i^{\text{type},3D}}{\partial x_3} \end{Bmatrix} = \underbrace{\begin{bmatrix} \frac{\partial \xi}{\partial x_1} & \frac{\partial \eta}{\partial x_1} & \frac{\partial \zeta}{\partial x_1} \\ \frac{\partial \xi}{\partial x_2} & \frac{\partial \eta}{\partial x_2} & \frac{\partial \zeta}{\partial x_2} \\ \frac{\partial \xi}{\partial x_3} & \frac{\partial \eta}{\partial x_3} & \frac{\partial \zeta}{\partial x_3} \end{bmatrix}}_{\mathbf{J}^{-1}: \text{inverse of the Jacobian Matrix}} \begin{Bmatrix} \frac{\partial N_i^{\text{type},3D}}{\partial \xi} \\ \frac{\partial N_i^{\text{type},3D}}{\partial \eta} \\ \frac{\partial N_i^{\text{type},3D}}{\partial \zeta} \end{Bmatrix} = \mathbf{J}^{-1} \frac{\partial N_i^{\text{type},3D}}{\partial \boldsymbol{\xi}} \quad (4.68)$$

where \mathbf{J}^{-1} is the inverse of the Jacobian matrix. \mathbf{J}^{-1} relates the derivatives with respect to the local (element) coordinates to the derivatives with respect to the global coordinates.

4.3 Solving the dynamic finite element equations of a piezoelectric transducer using numerical time-integration methods

4.3.1 Dynamic equations of a piezoelectric body

In the present section, we cover the dynamic behavior of electro-mechanically coupled systems. Point of departure for deriving a time-integration scheme is the equation of motion for a body with electro-mechanical coupling (cf. Eq. 4.46). For the sake of clarity, we repeat the system of equations at this point

$$\mathbf{M}_{uu}\ddot{\mathbf{U}} + \mathbf{R}_{uu}\dot{\mathbf{U}} + \mathbf{K}_{uu}\mathbf{U} + \mathbf{K}_{u\varphi}\Phi = \mathbf{f}_{uu}, \quad (4.69)$$

$$\mathbf{K}_{u\varphi}^T\mathbf{U} + \mathbf{K}_{\varphi\varphi}\Phi = \mathbf{f}_{\varphi\varphi}. \quad (4.70)$$

In the first step, we eliminate the electric potential Φ from Eq. (4.69) by rearranging Eq. (4.70) and by substituting the result in Eq. (4.69). Hence, the electric potential can be expressed as

$$\Phi = \mathbf{K}_{\varphi\varphi}^{-1}(\mathbf{f}_{\varphi\varphi} - \mathbf{K}_{u\varphi}^T\mathbf{U}). \quad (4.71)$$

After the condensation of the electric degrees-of-freedom from the equation of motion it reads

$$\mathbf{M}_{uu}\ddot{\mathbf{U}} + \mathbf{R}_{uu}\dot{\mathbf{U}} + \underbrace{(\mathbf{K}_{uu} + \mathbf{K}_{u\varphi}\mathbf{K}_{\varphi\varphi}^{-1}\mathbf{K}_{\varphi u})}_{\mathbf{K}^*}\mathbf{U} = \underbrace{\mathbf{f}_{uu} + \mathbf{K}_{u\varphi}\mathbf{K}_{\varphi\varphi}^{-1}\mathbf{f}_{\varphi\varphi}}_{\mathbf{f}^*}. \quad (4.72)$$

\mathbf{K}^* denotes the modified stiffness matrix and \mathbf{f}^* the modified load vector. After solving the adjusted system of equations (cf. Eq. (4.72)) for the mechanical displacements \mathbf{U} , the electric potential Φ can be recovered using Eq. (4.71).

Concerning time-integration techniques, we can distinguish between explicit and implicit algorithms. The characteristic feature of explicit methods is that the equilibrium state at the time $t + \Delta t$ is evaluated solely based on the results from the previous time step t . The disadvantage we have to cope with, however, is that this class of time-stepping methods is only conditionally stable. On the other side, implicit methods have no restrictions as to the time step size - and they are accordingly unconditionally stable. The time step is consequently only limited by the required accuracy. In the case of an implicit method the equilibrium state at the time $t + \Delta t$ cannot be evaluated solely based on the results from the previous time step t . The procedure is also dependent on knowing the variables at the time $t + \Delta t$.

Typical representatives of explicit and implicit algorithms are the central difference method (CDM) [223–225] and the Newmark method [225–228], respectively. These time-marching schemes are also commonly implemented in commercial software tools, such as Abaqus and Ansys. The CDM and the Newmark method are therefore deployed to solve structural dynamics problems throughout the present thesis. The following two subsections will serve to explain the basic principles needed to derive these two methods. The presentation is based on the methodology described in reference [225].

4.3.2 Central difference method

The CDM is a representative of the class of explicit time integration schemes. In this particular case of finite differences, we replace the first and second derivatives with respect to time of the displacement field at time step t by central difference formulae [229] (cf. Fig. 4.3)

$$\dot{\mathbf{U}}_t = \frac{\mathbf{U}_{t+\Delta t} - \mathbf{U}_{t-\Delta t}}{2\Delta t}, \quad (4.73)$$

$$\ddot{\mathbf{U}}_t = \frac{\mathbf{U}_{t+\Delta t} - 2\mathbf{U}_t + \mathbf{U}_{t-\Delta t}}{\Delta t^2}. \quad (4.74)$$

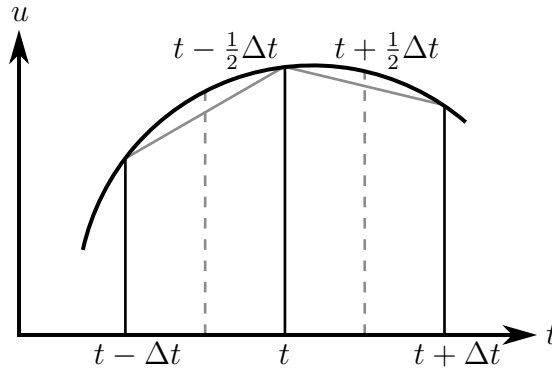


Figure 4.3: A sketch of the basic principle of the CDM. The analytical solution is depicted in black while the assumed solution is given in grey.

Substituting the relations given above into Eq. (4.72) yields

$$\mathbf{M}_{uu} \left(\frac{\mathbf{U}_{t+\Delta t} - 2\mathbf{U}_t + \mathbf{U}_{t-\Delta t}}{\Delta t^2} \right) + \mathbf{R}_{uu} \left(\frac{\mathbf{U}_{t+\Delta t} - \mathbf{U}_{t-\Delta t}}{2\Delta t} \right) + \mathbf{K}_{uu} \mathbf{U}_t + \mathbf{K}_{u\varphi} \mathbf{K}_{\varphi\varphi}^{-1} (\mathbf{f}_{\varphi\varphi} - \mathbf{K}_{u\varphi}^T \mathbf{U}_t) = \mathbf{f}_{uu}. \quad (4.75)$$

Solving Eq. (4.75) for the displacement field at the time $t + \Delta t$ results in

$$\mathbf{U}_{t+\Delta t} = \left(\frac{1}{\Delta t^2} \mathbf{M}_{uu} + \frac{1}{2\Delta t} \mathbf{R}_{uu} \right)^{-1} \left[\mathbf{f}_{uu} - \mathbf{K}_{u\varphi} \mathbf{K}_{\varphi\varphi}^{-1} \mathbf{f}_{\varphi\varphi} - \mathbf{K}_{uu} \mathbf{U}_t + \mathbf{K}_{u\varphi} \mathbf{K}_{\varphi\varphi}^{-1} \mathbf{K}_{u\varphi}^T \mathbf{U}_t + \frac{2}{\Delta t^2} \mathbf{M}_{uu} \mathbf{U}_t - \frac{1}{\Delta t^2} \mathbf{M}_{uu} \mathbf{U}_{t-\Delta t} + \frac{1}{2\Delta t} \mathbf{R}_{uu} \mathbf{U}_{t-\Delta t} \right]. \quad (4.76)$$

With regard to Eq. 4.76, we clearly see that the initial time step ($t = 0$) is dependent on results from the fictitious time step $t = -\Delta t$, which is why a specific start-up procedure is therefore required. In this case, we solve Eq. 4.76 with the help of the known initial conditions.

Instead of solving Eq. (4.76) directly, a different strategy can also be adopted. In the initial time step, where both the electric potential and the displacements are unknown, we propose to set the electric potential to zero

$$\Phi = 0.$$

Consequently, only Eq. (4.69) has to be solved when neglecting all electrical terms. The resulting displacement vector $\mathbf{U}_{t+\Delta t}$ is then used to calculate the electric potential via Eq. (4.71)

$$\Phi_{t+\Delta t} = \mathbf{K}_{\varphi\varphi}^{-1} (\mathbf{f}_{\varphi\varphi} - \mathbf{K}_{u\varphi}^T \mathbf{U}_{t+\Delta t}).$$

All mentioned calculations can also be performed on the element level. A brief explanation of the element by element approach is given in [111].

Keeping in mind that the CDM is only conditionally stable, the stability limit of this method has to be considered. It is commonly given in terms of the highest eigenfrequency (ω_{max}) of the system as

$$\Delta t \leq \frac{2}{\omega_{max}}, \quad (4.77)$$

where ω_{max} is the square root of the spectral radius ϱ which depends on the system matrices

$$\omega_{max} = \sqrt{\varrho(\mathbf{M}_{uu}^{-1} \mathbf{K}^*)}. \quad (4.78)$$

This can be conservatively estimated as

$$\omega_{max} \approx \frac{\sqrt{\varrho(\mathbf{K}^*)}}{\sqrt{\varrho(\mathbf{M}_{uu}^{-1})}} = \frac{\omega_{max}(\mathbf{K}^*)}{\omega_{min}(\mathbf{M}_{uu})}. \quad (4.79)$$

4.3.3 Newmark algorithm

The Newmark method is a typical representative of the class of implicit time-integration algorithms. The Newmark method [211, 227, 228] introduces two parameters: γ_N and β_N . These values indicate the influence of the acceleration at the end of the time step ($t + \Delta t$) on the velocity and displacement, respectively. If we assume a linear acceleration within the time interval (cf. Fig. 4.4), the velocity and displacement at time $t + \Delta t$ are given as

$$\dot{\mathbf{U}}_{t+\Delta t} = \dot{\mathbf{U}}_t + \underbrace{\left[(1 - \gamma_N) \ddot{\mathbf{U}}_t + \gamma_N \ddot{\mathbf{U}}_{t+\Delta t} \right]}_{\ddot{\mathbf{U}}_{t+\gamma_N \Delta t}} \Delta t, \quad (4.80)$$

$$\mathbf{U}_{t+\Delta t} = \mathbf{U}_t + \dot{\mathbf{U}}_t \Delta t + \left[\left(\frac{1}{2} - \beta_N \right) \ddot{\mathbf{U}}_t + \beta_N \ddot{\mathbf{U}}_{t+\Delta t} \right] \Delta t^2. \quad (4.81)$$

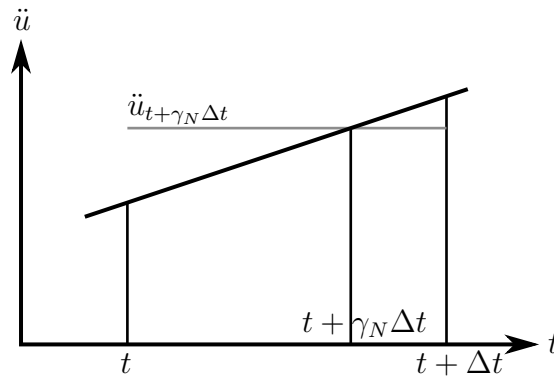


Figure 4.4: A sketch of the basic principle of the Newmark method, illustrating the influence of the Newmark parameter γ_N .

To obtain an unconditionally stable implicit time-integration scheme, the two Newmark parameters need to be chosen in such a way that

$$2\beta_N \geq \gamma_N \geq \frac{1}{2} \quad (4.82)$$

holds [225]. Different time-stepping algorithms can be obtained depending on the choice of γ_N and β_N . The Newmark parameters are therefore used to control the accuracy and stability of the numerical time-integration. If $\beta_N = 0$ an explicit algorithm is generated while for $\beta_N \neq 0$ implicit methods are obtained. Choosing $\gamma_N = 1/2$ and $\beta_N = 1/4$ results in the average acceleration method (trapezoidal rule). This method is commonly employed in commercial software such as Abaqus and accordingly used throughout the present thesis. The linear acceleration method, on the other hand, is obtained by choosing $\gamma_N = 1/2$ and $\beta_N = 1/6$. We have to keep in mind however, that the time-integration scheme is second order accurate if and only if $\gamma_N = 1/2$. If we want to introduce numerical/artificial damping ($\gamma_N \neq 1/2$), the second order accuracy is unfortunately lost. If Eq. 4.81 is solved at this point for the acceleration at the end of the time step, we obtain

$$\ddot{\mathbf{U}}_{t+\Delta t} = \frac{1}{\Delta t^2 \beta_N} [\mathbf{U}_{t+\Delta t} - \mathbf{U}_t] - \frac{1}{\Delta t \beta_N} \dot{\mathbf{U}}_t + \left(1 - \frac{1}{2\beta_N}\right) \ddot{\mathbf{U}}_t. \quad (4.83)$$

By substituting Eq. 4.83 into Eq. 4.80 we are able to compute the velocity at the time $t + \Delta t$

$$\dot{\mathbf{U}}_{t+\Delta t} = \frac{\gamma_N}{\Delta t \beta_N} [\mathbf{U}_{t+\Delta t} - \mathbf{U}_t] - \left(\frac{\gamma_N}{\beta_N} - 1\right) \dot{\mathbf{U}}_t - \left(\frac{\gamma_N}{2\beta_N} - 1\right) \Delta t \ddot{\mathbf{U}}_t. \quad (4.84)$$

At this point, the Newmark algorithm is applied to the equations of motion for a body with electro-mechanical coupling after the condensation of the electric degrees-of-freedom has been executed, cf. Eq. (4.72). Substituting Eqs. (4.83) and (4.84) into Eq. (4.72) consequently yields

$$\begin{aligned} & \mathbf{M}_{uu} \left(\frac{1}{\Delta t^2 \beta_N} [\mathbf{U}_{t+\Delta t} - \mathbf{U}_t] - \frac{1}{\Delta t \beta_N} \dot{\mathbf{U}}_t + \left(1 - \frac{1}{2\beta_N}\right) \ddot{\mathbf{U}}_t \right) + \\ & \mathbf{R}_{uu} \left(\frac{\gamma_N}{\Delta t \beta_N} [\mathbf{U}_{t+\Delta t} - \mathbf{U}_t] - \left(\frac{\gamma_N}{\beta_N} - 1\right) \dot{\mathbf{U}}_t - \left(\frac{\gamma_N}{2\beta_N} - 1\right) \Delta t \ddot{\mathbf{U}}_t \right) + \\ & \mathbf{K}_{uu} \mathbf{U}_{t+\Delta t} + \mathbf{K}_{u\varphi} \mathbf{K}_{\varphi\varphi}^{-1} (\mathbf{f}_{\varphi\varphi} - \mathbf{K}_{u\varphi}^T \mathbf{U}_{t+\Delta t}) = \mathbf{f}_{uu}. \end{aligned} \quad (4.85)$$

At this stage Eq. 4.85 can be solved for the unknown displacement field $\mathbf{U}_{t+\Delta t}$

$$\begin{aligned} & \underbrace{\left(\mathbf{K}_{uu} + \mathbf{R}_{uu} \frac{\gamma_N}{\Delta t \beta_N} + \mathbf{M}_{uu} \frac{1}{\Delta t^2 \beta_N} - \mathbf{K}_{u\varphi} \mathbf{K}_{\varphi\varphi}^{-1} \mathbf{K}_{u\varphi}^T \right)}_{\bar{\mathbf{K}}_{\text{piezo}}} \mathbf{U}_{t+\Delta t} = \mathbf{f}_{uu} + \\ & \left(\mathbf{M}_{uu} \frac{1}{\Delta t^2 \beta_N} + \mathbf{R}_{uu} \frac{\gamma_N}{\Delta t \beta_N} \right) \mathbf{U}_t + \left(\mathbf{M}_{uu} \frac{1}{\Delta t \beta_N} + \mathbf{R}_{uu} \left[\frac{\gamma_N}{\beta_N} - 1 \right] \right) \dot{\mathbf{U}}_t + \\ & \left(\mathbf{M}_{uu} \left[\frac{1}{2\beta_N} - 1 \right] + \mathbf{R}_{uu} \left[\frac{\gamma_N}{2\beta_N} - 1 \right] \Delta t \right) \ddot{\mathbf{U}}_t - \mathbf{K}_{u\varphi} \mathbf{K}_{\varphi\varphi}^{-1} \mathbf{f}_{\varphi\varphi}, \end{aligned} \quad (4.86)$$

where $\bar{\mathbf{K}}_{\text{piezo}}$ denotes the so-called effective dynamic stiffness matrix. Once $\bar{\mathbf{K}}_{\text{piezo}}$ has been triangularized, the solution for the displacements at each time step only requires the formation of the right-hand side plus a forward reduction and a backward substitution.

4.4 Representation of the geometry - Mapping

The integration of the system matrices - Eqs. (4.26) - (4.32) - is normally performed over the volume or surface of a single FE. On the other hand, all shape functions are typically defined on a reference element with an unique local element coordinate system. For that reason, a mapping between the reference and the physical domain is inevitable and given by

$$d\Omega = dx_1 dx_2 dx_3 = \det(\mathbf{J})d\xi d\eta d\zeta. \quad (4.87)$$

The Jacobian matrix \mathbf{J} - Eq. (4.68) - takes this mapping into account. It is defined by the mapping function $\mathbf{Q}^{(e)}$ and transforms the system matrices from the reference domain to the physical one.

This mapping procedure is of particular interest in the FEM, for the geometry of a structure needs to be solved using only a finite number of elements. Thus, it is very important to devise strategies to accurately describe the geometry of the structure under investigation. Depending on the functions used for the approximation of the independent field variables and the description of the geometry (mapping), we can distinguish three element formulations: (i) isoparametric, (ii) sub-parametric and (iii) super-parametric. In the isoparametric element concept, we use the same shape functions to interpolate the nodal coordinates and the unknown field variables. Sub- and super-parametric formulations are based on the idea of using different functions or polynomials of different order to describe the geometry and the unknowns. In the sub-parametric element concept, both the functions to approximate the geometry and the functions to interpolate the unknowns must be in the same functional space. Also, the functions to describe the unknowns are of higher order. If the super-parametric concept is applied, however, the chosen mapping functions are not in the same functional space. This is the case if the mapping is of higher polynomial order than the approximation of the independent field variables or if the mapping is based on non-polynomial functions. If a super-parametric formulation is favored we have to pay attention to the exact representation of rigid body modes [115]. However, we must bear in mind that, generally, the mapping procedure and the approximation of unknown field variables are independent of each other.

Although the isoparametric element concept, first introduced by Ergatoudis, Irons and Zienkiewicz [230, 231], is used almost exclusively in commercial h -version FEM software, we propose to apply: (i) the so-called blending function method [115, 120] as a special case of a super-parametric mapping approach and (ii) the sub-parametric element concept as proposed by Becker [215]. The first approach was chosen because it represents the geometry of the structure exactly. The charm of the second method, however, lies in the fact that commercial pre-processors can be employed to generate a high quality FE mesh. For these reasons, we use both concepts to describe the geometry within the framework of HO -FEMs. They are accordingly discussed in the following sections and have been implemented in the in-house HO -FEM code.

4.4.1 Blending function method

Regardless of the number of FEs the blending function method [115, 120] is able to ensure an accurate description of the geometry of the structure. This methodology was introduced by Gordon and Hall [232–235] at the beginning of the 1970s. Their ideas serve as a basis to implement almost any kind of curved edges or faces. The formulation of the blending function method in the present thesis closely follows the methodology outlined by Szabó and Babuška [115]. Applications of this method to complex structural analysis problems are illustrated in references [130, 236–240].

The implementation of the blending function method is based on a hexahedral element formulation. The reference element is depicted in Fig. 4.2. If we assume that the geometry of all edges and faces is known in a parametric form, the elemental mapping function $\mathbf{Q}^{(e)}$ is given as

$$\mathbf{x} = \mathbf{Q}^{(e)}(\xi, \eta, \zeta) = \sum_{i=1}^8 N_{1,1,1}^{N_i}(\xi, \eta, \zeta) \mathbf{X}_i + \sum_{i=1}^6 \mathbf{f}_i(\xi, \eta, \zeta) - \sum_{i=1}^{12} \mathbf{e}_i(\xi, \eta, \zeta). \quad (4.88)$$

The first term is equivalent to the linear mapping of an 8-node hexahedral FE using the well-known trilinear shape functions $N_{(1,1,1)}^{N_i}$ ($i = 1, \dots, 8$; listed in Appendix B) with \mathbf{X}_i denoting the nodal coordinates. The face blending is realized using the second term, where \mathbf{f}_i ($i = 1, \dots, 6$) describes the difference between the curved face and its bilinear approximation. The final term corresponds to the edge blending, where \mathbf{e}_i ($i = 1, \dots, 12$) describes the difference between the curved edge and the linear function connecting the two end points. This term is subtracted as it appears in the face blending function twice already. Finally, the mapping function is given as

$$\begin{aligned} \mathbf{x} = \mathbf{Q}^{(e)}(\xi, \eta, \zeta) = & \sum_{i=1}^8 N_{(1,1,1)}^{N_i}(\xi, \eta, \zeta) \mathbf{X}_i + \\ & \mathbf{F}_5(\eta, \zeta) \hat{B}(\xi) + \mathbf{F}_3(\eta, \zeta) \tilde{B}(\xi) + \mathbf{F}_2(\xi, \zeta) \hat{B}(\eta) + \\ & \mathbf{F}_4(\xi, \zeta) \tilde{B}(\eta) + \mathbf{F}_1(\xi, \eta) \hat{B}(\zeta) + \mathbf{F}_6(\xi, \eta) \tilde{B}(\zeta) - \\ & \mathbf{E}_1(\xi) \hat{B}(\eta) \hat{B}(\zeta) - \mathbf{E}_3(\xi) \tilde{B}(\eta) \hat{B}(\zeta) - \mathbf{E}_{11}(\xi) \tilde{B}(\eta) \tilde{B}(\zeta) - \\ & \mathbf{E}_8(\xi) \hat{B}(\eta) \tilde{B}(\zeta) - \mathbf{E}_4(\eta) \hat{B}(\xi) \hat{B}(\zeta) - \mathbf{E}_{12}(\eta) \hat{B}(\xi) \tilde{B}(\zeta) - \\ & \mathbf{E}_{10}(\eta) \tilde{B}(\xi) \tilde{B}(\zeta) - \mathbf{E}_2(\eta) \tilde{B}(\xi) \hat{B}(\zeta) - \mathbf{E}_5(\zeta) \hat{B}(\xi) \hat{B}(\eta) - \\ & \mathbf{E}_6(\zeta) \tilde{B}(\xi) \hat{B}(\eta) - \mathbf{E}_7(\zeta) \tilde{B}(\xi) \tilde{B}(\eta) - \mathbf{E}_8(\zeta) \hat{B}(\xi) \tilde{B}(\eta). \end{aligned} \quad (4.89)$$

The linear blending functions \tilde{B} and \hat{B} are defined as

$$\tilde{B}(\xi) = \frac{1}{2} [1 + \xi], \quad (4.90)$$

$$\hat{B}(\xi) = \frac{1}{2} [1 - \xi]. \quad (4.91)$$

In Eq. (4.89) \mathbf{F}_i and \mathbf{E}_i describe the parameterization of each face and edge, respectively. The Jacobian can be easily computed by employing Eq. (4.89). This is essential for the numerical integration of the system matrices, cf. Section 5.2.1. The application of the blending function method is schematically illustrated in Fig. 4.5.

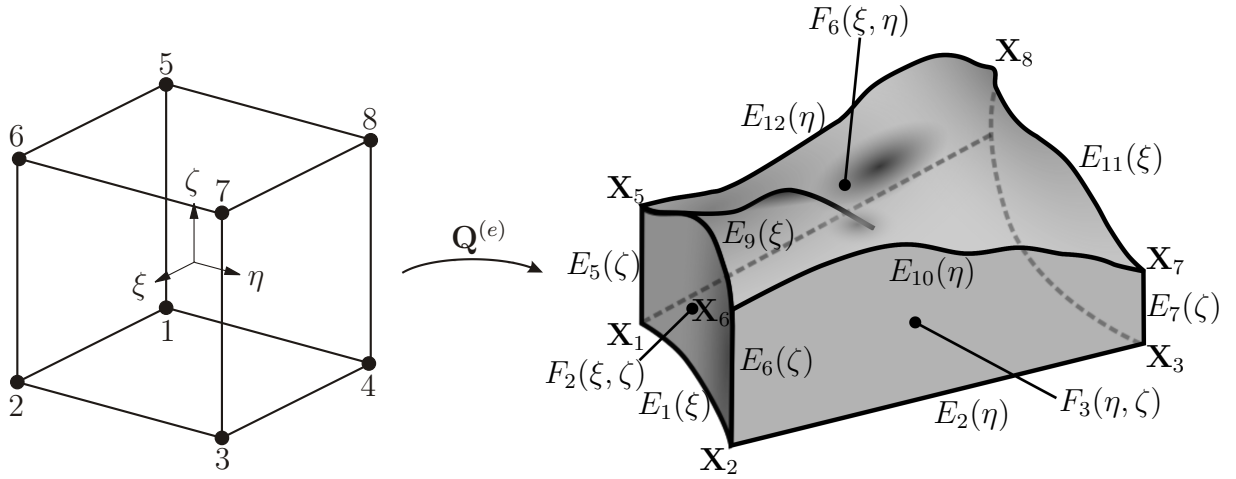


Figure 4.5: Mapping by the blending function method.

4.4.2 Sub-parametric mapping concept

The second mapping approach is to employ a sub-parametric methodology [211]. That is to say, the shape functions used for the approximation of the independent field variables are more complex than those of the geometry description. That is the case if the description of the geometry is given by a polynomial of lower order than that used for the approximation of the unknown function. Becker proposes to use the shape functions of a 20-node hexahedral FE of Serendipity type [215] also for *HO-FEMs*, cf. Fig. 4.6. The faces and edges can therefore assume a parabolic shape and the mapping function is given as [241]

$$\mathbf{x} = \mathbf{Q}^{(e)}(\xi, \eta, \zeta) = \sum_{i=1}^{20} N^{N_i}(\xi, \eta, \zeta) \mathbf{X}_i. \quad (4.92)$$

The basis functions for this kind of FE are given at this point without derivation. For details, we refer the interested reader to standard textbooks on the *h*-version of the FEM [211, 212, 241].

$$N^{N_i}(\boldsymbol{\xi}) = -\frac{1}{8}[1 + \xi\xi_i][1 + \eta\eta_i][1 + \zeta\zeta_i][-\xi\xi_i - \eta\eta_i - \zeta\zeta_i + 2] \quad \text{for } i = 1, \dots, 8, \quad (4.93)$$

$$N^{N_i}(\boldsymbol{\xi}) = +\frac{1}{4}[1 - \xi^2][1 + \eta\eta_i][1 + \zeta\zeta_i] \quad \text{for } i = 9, 11, 13, 15, \quad (4.94)$$

$$N^{N_i}(\boldsymbol{\xi}) = +\frac{1}{4}[1 - \eta^2][1 + \xi\xi_i][1 + \zeta\zeta_i] \quad \text{for } i = 10, 12, 14, 16, \quad (4.95)$$

$$N^{N_i}(\boldsymbol{\xi}) = +\frac{1}{4}[1 - \zeta^2][1 + \xi\xi_i][1 + \eta\eta_i] \quad \text{for } i = 17, 18, 19, 20. \quad (4.96)$$

(ξ_i, η_i, ζ_i) are the local coordinates of the *i*-th nodal point. The sub-parametric mapping concept is a feasible alternative to more complex approaches, as it is efficient in describing the geometry and because the accuracy can be regarded as adequate for most engineering applications [215]. By adopting this procedure, commercial pre-processors can be conveniently deployed to discretize the model (only an appropriate interface needs to be developed).

The integrand F_{type} (type: p, L, N) denotes a function specifying which of the three previously mentioned algorithms should be used to enforce the essential boundary conditions, while $\mathcal{C}(\mathbf{u})$ is the constraint to be enforced.

Concerning the **penalty method**, the integrand F_p is given as

$$F_p = \frac{1}{2} \beta_p \mathcal{C}(\mathbf{u})^2. \quad (4.99)$$

The constraint virtual work accordingly reads

$$\delta \Pi_{c,p} = \int_{\Gamma_{D,u}} \beta_p (\mathbf{u} - \bar{\mathbf{u}})^T \delta \mathbf{u} d\Gamma. \quad (4.100)$$

The penalty method is a simple and yet elegant procedure to account for displacement boundary conditions [116]. Most commercial FE tools are based on this method [106, 211, 212, 241]. The advantage of the penalty method is that no additional unknowns have to be introduced, ensuring that the bandwidth of the system matrices remains unaltered. On the other hand - depending on the magnitude of the penalty number β_p - the system of equations can become ill-conditioned.

Often, the **Lagrange multiplier method** is applied as an alternative to the penalty approach. Here, additional unknown parameters $\boldsymbol{\lambda}$ are introduced and the constraint equation is multiplied with these

$$F_L = \boldsymbol{\lambda} \mathcal{C}(\mathbf{u}). \quad (4.101)$$

Consequently, the virtual work not only depends on the actual configuration of the displacement field but also on the additional variables $\boldsymbol{\lambda}$. Hence, the number of unknowns is increased. Using F_L the constraint virtual work for the Lagrange multiplier method yields

$$\delta \Pi_{c,L} = \int_{\Gamma_{D,u}} \delta \boldsymbol{\lambda}^T (\mathbf{u} - \bar{\mathbf{u}}) d\Gamma + \int_{\Gamma_{D,u}} \boldsymbol{\lambda}^T \delta \mathbf{u} d\Gamma. \quad (4.102)$$

In the case of a structural system, we can identify the Lagrange multiplier as a function of the primary variable (function of the displacements) to overcome the mentioned disadvantage of the method (i.e. increasing the number of unknowns). According to [243] we can express the Lagrange multiplier $\boldsymbol{\lambda}$ as

$$\boldsymbol{\lambda} = -\boldsymbol{\sigma} \mathbf{n} = -\mathbf{t}. \quad (4.103)$$

The superposition of the penalty method and the Lagrange approach is referred to as **Nitsche's method** [163, 244–247]. Here, the integrand function F_N of this Ansatz is defined as

$$F_N = F_p + F_L = \frac{1}{2} \beta_S \mathcal{C}(\mathbf{u})^2 + \boldsymbol{\lambda} \mathcal{C}(\mathbf{u}). \quad (4.104)$$

The constraint virtual work is therefore given as

$$\delta \Pi_{c,N} = \delta \Pi_{c,p} + \delta \Pi_{c,L} = \int_{\Gamma_{D,u}} \beta_S (\mathbf{u} - \bar{\mathbf{u}})^T \delta \mathbf{u} d\Gamma + \int_{\Gamma_{D,u}} \delta \boldsymbol{\lambda}^T (\mathbf{u} - \bar{\mathbf{u}}) d\Gamma + \int_{\Gamma_{D,u}} \boldsymbol{\lambda}^T \delta \mathbf{u} d\Gamma. \quad (4.105)$$

The advantage of Nitsche's method is that it is a variationally consistent extension of the weak formulation. The homogeneous and inhomogeneous essential boundary conditions are satisfied in a weak/integral sense [244, 247, 248]. In Nitsche's method β_S can be used as a stabilization parameter. The major challenge, however, is to choose the value of this stabilization parameter β_S [249]. It has to be large enough to ensure the coercivity of the modified weak form [248, 250–253] but small enough in order to avoid ill-conditioning of the system matrices. It can, therefore, be chosen much smaller than in the pure penalty method so as to ensure that the condition number is not dramatically increased. In references [251–253] it was demonstrated that β_S depends on the mesh-size, the polynomial degree and the material parameters. The implementation of this method is based on an empirical choice of the stabilization parameter as proposed in [163, 172, 249, 254].

4.5.2 Neumann boundary conditions

Homogeneous natural boundary conditions are directly accounted for in the formulation of the weak form. On the other hand, inhomogeneous Neumann boundary conditions are imposed by explicitly including the load vector. As the calculation of the load vector is not straightforward - due to surface loads - it will be discussed subsequently [116]. Such distributed loads can be determined utilizing Eq. (4.31). Only the second term in Eq. (4.31) is of particular concern. Thus, it is stated again for the sake of clarity:

$$\mathbf{f}_{\text{surf}}^{(e)} = \int_{\Gamma_{e,N,u}} \mathbf{N}_u^T \bar{\mathbf{t}} d\Gamma. \quad (4.106)$$

As the integration has to be performed on the reference domain, the differential $d\Gamma$ has to be mapped to the local coordinate system. This can be achieved by using the first fundamental form of Gauß [255]. Now the differential surface element $d\Gamma$ is given by

$$d\Gamma = \sqrt{\det(\mathcal{D}\mathcal{D}^T)} dr ds = \sqrt{EG - F^2} dr ds, \quad (4.107)$$

where \mathcal{D} is the coefficient matrix of the metric tensor

$$\mathcal{D} = \begin{bmatrix} \frac{\partial x_1}{\partial r} & \frac{\partial x_2}{\partial r} & \frac{\partial x_3}{\partial r} \\ \frac{\partial x_1}{\partial s} & \frac{\partial x_2}{\partial s} & \frac{\partial x_3}{\partial s} \end{bmatrix} \quad (4.108)$$

and r and s are the local (in-plane) coordinates of the corresponding face, cf. Fig. 4.7. The variables E , F and G are abbreviations for

$$E = \left(\frac{\partial x_1}{\partial r} \right)^2 + \left(\frac{\partial x_2}{\partial r} \right)^2 + \left(\frac{\partial x_3}{\partial r} \right)^2, \quad (4.109)$$

$$G = \left(\frac{\partial x_1}{\partial s} \right)^2 + \left(\frac{\partial x_2}{\partial s} \right)^2 + \left(\frac{\partial x_3}{\partial s} \right)^2, \quad (4.110)$$

and

$$F = \frac{\partial x_1}{\partial r} \frac{\partial x_1}{\partial s} + \frac{\partial x_2}{\partial r} \frac{\partial x_2}{\partial s} + \frac{\partial x_3}{\partial r} \frac{\partial x_3}{\partial s}. \quad (4.111)$$

We have to perform this integration on all element faces, where Neumann boundary conditions are imposed.

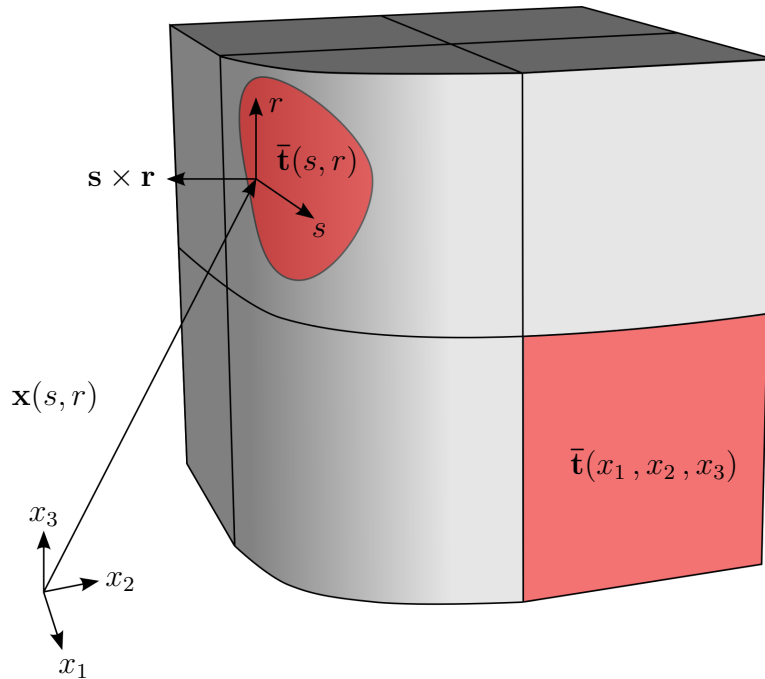


Figure 4.7: Mapping of the element surface for the integration of the Neumann boundary condition (parameterized surface).

4.6 Diagonalization of the mass matrix

The mass matrix defined by Eq. (4.26) is commonly referred to as a consistent mass matrix [212]. The term *consistent mass matrix* was coined as its definition is derived from the variational formulation. The computational costs of higher order approaches, however, motivate the use of a diagonal mass matrix \mathbf{M}_{uu}^{diag} . Explicit time integration schemes benefit greatly from the fact that the inversion of a lumped mass matrix is straightforward, because only the reciprocal of each of its main diagonal elements has to be computed [123]. The consequence of a diagonal mass matrix is that only matrix-vector operations are needed to solve the FE equations of motion. That is why, for high frequency and large scale dynamic problems, explicit time integration algorithms are one key ingredient to ensure an efficient and fast simulation.

In the following subsections, we address three techniques that can be employed to compute a lumped mass matrix. Note however, that these approaches can **only** be applied to **nodal-based** shape functions, cf. Sections 6.1.1 and 6.1.2. For hierarchic shape functions based on Legendre polynomials or trigonometric functions (Sections 6.1.3 and 6.1.4) there are no feasible lumping techniques yet. Again, for clarification, we provide the definition of the consistent mass matrix - cf. Eq. (4.26):

$$\mathbf{M}_{uu}^{(e)} = \int_{\Omega_e} \rho \mathbf{N}_u^T \mathbf{N}_u d\Omega.$$

4.6.1 Nodal quadrature technique

An elegant way to diagonalize the mass matrix is to employ the nodal quadrature technique. The basic idea is to use the same points that define the shape functions also as quadrature points. Accordingly, an integration formula with quadrature points at the nodes will show the following form [212]

$$M_{uu}^{diag,(i,j)} = \int_{-1}^1 \int_{-1}^1 \int_{-1}^1 \rho N_{u,i}(\xi, \eta, \zeta) N_{u,j}(\xi, \eta, \zeta) \det(\mathbf{J}) d\xi d\eta d\zeta,$$

$$M_{uu}^{diag,(i,j)} = \rho \sum_{k=1}^{p_\xi+1} \sum_{l=1}^{p_\eta+1} \sum_{m=1}^{p_\zeta+1} w_k^{(p_\xi+1)} w_l^{(p_\eta+1)} w_m^{(p_\zeta+1)} N_{u,i}(\xi_k^{(p_\xi+1)}, \eta_l^{(p_\eta+1)}, \zeta_m^{(p_\zeta+1)}) N_{u,j}(\xi_k^{(p_\xi+1)}, \eta_l^{(p_\eta+1)}, \zeta_m^{(p_\zeta+1)}) \det(\mathbf{J}). \quad (4.112)$$

For all nodal based shape functions the following equation holds

$$N_{u,i}(\xi_j^{(p_\xi+1)}, \eta_j^{(p_\eta+1)}, \zeta_j^{(p_\zeta+1)}) = \delta_{ij}. \quad (4.113)$$

The effect of such a rule on the mass matrix is to diagonalize it, that is

$$M_{uu}^{diag,(i,j)} = \begin{cases} \rho w_i^{(p_\xi+1)} w_i^{(p_\eta+1)} w_i^{(p_\zeta+1)} \det(\mathbf{J}) & i = j, \\ 0 & i \neq j. \end{cases} \quad (4.114)$$

The quadrature rule used above is an example of a Gauß-Lobatto-Legendre integration rule. These rules are very similar to standard Gaussian quadrature rules (cf. Section 5.2.1), the only difference being that the end points of the interval are always included [212].

4.6.2 Row-sum technique

The simplest of all mass-lumping algorithms is the so-called row-sum technique. It is very easy to implement and therefore widely used in the context of low order (h -version) FEs. The fundamental principle is that the components of each row of the mass matrix are summed and lumped on the diagonal entry [241]

$$M_{uu}^{diag,(i,j)} = \begin{cases} \sum_{k=1}^{n_{dof}} \left(\int_{-1}^1 \int_{-1}^1 \int_{-1}^1 \rho N_{u,i} N_{u,k} \det(\mathbf{J}) d\xi d\eta d\zeta \right) & i = j, \\ 0 & i \neq j. \end{cases} \quad (4.115)$$

We can re-write Eq. (4.115) also as

$$M_{uu}^{diag,(i,j)} = \begin{cases} \int_{-1}^1 \int_{-1}^1 \int_{-1}^1 \rho N_{u,i} \det(\mathbf{J}) d\xi d\eta d\zeta & i = j, \\ 0 & i \neq j. \end{cases} \quad (4.116)$$

This is due to the fact, that nodal based shape functions posses the partition of unity property

$$\sum_{n=1}^{p+1} N_n(\xi, \eta, \zeta) = 1. \quad (4.117)$$

In a last step, Eq. (4.116) has to be numerically integrated

$$M_{uu}^{diag,(i,j)} = \begin{cases} \sum_{k=1}^{p_\xi+1} \sum_{l=1}^{p_\eta+1} \sum_{m=1}^{p_\zeta+1} w_k^{(p_\xi+1)} w_l^{(p_\eta+1)} w_m^{(p_\zeta+1)} N_{u,o}(\xi_k^{(p_\xi+1)}, \eta_l^{(p_\eta+1)}, \zeta_m^{(p_\zeta+1)}) \det(\mathbf{J}) & i = j, \\ 0 & i \neq j. \end{cases} \quad (4.118)$$

o is the index of the higher order shape functions and is defined by

$$o = k + l + m. \quad (4.119)$$

When applied to p -type FEs ($p > 2$) the row-sum technique encounters problems due to the possibility of negative entries in the mass matrix [212]. This drawback, however, is resolved by the algorithm discussed in the following subsection.

4.6.3 HRZ-lumping technique

The HRZ-lumping technique was first proposed by Hinton *et al.* [256]. The advantage of this algorithm is that it always produces positive lumped masses [212]. The idea behind this method is to scale the components of the lumped mass matrix with the total mass of the FE. Consequently, the mass distribution will be conserved. The consistent mass matrix is calculated first, cf. Eq. (4.26). In the next step, we use the following formula to compute the diagonal mass matrix

$$M_{uu}^{diag,(i,j)} = \begin{cases} cM^{(i,j)} & i = j, \\ 0 & i \neq j. \end{cases} \quad (4.120)$$

The variable c stands for the scaling factor of the components of the diagonal mass matrix and is given as

$$c = \frac{d \cdot m^{(e)}}{\sum_{i=1}^{n_{dof}} M^{(i,i)}} \quad (4.121)$$

with $m^{(e)}$ denoting the total mass of the corresponding FE and $M^{(i,i)}$ as the i -th component of the diagonal of the consistent mass matrix. Both values can be determined using

$$m^{(e)} = \int_{-1}^1 \int_{-1}^1 \int_{-1}^1 \rho \det(\mathbf{J}) d\xi d\eta d\zeta \quad (4.122)$$

and

$$M^{(i,i)} = \int_{-1}^1 \int_{-1}^1 \int_{-1}^1 \rho N_{u,i}(\xi, \eta, \zeta) N_{u,i}(\xi, \eta, \zeta) \det(\mathbf{J}) d\xi d\eta d\zeta. \quad (4.123)$$

According to Hughes [212] this is, at present, the only procedure that can be recommended for arbitrary FEs (with nodal basis). Depending on the dimension d of the problem, the mass needs to be scaled ($d = 1, 2, 3$). In the context of the SCM (cf. Chapter 8 numerical results) the HRZ-lumping technique is used to lump spectral cells (SCs) that are cut by the physical boundaries [178].

Chapter 5

Higher Order Fictitious Domain Method

In the introduction (cf. Section 1.2), we clearly demonstrated that novel modeling techniques are required to effectively simulate the dynamic behavior of modern lightweight structures. This is especially important concerning wave propagation analysis in the context of SHM. The wide-spread use of reinforced plastics and sandwich panels in the aeronautical and wind energy industries calls for numerical approaches that are able to model complex structures. The requirement for body-fitted meshes in the conventional FEM, however, demands a high degree of manual input by the user. Since the generation of a high quality mesh is a very error-prone task, there is the need for a procedure that can easily be automated. Using such a methodology even complex cellular and biological materials (sandwich plates, bones e.g.) could be straightforwardly modelled, cf. Figs. 5.1 and 5.2.

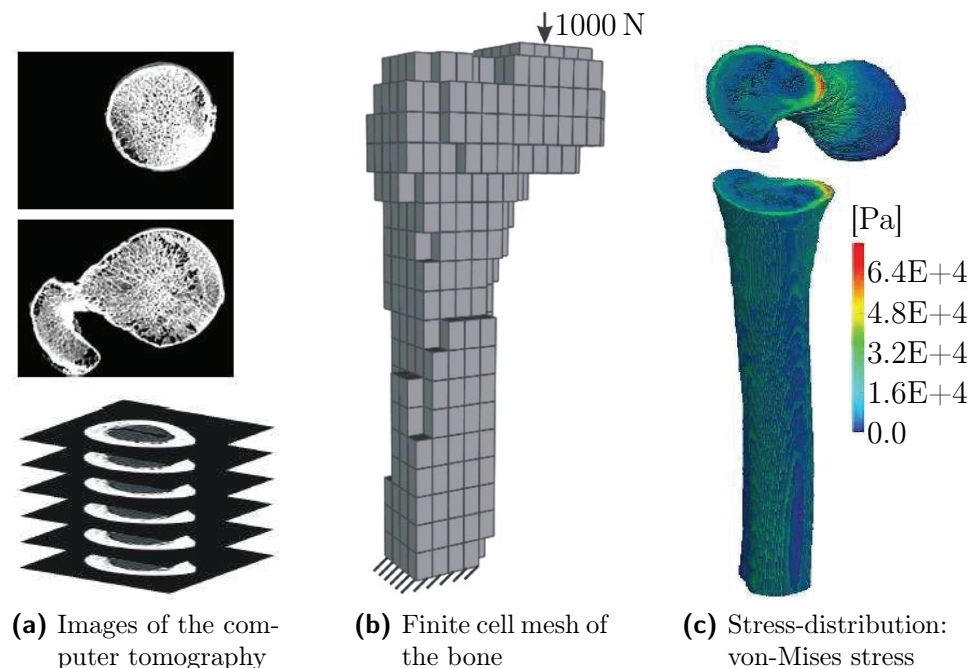


Figure 5.1: The FCM applied for the analysis of a proximal femur bone. The geometry is described by voxel-based data obtained using a computer tomograph (CT-data) [163, 257].

One prime candidate is seen in the application of higher order fictitious domain methods, such as the FCM and the recently proposed SCM [173, 177, 178]. For a detailed review on recent developments in the context of the FCM we refer the reader to an article by Schillinger and Ruesch [258]. The main benefits generated on the grounds of these approaches are a fully automated meshing procedure (fictitious domain concept) and high rates of convergence (higher order shape functions) [162, 166, 259].

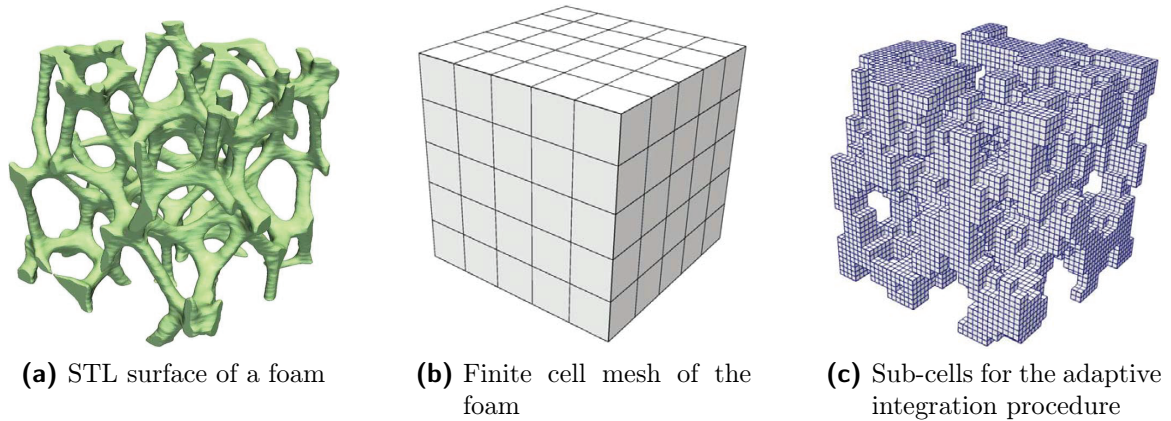


Figure 5.2: The FCM applied for the analysis of an aluminum foam structure. The geometry is described by a STL (surface tessellation language) file derived from voxel-based data obtained using a computer tomograph [163, 257].

In the present chapter, we provide the basic principles of the FCM for transient computations involving smart materials. We derive the variational formulation based on the principle of virtual work, as presented in Chapter 4. Fundamentals such as the geometry approximation by an adaptive integration strategy are discussed in detail. The whole framework of the fictitious domain concept is presented without reference to specific shape functions. This methodology facilitates the extension to different sets of Ansatz functions, as investigated in Chapter 6. The main objective here is to extend the FCM to high-frequency structural dynamics and to introduce new shape functions to the finite cell (FC) framework.

Depending on the shape functions (Chapter 6) that are used to approximate the independent field variables, the so-called p - and B-spline versions of the FCM, cf. [162–164, 166, 173, 177] can be distinguished. By introducing spectral shape functions the fictitious domain concept is extended to the SCM. The term is chosen analogously to the differentiation between the FEM and the SEM [106]. The present chapter therefore lays the foundation for the usage of higher order fictitious domain concepts for ultrasonic guided wave propagation.

5.1 Basic concept of the finite and spectral cell methods for smart structure applications

The fundamental idea of fictitious domain methods is that the mathematical model problem (defined in terms of a variational formulation) is not solved on the physical domain Ω but

instead over the so-called embedding domain Ω_{em} . Generally speaking, the physical domain can be arbitrarily complex when practice-oriented problems are considered. Ω is therefore embedded in a fictitious domain Ω_{fict} resulting in an embedding domain Ω_{em} with a simple geometry, cf. Fig. 5.3.

We introduce the indicator function α , cf. Fig. 5.4, to discriminate between the physical and the fictitious domain. α is a scalar value which is used to scale the material matrices $(\mathbf{C}, \mathbf{e}, \boldsymbol{\kappa})$ and the mass density ρ of the material. Setting $\alpha = 0$ corresponds to a void [164]. In this way, all points $\mathbf{X} \in \Omega_{em} \setminus \Omega$ which are not located in the physical domain do not contribute to the weak form. We have to keep in mind, that the accuracy of the simulation results deteriorates significantly if the system matrices are ill-conditioned. For that reason, we set α to a very small value which is close to 0 to circumvent these conditioning problems.

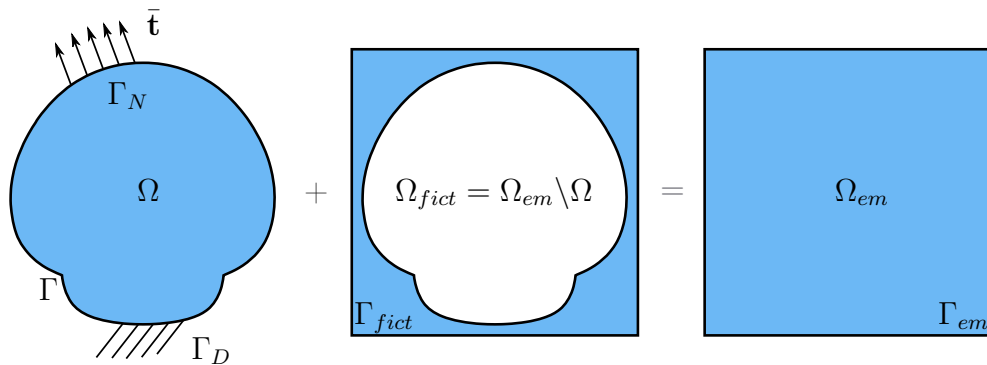


Figure 5.3: The physical domain Ω is extended by a so-called fictitious domain Ω_{fict} . This results in an easy discretization of the whole embedding domain Ω_{em} , while Γ and Γ_{em} denote the boundary of the physical and embedding domain, respectively.

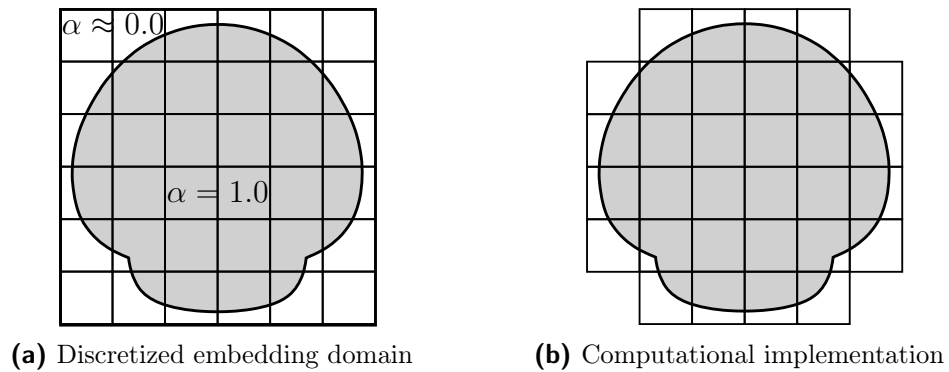


Figure 5.4: FC discretization: The embedding domain Ω_e is discretized using rectangular cells. The indicator function α serves to control the influence of the fictitious domain on the accuracy of the results.

The embedding domain is now discretized in a mesh using rectangular elements which are independent of the original domain, cf. Fig. 5.4. The main advantage of the fictitious domain concept is that we overcome the drawback of having to create a body-fitted mesh. The complexity of the mesh generation procedure is therefore reduced by embedding

the physical domain in a fictitious domain in such a way that their union (fictitious domain + physical domain) yields a simple geometry that can easily be discretized using rectangular hexahedral finite “elements”. The origin of this method can be traced back to classical fictitious domain or immersed boundary methods - first used for computational fluid dynamics applications [174, 175, 260, 261]. These finite “elements” of the embedding domain do not necessarily fulfill the usual geometric properties of elements for the physical domain Ω , as they may be intersected by the boundary of Ω . Accordingly, the term *finite cells* was coined to distinguish these elements from classical FEs.

Analogously to Chapter 4, the principle of virtual work is the point of departure for deriving the FCM. For the sake of clarity, we repeat the necessary equations at this point

$$\begin{aligned} \delta\chi_u = & - \int_{\Omega} (\mathbf{L}_u \delta \mathbf{u})^T \mathbf{C} (\mathbf{L}_u \mathbf{u}) \, d\Omega - \int_{\Omega} (\mathbf{L}_u \delta \mathbf{u})^T \mathbf{e}^T (\mathbf{L}_\varphi \varphi) \, d\Omega + \int_{\Omega} \delta \mathbf{u}^T \mathbf{f}_b \, d\Omega \\ & - \int_{\Omega} \delta \mathbf{u}^T \rho \ddot{\mathbf{u}} \, d\Omega + \int_{\Gamma_{N,u}} \delta \mathbf{u}^T \bar{\mathbf{t}} \, d\Gamma, \end{aligned} \quad (5.1)$$

$$\begin{aligned} \delta\chi_\varphi = & - \int_{\Omega} (\mathbf{L}_\varphi \delta \varphi)^T \mathbf{e} (\mathbf{L}_u \mathbf{u}) \, d\Omega + \int_{\Omega} (\mathbf{L}_\varphi \delta \varphi)^T \boldsymbol{\kappa} (\mathbf{L}_\varphi \varphi) \, d\Omega \\ & - \int_{\Omega} \delta \varphi^T q_b \, d\Omega - \int_{\Gamma_{N,\varphi}} \delta \varphi^T \bar{Q} \, d\Gamma. \end{aligned} \quad (5.2)$$

Following the FC procedure, the original physical domain Ω is now embedded into the domain Ω_{em} , referred to as embedding domain, with the boundary Γ_{em} . In a two-dimensional setting the described methodology is illustrated in Fig. 5.3. The interface between Ω and Ω_{em} is defined as

$$\Gamma_I = \Gamma = \Gamma_{fict} \setminus \Gamma_{em}. \quad (5.3)$$

Adhering to the ideas presented in [262], we extend the displacement field and the electric potential to the embedding domain in such a way that

$$\mathbf{u} = \begin{cases} \mathbf{u}_{phys} & \text{in } \Omega, \\ \mathbf{u}_{fict} & \text{in } \Omega_{fict} = \Omega_{em} \setminus \Omega, \end{cases} \quad (5.4)$$

and

$$\varphi = \begin{cases} \varphi_{phys} & \text{in } \Omega, \\ \varphi_{fict} & \text{in } \Omega_{fict} = \Omega_{em} \setminus \Omega, \end{cases} \quad (5.5)$$

hold. Thereafter, the continuity at the interface Γ_I between the domains is ensured by the following conditions

$$\mathbf{u}_{phys} = \mathbf{u}_{fict} \quad \text{on } \Gamma_I, \quad (5.6)$$

$$\mathbf{t}_{phys} = \mathbf{t}_{fict} \quad \text{on } \Gamma_I, \quad (5.7)$$

$$\varphi_{phys} = \varphi_{fict} \quad \text{on } \Gamma_I, \quad (5.8)$$

$$Q_{phys} = Q_{fict} \quad \text{on } \Gamma_I. \quad (5.9)$$

Homogeneous Dirichlet and Neumann boundary conditions are imposed on the boundary of the embedding domain [166]

$$\bar{\mathbf{u}} = \mathbf{0} \quad \text{on } \Gamma_{D,u,em}, \quad (5.10)$$

$$\bar{\mathbf{t}} = \mathbf{0} \quad \text{on } \Gamma_{N,u,em}, \quad (5.11)$$

$$\bar{\varphi} = 0 \quad \text{on } \Gamma_{D,\varphi,em}, \quad (5.12)$$

$$\bar{Q} = 0 \quad \text{on } \Gamma_{N,\varphi,em}, \quad (5.13)$$

where $\Gamma_{D,u,em}$, $\Gamma_{N,u,em}$, $\Gamma_{D,\varphi,em}$ and $\Gamma_{N,\varphi,em}$ are the Dirichlet and Neumann boundaries for mechanical and electrical variables, respectively

$$\Gamma_{N,u,em} \cup \Gamma_{D,u,em} \cup \Gamma_{N,\varphi,em} \cup \Gamma_{D,\varphi,em} = \Gamma_{em}, \quad (5.14)$$

$$\Gamma_{N,u,em} \cap \Gamma_{D,u,em} \cap \Gamma_{N,\varphi,em} \cap \Gamma_{D,\varphi,em} = \emptyset. \quad (5.15)$$

In the next step, we extend the variational formulation given in Eqs. (5.1) and (5.2) to the embedding domain Ω_{em}

$$\begin{aligned} \delta\chi_u^{em} = & - \int_{\Omega_{em}} (\mathbf{L}_u \delta \mathbf{u})^T \mathbf{C}_{em} (\mathbf{L}_u \mathbf{u}) d\Omega - \int_{\Omega_{em}} \delta \mathbf{u}^T \rho_{em} \ddot{\mathbf{u}} d\Omega - \int_{\Omega_{em}} (\mathbf{L}_u \delta \mathbf{u})^T \mathbf{e}_{em}^T (\mathbf{L}_\varphi \varphi) d\Omega \\ & + \left[\int_{\Omega_{em}} \delta \mathbf{u}^T \alpha \mathbf{f}_b d\Omega + \int_{\Gamma_{N,u}} \delta \mathbf{u}^T \bar{\mathbf{t}} d\Gamma + \int_{\Gamma_{N,u,em}} \delta \mathbf{u}^T \bar{\mathbf{t}} d\Gamma \right], \end{aligned} \quad (5.16)$$

$$\begin{aligned} \delta\chi_\varphi^{em} = & - \int_{\Omega_{em}} (\mathbf{L}_\varphi \delta \varphi)^T \mathbf{e}_{em} (\mathbf{L}_u \mathbf{u}) d\Omega + \int_{\Omega_{em}} (\mathbf{L}_\varphi \delta \varphi)^T \boldsymbol{\kappa}_{em} (\mathbf{L}_\varphi \varphi) d\Omega \\ & - \left[\int_{\Omega_{em}} \delta \varphi^T \alpha q_b d\Omega + \int_{\Gamma_{N,\varphi}} \delta \varphi^T \bar{Q} d\Gamma + \int_{\Gamma_{N,\varphi,em}} \delta \varphi^T \bar{Q} d\Gamma \right], \end{aligned} \quad (5.17)$$

in which \mathbf{C}_{em} , ρ_{em} , \mathbf{e}_{em} , $\boldsymbol{\kappa}_{em}$ denote the material properties of the embedding domain. They are defined as

$$\mathbf{C}_{em} = \alpha \mathbf{C}, \quad (5.18)$$

$$\rho_{em} = \alpha \rho, \quad (5.19)$$

$$\mathbf{e}_{em} = \alpha \mathbf{e}, \quad (5.20)$$

$$\boldsymbol{\kappa}_{em} = \alpha \boldsymbol{\kappa}. \quad (5.21)$$

The indicator function α only depends on the location of the point of interest and is given by

$$\alpha(\mathbf{x}) = \begin{cases} 1.0 & \forall \mathbf{x} \in \Omega \\ \alpha_0 & \forall \mathbf{x} \in \Omega_{em} \setminus \Omega. \end{cases} \quad (5.22)$$

Depending on the value α_0 of the indicator function, either inclusions ($\alpha_0 \neq 0$) or voids ($\alpha_0 \approx 0$) can be modeled [129, 164, 167]. It is also used to switch between different material data for single cells or integration sub-cells.

The linear functional in the square brackets in Eq. (5.16) considers the volume loads \mathbf{f}_b , the prescribed tractions/surface loads $\bar{\mathbf{t}}$ along $\Gamma_{N,u}$ - interior to Ω_{em} - and the prescribed tractions/surface loads at the boundary of the embedding domain $\Gamma_{N,u,em}$. The equivalent term in Eq. (5.17) describes the virtual work done by a volume charge q_b and the virtual work done by surface charges \bar{Q} prescribed along $\Gamma_{N,\varphi}$ and at the boundary of the embedding domain $\Gamma_{N,\varphi,em}$. Due to the fact that the application of Neumann boundary conditions on the boundary of the embedding domain is meaningless, the last term in both brackets is identical 0. If we insert Eqs. (5.18)-(5.22) into Eqs. (5.16), and (5.17), the principle of virtual work can be expressed as

$$\begin{aligned} \delta\chi_u^{em} = & - \int_{\Omega} (\mathbf{L}_u \delta \mathbf{u})^T \mathbf{C} (\mathbf{L}_u \mathbf{u}) d\Omega - \int_{\Omega_{em} \setminus \Omega} (\mathbf{L}_u \delta \mathbf{u})^T \alpha_0 \mathbf{C} (\mathbf{L}_u \mathbf{u}) d\Omega \\ & - \int_{\Omega} \delta \mathbf{u}^T \rho \ddot{\mathbf{u}} d\Omega - \int_{\Omega_{em} \setminus \Omega} \delta \mathbf{u}^T \alpha_0 \rho \ddot{\mathbf{u}} d\Omega \\ & - \int_{\Omega} (\mathbf{L}_u \delta \mathbf{u})^T \mathbf{e}^T (\mathbf{L}_\varphi \varphi) d\Omega - \int_{\Omega_{em} \setminus \Omega} (\mathbf{L}_u \delta \mathbf{u})^T \alpha_0 \mathbf{e}^T (\mathbf{L}_\varphi \varphi) d\Omega \\ & + \left[\int_{\Omega} \delta \mathbf{u}^T \mathbf{f}_b d\Omega + \int_{\Omega_{em} \setminus \Omega} \delta \mathbf{u}^T \alpha_0 \mathbf{f}_b d\Omega + \int_{\Gamma_{N,u}} \delta \mathbf{u}^T \bar{\mathbf{t}} d\Gamma \right], \end{aligned} \quad (5.23)$$

$$\begin{aligned} \delta\chi_\varphi^{em} = & - \int_{\Omega} (\mathbf{L}_\varphi \delta \varphi)^T \mathbf{e} (\mathbf{L}_u \mathbf{u}) d\Omega - \int_{\Omega_{em} \setminus \Omega} (\mathbf{L}_\varphi \delta \varphi)^T \alpha_0 \mathbf{e} (\mathbf{L}_u \mathbf{u}) d\Omega \\ & + \int_{\Omega} (\mathbf{L}_\varphi \delta \varphi)^T \boldsymbol{\kappa} (\mathbf{L}_\varphi \varphi) d\Omega + \int_{\Omega_{em} \setminus \Omega} (\mathbf{L}_\varphi \delta \varphi)^T \alpha_0 \boldsymbol{\kappa} (\mathbf{L}_\varphi \varphi) d\Omega \\ & - \left[\int_{\Omega} \delta \varphi^T q_b d\Omega + \int_{\Omega_{em} \setminus \Omega} \delta \varphi^T \alpha_0 q_b d\Omega + \int_{\Gamma_{N,\varphi}} \delta \varphi^T \bar{Q} d\Gamma \right]. \end{aligned} \quad (5.24)$$

If only one material is considered ($\alpha_0 = 1.0$; no voids or inclusions), the conventional FE equations are derived and both formulations are identical

$$\delta\chi_u^{em} = \delta\chi_u, \quad (5.25)$$

$$\delta\chi_\varphi^{em} = \delta\chi_\varphi. \quad (5.26)$$

We have to bear in mind that the union of all n_c cells which are not completely located outside the physical domain form the embedding domain (Fig. 5.4b)

$$\Omega_{em} = \bigcup_{c=1}^{n_c} \Omega_c, \quad (5.27)$$

where Ω_c is the domain represented by a single cell with the boundary Γ_c . Therefore, the weak form at the discretized level turns into

$$\begin{aligned} \delta\chi_u^{em} = & \sum_{c=1}^{n_c} \left(\int_{\Omega_c} (\mathbf{L}_u \delta \mathbf{u})^T \mathbf{C}_{em} (\mathbf{L}_u \mathbf{u}) d\Omega + \int_{\Omega_c} \delta \mathbf{u}^T \rho_{em} \ddot{\mathbf{u}} d\Omega \right. \\ & \left. + \int_{\Omega_c} (\mathbf{L}_u \delta \mathbf{u})^T \mathbf{e}_{em}^T (\mathbf{L}_\varphi \varphi) d\Omega - \left[\int_{\Omega_c} \delta \mathbf{u}^T \alpha \mathbf{f}_b d\Omega + \int_{\Gamma_{N,u,c}} \delta \mathbf{u}^T \bar{\mathbf{t}} d\Gamma \right] \right) = 0, \end{aligned} \quad (5.28)$$

$$\begin{aligned} \delta\chi_\varphi^{em} = & \sum_{c=1}^{n_c} \left(\int_{\Omega_c} (\mathbf{L}_\varphi \delta \varphi)^T \mathbf{e}_{em} (\mathbf{L}_u \mathbf{u}) d\Omega - \int_{\Omega_c} (\mathbf{L}_\varphi \delta \varphi)^T \boldsymbol{\kappa}_{em} (\mathbf{L}_\varphi \varphi) d\Omega \right. \\ & \left. + \left[\int_{\Omega_c} \delta \varphi^T \alpha q_b d\Omega + \int_{\Gamma_{N,\varphi,c}} \delta \varphi^T \bar{Q} d\Gamma \right] \right) = 0. \end{aligned} \quad (5.29)$$

Now the same basis functions (Chapter 6) as in the *HO*-FEMs are employed to describe the independent field variable within each of the n_c cells. Again, the independent field variables can be expressed by means of shape functions (\mathbf{N}_u , \mathbf{N}_φ) and nodal degrees-of-freedom connected to a cell (\mathbf{u}_c , φ_c). It is principally possible to use different shape functions for both the displacement field and the electric potential. The independent variables on the cell level are therefore given as

$$\mathbf{u} = \mathbf{N}_u \mathbf{u}_c, \quad (5.30)$$

$$\varphi = \mathbf{N}_\varphi \varphi_c. \quad (5.31)$$

In the present thesis, however, the components of both shape function matrices corresponding to the same node/mode are identical. Due to the fact that the governing variational formulation contains only derivatives of first order, C_0 -continuous shape functions are sufficient. Only in Chapter 6, we introduce and discuss different types of shape functions. Substituting Eqs. (5.30) and (5.31) into the principle of virtual work - Eqs. (5.28) and (5.29) - yields

$$\begin{aligned} \delta\chi_u^{em} = & \mathbf{A} \sum_{c=1}^{n_c} \delta \mathbf{u}^T \left(\int_{\Omega_c} \mathbf{B}_u^T \mathbf{C}_{em} \mathbf{B}_u d\Omega \mathbf{u} + \int_{\Omega_c} \rho_{em} \mathbf{N}_u^T \mathbf{N}_u d\Omega \ddot{\mathbf{u}} + \int_{\Omega_c} \mathbf{B}_u^T \mathbf{e}_{em}^T \mathbf{B}_\varphi d\Omega \right. \\ & \left. - \left[\int_{\Omega_c} \alpha \mathbf{N}_u^T \mathbf{f}_b d\Omega + \int_{\Gamma_{N,u,c}} \mathbf{N}_u^T \bar{\mathbf{t}} d\Gamma \right] \right) = 0, \end{aligned} \quad (5.32)$$

$$\begin{aligned} \delta\chi_\varphi^{em} = & \mathbf{A} \sum_{c=1}^{n_c} \delta \varphi^T \left(\int_{\Omega_c} \mathbf{B}_\varphi^T \mathbf{e}_{em} \mathbf{B}_u d\Omega - \int_{\Omega_c} \mathbf{B}_\varphi^T \boldsymbol{\kappa}_{em} \mathbf{B}_\varphi d\Omega \right. \\ & \left. + \left[\int_{\Omega_c} \alpha \mathbf{N}_\varphi^T q_b d\Omega + \int_{\Gamma_{N,\varphi,c}} \mathbf{N}_\varphi^T \bar{Q} d\Gamma \right] \right) = 0. \end{aligned} \quad (5.33)$$

Since the Eqs. (5.32) and (5.33) are valid for arbitrary virtual displacements and virtual electric potentials, the terms contained in the round brackets must vanish. Consequently, the FC formulation for the global system of equations is given in matrix notation in the following form

$$\begin{bmatrix} \mathbf{M}_{uu}^{FCM} & \mathbf{0} \\ \mathbf{0} & \mathbf{0} \end{bmatrix} \begin{Bmatrix} \ddot{\mathbf{U}} \\ \ddot{\Phi} \end{Bmatrix} + \begin{bmatrix} \mathbf{K}_{uu}^{FCM} & \mathbf{K}_{u\varphi}^{FCM} \\ \mathbf{K}_{\varphi u}^{FCM} & -\mathbf{K}_{\varphi\varphi}^{FCM} \end{bmatrix} \begin{Bmatrix} \mathbf{U} \\ \Phi \end{Bmatrix} = \begin{Bmatrix} \mathbf{f}_{uu}^{FCM} \\ \mathbf{f}_{\varphi\varphi}^{FCM} \end{Bmatrix}, \quad (5.34)$$

where

$$\mathbf{K}_{uu}^{FCM} = \mathbf{A} \mathbf{K}_{uu}^{(c)}, \quad (5.35)$$

$$\mathbf{K}_{\varphi\varphi}^{FCM} = \mathbf{A} \mathbf{K}_{\varphi\varphi}^{(c)}, \quad (5.36)$$

$$\mathbf{K}_{u\varphi}^{FCM} = \mathbf{A} \mathbf{K}_{u\varphi}^{(c)}, \quad (5.37)$$

$$\mathbf{M}_{uu}^{FCM} = \mathbf{A} \mathbf{M}_{uu}^{(c)}, \quad (5.38)$$

$$\mathbf{f}_{uu}^{FCM} = \mathbf{A} \mathbf{f}_{uu}^{(c)}, \quad (5.39)$$

$$\mathbf{f}_{\varphi\varphi}^{FCM} = \mathbf{A} \mathbf{f}_{\varphi\varphi}^{(c)}, \quad (5.40)$$

$$\mathbf{U} = \mathbf{A} \mathbf{u}_c, \quad (5.41)$$

$$\Phi = \mathbf{A} \varphi_c. \quad (5.42)$$

Analogously to the FEM using higher order shape functions (Chapter 4) the following notation is introduced:

$$\text{Cell mass matrix:} \quad \mathbf{M}_{uu}^{(c)} = \int_{\Omega_c} \rho_{em} \mathbf{N}_u^T \mathbf{N}_u d\Omega, \quad (5.43)$$

$$\text{Mechanical cell stiffness matrix:} \quad \mathbf{K}_{uu}^{(c)} = \int_{\Omega_c} \mathbf{B}_u^T \mathbf{C}_{em} \mathbf{B}_u d\Omega, \quad (5.44)$$

$$\text{Direct piezoelectric cell coupling matrix:} \quad \mathbf{K}_{u\varphi}^{(c)} = \int_{\Omega_c} \mathbf{B}_u^T \mathbf{e}_{em}^T \mathbf{B}_\varphi d\Omega, \quad (5.45)$$

$$\text{Inverse piezoelectric cell coupling matrix:} \quad \mathbf{K}_{\varphi u}^{(c)} = \int_{\Omega_c} \mathbf{B}_\varphi^T \mathbf{e}_{em} \mathbf{B}_u d\Omega = \mathbf{K}_{u\varphi}^{(c)T}, \quad (5.46)$$

$$\text{Dielectric cell stiffness matrix:} \quad \mathbf{K}_{\varphi\varphi}^{(c)} = \int_{\Omega_c} \mathbf{B}_\varphi^T \boldsymbol{\kappa}_{em} \mathbf{B}_\varphi d\Omega, \quad (5.47)$$

$$\text{External mechanical cell force vector:} \quad \mathbf{f}_{uu}^{(c)} = \int_{\Omega_c} \alpha \mathbf{N}_u^T \mathbf{f}_b d\Omega + \int_{\Gamma_{c,N,u}} \mathbf{N}_u^T \bar{\mathbf{t}} d\Gamma, \quad (5.48)$$

Electric cell charge vector:

$$\mathbf{f}_{\varphi\varphi}^{(c)} = - \int_{\Omega_c} \alpha \mathbf{N}_{\varphi}^T q_b d\Omega - \int_{\Gamma_{c,N,\varphi}} \mathbf{N}_{\varphi}^T \bar{Q} d\Gamma. \quad (5.49)$$

The accuracy of the geometry approximation and the methodology to capture the boundaries of the physical domain are discussed in the following section.

5.2 Representation of the geometry - Adaptive integration

The basic concept of fictitious domain methods is to shift the discretization effort (manual input by the user) to an adaptive integration scheme to resolve the physical boundaries of the model. Such a quadrature scheme has been proposed in references [166, 263], for example. Fig. 5.5 depicts a schematic illustration of the integration technique employed. The Gaussian quadrature exhibits a fast convergence provided that integrand is smooth. However, in the fictitious domain concept this assumption is violated by introducing the indicator function α within the FCs. The FCM consequently uses a composed Gaussian quadrature to improve the integration accuracy in cells cut by geometric boundaries. For integration purposes, the original cells are divided into a set of sub-cells by means of a quadtree/octree space partitioning scheme [162, 263].

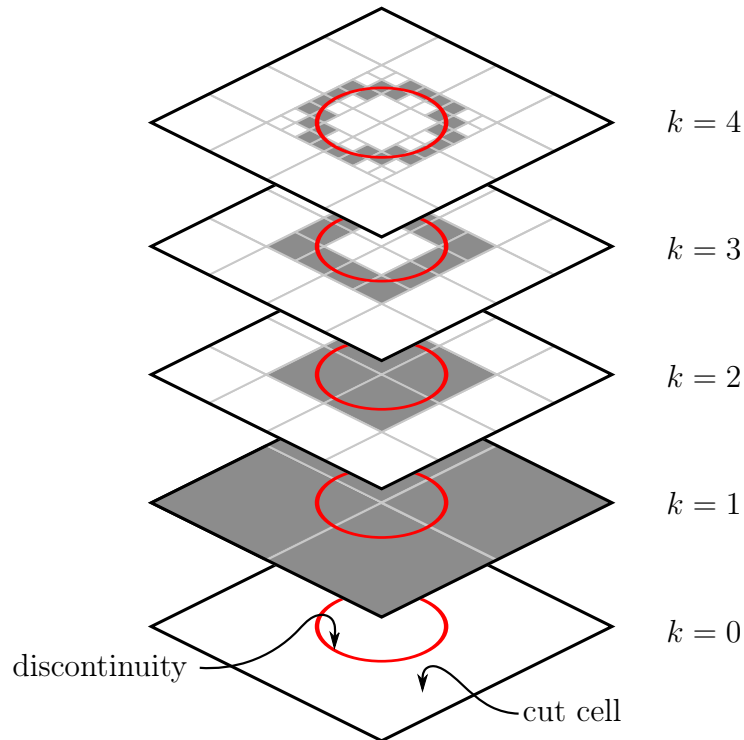


Figure 5.5: Sub-cells for the adaptive integration scheme. The original FC is refined if it is cut by the boundary of the actual structure. Several refinement levels are required until the boundary is appropriately resolved. This is checked by computing the area of the domain we are interested in. If a certain relative error is reached, the refinement is stopped.

Several refinement levels are required in order to ensure sufficiently accurate results. Starting from the original FC of level $k = 0$, each sub-cell of level $k = i$ is first checked whether it is cut by a geometric boundary. If true, the relevant cell is replaced by 2^d equally spaced cells of level $k = i + 1$, whereas d denotes the dimensionality of the problem. Each of the sub-cells is equipped with $(p + 1)^d$ Gauß points to ensure an accurate computation of the integrand. In Fig. 5.6 the FCs are plotted in blue (thick lines), whereas the sub-cells used for integration purposes only are drawn in light grey lines (thin lines). By employing this technique we shift the effort of meshing complex structures to the numerical integration of the system matrices and load vectors. In order to avoid ill-conditioning problems of the resulting equation system, the indicator function is set to small (positive) values $\alpha \approx 10^{-15} \dots 10^{-4}$ for integration points inside the fictitious domain [257]. According to Ruess *et al.* [254] α_0 - Eq. 5.22 - can be chosen reliably according to the problem's elasticity parameters as

$$\alpha_0 = \left(\tilde{\lambda} + \tilde{\mu} \right) \cdot \epsilon^* = \frac{E}{2(1 + \nu)(1 - 2\nu)} \cdot \epsilon. \quad (5.50)$$

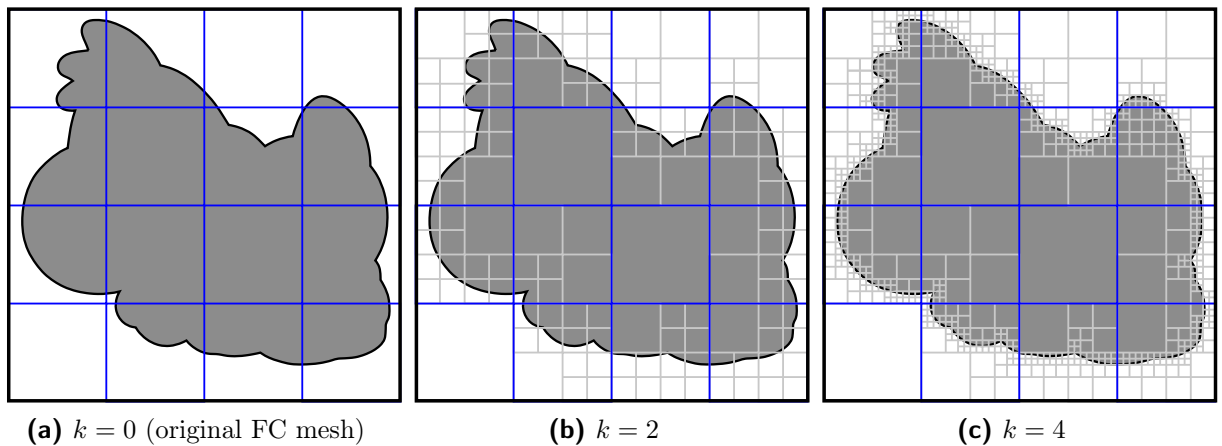


Figure 5.6: Complex geometry divided by a quadtree decomposition.

The integration concept influences both the accuracy of the fictitious domain method and the computational time that is required to build the system matrices. It is therefore important to devise efficient strategies for the numerical integration. In the following subsections, we will accordingly discuss and assess different quadrature approaches.

5.2.1 Gauß quadrature

The integration of the system matrices is a time consuming part of each *HO-FE* and *FC* software. However, the integration has to be performed numerically because it is not always possible to find an analytic solution. Usually, the standard Gaussian quadrature [229] is therefore applied, as discussed in the following.

The basic idea of a Gauß-type quadrature is the summation of weighted function values on non-equidistantly distributed integration points. Without loss of generality, the n -point

* ϵ : IEEE 754 standard unit roundoff/macheps ($\epsilon = 2^{-53} \approx 1.11 \cdot 10^{-16}$)

quadrature rule is enforced on a reference domain $[-1, 1]$. For one-dimensional integrands the formula reads

$$I = \int_{\xi=-1}^1 f(\xi) d\xi = \sum_{i=1}^n w_i^{(n)} f(\xi_i^{(n)}) \quad (5.51)$$

where $\xi_i^{(n)}$ are the integration points (associated with a n -point quadrature rule), at which the integrand has to be evaluated and $w_i^{(n)}$ denote the corresponding weights. Since the formula contains $2n$ unknown parameters, this quadrature rule can be conceived, in such a way that all polynomials up to order $2n - 1$ are exactly integrated. Furthermore, it can be proven that the integration points for a standard n -point Gaussian quadrature rule coincide with the roots of the Legendre polynomials $le_n(\xi)$ of degree n (Eq. (6.21)) [264]. Hence, the complexity of the problem is reduced (integration points are known a priori) and the weights can be determined by

$$w_i^{(n)} = \frac{2}{(1 - \xi_i^{(n)2}) \left(\frac{dle_n(\xi)}{d\xi} \right)^2}. \quad (5.52)$$

Nonetheless, we always have to be aware of the fact that - due to the mapping from the physical domain into the reference domain - the integrand, arising in the computation of the element matrices, will not be a rational polynomial function any more. Hence, the matrices for distorted elements are not evaluated exactly but only approximated. Concerning the FCM the evaluation of the integrals is always exact for cells that are not intersected by the physical boundary.

We can extend the one-dimensional formula to three dimensions without any problems. The implementation is based on the Cartesian product of three one-dimensional quadrature rules for the distinct local variables ξ , η , and ζ , respectively [117]. Thus, we use the following formula in order to solve an integral over a three-dimensional domain Ω

$$I = \int_{-1}^1 \int_{-1}^1 \int_{-1}^1 f(\xi, \eta, \zeta) d\xi d\eta d\zeta = \sum_{i=1}^{n_1} \sum_{j=1}^{n_2} \sum_{k=1}^{n_3} w_i^{(n_1)} w_j^{(n_2)} w_k^{(n_3)} f(\xi_i^{(n_1)}, \eta_j^{(n_2)}, \zeta_k^{(n_3)}). \quad (5.53)$$

The product formula has the advantage that it provides for different orders of approximation for each partial integration with respect to the local coordinates ξ , η and ζ . Thus, an anisotropic refinement can be straightforwardly facilitated by the Gaussian quadrature rule.

The transformation from an arbitrary domain to the reference domain is done utilizing the Jacobian matrix \mathbf{J} which describes the relation between the derivatives with respect to local and global coordinates

$$\frac{\partial}{\partial \boldsymbol{\xi}} = \begin{Bmatrix} \frac{\partial}{\partial \xi} \\ \frac{\partial}{\partial \eta} \\ \frac{\partial}{\partial \zeta} \end{Bmatrix} = \begin{bmatrix} \frac{\partial x_1}{\partial \xi} & \frac{\partial x_2}{\partial \xi} & \frac{\partial x_3}{\partial \xi} \\ \frac{\partial x_1}{\partial \eta} & \frac{\partial x_2}{\partial \eta} & \frac{\partial x_3}{\partial \eta} \\ \frac{\partial x_1}{\partial \zeta} & \frac{\partial x_2}{\partial \zeta} & \frac{\partial x_3}{\partial \zeta} \end{bmatrix} \begin{Bmatrix} \frac{\partial}{\partial x_1} \\ \frac{\partial}{\partial x_2} \\ \frac{\partial}{\partial x_3} \end{Bmatrix} = \mathbf{J} \frac{\partial}{\partial \mathbf{x}}. \quad (5.54)$$

Taking the mapping - Eqs. (4.88) or (4.92) - into account, we can compute the integral over the domain Ω in global coordinates, using the following formula

$$\begin{aligned} I &= \int_{x_{1s}}^{x_{1e}} \int_{x_{2s}}^{x_{2e}} \int_{x_{3s}}^{x_{3e}} f(x_1, x_2, x_3) dx_1 dx_2 dx_3 = \int_{-1}^1 \int_{-1}^1 \int_{-1}^1 f(\xi, \eta, \zeta) \det(\mathbf{J}) d\xi d\eta d\zeta \\ &\approx \sum_{i=1}^{n_1} \sum_{j=1}^{n_2} \sum_{k=1}^{n_3} w_i^{(n_1)} w_j^{(n_2)} w_k^{(n_3)} \det(\mathbf{J})|_{(\xi_i^{(n_1)}, \eta_j^{(n_2)}, \zeta_k^{(n_3)})} f(\xi_i^{(n_1)}, \eta_j^{(n_2)}, \zeta_k^{(n_3)}). \end{aligned} \quad (5.55)$$

The number of integration points should be chosen depending on the curvature of the element faces and the smoothness of the integrand. In case of the FCM, we have to be aware that the numerical quadrature for cut cells poses certain difficulties as discussed in the following subsection. In commercial software tools, the number of integration points is varied for each local variable and $p_i + 1$ integration points for each partial integration are recommended ($n_1 = p_\xi + 1$, $n_2 = p_\eta + 1$, $n_3 = p_\zeta + 1$). For cases with a high demand on precision, however, Düster recommends to use $p_i + 3$ integration points to integrate with respect to each local variable [116] ($n_1 = p_\xi + 3$, $n_2 = p_\eta + 3$, $n_3 = p_\zeta + 3$).

5.2.2 Adaptive quadrature scheme

In the FCM, the integration over the physical domain Ω has been replaced by an integration over the embedding domain Ω_{em} , cf. Figs. 5.3 and 5.4. Adhering to the FCM procedure, the numerical integration method, to obtain the system matrices and vectors, has to deal with discontinuous integrands when FCs are intersected by the physical boundary Γ (cut cells). The most commonly used quadrature formula within FEM software is the Gauß quadrature presented in Section 5.2.1. This method was devised for polynomial functions and works well for smooth integrands where it shows a high convergence rate. Yet, if non-smooth integrands are considered, its numerical performance deteriorates significantly. This fact poses one of the main problems when applied to the FCM. A remedy is to utilize an adapted integration scheme that is able to capture the discontinuity of the integrand. Düster *et al.* [166] therefore proposed a composed integration scheme for cells intersected by the physical boundary.

Within the scope of the FCM, a linear approximation of the geometry is sufficient because all cells are brick-shaped. Thus, the mapping from the reference cell to the global coordinate system is defined as

$$\mathbf{x} = \mathbf{Q}^{(c)}(\xi, \eta, \zeta) = \sum_{i=1}^8 \mathbf{N}_{(1,1,1)}^{N_i}(\xi, \eta, \zeta) \mathbf{X}_i, \quad \mathbf{N}_{(1,1,1)}^{N_i} = \begin{bmatrix} N_{(1,1,1)}^{N_i} & 0 & 0 \\ 0 & N_{(1,1,1)}^{N_i} & 0 \\ 0 & 0 & N_{(1,1,1)}^{N_i} \end{bmatrix}, \quad (5.56)$$

where $\mathbf{X}_i = (X_{1i}, X_{2i}, X_{3i})^T$ denotes the global coordinates of the eight nodal points and $N_{(1,1,1)}^{N_i}$ are the well-known trilinear shape functions

$$N_{(1,1,1)}^{N_i} = \frac{1}{8}(1 + \xi_i \xi)(1 + \eta_i \eta)(1 + \zeta_i \zeta), \quad i = 1, \dots, 8. \quad (5.57)$$

In this case (ξ_i, η_i, ζ_i) are the local coordinates of the i -th node. As mentioned before, the discretization is carried out employing rectangular hexahedral cells (mostly even cubes), so that the mapping reduces to

$$\mathbf{x}(\xi, \eta, \zeta) = \begin{bmatrix} X_{1_1} + \frac{1}{2}(1 + \xi)h_{x_1} \\ X_{2_1} + \frac{1}{2}(1 + \eta)h_{x_2} \\ X_{3_1} + \frac{1}{2}(1 + \zeta)h_{x_3} \end{bmatrix} \quad (5.58)$$

resulting in a constant and diagonal Jacobian matrix

$$\mathbf{J}^{(c)} = \frac{1}{2} \begin{bmatrix} h_{x_1} & 0 & 0 \\ 0 & h_{x_2} & 0 \\ 0 & 0 & h_{x_3} \end{bmatrix}. \quad (5.59)$$

In Eqs. (5.58) and (5.59), h_{x_1} , h_{x_2} and h_{x_3} represent the cell sizes with respect to the global coordinate system in the direction of the x_1 -, x_2 - and x_3 -axis, respectively. $(X_{1_1}, X_{2_1}, X_{3_1})$ are the global coordinates of the anchor point (first point) of the FC. A constant Jacobian matrix offers the advantage that the shape functions defined on the reference domain remain polynomials even after being mapped onto the global coordinate system. That is to say, if the material properties are constant and the cells are not intersected by the boundary, we obtain a smooth integrand and the system matrices can be integrated exactly by employing quadrature formulae. If the FC is completely inside the physical domain, the stiffness matrix of a FC, $\mathbf{K}_{uu}^{(c)}$, can be calculated using the standard formula

$$\mathbf{K}_{uu}^{(c)} = \int_{\zeta=-1}^1 \int_{\eta=-1}^1 \int_{\xi=-1}^1 \mathbf{B}_u^T \mathbf{C} \mathbf{B}_u \det(\mathbf{J}^{(c)}) d\xi d\eta d\zeta. \quad (5.60)$$

In this case - as the FC is not divided into sub-cells - the procedure is identical to the computation of a *HO*-FE.

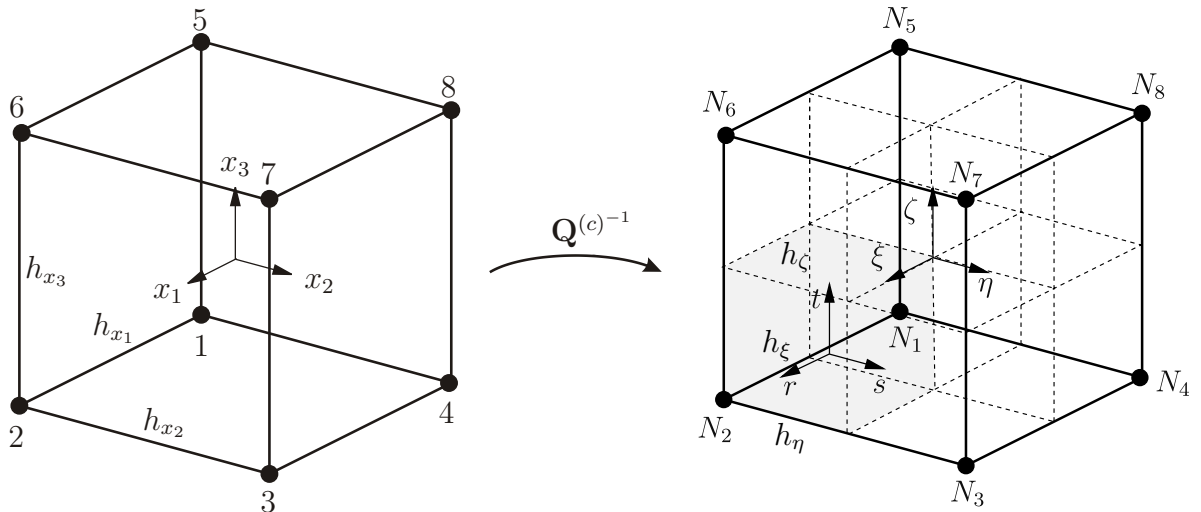


Figure 5.7: Composed integration of hexahedral cells based on sub-cells. The hexahedral reference domain is hierarchically divided into a set of sub-domains. By applying this procedure, the accuracy of the Gauß quadrature over domains containing non-smooth functions can be increased step-by-step.

Hence, the stiffness matrix for a single FC that is completely inside the physical domain can be stored in pre-computed arrays in terms of the unknown cell size and elastic coefficients of the applied constitutive law. This approach results in significant savings in computational time [265–267].

On the other hand, we have to take a different approach for the numerical integration of the stiffness matrix if the considered FCs are divided by the geometrical boundary. A standard Gaussian quadrature will not suffice in that case. A composed integration scheme is consequently proposed by Parvizian *et al.* [162], where the FC to be integrated is divided into n_{sc} sub-cells, cf. Fig. 5.7. Note that these cells are only introduced for integration purposes. The shape functions and accordingly the degrees-of-freedom are not changed by the sub-division of the initial FC.

The coordinate transform between the local coordinate system of the original FC $\boldsymbol{\xi} = (\xi, \eta, \zeta)^T$ and that of the cube-shaped sub-cells $\mathbf{r} = (r, s, t)^T$ is again a linear mapping function ($\mathbf{Q}^{(sc)}$)

$$\boldsymbol{\xi}(r, s, t) = \mathbf{Q}^{(sc)}(r, s, t) \begin{bmatrix} \xi_1 + \frac{1}{2}(1+r)h_\xi \\ \eta_1 + \frac{1}{2}(1+s)h_\eta \\ \zeta_1 + \frac{1}{2}(1+t)h_\zeta \end{bmatrix}, \quad r, s, t \in [-1, 1], \quad (5.61)$$

where (ξ_1, η_1, ζ_1) are the local coordinates of the anchor point (first point) of the sub-cell. h_ξ , h_η and h_ζ denote the size of the sub-cell. Since a hierarchical division of the initial cell is promoted, the sub-cell size is given by

$$h_\xi = h_\eta = h_\zeta = \frac{2}{2^k}, \quad (5.62)$$

where k denotes the sub-division level of the initial FC, cf. Fig. 5.4a. Due to the shape of the sub-cells we obtain a constant Jacobian matrix for the mapping

$$\mathbf{J}^{(sc)} = \frac{1}{2} \begin{bmatrix} h_\xi & 0 & 0 \\ 0 & h_\eta & 0 \\ 0 & 0 & h_\zeta \end{bmatrix}. \quad (5.63)$$

The stiffness matrix of the initial FC can now be determined by carrying out the described integration procedure. The composed numerical integration over the n_{sc} sub-cells results in the following expression

$$\mathbf{K}_{uu}^{(c)} = \sum_{i=1}^{n_{sc}} \left(\int_{t=-1}^1 \int_{s=-1}^1 \int_{r=-1}^1 \alpha(\mathbf{x}(\boldsymbol{\xi}(\mathbf{r}))) [\mathbf{B}_u(\boldsymbol{\xi}(\mathbf{r}))^T \mathbf{C} \mathbf{B}_u(\boldsymbol{\xi}(\mathbf{r})) \det(\mathbf{J}^{(c)}) \det(\mathbf{J}^{(sc)})] dr ds dt \right). \quad (5.64)$$

From Eq. (5.64) we can infer, that it is necessary to account for two mappings (coordinate transforms). $\mathbf{J}^{(c)}$ accounts for the transformation of the global coordinates $\mathbf{x} = (x_1, x_2, x_3)^T$ to the reference frame $\boldsymbol{\xi} = (\xi, \eta, \zeta)^T$, while $\mathbf{J}^{(sc)}$ facilitates the change of variables to the sub-cell coordinate system $\mathbf{r} = (r, s, t)^T$. It is therefore easily possible to create an equidistant grid of sub-cells or to deploy an adaptive algorithm based on a quadtree/octree data

structure, cf. Fig. 5.5. Naturally, the latter approach is computationally more efficient and thus recommended. The adaptive algorithm is used to automatically control the refinement level. Consequently, an accurate numerical integration of the whole domain is guaranteed. In principle, it is also possible to use a different quadrature scheme for every sub-cell. In analogy to FE terminology it is spoken of h - and p -refinement. In this case, p -refinement refers to elevating the number of Gauß points, while h -refinement describes the process of increasing the number of sub-cells [168]. In the present thesis, we choose to numerically integrate each sub-cell employing a standard Gaussian quadrature rule. For the sake of simplicity, a $n_1 \times n_2 \times n_3$ -points Gaussian quadrature is applied in the provided numerical examples. n_1 , n_2 and n_3 denote the number of integration points for each local variable ($n_1 = p_\xi + 1$, $n_2 = p_\eta + 1$ and $n_3 = p_\zeta + 1$).

5.2.3 Improved adaptive integration concepts

Two modifications of the standard adaptive integration approach, as discussed in the previous subsection, are proposed by Ruess *et al.* [254] and Abedian *et al.* [168]. Generally speaking, the approach introduced in reference [168] is a straight-forward extension of the method proposed in [254]. Both approaches serve to reduce the numerical effort significantly. The basic idea is illustrated in Fig. 5.8. In the standard approach, cf. Fig. 5.8a, each sub-cell is integrated with $(p+1)^d$ Gauß points. Du to the space tree partitioning the quadrature points are concentrated at the geometrical boundary of the structure, ensuring an accurate integration. Instead of executing this sub-cell integration in both domains, that is in the fictitious and physical domain - as in the standard approach -, a modification is proposed in reference [254].

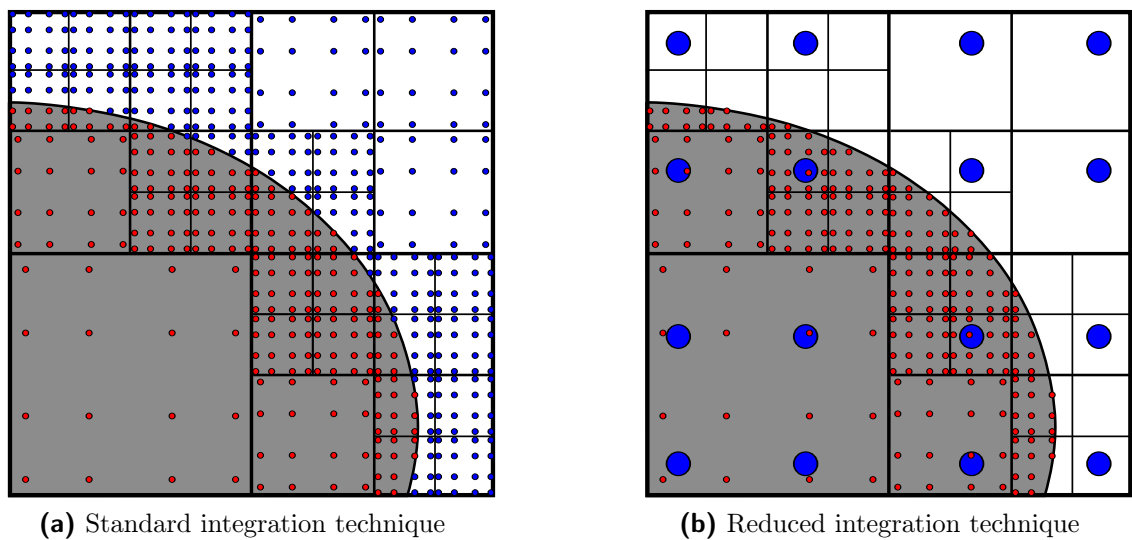


Figure 5.8: Basic idea of the improved integration concept according to Ruess *et al.* [254].

The methodology developed by Ruess *et al.* [254] is laid out in the following. In a first step, we compute the stiffness matrix $\mathbf{K}_{uu,\alpha_0}^{(c)}$ for the whole cell, neglecting the physical boundary and applying α_0 as indicator term, cf. Eq. (5.22) (blue/large integration points in Fig. 5.8b). Thereafter, we restrict the composed sub-cell integration to compute $\mathbf{K}_{uu,\Omega}^{(c)}$,

to the physical domain Ω using $(1 - \alpha_0)$ as penalty factor (red/small integration points in Fig. 5.8b). In the last step, we add both matrices

$$\mathbf{K}_{uu}^{(c)} = \mathbf{K}_{uu,\alpha_0}^{(c)} + \mathbf{K}_{uu,\Omega}^{(c)}. \quad (5.65)$$

The improvement can be seen in the fact that the number of integration points within the fictitious domain is notably reduced (compare Figs. 5.8a and 5.8b depicting the number of integration points employed in the standard adaptive algorithm and in the improved method, respectively).

A further improvement of the efficiency of the sub-cell integration technique is proposed by Abedian *et al.* in [168]. Again, two distinct features are addressed in this specific extension, cf. Fig. 5.9. First, it is assumed that an integration with less than $(p + 1)^d$ quadrature points is sufficient because of the decreasing size of the sub-cells. The number of Gauß points is therefore reduced in each direction by k (usually equal to 1) from $p + 1$ to 1 according to the sub-division level. During the execution of the numerical integration we disregard all points within the fictitious domain ($\alpha = 0$), cf. Fig. 5.9a. In contrast to the methodology proposed by Ruess *et al.* [254] we set the value of the indicator function to $\alpha = 1$. The contribution of the extension/fictitious domain is then captured by integrating over the original cell domain ($\alpha = \alpha_0$) and by neglecting all points within the physical domain ($\alpha = 0$), cf. Fig. 5.9b.

Both novel adaptive integration techniques reduce the number of integration significantly. Since the calculation of the system matrices is the most time-consuming part in higher order fictitious domain methods, the computational costs can be decreased notably. From our point of view, however, detailed convergence studies are still needed to verify the performance of these approaches.

Both the standard adaptive integration technique and the methodology proposed by Abedian *et al.* [168] were implemented and tested in the present thesis. However, a thorough analysis of the improved algorithm was not performed.

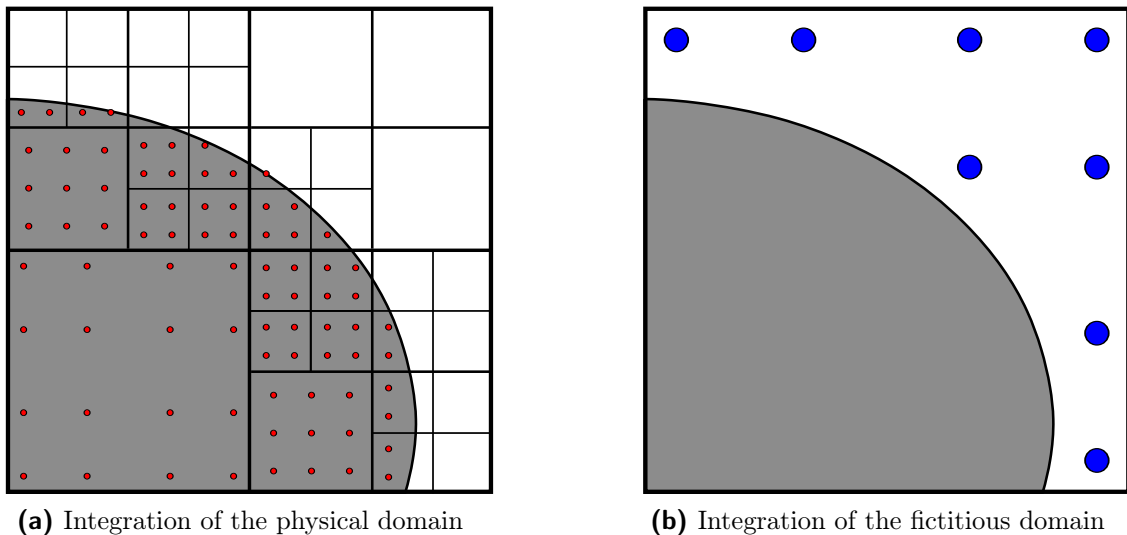


Figure 5.9: Basic idea of the improved integration concept according to Abedian *et al.* [168].

All explanations are also valid for the computation of the mass matrix and the load vector corresponding to volume loads. Other approaches need to be employed to account for non-

homogenous Neumann boundary conditions defined on the boundary of the structure. For a detailed description of the implementation of non-homogenous Neumann and Dirichlet boundary conditions, we refer the inclined reader to articles by Parvizian *et al.*, Düster *et al.*, Ruess *et al.* and Vinci [162, 166, 247, 265, 268].

As mentioned before, the integration of the sub-cells is performed by employing standard Gaussian quadrature rules. In the context of *HO*-FEs, however, two integration techniques were proposed in order to improve the accuracy and decrease the computational time. These methods - namely the vector integration and *hp*-spectral quadrature algorithm - can also be applied to compute the sub-cell matrices, which is why they are briefly mentioned in the following subsection.

5.2.4 Vector integration and *hp*-spectral quadrature algorithm

Since the numerical integration of the element/cell matrices is the most time-consuming procedure when considering the higher order methods [116, 269] it is worth spending the effort to implement new quadrature schemes which promise to entail only a fraction of the computational costs compared to standard Gaussian algorithms. Two suitable methods have been proposed for the *p*-version of the FEM by Hinnant [270] and for the SEM Melenk *et al.* [269, 271]. The merits of both algorithms are briefly mentioned in the following paragraphs. Both approaches can be used for cells that are not cut by the physical boundary.

First established by Hinnant [270], the basic idea of the vector integration is to divide the integrand into two parts and to numerically integrate each part separately. When comparing its efficiency with a standard Gaussian quadrature, it is found that the vector integration needs only a small fraction of the computational effort. According to [270, 272–275] the proposed method is especially suited for quadrilateral and hexahedral *HO*-FEs based on the *p*-version of FEM. Note however, that the term *vector* does not refer to the architecture of the computer on which this technique is implemented. Instead, it is related to the mathematical structure of the integration scheme itself.

Melenk *et al.* [269] proposed the so-called *hp*-spectral quadrature algorithm. Mainly, the idea is based on employing the sum factorization technique and on adapting the shape functions to the quadrature scheme. It is therefore essentially a modified sum factorization technique which promises a computational speed-up in comparison to standard procedures.

Chapter 6

Shape Functions

In the current chapter, we introduce different types of shape functions that can be used to develop *HO*-FEMs and fictitious domain methods. We discuss both nodal-based sets of shape functions, where the physical interpretation of the degrees-of-freedom is admissible, and modal-based sets of shape functions, where the physical interpretation of the degrees-of-freedom is inadmissible. Different numerical schemes can be derived by introducing these sets into the numerical frameworks described in Chapters 4 and 5. Thus, the focus lies on discussing the basic properties of the following four sets of shape functions:

1. Standard shape functions based on Lagrange polynomials defined on an equidistant nodal distribution. This non-hierarchic set of shape functions is known from the h -versions of the FEM and the FCM.
2. Spectral shape functions based on Lagrange polynomials defined on a Gauß-Lobatto-Legendre nodal distribution. This non-hierarchic set of shape functions is known from the SEM and the SCM.
3. Hierarchic shape functions based on the normalized integrals of the Legendre polynomials. This set of shape functions is known from the p -versions of the FEM and the FCM.
4. Hierarchic shape functions based on a Fourier series. This set of shape functions is known from the Fourier- p -versions of the FEM and the FCM.

In the body of literature, these four sets of Ansatz functions are frequently encountered in various areas of application. No objective comparison between the different higher order basis functions has been conducted, yet. In the present chapter, we therefore provide detailed information about each individual set of shape functions and compile the main advantages and drawbacks. Another promising set of basis functions, used to define isogeometric elements (IGEs), is constituted by non-uniform rational B-splines (NURBS) and more recently by T-splines. As this kind of element was already discussed in [125], there is no need to include it in this comparison. Accordingly, we only discuss C_0 -continuous higher order shape functions in the following.

The structure of the current chapter is as follows: Each set of Ansatz functions is introduced in a one-dimensional interval. Here, the basic properties of these functions can be easily highlighted and discussed. The introduction of the different types of shape functions is followed by a comparison and by conclusions regarding their applicability to wave propagation problems.

6.1 One-dimensional shape functions

Numbering conventions

Before we introduce the employed shape functions, a few comments on the numbering conventions are in order. In Fig. 6.1 we illustrate a distinct difference in the notation for non-hierarchical and hierarchic shape functions. In the hierarchic case the numbering is connected to the polynomial degree of the basis functions.

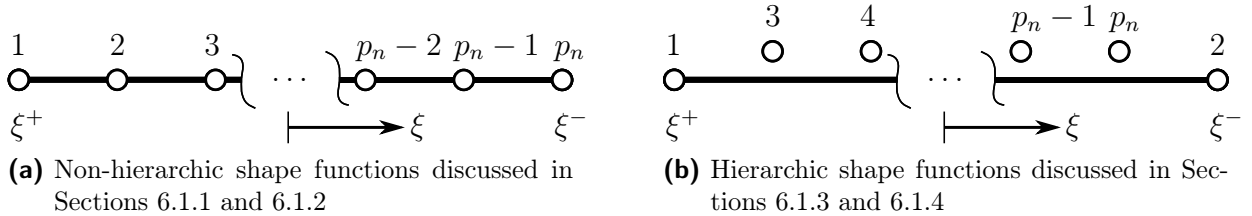


Figure 6.1: Numbering conventions for the degrees-of-freedom for the one-dimensional shape functions ($\xi^+ = +1$, $\xi^- = -1$). p_n denotes the point number ($p_n \leq p_\xi + 1$; p_ξ : polynomial degree).

For the Lagrange-type basis functions, it is customary to number the physical nodes beginning at $\xi = -1$ in a regular fashion, in the positive direction of the local coordinate axis. For hierarchic basis functions, however, we usually start by numbering the two corner nodes, followed by accounting for the internal degrees-of-freedom. Since those degrees-of-freedom do not correspond to physical nodes in the case of hierarchic FEs, they are depicted outside the structure, cf. Fig. 6.1b [215]. In the remainder of the thesis, these degrees-of-freedom will be referred to as modes. The term *modes* is based on the terminology commonly encountered in the literature about the p -version of the FEM.

6.1.1 One-dimensional shape functions: FEM

The standard FE shape functions are given by a set of Lagrange polynomials $l_{a_n}(\xi)$ defined using an equidistant nodal distribution [211, 212, 241]

$$N_n^{\text{FEM},p}(\xi) = l_{a_n}(\xi) = \prod_{k=1, k \neq n}^{p+1} \frac{\xi - \xi_k}{\xi_n - \xi_k}, \quad (6.1)$$

$$\xi_k = -1 + 2 \frac{k-1}{p}, \quad k = 1, 2, \dots, p+1, \quad (6.2)$$

where the points ξ_k are called nodes. In the conventional FEM the nodes retain a physical meaning and all degrees-of-freedom are connected to them. At the individual nodes, the shape functions fulfill the following relation

$$N_n^{\text{FEM},p}(\xi_k) = \delta_{nk}, \quad (6.3)$$

which is why the function value of a shape function at the position of the corresponding node is equal to 1, whereas it is equal to zero at all other nodes. Note however, that for each polynomial degree p a new set of shape functions has to be computed. Exemplarily, the shape functions for the polynomial orders $p = 1, \dots, 4$ are given in the following

$p = 1$

$$N_1^{\text{FEM},1}(\xi) = \frac{1}{2}(1 - \xi), \quad (6.4a)$$

$$N_2^{\text{FEM},1}(\xi) = \frac{1}{2}(1 + \xi), \quad (6.4b)$$

$p = 2$

$$N_1^{\text{FEM},2}(\xi) = \frac{1}{2}\xi(\xi - 1), \quad (6.5a)$$

$$N_2^{\text{FEM},2}(\xi) = 1 - \xi^2, \quad (6.5b)$$

$$N_3^{\text{FEM},2}(\xi) = \frac{1}{2}\xi(\xi + 1), \quad (6.5c)$$

$p = 3$

$$N_1^{\text{FEM},3}(\xi) = -\frac{1}{16}(3\xi + 1)(3\xi - 1)(\xi - 1), \quad (6.6a)$$

$$N_2^{\text{FEM},3}(\xi) = +\frac{9}{16}(\xi + 1)(3\xi - 1)(\xi - 1), \quad (6.6b)$$

$$N_3^{\text{FEM},3}(\xi) = -\frac{9}{16}(\xi + 1)(3\xi + 1)(\xi - 1), \quad (6.6c)$$

$$N_4^{\text{FEM},3}(\xi) = +\frac{1}{16}(\xi + 1)(3\xi + 1)(3\xi - 1), \quad (6.6d)$$

$p = 4$

$$N_1^{\text{FEM},4}(\xi) = +\frac{1}{6}\xi(2\xi - 1)(2\xi + 1)(\xi - 1), \quad (6.7a)$$

$$N_2^{\text{FEM},4}(\xi) = -\frac{4}{3}\xi(\xi - 1)(\xi + 1)(2\xi - 1), \quad (6.7b)$$

$$N_3^{\text{FEM},4}(\xi) = (\xi - 1)(\xi + 1)(2\xi - 1)(2\xi + 1), \quad (6.7c)$$

$$N_4^{\text{FEM},4}(\xi) = -\frac{4}{3}\xi(\xi - 1)(\xi + 1)(2\xi + 1), \quad (6.7d)$$

$$N_5^{\text{FEM},4}(\xi) = +\frac{1}{6}\xi(2\xi - 1)(2\xi + 1)(\xi + 1). \quad (6.7e)$$

Fig. 6.2 depicts the basis functions for the conventional FEM. Since the set of shape functions is different for each polynomial degree, it is said to be non-hierarchical. Implications of this feature are discussed in Section 6.3.

Moreover, nodal-based shape function types have the partition of unity property

$$\sum_{n=1}^{p+1} N_n^{\text{FEM},p}(\xi) = 1. \quad (6.8)$$

This property ensures that rigid body motions are correctly captured when using the FEM.

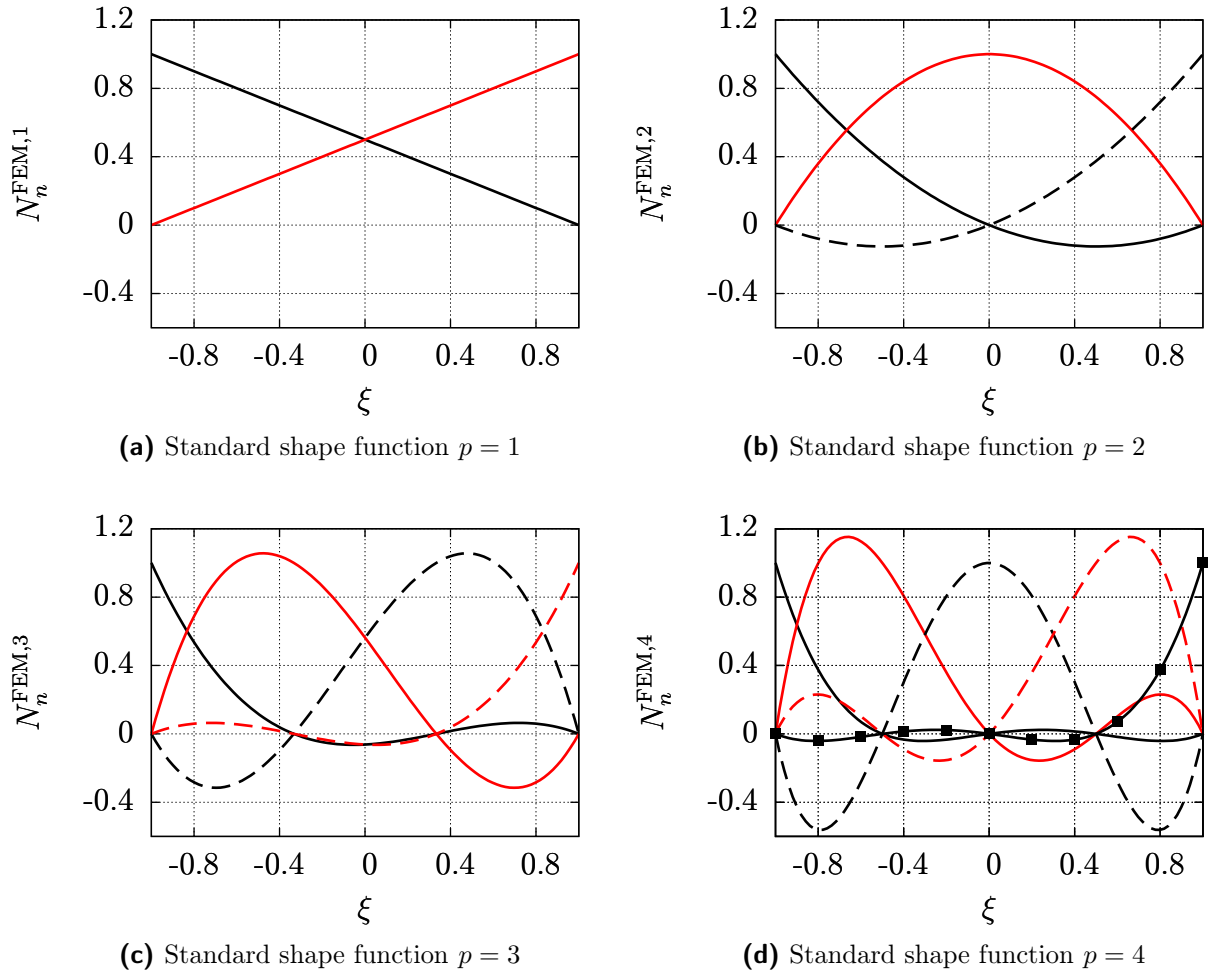


Figure 6.2: Standard shape functions: A solid black line denotes $N_1^{\text{FEM},p}$, a solid red (bright) line represents $N_2^{\text{FEM},p}$, a dashed black line stands for $N_3^{\text{FEM},p}$, a dashed red (bright) line marks $N_4^{\text{FEM},p}$ and $N_5^{\text{FEM},p}$ is signified by a black line marked with filled squares (■).

6.1.2 One-dimensional shape functions: SEM

The Ansatz functions for the SEM are also based on Lagrange polynomials. The presentation of the spectral shape functions follows is closely related to the one in the monograph by Ostachowicz *et al.* [106]. These p -type elements [276] are based on a Gauß-Lobatto-Legendre (GLL) nodal distribution. The Gauß-Lobatto points $(\xi_j, j = 1, \dots, (p + 1))$ are defined in such a way that

$$\xi_k = \begin{cases} -1 & \text{if } k = 1 \\ \xi_{0,k-1}^{lo,p-1} & \text{if } 2 \leq k \leq p \\ +1 & \text{if } k = p + 1 \end{cases} \quad (6.9)$$

Here, $\xi_{0,n}^{lo,p-1}$ ($n = 1, \dots, (p-1)$) denotes the roots of the $(p-1)^{\text{th}}$ -order Lobatto polynomial

$$lo_{p-1}(\xi) = \frac{1}{2^p p!} \frac{d^{p+1}}{d\xi^{p+1}} [(\xi^2 - 1)^p]. \quad (6.10)$$

The shape functions based on Lagrange polynomials are therefore given by

$$N_n^{\text{SEM},p}(\xi) = \prod_{k=1, k \neq n}^{p+1} \frac{\xi - \xi_k}{\xi_n - \xi_k}, \quad k = 1, 2, \dots, p+1. \quad (6.11)$$

In this case, all degrees-of-freedom also retain their physical meaning. If we use a GLL grid in conjunction with the Gauß-Lobatto-Legendre quadrature rule, the elemental mass matrix is under-integrated but also diagonal. This is due to the fact that the integration points for the quadrature formula coincide with the nodal coordinates, cf. Section 4.6.1. We have to bear in mind, however, that this set of shape functions is again non-hierarchic by construction. Exemplarily, the shape functions for the polynomial orders $p = 1, \dots, 4$ are given in the following

$p = 1$

$$N_1^{\text{SEM},1}(\xi) = \frac{1}{2}(1 - \xi), \quad (6.12a)$$

$$N_2^{\text{SEM},1}(\xi) = \frac{1}{2}(1 + \xi), \quad (6.12b)$$

$p = 2$

$$N_1^{\text{SEM},2}(\xi) = \frac{1}{2}\xi(\xi - 1), \quad (6.13a)$$

$$N_2^{\text{SEM},2}(\xi) = 1 - \xi^2, \quad (6.13b)$$

$$N_3^{\text{SEM},2}(\xi) = \frac{1}{2}\xi(\xi + 1), \quad (6.13c)$$

$p = 3$

$$N_1^{\text{SEM},3}(\xi) = -\frac{1}{8}(5\xi^2 - 1)(\xi - 1), \quad (6.14a)$$

$$N_2^{\text{SEM},3}(\xi) = +\frac{5}{8}(\xi^2 - 1)(\sqrt{5}\xi - 1), \quad (6.14b)$$

$$N_3^{\text{SEM},3}(\xi) = -\frac{5}{8}(\xi^2 - 1)(\sqrt{5}\xi - 1), \quad (6.14c)$$

$$N_4^{\text{SEM},3}(\xi) = +\frac{1}{8}(5\xi^2 - 1)(\xi - 1), \quad (6.14d)$$

$p = 4$

$$N_1^{\text{SEM},4}(\xi) = +\frac{1}{8}\xi(7\xi^2 - 3)(\xi - 1), \quad (6.15a)$$

$$N_2^{\text{SEM},4}(\xi) = -\frac{7}{24}\xi(\xi^2 - 1)(7\xi - \sqrt{21}), \quad (6.15b)$$

$$N_3^{\text{SEM},4}(\xi) = +\frac{1}{21}(\xi^2 - 1)(49\xi^2 - 21), \quad (6.15c)$$

$$N_4^{\text{SEM},4}(\xi) = -\frac{7}{24}\xi(\xi^2 - 1)(7\xi + \sqrt{21}), \quad (6.15d)$$

$$N_5^{\text{SEM},4}(\xi) = +\frac{1}{8}\xi(7\xi^2 - 3)(\xi + 1). \quad (6.15e)$$

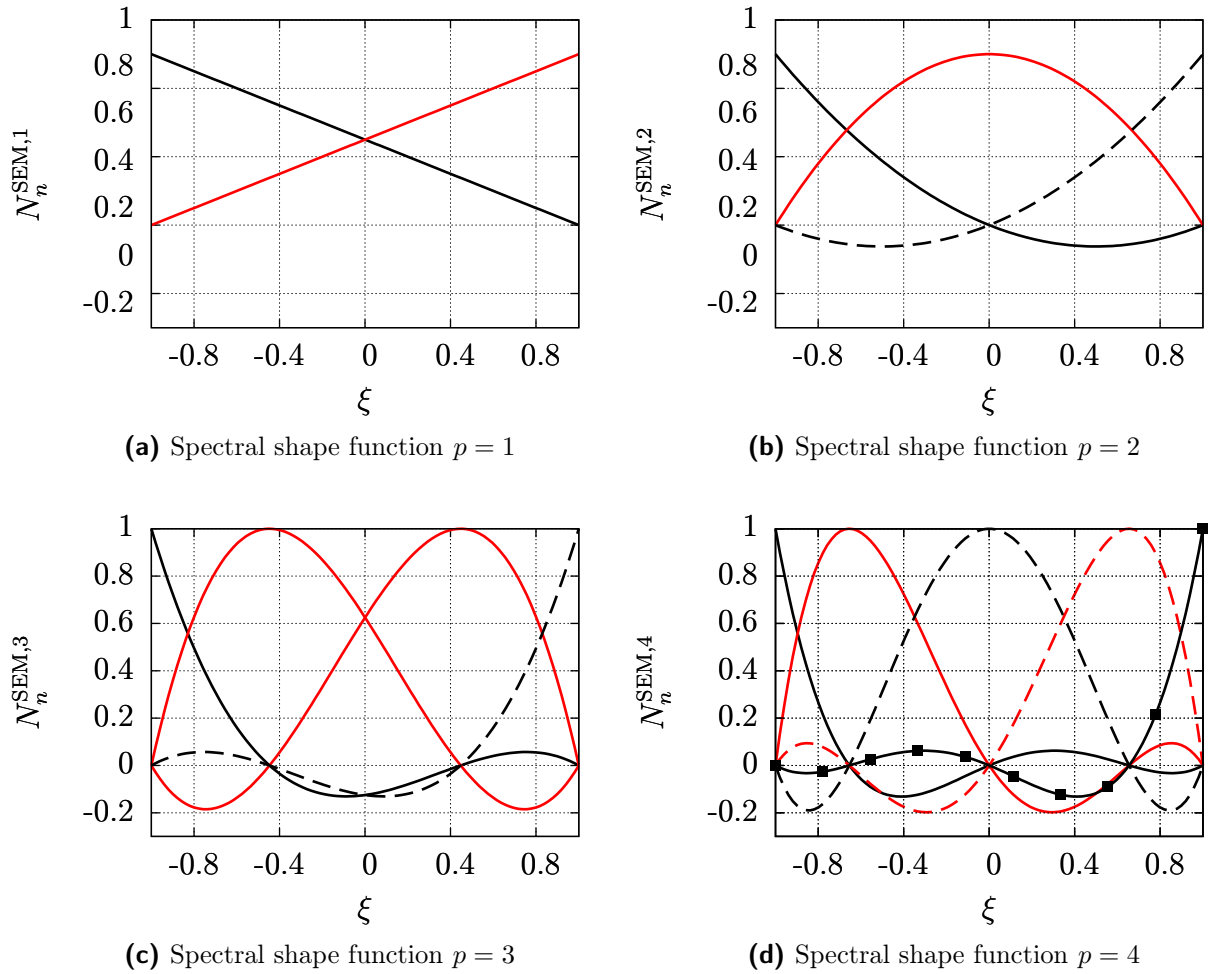


Figure 6.3: Spectral shape functions: A solid black line denotes $N_1^{\text{SEM},p}$, a solid red (bright) line represents $N_2^{\text{SEM},p}$, a dashed black line stands for $N_3^{\text{SEM},p}$, a dashed red (bright) line marks $N_4^{\text{SEM},p}$ and $N_5^{\text{SEM},p}$ is signified by a black line marked with filled squares (■).

Fig. 6.3 depicts the basis functions for the SEM.

Moreover, nodal-based shape function types have the partition of unity property

$$\sum_{n=1}^{p+1} N_n^{\text{SEM},p}(\xi) = 1. \quad (6.16)$$

This property ensures that rigid body motions are correctly captured when using the SEM.

6.1.3 One-dimensional shape functions: p -FEM

The shape functions of the p -version of the FEM are based on the normalized integrals of the Legendre polynomials. The presentation of the shape functions closely follows the one given in the monographs by Szabó and Babuška [115, 120]. The standard linear shape functions (cf. Eqs. (6.4)) - also referred to as nodal shape functions - serve as the starting point:

$$N_1^{p\text{-FEM}}(\xi) = \frac{1}{2}(1 - \xi), \quad (6.17a)$$

$$N_2^{p\text{-FEM}}(\xi) = \frac{1}{2}(1 + \xi). \quad (6.17b)$$

An important feature of the Ansatz functions for the p -FEM is that they constitute a hierarchic set of basis functions. The fundamental difference between hierarchic and non-hierarchic sets is that in the hierarchic case all lower order shape functions are contained in the set of higher order basis functions [116]. Higher order shape functions are therefore only added to the set of already existing shape functions. In the p -FEM, they are defined in terms of the normalized integrals of the Legendre polynomials as

$$N_n^{p\text{-FEM}}(\xi) = \frac{1}{\|le_{n-2}\|} \int_{x_1=-1}^{\xi} le_{n-2}(x_1) dx_1, \quad n = 3, 4, \dots, p+1, \quad (6.18)$$

with the norm of the Legendre polynomial

$$\|le_{n-2}\| = \sqrt{\frac{2}{2n-3}}. \quad (6.19)$$

These functions have the property that $N_n^{p\text{-FEM}}(\mp 1) = 0$. Consequently, only the corner nodes ($n = 1, 2$) retain a physical meaning, whereas the internal variables ($n = 3, 4, \dots, p+1$) cannot be interpreted physically. The Legendre polynomials are a special case of Jacobi polynomials [117] that satisfy the Legendre differential equation

$$(1 - x_1^2)x_2'' - 2x_1x_2' + n(n+1)x_2 = 0, \quad n = 1, 2, \dots \quad -1 \leq x_1 \leq 1. \quad (6.20)$$

They can be computed by applying the Rodriguez formula

$$le_n(x_1) = \frac{1}{2^n n!} \frac{d^n}{dx_1^n} [(x_1^2 - 1)^n], \quad n = 1, 2, \dots \quad -1 \leq x_1 \leq 1. \quad (6.21)$$

For a computationally more efficient implementation, we recommend a recursion formulae [116]. The p -version shape functions of orders $p = 2, 3, 4$ are given in the following

$$N_3^{p\text{-FEM}}(\xi) = \frac{1}{4}\sqrt{6}(\xi^2 - 1), \quad (6.22a)$$

$$N_4^{p\text{-FEM}}(\xi) = \frac{1}{4}\sqrt{10}\xi(\xi^2 - 1), \quad (6.22b)$$

$$N_5^{p\text{-FEM}}(\xi) = \frac{1}{16}\sqrt{14}(5\xi^4 - 6\xi^2 + 1). \quad (6.22c)$$

Fig. 6.4 depicts the basis functions for the p -version of the FEM.

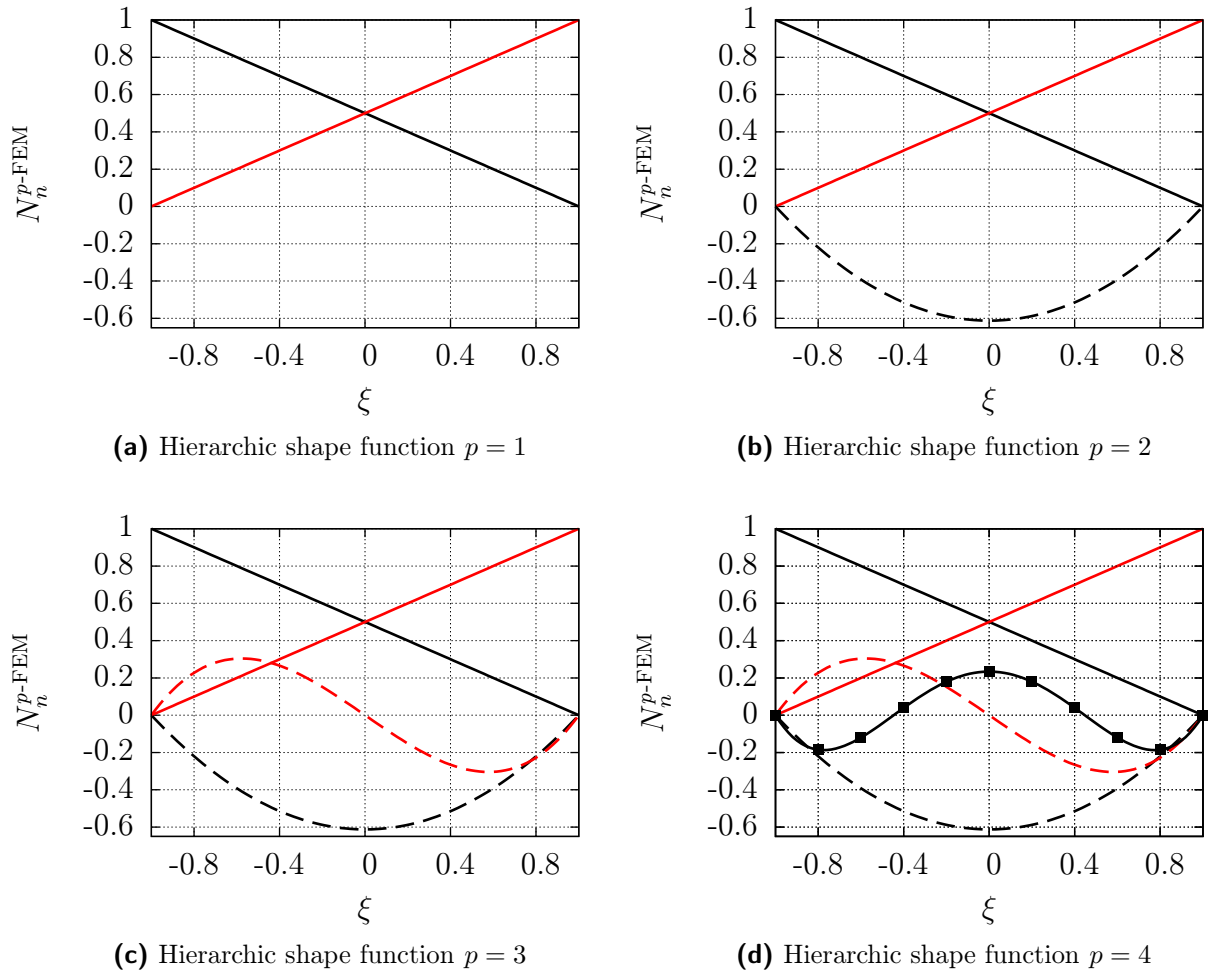


Figure 6.4: Hierarchic shape functions based on the normalized integrals of the Legendre polynomials: A solid black line denotes N_1^{p-FEM} , a solid red (bright) line represents N_2^{p-FEM} , a dashed black line stands for N_3^{p-FEM} , a dashed red (bright) line marks N_4^{p-FEM} and N_5^{p-FEM} is signified by a black line marked with filled squares (■).

6.1.4 One-dimensional shape functions: Fourier- p -FEM

A different approach to constructing higher order hierarchical basis functions is to employ trigonometric functions. To our knowledge initially proposed by Milsted and Hutchinson [277], their primary field of application is the vibration analysis of thin-walled structures and beams [127, 277–286]. In 1997, the term *Fourier-p-element* was coined by Leung and co-workers [282]. Here, the name is used when a Fourier series (trigonometric polynomials) is employed as a FE Ansatz function. Initially, it was developed to overcome the ill-conditioning caused by polynomial degrees higher than $p = 8$ [278, 287].

Again, the standard linear shape functions (cf. Eqs. (6.4)) - also referred to as nodal shape functions - serve as the starting point:

$$N_1^{\text{Fourier-}p\text{-FEM}}(\xi) = \frac{1}{2}(1 - \xi), \quad (6.23a)$$

$$N_2^{\text{Fourier-}p\text{-FEM}}(\xi) = \frac{1}{2}(1 + \xi). \quad (6.23b)$$

Since this set of Ansatz functions is hierarchic too, the statements of Section 6.1.3 are also valid for trigonometric polynomials. Higher order basis functions are developed employing the following formula

$$N_n^{\text{Fourier-}p\text{-FEM}}(\xi) = \sin\left(\left[n - 2\right]\frac{1}{2}\pi(\xi + 1)\right), \quad n = 3, 4, \dots, p + 1. \quad (6.24)$$

Fig. 6.5 depicts the basis functions for the Fourier- p -version of the FEM.

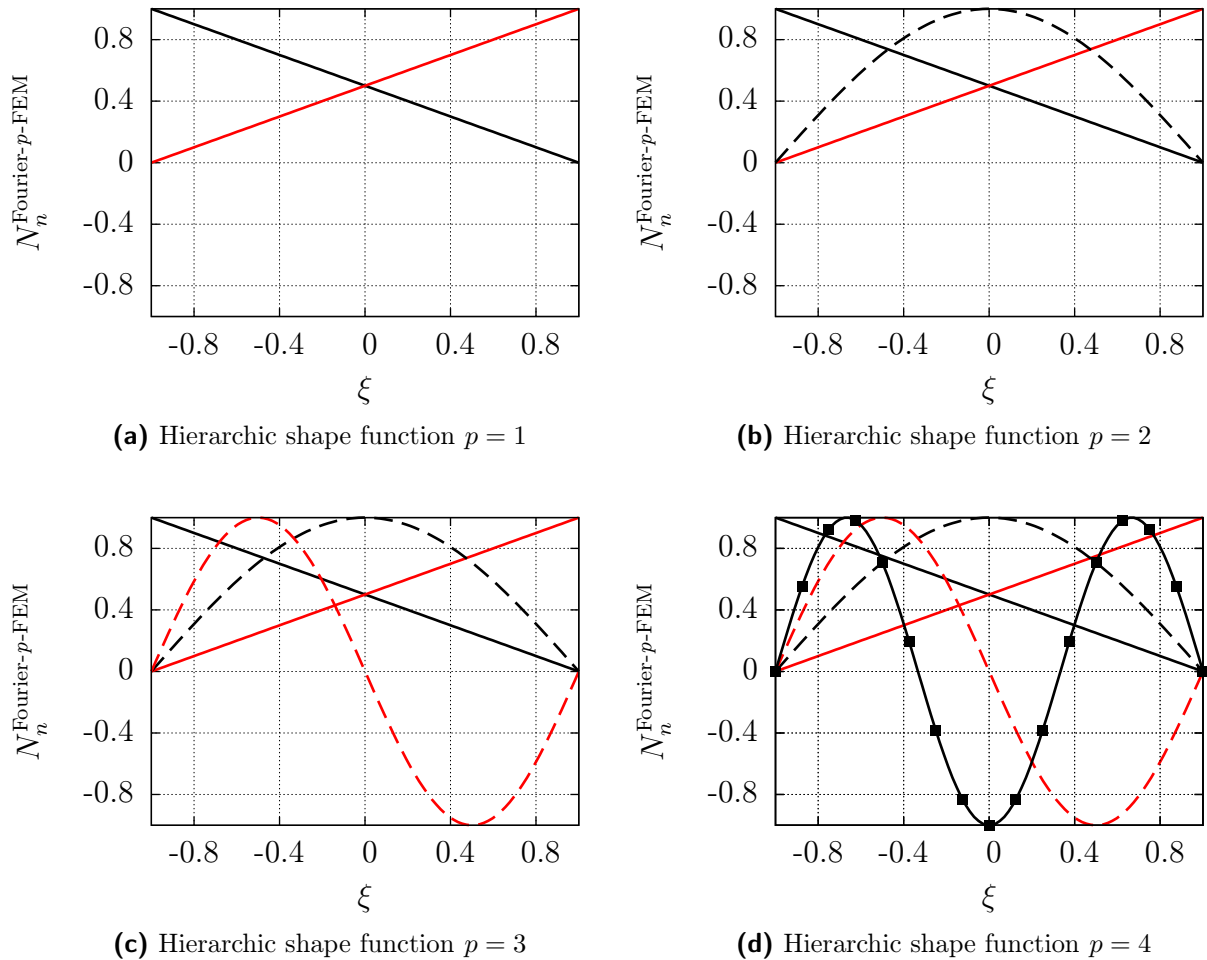


Figure 6.5: Hierarchic shape functions based on sine-functions (Fourier polynomials): A solid black line denotes $N_1^{\text{Fourier-}p\text{-FEM}}$, a solid red (bright) line represents $N_2^{\text{Fourier-}p\text{-FEM}}$, a dashed black line stands for $N_3^{\text{Fourier-}p\text{-FEM}}$, a dashed red (bright) line marks $N_4^{\text{Fourier-}p\text{-FEM}}$ and $N_5^{\text{Fourier-}p\text{-FEM}}$ is signified by a black line marked with filled squares (■).

The Fourier polynomials of orders $p = 2, 3, 4$ are given in the following

$$N_3^{\text{Fourier-}p\text{-FEM}}(\xi) = \sin\left(\frac{1}{2}\pi(\xi + 1)\right), \quad (6.25a)$$

$$N_4^{\text{Fourier-}p\text{-FEM}}(\xi) = \sin(\pi(\xi + 1)), \quad (6.25b)$$

$$N_5^{\text{Fourier-}p\text{-FEM}}(\xi) = \sin\left(\frac{3}{2}\pi(\xi + 1)\right). \quad (6.25c)$$

6.1.5 Generation of one-dimensional hierarchic shape functions

A wide variety of different types of basis functions can be used in conjunction with a FE-based approach. For an optimal choice of the Ansatz functions, the mass matrix \mathbf{M}_{uu} would become diagonal [288]. Unfortunately, this is in general not possible due to the mapping of the reference to the physical domain. The condition number of the system matrices (Section 6.3.2) therefore plays an important role when choosing suitable shape functions. Reference [115] points out that simple polynomial functions with certain orthogonality properties are an appropriate choice. Also, it is mentioned that the shape functions should be hierarchic and that it is important to keep the number of shape functions that do not vanish at the corner nodes, edges and faces as low as possible.

In Sections 6.1.3 and 6.1.4, we already discussed two sets of basis functions that meet the requirements stated above. We can straightforwardly generate additional sets of hierarchic basis functions by using the procedure laid out in the following [288].

The first two one-dimensional shape functions are chosen as the linear polynomials (identical to the approaches discussed in Sections 6.1.3 and 6.1.4)

$$N_1^{\text{hierarchic}}(\xi) = \frac{1}{2}(1 - \xi),$$

$$N_2^{\text{hierarchic}}(\xi) = \frac{1}{2}(1 + \xi).$$

Moreover, all higher order shape functions ($p \geq 2$) should be zero at the boundaries of the reference interval

$$N_i^{\text{hierarchic}}(\xi = -1) = N_i^{\text{hierarchic}}(\xi = 1) = 0, \quad i \geq 3. \quad (6.27)$$

In order to ensure the sparsity of the mass matrix \mathbf{M}_{uu} for one-dimensional problems, we require that the one-dimensional functions are orthogonal

$$\int_{-1}^1 N_i^{\text{hierarchic}} N_j^{\text{hierarchic}} d\xi = \delta_{ij}, \quad i, j \geq 3. \quad (6.28)$$

The conditions given in Eq. (6.27) can be enforced by defining higher order shape functions as

$$N_i^{\text{hierarchic}}(\xi) = (1 - \xi^2) \phi_{i-3}(\xi), \quad i \geq 3 \quad (6.29)$$

where $\phi_j(\xi)$ with $j \geq 0$ are an arbitrary set of polynomials of order j . Solin *et al.* [117] propose to use orthogonal polynomials such as the family of Jacobi polynomials. In reference [288], Betz *et al.* recently suggested the normalized Gegenbauer polynomials as a suitable candidate. They claim that the sparsity of the mass matrix is maximized for this particular choice if rectangular domains are considered (FCM/SCM). However, this statement still needs to be investigated in detailed future research.

In the present thesis, we decided to study well established shape functions in the context of wave propagation analysis. A wide variety of different basis functions would also have been possible, but - for the sake of clarity - we chose to limit our discussions to the four different basis function sets, discussed in Sections 6.1.1 - 6.1.4. These Ansatz functions are well documented in the wide body of literature and have consequently been employed.

6.2 Multi-dimensional shape functions

The implementation of two-/three-dimensional Ansatz functions is based on a quadrilateral/hexahedral element formulation [106, 115, 116]. The main advantage compared to trilateral/tetrahedral formulations is its higher accuracy [116, 289]. Generally speaking, two-/three-dimensional shape functions are only the tensor product of the one-dimensional Ansatz functions defined in Section 6.1

$$N_{l(i,j,k)}^{\text{type},3D}(\boldsymbol{\xi}) = N_i(\xi) \cdot N_j(\eta) \cdot N_k(\zeta), \quad \begin{array}{l} i = 1, 2, \dots, p_\xi + 1 \\ j = 1, 2, \dots, p_\eta + 1 \\ k = 1, 2, \dots, p_\zeta + 1 \\ l = 1, 2, \dots, (p_\xi + 1) \cdot (p_\eta + 1) \cdot (p_\zeta + 1), \end{array} \quad (6.30)$$

with p_ξ , p_η , p_ζ denoting the polynomial orders in each of the local coordinates. The superscript *type* indicates the shape functions being used (FEM, SEM, p -FEM and Fourier- p -FEM). As illustrated in the following sections, there is a distinct difference between hierarchic and non-hierarchic shape functions, especially concerning efforts to ensure inter-element continuity but also in regard to the classification of individual Ansatz functions.

The indices i , j , k of the shape functions denote the numbering of the one-dimensional Ansatz functions regarding the local coordinates ξ -, η - and ζ -, respectively. The hexahedral element formulation is commonly based on the so-called tensor product space [115]. Another possibility is to employ the trunk space. This Ansatz space, however, is only viable for hierarchic shape functions. The difference between the trunk space and the tensor product space is relevant for face and internal modes only. A more detailed description of the different Ansatz spaces is given in Appendix C. For the explanation, the face modes are considered first. To generate face modes two higher order polynomials (in the in-plane local coordinates) and a linear one (in the out-of-plane local coordinate) are multiplied. Face 1 is chosen exemplarily, cf. Fig. 4.2. The indices i , j denote the polynomial degrees of the face modes in ξ and η , respectively.

Face modes (face 1): $N_{(i,j,1)}^{F_1}(\xi, \eta, \zeta) = \frac{1}{2}(1 - \zeta) N_{i+1}^{p\text{-FEM}}(\xi) N_{j+1}^{p\text{-FEM}}(\eta)$

- trunk space
 - $i = 2, \dots, p_\xi - 2$
 - $j = 2, \dots, p_\eta - 2$
 - $i + j = 4, \dots, \max\{p_\xi, p_\eta\}$
- tensor product space
 - $i = 2, \dots, p_\xi$
 - $j = 2, \dots, p_\eta$

The definition of the set of internal modes is analogous. Here, three higher order polynomials in all three local coordinates are multiplied. The indices i , j , k accordingly denote the polynomial degrees of the bubble modes in ξ -, η - and ζ -direction, respectively.

Internal modes: $N_{(i,j,k)}^{int}(\xi, \eta, \zeta) = N_{i+1}^{p\text{-FEM}}(\xi)N_{j+1}^{p\text{-FEM}}(\eta)N_{k+1}^{p\text{-FEM}}(\zeta)$,

- trunk space
 - $i = 2, \dots, p_\xi - 4$
 - $j = 2, \dots, p_\eta - 4$
 - $k = 2, \dots, p_\zeta - 4$
 - $i + j + k = 6, \dots, \max\{p_\xi, p_\eta, p_\zeta\}$
- tensor product space
 - $i = 2, \dots, p_\xi$
 - $j = 2, \dots, p_\eta$
 - $k = 2, \dots, p_\zeta$

Considering the definitions above, it becomes obvious that the number of degrees-of-freedom increases very fast when using the tensor product space. Therefore, the numerical costs can be reduced significantly by employing the trunk space [116]. This, however, depends on the intended applications.

6.3 Comparison of different one-dimensional Ansatz functions

In the current section, we use the term *p-element* for both sets of hierarchic shape functions, introduced in Sections 6.1.3 and 6.1.4, while the term *Lagrange-type element* is employed to refer to the basis functions discussed in Sections 6.1.1 and 6.1.2.

In principle, the solutions that can be obtained by using the different shape functions are quite similar. If the polynomial degree p is the same, both Lagrange and Legendre polynomials are able to fully describe a general polynomial of order p

$$P(\xi) = a_0 + a_1\xi + a_2\xi^2 + \dots + a_p\xi^p. \quad (6.31)$$

Only the constants a_n (degrees-of-freedom) are different [215]. Considering trigonometric Ansatz functions (Section 6.1.4), this does not apply anymore.

6.3.1 Hierarchic vs. non-hierarchic shape functions

One important advantage of hierarchic over non-hierarchic sets of basis functions is indicated in Fig. 6.6.

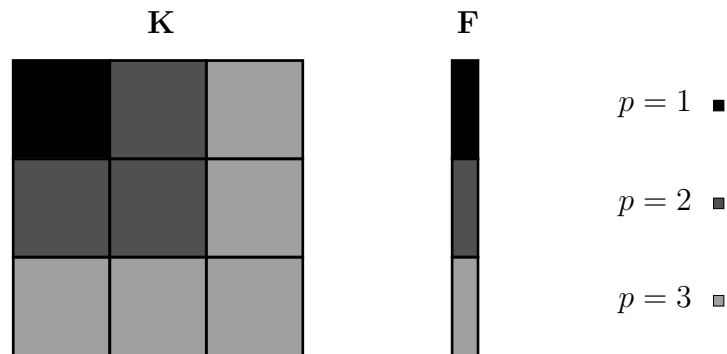


Figure 6.6: Hierarchic structure of stiffness matrix and load vector for $p = 3$.

When increasing the polynomial degree by one order, only one shape function needs to be added to a hierarchic set [115], while a non-hierarchic set of Ansatz functions has to be generated anew (one-dimensional case). If an element refinement is necessary, the totally new set of shape functions requires all calculations to obtain the system matrices to be repeated [241]. This feature has an immediate effect on the structure of the system matrices. That is to say, the system matrices and the load vector corresponding to the polynomial order p are a sub-set of the global system matrices and the load vector for the polynomial degree $p + 1$. In Fig. 6.6, we use different shades of grey to illustrate the advantage of hierarchic Ansatz functions concerning p -refinement procedures. When the polynomial degree for the approximation of the unknown field is successively increased, only those parts of the system matrices that are indicated in brighter shades need to be computed while all components of the matrices have to be re-calculated in case of a non-hierarchic set of shape functions.

Another point we have to take into account is that the degrees-of-freedom have no physical interpretation in the p -version of the FEM [215]. If Lagrange-type shape functions are employed the degrees-of-freedom correspond to the nodal values of the independent field variables. In the case of hierarchic Ansatz functions, only the nodal modes can be interpreted as field variables, whereas all higher order degrees-of-freedom are merely unknown parameters determining the solution space. A more involved post processing is therefore required when dealing with hierarchic Ansatz functions.

There are further advantages connected to the hierarchic structure of the set of shape functions and the fact that it constitutes a modal basis instead of a nodal one, such as the p -version FEs' inherent ability for a local p -refinement. Due to the fact that we can freely choose the polynomial degree for all edges, faces and the interior of the p -element, a local, adaptive p -refinement seems easily feasible. These special transition elements can be derived automatically without any additional considerations. We only have to ensure the compatibility at adjacent faces and edges between neighboring FEs [117, 119], cf. Section 6.4. Moreover, the hierarchic nature of the shape functions itself facilitates an easy implementation of adaptive refinement strategies (structure of the system matrices). In contrast to the behavior of p -elements, a local refinement cannot be easily achieved by using both SEs and conventional FEs. Both schemes need especially generated transition elements to ensure continuity. These special kinds of FEs are, however, difficult to develop.

One of the main reasons why the p -version of FEM is hardly used for ultrasonic guided wave propagation analysis is that there is no mass-lumping technique available yet. However, a diagonal mass matrix is indispensable in order to fully exploit the advantages of an explicit time integration. If we use a consistent mass matrix formulation, a system of equations has to be solved for each time-step - while a diagonalized mass matrix requires only matrix-vector-operations. It is therefore highly advantageous to be able to employ explicit time-marching schemes in wave propagation analysis. Remember, that the methods developed in the present thesis are primarily applied to ultrasonic guided wave propagation problems. In consequence, it is imperative to have efficient time-integration methods at hand. As the time-step is naturally limited by the high-frequency regime, explicit time-stepping algorithms are only advantageous over implicit ones if the mass matrix is a diagonal matrix [151, 152]. In this thesis, we employ an implicit algorithm such as the Newmark-method (cf. Section 4.3.3) where a consistent mass matrix formulation is chosen. Yet, the use of implicit time-marching schemes for high frequency wave propagation problems tends to be numerically costly [78]. Considering FEMs based on Lagrange-type

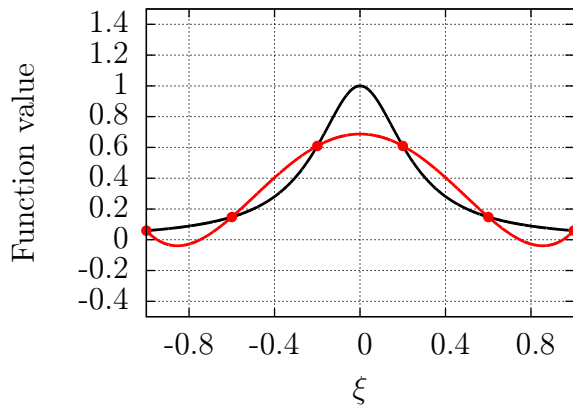
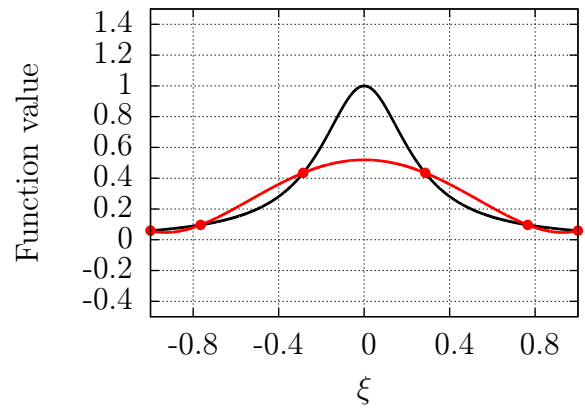
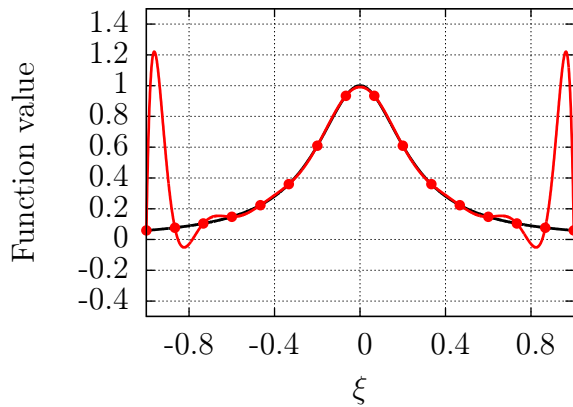
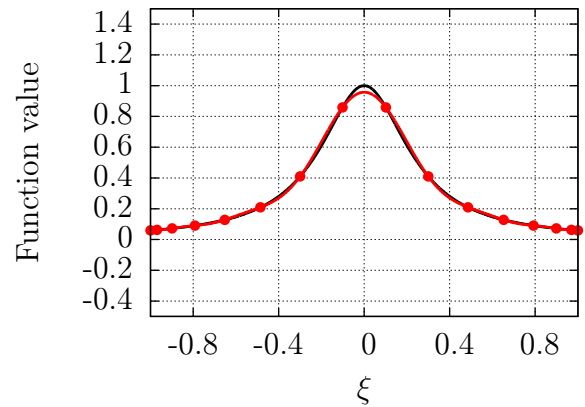
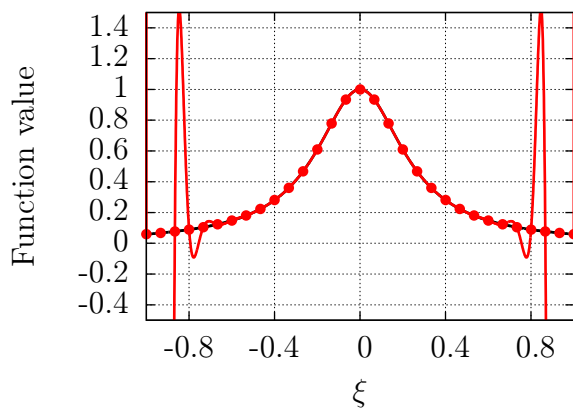
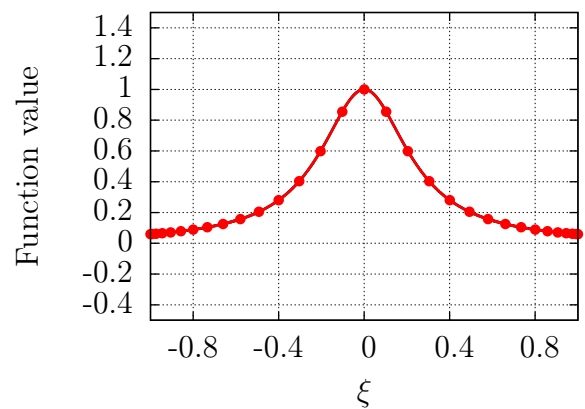
shape functions, we can diagonalize the mass matrix by using a special nodal quadrature rule, the row-sum technique or the HRZ-lumping method [151–153] (cf. Section 4.6), to ensure that explicit time integration schemes become feasible, cf. Section 4.3.2.

Trigonometric functions possess some advantages over polynomial Ansatz functions. They are indefinitely derivable and no recurrence formulae are needed to generate them, which serves to minimize the round-off errors [279, 280, 283]. These two features result in a better conditioned system of equations compared to other kinds of hierarchic shape functions, cf. Section 6.3.2. To date, these shape functions are almost exclusively used for modal analysis applications.

Table 6.1: Comparison of key features of the different shape function types (one-dimensional case).

Feature \ Method	FEM	SEM	p -FEM	Fourier- p -FEM
Inter-element continuity	C_0	C_0	C_0	C_0
Degrees-of-freedom (interpretation)	physical	physical	unknowns	unknowns
Mass-lumping	yes	yes	no	no
	row-sum	row-sum	-	-
	nodal-quad.	nodal-quad.	-	-
	HRZ	HRZ	-	-
Hierarchic set of functions	no	no	yes	yes
Number of common degrees-of-freedom between adjacent elements	1	1	1	1
Runge phenomenon (oscillations)	yes	no	no	no

One frequently mentioned drawback of higher order Ansatz functions based on an equidistant nodal distribution is the occurrence of the so-called Runge phenomenon [87, 183], cf. Fig. 6.7. This effect is related to the interpolation of functions. According to [290–293], the idea to interpolate functions deploying a polynomial interpolation scheme in equispaced points is fundamentally wrong. In case we want to interpolate a smooth function by polynomials in $p + 1$ equally spaced points, the error may increase at a rate of 2^p and therefore the approximation fails to converge even if $p \rightarrow \infty$ [291]. Here, oscillations with high amplitudes close to the boundaries of the interval are a characteristic sign, because this is where the error between the original function and its interpolation polynomial increases rapidly [87], cf. Fig. 6.7. As mentioned before, this can be observed when applying equidistant nodal distributions, rendering them unsuitable for the interpolation of higher order polynomial functions. We can minimize these oscillations, however, by using nodal distributions that are denser (clustered) at the ends of the interval (unevenly spaced points) [292]. Such distributions decrease the Lebesgue constant [293]. The Lebesgue constant is a measure of how suitable the interpolant of a function (at the chosen nodal distribution) is in comparison with the best polynomial approximation of the function (it therefore bounds the interpolation error).

(a) Equispaced nodal distribution: $N = 6$ (b) GLL nodal distribution: $N = 6$ (c) Equispaced nodal distribution: $N = 16$ (d) GLL nodal distribution: $N = 16$ (e) Equispaced nodal distribution: $N = 31$ (f) GLL nodal distribution: $N = 31$

Annotations: The function to be interpolated is the witch of Agnesi curve - $f(\xi) = 1/(1 + 16\xi^2)$ - a classical example to demonstrate that the interpolation error can increase without bounds.

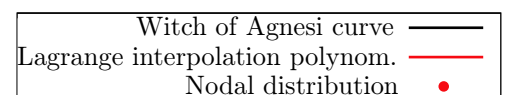


Figure 6.7: Runge phenomenon: Comparison of Lagrange interpolation polynomials through an equidistant nodal distribution and a GLL one.

For a detailed investigation of polynomial interpolation in the context of higher order methods, the interested reader is referred to [290–293] and the references cited therein.

Tab. 6.3.1 summarizes selected properties of the discussed one-dimensional shape functions. Thus, their advantages and disadvantages can be judged at a glance.

6.3.2 Critical time-step and condition number

In the present section, we investigate the critical time step Δt_{cr} and the condition number κ . To this end, a one-dimensional and a three-dimensional model are proposed. The one-dimensional case is to be examined first. We study one straight truss element (one degree-of-freedom per node) as sketched in Fig. 6.8. The displacement degree-of-freedom at the left boundary is constraint.

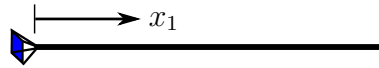


Figure 6.8: Basic model of condition number computations.. The length of this bar is $l = 1$ m and the cross section has an area $A = 1$ m². The displacement degree-of-freedom at the left boundary is fixed. The material data are given in Tab. 6.2.

An undistorted cubic element serves as a basis for the evaluation of the critical time-step and the condition number of three-dimensional *HO*-FE approaches. Consequently, only the influence of the different shape functions on κ is apparent. The cube is fixed at the bottom surface (all translational degrees-of-freedom are set to zero, cf. Fig. 6.9).

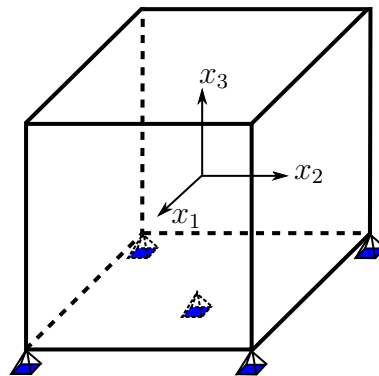


Figure 6.9: Basic model of condition number computations. The side length of this cube is $l = 1$ m. The displacement degrees-of-freedom at the bottom surface are fixed (all translational degrees-of-freedom are set to zero). The material data are given in Tab. 6.2.

Table 6.2: Material data for steel.

Young's modulus (E)	Poisson's ratio (ν)	Mass density(ρ)
2.1×10^{11} N/m ²	0.33	7850 kg/m ³

Critical time step

The applicability of the different *HO*-FEMs to high-frequency structural dynamics is also determined by the critical time-step. Considering the stability limit of the CDM (Eq. (4.77)), given again at this point again

$$\Delta t \leq \frac{2}{\omega_{max}} = \frac{2}{\sqrt{\varrho(\mathbf{M}_{uu}^{-1}\mathbf{K}^*)}},$$

it is easy to accept that the method with the largest time-step size is favorable. In the following, it will suffice to list only the results for the three-dimensional case, since those for the one-dimensional one are basically identical. The evolution of the critical time-step is depicted in Fig. 6.10. We observe that the Fourier- p -FEM offers advantages (larger time-step) up to a polynomial degree of $p = 9$. All other approaches show an identical performance for this particular example. We attribute this behavior to the fact that the same polynomial space is described by all three *HO*-FEMs.

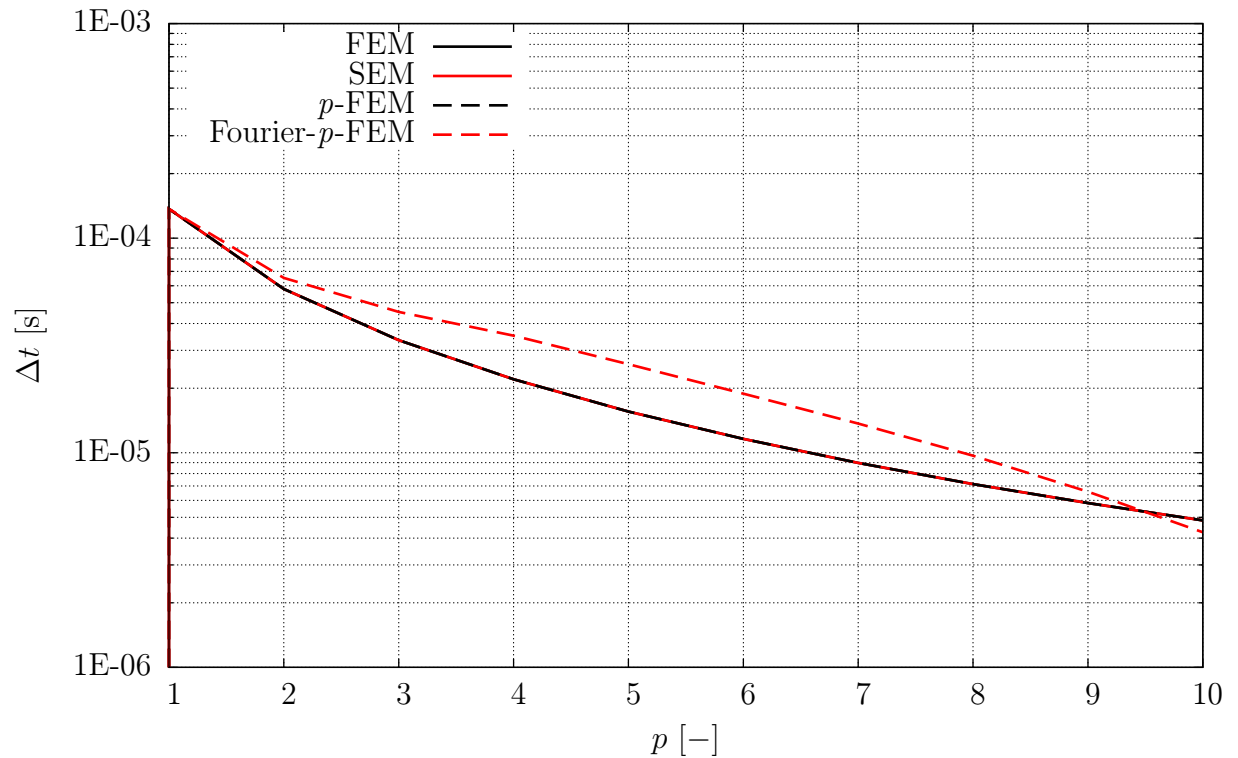


Figure 6.10: Critical time-step size for the CDM using the system matrices for the FEM, the SEM, the p -FEM and the Fourier- p -FEM (three-dimensional case - one undistorted (cube-shaped) element).

Comparison of the condition numbers for different Ansatz functions

The condition number κ of the element matrix can be used as a further criterion to rate the influence of the shape functions. The condition number is generally related to the number

of digits n_l lost in the calculation due to round-off errors [294]

$$n_l \approx \lg(\kappa). \quad (6.32)$$

If we employ iterative approaches, such as the pre-conditioned conjugate gradient method [229], the number of iterations depends on the condition number where a higher condition number increases the number of iterations needed to achieve a chosen accuracy. If direct solvers, such as the Cholesky decomposition or the Gaussian elimination [264], are preferred, the accuracy of the solution deteriorates if the system of equations is ill-conditioned due to the accumulation of round-off errors. Thus, it is desirable to generate a system of equations in such a way that a low condition number can be achieved [116].

The condition number of a positive definite or positive semi-definite matrix \mathbf{A} can be calculated with the help of the largest $\lambda_{max}(\mathbf{A})$ and smallest eigenvalue $\lambda_{min}(\mathbf{A})$ of that matrix [255, 295]

$$\kappa(\mathbf{A}) = \frac{\lambda_{max}(\mathbf{A})}{\lambda_{min}(\mathbf{A})}. \quad (6.33)$$

To evaluate the performance of the proposed shape functions, we compute the condition number of the stiffness matrix \mathbf{K}_{uu} , while the polynomial order of the Ansatz function is raised successively ($p = 1, \dots, 10$). The results for the one-dimensional case are displayed in Fig. 6.11, while the results for the three-dimensional case are displayed in Fig. 6.12.

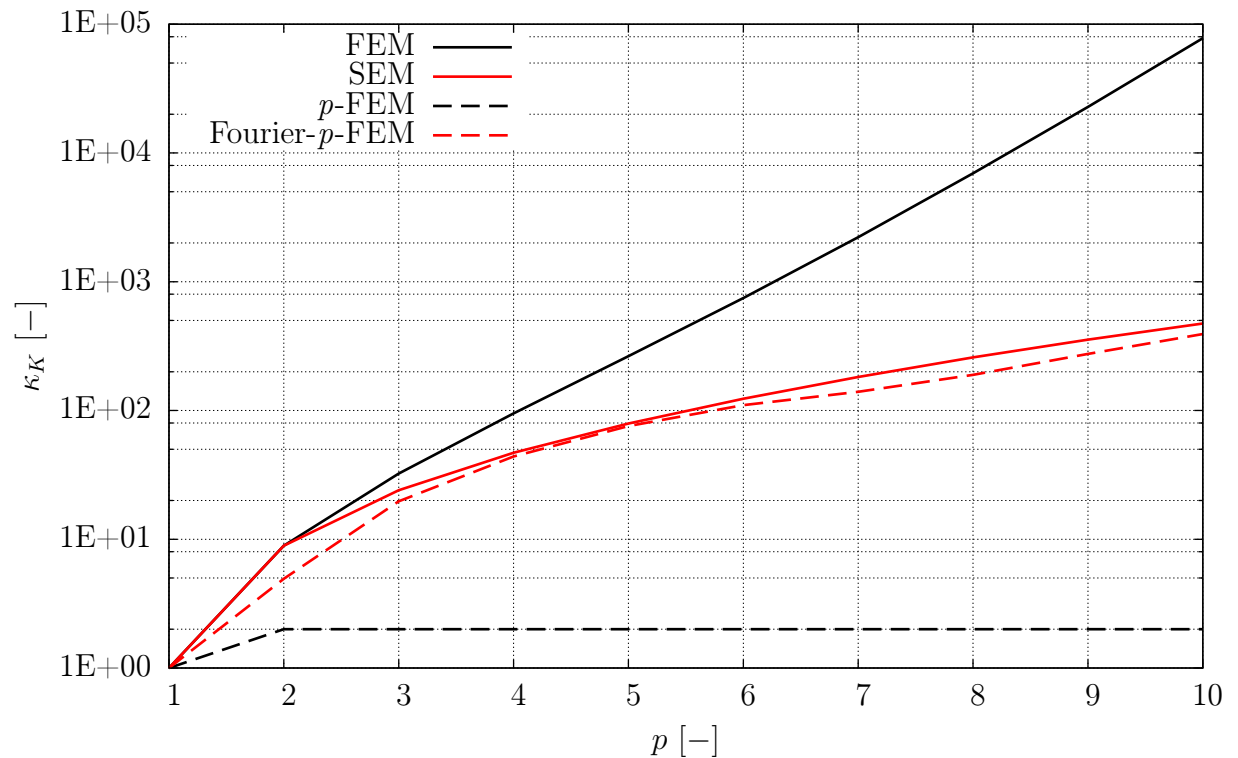


Figure 6.11: Condition number of the stiffness matrix for the FEM, the SEM, the p -FEM and the Fourier- p -FEM (one-dimensional case - one undistorted element).

For one-dimensional applications, the p -version of the FEM provides the smallest condition number by far, cf. Fig. 6.3.2. This behavior is explained by the more diagonally dominant

structure of the stiffness matrix. In the one-dimensional case it is therefore advisable to deploy p -version FEs. Apart from the FEM based on Lagrange polynomials defined on an equispaced grid, all other approaches perform reasonably well.

In a three-dimensional domain, however, this behavior changes significantly. The polynomial degree is again limited to 10, as higher polynomial orders are of no practical interest for wave propagation problems - according to the findings reported by Willberg *et al.* [78]. The SE exhibits the smallest condition number, cf. Fig. 6.12. This behavior is very different to that of the one-dimensional case. It can be observed that the slope of the curve corresponding to the FEM increases at a progressive rate. FEs based on Lagrange polynomials defined on an equispaced nodal distribution are thus to be recommended. Consequently, numerical problems will arise if this method is applied when using polynomial degrees $p \geq 10$. SEs on the other hand do not show numerical ill-conditioning even for higher polynomial orders p . FEs based on hierarchical shape functions perform quite reasonably - in between the two methods mentioned before.

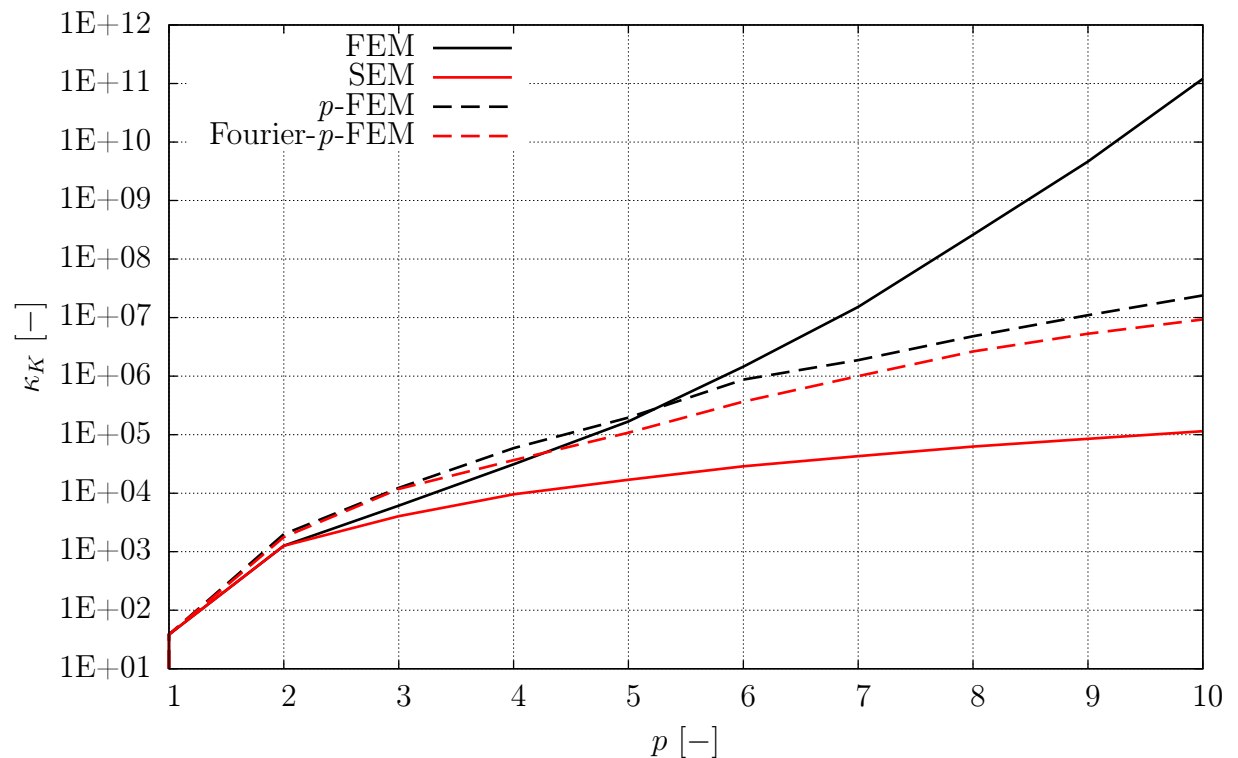


Figure 6.12: Condition numbers of the system matrices for the FEM, the SEM, the p -FEM and the Fourier- p -FEM (three-dimensional case - one undistorted (cube-shaped) element).

6.4 C_0 -continuity

The basic idea of the FEM is to divide the computational domain into sub-domains. These FEs are then used to discretize both the geometry and the unknown solution of the underlying mathematical problem which can often be formulated according to a variational principle. In the present thesis, the underlying variational principle requires at least a C_0 -

continuous approximation of the independent variables, meaning that adjacent elements have to have the same approximation values across mutual nodes, edges and faces. Thus, we have to ensure that neighbouring FEs share the same degrees-of-freedom at these common nodes, edges and faces.

Non-hierarchical shape functions

In the case of non-hierarchical (nodal) shape functions, higher order shape functions are defined by introducing additional nodes. The continuity of the independent variables between adjacent FEs can be achieved straightforwardly for such nodal-based shape functions. Here, the numbering of the degrees-of-freedom plays a vital role. This is done by constructing a topology matrix \mathbf{LM} (location matrix). The dimensions of the topology matrix are $[n_e \times n_{dof}]$ where n_e is the number of FEs and n_{dof} is the number of degrees-of-freedom per element. Hence, the component LM_{ij} contains the global number of the j^{th} local degree-of-freedom of element i . Here, it becomes evident that the topology matrix assigns the local degrees-of-freedom to the corresponding position in the global system of equations. Every component of the element matrix is added to the corresponding entry in the global matrix which is indicated by LM_{ij} . Thus, to obtain the global system of equations we have to repeat this procedure for each FE. Symbolically, the assembly process can be expressed as

$$\mathbf{K} = \sum_{e=1}^{n_e} \mathbf{S}^{(e)T} \mathbf{K}_{uu}^{(e)} \mathbf{S}^{(e)}, \quad (6.34)$$

$$\mathbf{M} = \sum_{e=1}^{n_e} \mathbf{S}^{(e)T} \mathbf{M}_{uu}^{(e)} \mathbf{S}^{(e)}, \quad (6.35)$$

$$\mathbf{F} = \sum_{e=1}^{n_e} \mathbf{S}^{(e)T} \mathbf{f}_{uu}^{(e)}. \quad (6.36)$$

where $\mathbf{S}^{(e)}$ is an element mapping matrix consisting only of zeros and ones corresponding to the components of the location matrix, the size of $\mathbf{S}^{(e)}$ is $[n_{dof} \times n_{sys}]$ with n_{sys} being the number of degrees-of-freedom of the whole FE model.

Hierarchical shape functions

Owing to the fact that higher order modes (edge modes and face modes) are generated without introducing additional physical nodes, special care has to be taken to guarantee a C_0 -continuous approximation over the edges and faces of adjacent FEs.

For the sake of simplicity, we choose a two-dimensional setting to explain the necessary steps in order to ensure the C_0 -continuity over the edges of neighboring FEs. For adaptive discretization techniques, it is desirable to be able to assign different polynomial orders to every FE. If two adjacent elements do not share the same polynomial degree at common edges or faces, the first step to assure continuity is to adjust their polynomial degrees. This can be achieved using either the minimum or the maximum rule [117, 119]. That is to say, either the lower or the higher polynomial degree of adjacent edges or faces is assigned to the other element's edge or face. After having adjusted the polynomial degree of these elements, the degrees-of-freedom have to be numbered. This is, to some extent, an arbitrary process.

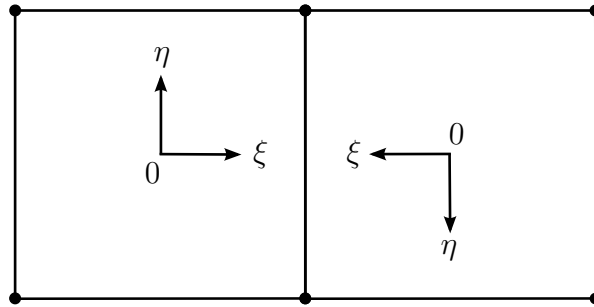
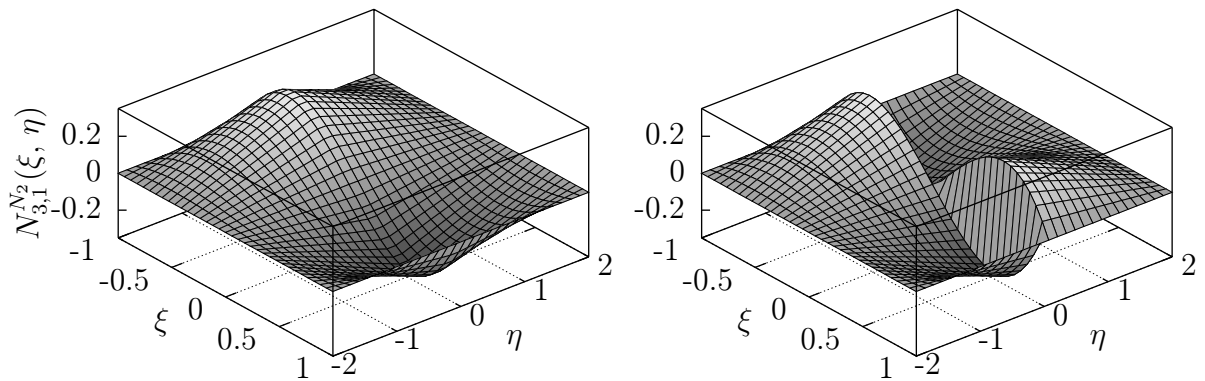
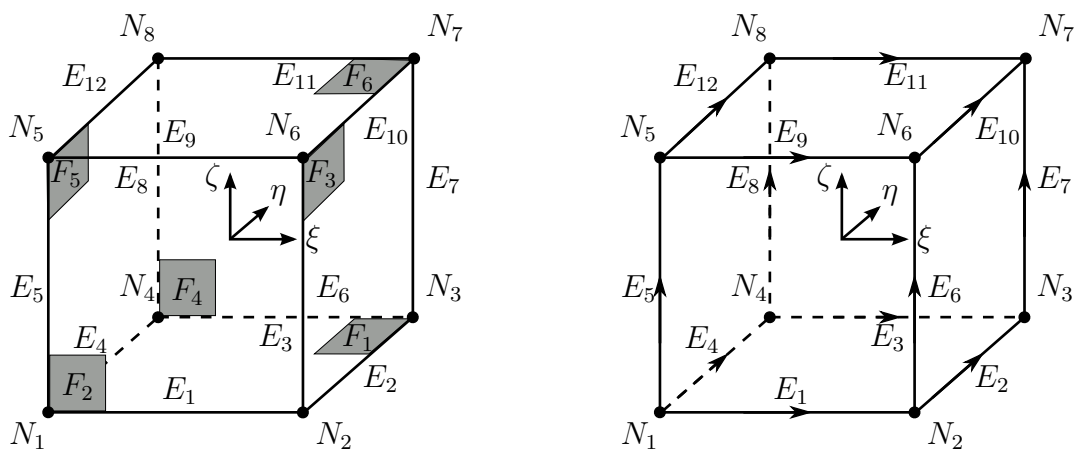


Figure 6.13: Non-conforming local coordinate systems and edge orientations of adjacent two-dimensional FEs.



(a) correct edge orientation of adjacent elements **(b)** incorrect edge orientation of adjacent elements

Figure 6.14: C_0 - and C_{-1} -continuous approximation at the boundary of two adjacent FEs. The Ansatz functions are of odd polynomial degree ($p_{edge} = 3$). Due to an incorrect edge orientation of adjacent FEs the corresponding shape functions are mismatched.



(a) Definition of nodes, edges, faces and local coordinate system

(b) Definition of local edge orientation

Figure 6.15: Standard hexahedral element ($-1 \leq \xi \leq 1$, $-1 \leq \eta \leq 1$, $-1 \leq \zeta \leq 1$) augmented with locally defined edge directions.

The results of this numbering process are stored in the topology matrix **LM**. The assembly algorithm explained above works fine as long as the local coordinate systems of adjacent FEs coincide. If one local coordinate system is rotated against the other, C_0 -continuity cannot be guaranteed since the edge orientation of a common edge differs as a result of the rotation, cf. Fig. 6.13. If we use commercially available mesh generators, this situation is frequently encountered - causing non-matching modes (Fig. 6.14). However, this obstacle can be overcome by drawing on the approaches introduced in references [117, 119, 215, 296, 297]. It has to be noted that the inter-element continuity is only violated when shape functions of odd degree are deployed. The FEs have to be endowed with a local as well as a global edge orientation in order to solve this inter-element continuity problem. If we independently choose local and global orientations, they will usually turn out mismatched. The local orientations of edges and faces on the reference domain are illustrated in Fig. 6.15. They are uniquely defined by the local coordinate system. On the other hand, global orientations are assigned with respect to the global numbering of the corner nodes. One suggestion would be to define the global orientation of edges according to the enumeration of their vertices. The positive orientation is defined in the direction of increasing nodal numbers [117].

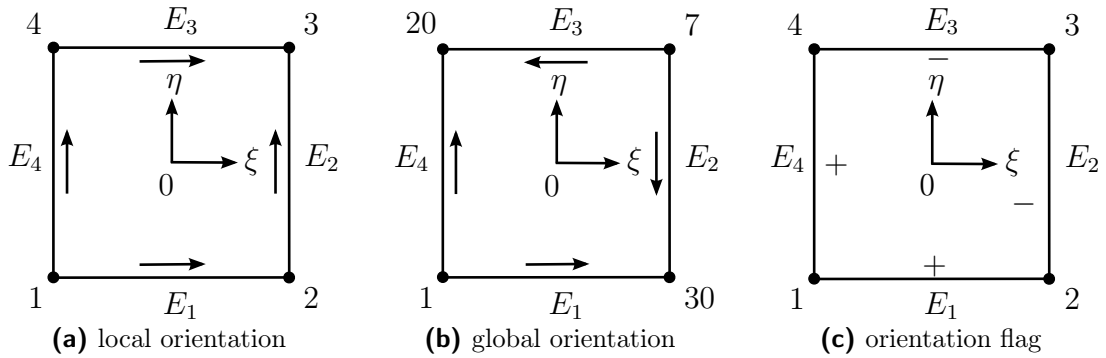


Figure 6.16: Definition of the local and the global orientation of edges.

Fig. 6.16 illustrates how the edge orientation flags (q_i^e) are determined. They must be stored element-wise for all edges. If the local orientation matches the global one $q_i^e = +1$ otherwise $q_i^e = -1$. That is to say, an array of four q_i^e values has to be saved for every two-dimensional quadrilateral element of the structure. Accordingly, an array of twelve edge orientation flags has to be stored for every three-dimensional hexahedral element. References [117, 119] indicate that it is sufficient to multiply all odd order edge functions associated with an orientation flag $q_i^e = \pm 1$ in order to ensure C_0 -continuity for adjacent edges

$$\bar{N}_{(k,1,1)}^{E_i}(\boldsymbol{\xi}) = (q_i^e)^k \cdot N_{(k,1,1)}^{E_i}(\boldsymbol{\xi}). \quad (6.37)$$

A similar algorithm is employed to ensure the continuity of adjacent faces of hexahedral FEs. For each face, the vertex with lowest global number A is selected - and additionally the two edges (AB and AC) originating from it. We define the edges in such a way that the inequality

$$\text{index}(A) < \text{index}(B) < \text{index}(C) \quad (6.38)$$

is valid. Edge AB depicts the global x_1 -direction, whereas side AC corresponds to the global x_2 -direction. Thus, the global face coordinate system is defined as displayed in Fig. 6.17.

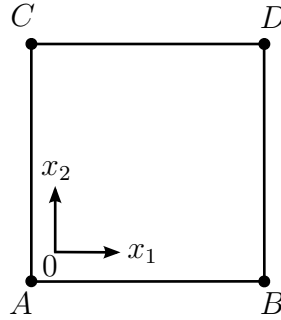


Figure 6.17: Definition of the global face coordinate system.

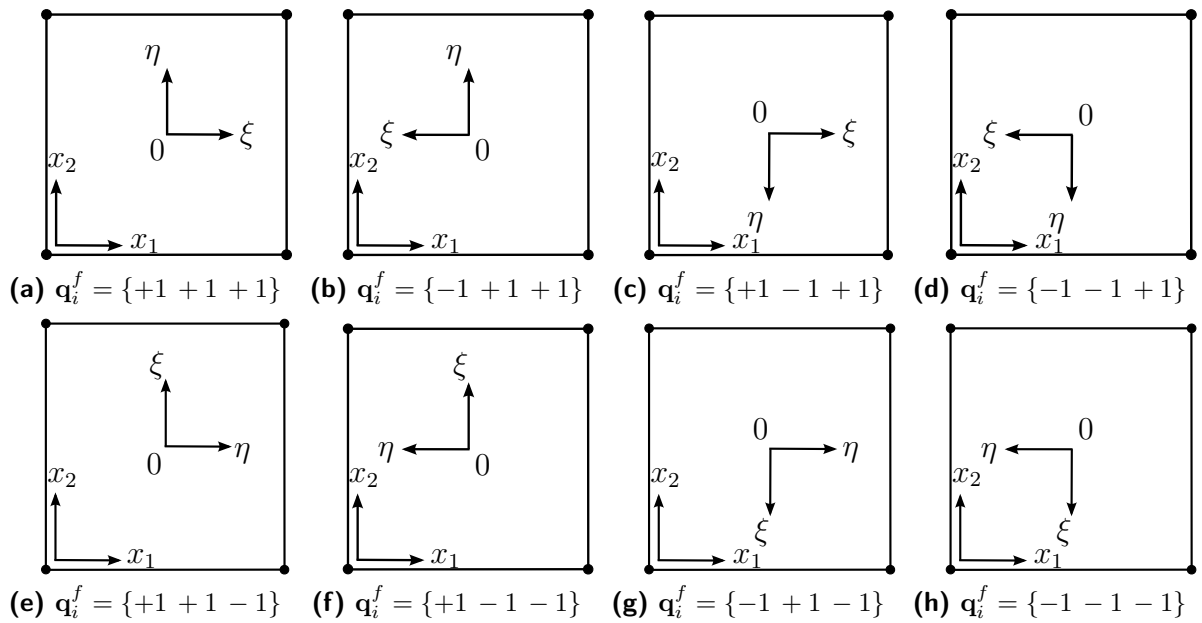


Figure 6.18: Definition of the local and global orientation of faces.

There are eight (2^3) distinct possibilities of how the local and global face coordinate system can be oriented towards each other, as illustrated in Fig. 6.18. Thus, for every face the vector \mathbf{q}_i^f needs to be stored containing the three face orientation flags. The third component indicates whether the local ξ - and η -axis match the direction of the global x_1 - and x_2 -axis, respectively. If the directions are the same $q_i^f(3) = +1$. In case the ξ -direction coincides with the x_2 -direction $q_i^f(3)$ is set equal to -1 . Assuming the first case, the flag $q_i^f(1)$ suggests whether the orientation of the local ξ -axis matches that of the globally defined x_1 -axis and $q_i^f(2)$ denotes if the orientation of the η -axis coincides with that of the global x_2 -axis. Should $q_i^f(3)$ be equal to -1 , the flag $q_i^f(1)$ indicates if the local ξ -direction has the same orientation as the global x_2 -direction and $q_i^f(2)$ describes whether the orientations of the local η -direction and the global x_1 -direction coincide. Unless \mathbf{q}_i^f is equal to $\mathbf{1}$ the face modes have to be transformed in a similar way as was suggested for the edge modes. For

the detailed derivation of a suitable transformation rule it is referred to [117]. It has to be noted that sign factors can be used again in order to ensure continuity for neighboring elements

$$\bar{N}_{(1,p_1,p_2)}^{F_i}(\boldsymbol{\xi}) = [q_i^f(1)]^{p_1} \cdot [q_i^f(2)]^{p_2} \cdot N_{(1,p_1,p_2)}^{F_i}(\boldsymbol{\xi}), \quad (6.39)$$

$$p_1 = 2, 3, \dots, p_2 = 2, 3, \dots, q_i^f(3) = +1,$$

$$\bar{N}_{(1,p_1,p_2)}^{F_i}(\boldsymbol{\xi}) = [q_i^f(1)]^{p_2} \cdot [q_i^f(2)]^{p_1} \cdot N_{(1,p_2,p_1)}^{F_i}(\boldsymbol{\xi}), \quad (6.40)$$

$$p_1 = 2, 3, \dots, p_2 = 2, 3, \dots, q_i^f(3) = -1.$$

The proposed procedures guarantee that a C_0 -steady approximation of the independent variables is achieved. For a detailed description of the three-dimensional Ansatz functions for the p -version of FEM (nodal, edge, face and internal modes) the reader is referred to Appendix B.

Chapter 7

Convergence Studies

In the current chapter, we study the accuracy and convergence properties of the proposed *HO*-FEMs with respect to wave propagation analysis in thin-walled structures. Based on these results we propose a guideline on how the polynomial degree and the element size have to be chosen to ensure accurate and efficient simulation results. Thus, the following sections focus on the discretization's influence on the quality of the numerical solution. To this end, we consider a two-dimensional plane strain model. A two- instead of a three-dimensional model was chosen in order to reduce the computational time. Moreover, a two-dimensional setting is also suitable to represent all important phenomena such as mode conversion and physical dispersion of the ultrasonic guided waves. Sections 8.5 and 8.6 illustrate that the guidelines derived drawing on a two-dimensional model are applicable also for three-dimensional wave propagation problems. Material damping, however, is not included as it has a negligible effect on the principal convergence behavior of the different FE approaches.

7.1 Model set-up

The convergence study is conducted with the model depicted in Fig. 7.1, where the geometry, dimensions and boundary conditions of the benchmark problem are shown. The plate under consideration is made of aluminum (cf. Tab. 2.1) and its length $l_p = 500$ mm was chosen to ensure that reflections from the right boundary will not affect the signal at points *A* and *B* during the simulation time. Since only a single load is introduced at the top surface both fundamental modes, S_0 and A_0 , are excited. The time-dependent amplitude is given by Eq. (7.1) and the central frequency is $f_c = 250$ kHz. The number of periods contained in the signal is $n = 5$. In the following paragraphs, we introduce the methodology that is employed to evaluate the performance of the proposed *HO*-FE approaches.

Hann-function

Ultrasonic guided waves (Lamb waves) are commonly excited using surface-bonded piezoelectric actuators, driven with a time-dependent amplitude. In this thesis, a sine-burst signal modulated by a Hann-window is favored. The time-dependent signal is accordingly given by

$$F(t) = \hat{F} \sin \omega t \sin^2 \left(\frac{\omega t}{2n} \right), \quad 0 \leq t \leq \frac{n}{f_c}, \quad (7.1)$$

where $\omega = 2\pi f_c$ denotes the central circular frequency. This kind of pulse has the advantage of a narrow-banded frequency content. The number of cycles within the signal n determines the width of the excited frequency band and the side-lobes around the central frequency f_c . For a narrow frequency bandwidth, we have to choose n as high as possible which of course increases the excitation time for a given frequency. $n = 5$ is therefore an acceptable compromise between the frequency bandwidth and the excitation time.

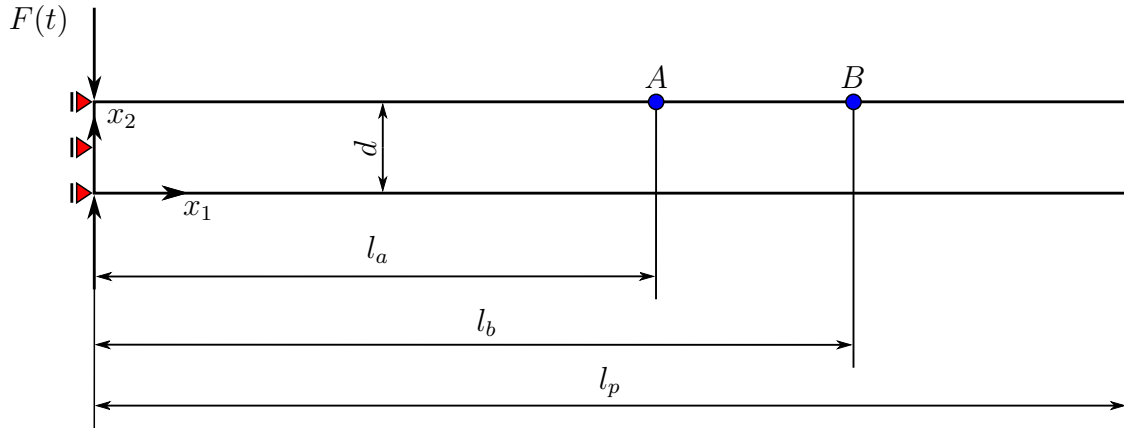


Figure 7.1: Two-dimensional model with loads and boundary conditions for the convergence study. One point force with the time-dependent behavior is employed to excite the structure. The excitation function is given by Eq. (7.1). At the left boundary ($x_1 = 0$), symmetry boundary conditions are applied. The dimensions of the aluminum (see Tab. 2.1) plate are: $l_a = 100$ mm, $l_b = 200$ mm, $l_p = 500$ mm, $d = 2$ mm.

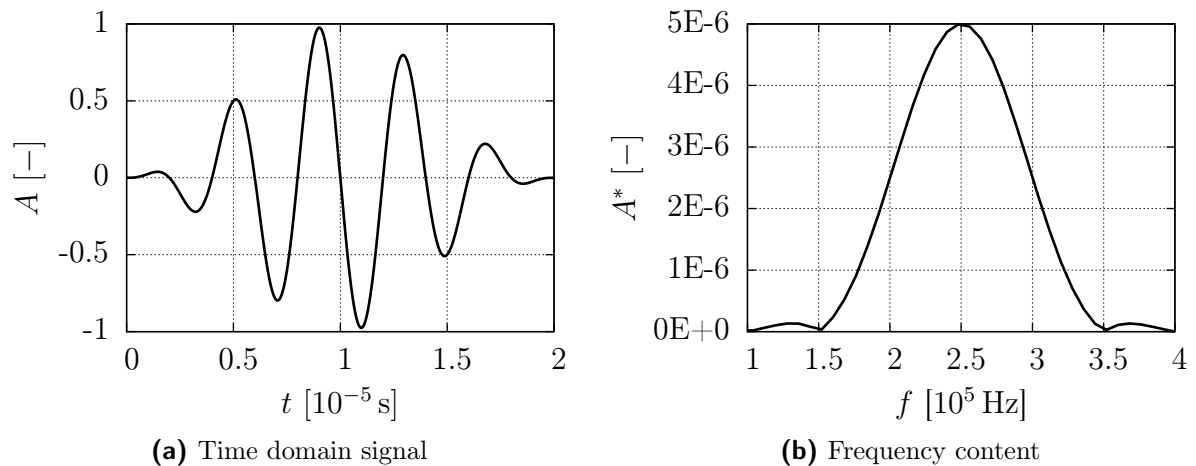


Figure 7.2: Sine-burst ($f_c = 250$ kHz, $n = 5$).

Signal analysis - Hilbert transform

We measure the time-of-flight t_c of the propagating Lamb wave packet between two arbitrary points A and B (Fig. 7.3) to determine the quality of the numerical solution. The

time-of-flight computed using a numerical approach ($t_{c_{num}}$) is compared to the value computed using a reference solution ($t_{c_{ref}}$). In order to extract this value from the FE model or the reference solution, the time signal of the displacement field at the corresponding point (A or B) is subjected to a Hilbert transform [298, 299]

$$H_{A,B}(u(t)) = \frac{1}{\pi} \int_{-\infty}^{\infty} u_{A,B}(\tau) \cdot \frac{1}{t - \tau} d\tau. \quad (7.2)$$

Using the Hilbert transform $H_{A,B}$ of the time-dependent signal $u_{A,B}$, the envelope $e_{A,B}$ of the displacement history is computed [300]. In the next step, we evaluate the time-of-flight by comparing the positions of the centroids of the envelopes of the time signals at these two points. The envelope can be computed deploying the following relation

$$e_{A,B}(t) = \sqrt{H_{A,B}(u_{A,B}(t))^2 + u_{A,B}(t)^2} \quad (7.3)$$

and the coordinate of its centroid is obtained by computing the static moment of the envelope as

$$t_{A,B} = \frac{\int_0^{t_{end}} e_{A,B}(t) \cdot t dt}{\int_0^{t_{end}} e_{A,B}(t) dt}. \quad (7.4)$$

The time-of-flight t_c between points A and B serves as a quality measure for the numerical results. It can be computed as the difference between the propagation times

$$t_c = t_B - t_A. \quad (7.5)$$

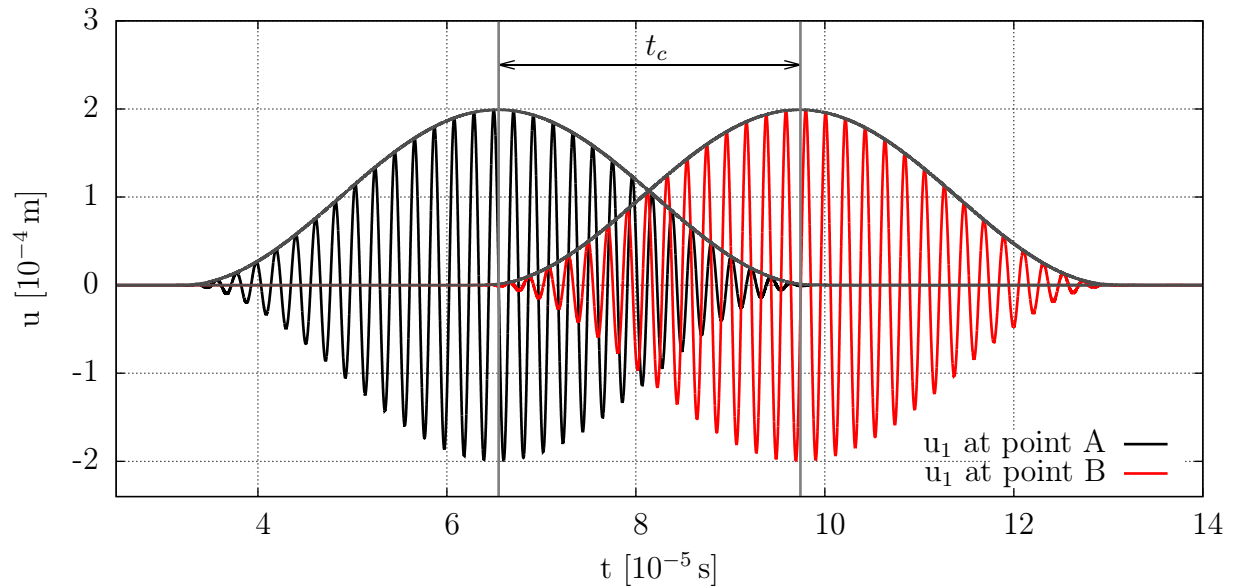


Figure 7.3: Time-of-flight as difference of the centroid of two Hilbert envelopes at point A and B for the S_0 -mode.

Basically, using this methodology, the comparison of the time-of-flights of individual Lamb wave modes equals the evaluation of the resulting group velocities - exactly only for narrow-banded signals.

As a second measure, we compute the area under the envelope A_u of the signal at point A ($u_{A,\text{mag}}$ - magnitude of the displacements at point A) and compare it to the reference value, cf. Fig. 7.4. This indicates whether the amplitude is accurately captured within the simulation interval

$$A_u = \int_t u_{A,\text{mag}}(t) dt. \quad (7.6)$$

The discussed methodology is used throughout the present thesis to investigate the convergence properties of the different numerical approaches. Both the time-of-flight t_c and the area under the displacement history A are assessed. In the present thesis, we compute the reference solution using an analytical approach. Details can be found in references [10] and [87].

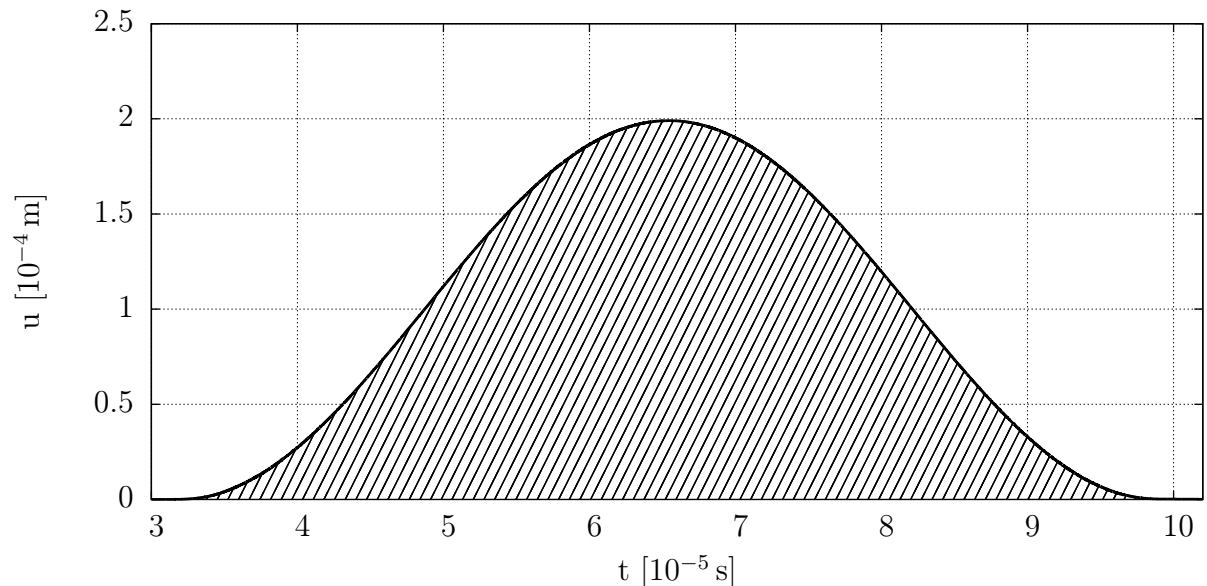


Figure 7.4: Area below the Hilbert envelope of the displacement signal at point A for the S_0 -mode.

In the following sections, we study the convergence behavior of each set of shape functions separately before comparing them to each other. To this end, the polynomial orders in x_1 - (in-plane)- and x_2 - (out-of-plane)-direction are studied independently. Thus, we conduct two different convergence studies.

First convergence study: h -refinement in x_1 -direction First, we assess the discretization in x_1 -direction. The polynomial degree in x_2 -direction is therefore set to $p_{x_2} = 6$ and the structure is discretized deploying one HO -FE over the thickness. In reference [78], it has been found that such a discretization over the thickness of the structure provides highly accurate results. Consequently, the convergence results can be regarded as independent of the discretization in the out-of-plane direction. Thereupon, different numerical

models with varying polynomial orders in the in-plane-direction ($p_{x_1} = 2, 3, 4, 5, 6$) are investigated. For each model, a h -refinement is performed until the results are converged. Convergence is deemed to be achieved when the relative error in the time-of-flight measurement is below 1%. Admittedly, the error threshold is a somewhat arbitrary value and can also be chosen differently depending on the intended applications. In reference [39], it has been demonstrated that even small differences in the time-of-flight potentially lead to severe problems in the damage detection process. This is also the reason for choosing a fairly small error threshold - despite other uncertainties in real-life structures (geometry, material properties e.g.).

The number of nodes/modes per anti-symmetric wavelength serves as a dimensionless of the discretization. For numerical models (using a structured/regular grid), the number of nodes/modes per anti-symmetric wavelength χ_{A_0} is given as

$$\chi_{A_0} = \frac{n_{dof}}{2(p_{x_2} + 1)l_p} \cdot \lambda_{A_0} \quad (7.7)$$

where p_{x_2} denotes the polynomial degree in x_2 -direction, l_p is the length of the plate and λ_{A_0} represents the wavelength of the fundamental anti-symmetric Lamb wave mode - at the center frequency f_c of the excitation signal. Since the anti-symmetric mode has a shorter wavelength, it is the more critical mode from a modeling point of view - its resolution demands a smaller element size. Therefore, λ_{A_0} is the reference value for the wavelength. The relative error is determined by comparing the numerical to the reference solution. This can be expressed as

$$E_{rel} = \frac{|a_{ref} - a_{num,type}|}{|a_{ref}|} \cdot 100 \text{ [%]}. \quad (7.8)$$

In this case, a depicts either the time-of-flight t_c or the area beneath the envelope of the time signal A .

Second convergence study: p -refinement in x_2 -direction After having assessed the discretization in the in-plane-direction the polynomial degree in the out-of-plane-direction is studied. Willberg *et al.* [78] were able to show that for $p_{x_2} = 6$ and $\chi_{A_0} \geq 20$ the results are highly accurate. Accordingly, we choose the element size in such a way that it corresponds to more than 35 nodes/modes per wavelength in x_1 -direction, while the polynomial order p_{x_1} is fixed to 8. This procedure ensures that the second study only focuses on the convergence behavior with respect to the out-of-plane discretization. For this purpose, a p -refinement is conducted for the out-of-plane polynomial degree p_{x_2} and it is varied between 2 and 8. The evaluation of the simulation results follows the methodology discussed above (Paragraph Signal analysis - Hilbert transform).

The results of both convergence studies (h -refinement in x_1 -direction and p -refinement in x_2 -direction) are then used to determine the optimal polynomial degree template and the appropriate value for χ_{A_0} . The proposed guidelines will lead to accurate wave propagation results.

Accordingly, the following three sections are devoted to studying the convergence behavior of:

1. the SEM (Section 7.2),

2. the p -version of the FEM (Section 7.3),
3. the Fourier- p -version of the FEM (Section 7.4).

Concerning the SEM, the performance of different lumping techniques is of special interest. Studying their behavior will help us to decide whether a diagonalization of the mass matrix is an advantageous approach for wave propagation analysis.

In the case of the p -FEM and the Fourier- p -FEM, we investigate the impact of using either the tensor product space or the trunk space on the numerical results.

Thereafter, the best schemes for each set of Ansatz functions using the “optimal” polynomial degree template are compared to one another in Section 7.5.

7.2 Convergence behavior of the spectral element method

Basically, there are two different types of time-integration techniques: (i) explicit methods and (ii) implicit methods. A representative of each class was discussed in Sections 4.3.2 and 4.3.3, respectively. Assuming a consistent mass matrix formulation is employed, a system of equations needs to be solved for every time-step in either of the two methods (cf. Eqs. (4.76) and (4.86)). If, however, both the mass matrix \mathbf{M}_{uu} and the damping matrix \mathbf{R}_{uu} are diagonal matrices, the CDM only requires matrix-vector-operations in each time-step. An explicit time-stepping algorithm can therefore be regarded as one key component of an efficient simulation tool for ultrasonic guided wave analysis. Thus, different mass-lumping techniques for the SEM and their performances are of particular interest. Moreover, according to Dauksher and Emery [151–153], implicit time-stepping algorithms fail to provide any advantages over explicit ones when wave propagation problems are considered. Although implicit schemes are unconditionally stable, the time-step is nonetheless restricted by several factors such as the frequency content of the signal and the accuracy requirements for example. The highest frequency of interest should be resolved with at least 20 sampling points per period [211]

$$\Delta t \leq \frac{1}{20}T. \quad (7.9)$$

Δt denotes the time-step and T is the period time. Pertaining to the accuracy of implicit time-marching schemes, Dauksher and Emery [151–153] found that the time-step of an implicit method must be less than that used in explicit analysis. Generally speaking, the time-step for an explicit method should be selected in such a way that the wave does not travel one element width in one time-step. According to the Courant-Friedrichs-Levy (CFL; [301]) condition, a sufficient time step would be

$$\Delta t = \frac{b_e}{c_g}. \quad (7.10)$$

For typical guided wave propagation analysis (concerning an aluminum plate in this case), the element size b_e is in the range of a few millimeters, while the group velocities of the fundamental modes are $c_{g,S_0} \approx 5414$ m/s and $c_{g,A_0} \approx 2900$ m/s. Accordingly, the time-step Δt should be less than approximately $1 \cdot 10^{-8}$ s. This is within the range of an explicit central difference time integration scheme.

The results obtained by Dauksher and Emery, mentioned in the previous paragraphs, justify a more detailed investigation of the SEM with a consistent or diagonal mass matrix. To this end, the simulation results obtained using the SEM with a consistent mass matrix formulation are compared to three different formulations employing lumped mass matrices. The three different methods to diagonalize the mass matrix in the context of nodal-based shape functions are:

1. the Gauß-Lobatto-Legendre quadrature (cf. Section 4.6.1),
2. the row-sum technique (cf. Section 4.6.2),
3. the HRZ algorithm (cf. Section 4.6.3).

We employ the same time-integration algorithm for every simulation in order to facilitate the comparability between the different *HO*-FE schemes. For that reason, we solve the equations of motion using the Newmark method.

7.2.1 *h*-Refinement in x_1 -direction

The model set-up and the strategy to evaluate the results have already been explained in Section 7.1. Therefore, only the convergence graphs are shown at this point, cf. Figs. 7.5 and 7.6. The results of the convergence studies are obtained using a uniform *h*-refinement. Figs. 7.5 and 7.6 display the relative error in the time-of-flight or the area below the envelope versus the number nodes per anti-symmetric wavelength χ_{A_0} . Each sub-figure represents the convergence results for a fixed polynomial degree in the in-plane direction (x_1). It should be noted that the results of the proposed lumping techniques are virtually coincidental. There are no noticeable differences in the convergence behavior concerning the individual diagonalized mass matrix SEM approaches.

In reference [152], Dauksher and Emery already pointed out that a row-summing procedure can result in accurate solutions with SEs using a CGL nodal distribution. They were able to show that the solution characteristics of SEs based on a Chebyshev grid are only negligibly affected by the diagonalization [151, 152]. Additional insights are that an increased polynomial order moderates the effects of lumping and that no negative diagonal terms are generated. These properties are confirmed for SEs based on a GLL grid, cf. Figs. 7.5 and 7.6. Moreover, Dauksher and Emery claim that - for a given accuracy - their results indicate that explicit spectral solutions require fewer nodes per wavelength than comparable consistent mass matrix solutions [151]. Our results confirm these findings of Dauksher and Emery [151, 152] and highlight the fact that the different lumping techniques essentially produce very similar results. Generally speaking, we found that the relative error converges faster to zero with an increasing FE shape function order - and a finer grid resolution also serves to reduce the error in the time-of-flight.

The main conclusion that should be drawn considering the presented results is that none of the lumping techniques applied to the SEM causes deteriorated results in this particular example. The advantages of a diagonal mass matrix can consequently be exploited for wave propagation analysis using the SEM.

The peaks that are observed in the convergence graphs are explained in detail in Section 7.8. There, we found that this behavior can be attributed to eigenfrequencies on the element level.

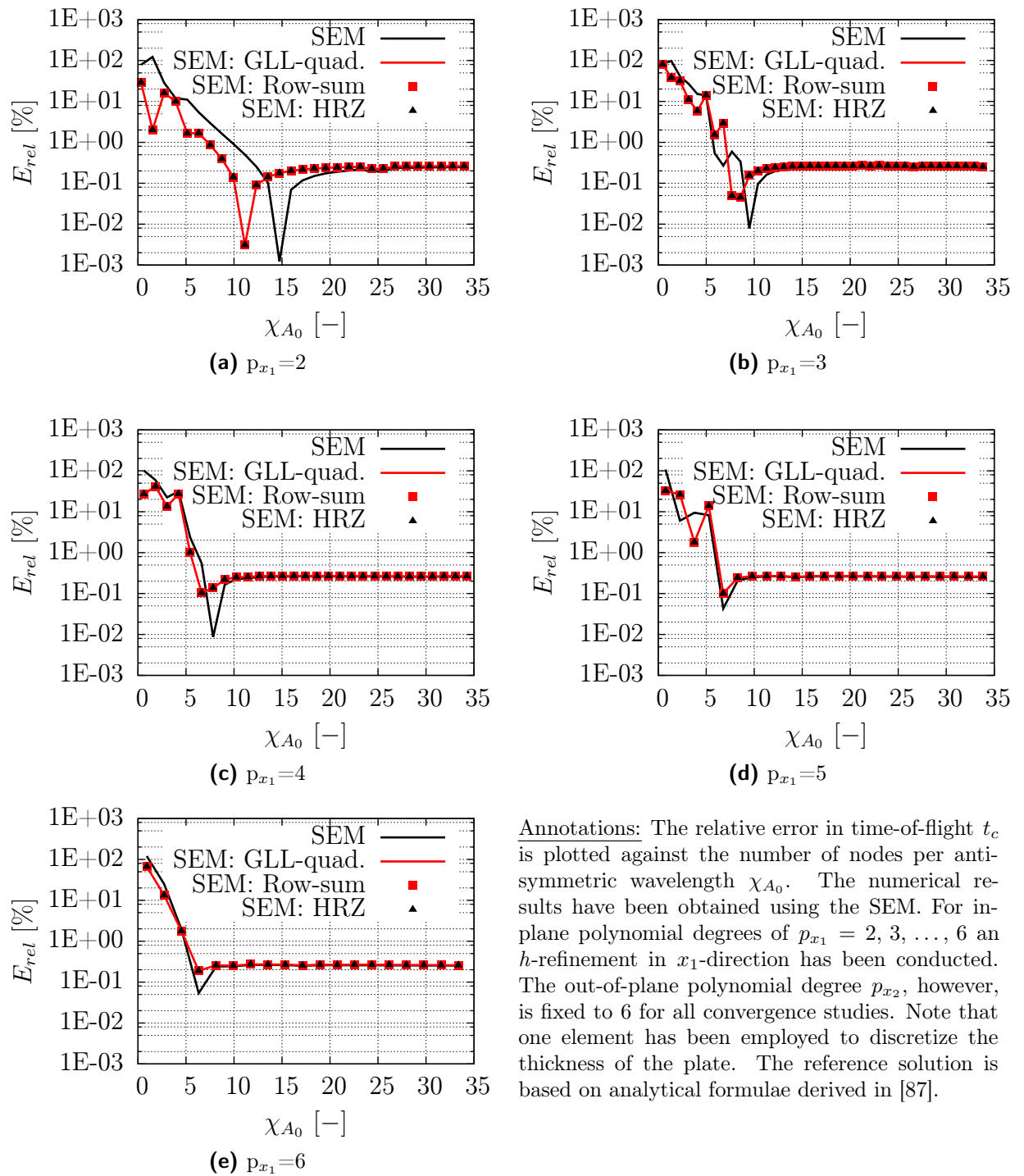
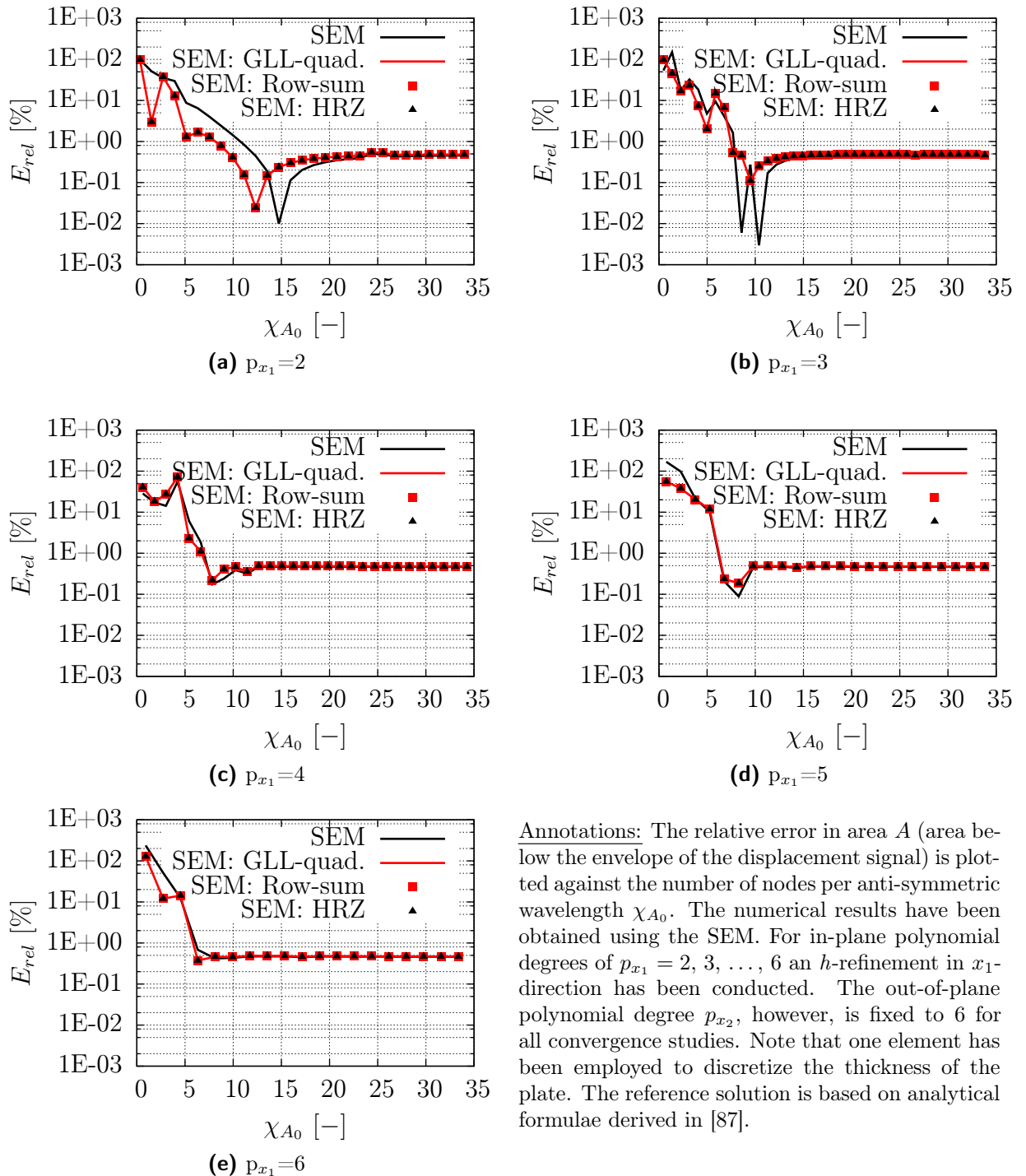


Figure 7.5: Convergence curves for the wave propagation analysis for the numerical model of a two-dimensional aluminum plate.

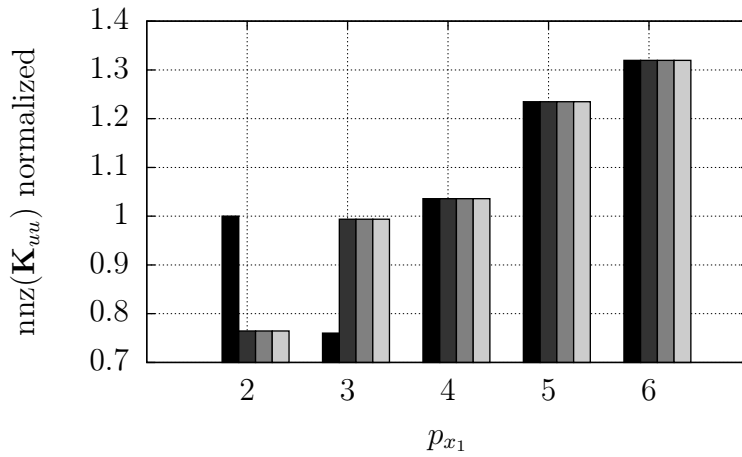
To judge the numerical performance of the different SE-approaches, the number of non-zero components (nnz) within the global stiffness matrix $\text{nnz}(\mathbf{K}_{uu})$ and the global mass matrix $\text{nnz}(\mathbf{M}_{uu})$ are considered - as a means to describe the memory requirement (RAM) of the personal computer being used to run the simulations. Furthermore, we monitor the computational time t_{cpu} , needed for the solution of the equations of motion. As the

software implementation of the different sets of shape functions is not equally optimized in our in-house *HO*-FE program, this seems to be an appropriate value. From an engineering point of view, an error threshold of 1 % is sufficient, at least according to our opinion. Thus, we record the memory requirements and the computational time for those simulations that reach the threshold first.

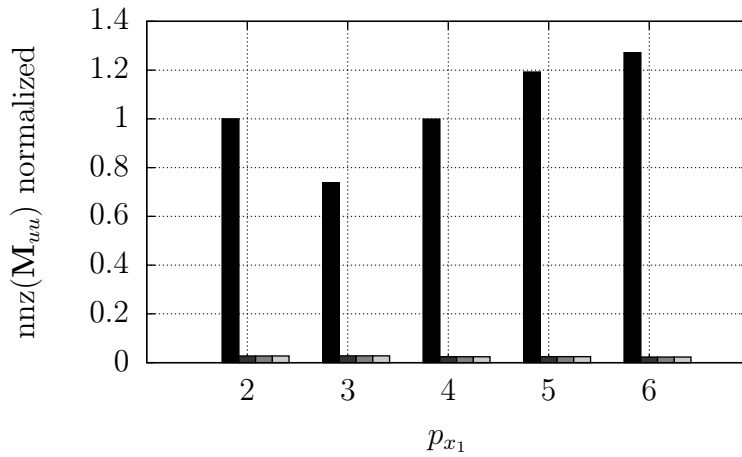


Annotations: The relative error in area A (area below the envelope of the displacement signal) is plotted against the number of nodes per anti-symmetric wavelength χ_{A_0} . The numerical results have been obtained using the SEM. For in-plane polynomial degrees of $p_{x_1} = 2, 3, \dots, 6$ an h -refinement in x_1 -direction has been conducted. The out-of-plane polynomial degree p_{x_2} , however, is fixed to 6 for all convergence studies. Note that one element has been employed to discretize the thickness of the plate. The reference solution is based on analytical formulae derived in [87].

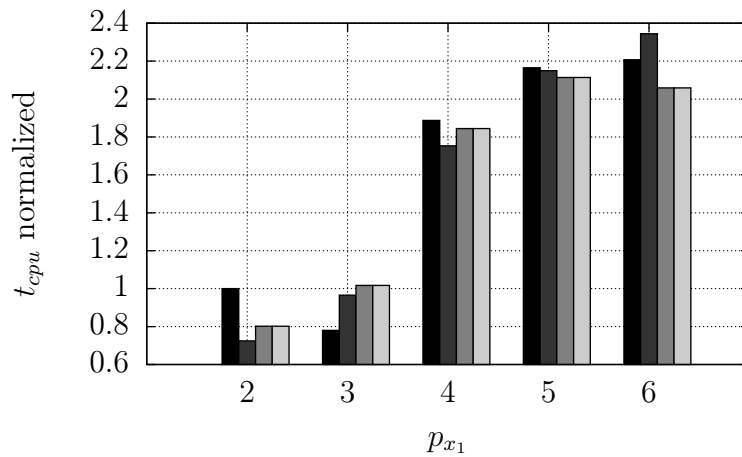
Figure 7.6: Convergence curves for the wave propagation analysis for the numerical model of a two-dimensional aluminum plate.



(a) Number of non-zero components in the global stiffness matrix \mathbf{K}_{uu}



(b) Number of non-zero components in the global mass matrix \mathbf{M}_{uu}



(c) Computational time for the solution of the equation of motion using the Newmark method

Annotations: The Newmark method is used as an implicit time-integration algorithm. The results are assessed at a relative error in time-of-flight of $E_{rel} = 1\%$. All values are normalized to the simulation results obtained using the in-plane polynomial degree $p_{x_1} = 2$. The out-of-plane polynomial degree p_{x_2} is fixed to 6 for all convergence studies.

Figure 7.7: Comparison of the performance of different SE-schemes. The methods are evaluated concerning their memory requirements (number of non-zero components in the system matrices - nnz) and the computational time needed for the time-integration of the equations of motion.

Initially, we note that all approaches reach an acceptable accuracy with considerably less than 20 nodes per wavelength, typically mentioned in current literature [76, 77]. The evaluation of the performance with respect to the memory requirements and the computational time is shown in Fig. 7.7. All results are normalized with respect to the solution for $p_{x_1} = 2$. From the bar graphs, it is apparent that for the SEM deploying a **consistent mass matrix** formulation $p_{x_1} = 3$ is the “optimal” choice, whereas $p_{x_1} = 2$ displays the best performance if a **diagonalized mass matrix** is used. With regard to the overall behavior, the **SEM deploying a GLL nodal quadrature** can be recommended. The most significant benefit is gained in terms of the computational-time, cf. Fig. 7.7c, while the memory requirements for the stiffness matrix are approximately equal. Naturally, a lumped mass matrix will serve to decrease the memory requirements for storing the global mass matrix significantly.

7.2.2 p -Refinement in x_2 -direction

While the previous subsection focused on determining the optimal polynomial order in the in-plane direction, the same is now implemented for the out-of-plane direction. The results of the p -refinement procedure are displayed in Figs. 7.8a and 7.8b.

Regarding the accuracy, we note that the different SE-schemes reach the same relative error. The optimal polynomial order in out-of-plane direction can be chosen as $p_{x_2} = 3$ or $p_{x_2} = 4$. Simulations employing both values results in a relative error of less than 1%. However, as the error reaches a constant plateau at $p_{x_2} = 4$, the solution is deemed to be converged. This value is consequently chosen as the optimal order in the out-of-plane direction.

Accordingly, the following passage proposes a guideline on how to choose an appropriate discretization (for wave propagation analysis):

1. Choose the polynomial degree in the in-plane direction to be:
 - a) $p_{x_1} = 3$ for the SEM deploying a consistent mass matrix formulation.
 - b) $p_{x_1} = 2$ for the SEM deploying a lumped mass matrix formulation.
2. Choose the polynomial degree in out-of-plane direction to be $p_{x_2} = 4$ for all SE-approaches.
3. Choose the number of nodes per wavelength to be:
 - a) $\chi_{A_0} = 7$ if an error threshold of 1% should be reached for the SEM deploying a consistent mass matrix formulation.
 - b) $\chi_{A_0} = 8$ if an error threshold of 1% should be reached for the SEM deploying a lumped mass matrix formulation.

In case a lower threshold is desired, the number of nodes per wavelength has to be adjusted according to results depicted in Figs. 7.5 and 7.6.

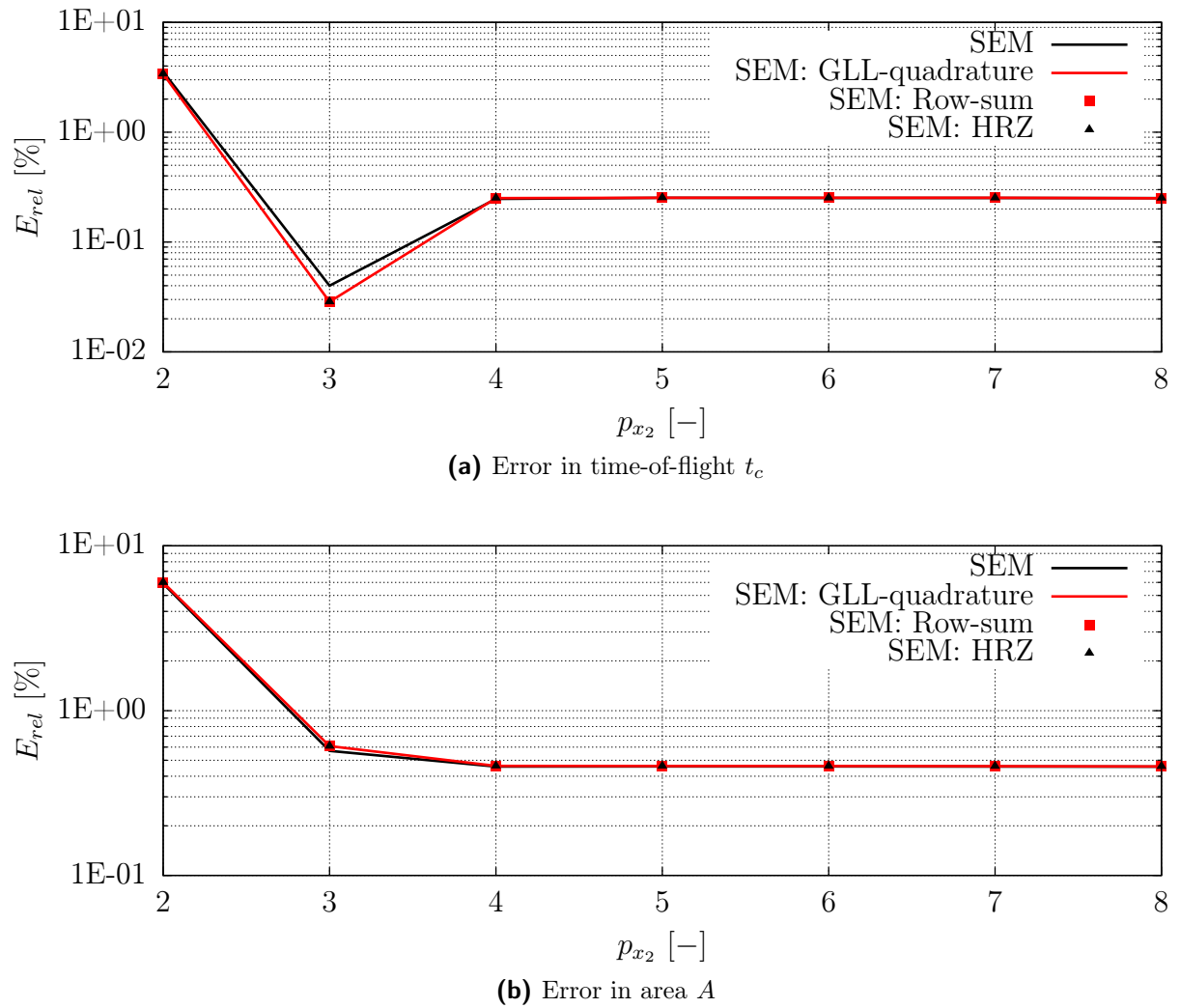


Figure 7.8: Convergence curves for the wave propagation analysis for the numerical model of a two-dimensional aluminum plate. The relative error in (a) time-of-flight t_c and (b) area A (area below the envelope of the displacement signal) is plotted against the out-of-plane polynomial degree p_{x_2} . The numerical results have been obtained using the SEM. A p -refinement in x_2 -direction has been conducted. The in-plane polynomial degree p_{x_1} , however, is fixed to 8 for all convergence studies. A discretization employing $\chi_{A_0} > 35$ nodes per anti-symmetric wavelength is used in the in-plane direction. Note that one element has been employed to discretize the thickness of the plate. The reference solution is based on analytical formulae derived in [87].

7.3 Convergence behavior of the p -version of the finite element method

In this section, we compare the computational efficiency of the trunk space and the tensor product space applied for the p -version of the FEM. The possibility to employ these different Ansatz spaces is straightforwardly given for hierarchic shape functions. The per-

performances of the p -version of the FEM and the Fourier- p -FEM are therefore investigated in the following two sections, respectively.

7.3.1 h -Refinement in x_1 -direction

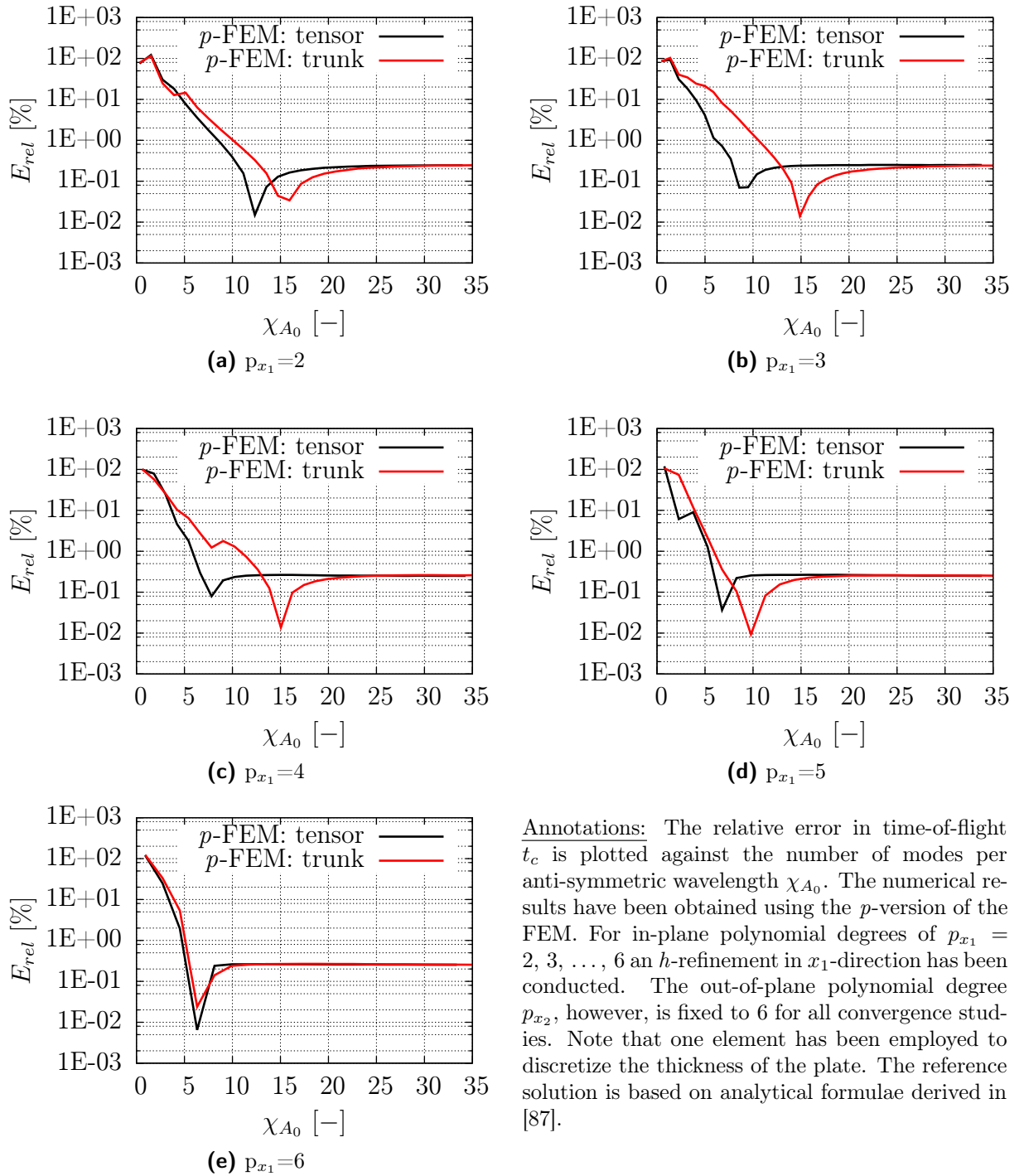


Figure 7.9: Convergence curves for the wave propagation analysis for the numerical model of a two-dimensional aluminum plate.

The convergence behavior exhibited by the p -version FEs is in principle similar to the one described in Section 7.2. All statements given there are still valid for a hierarchic set of shape functions.

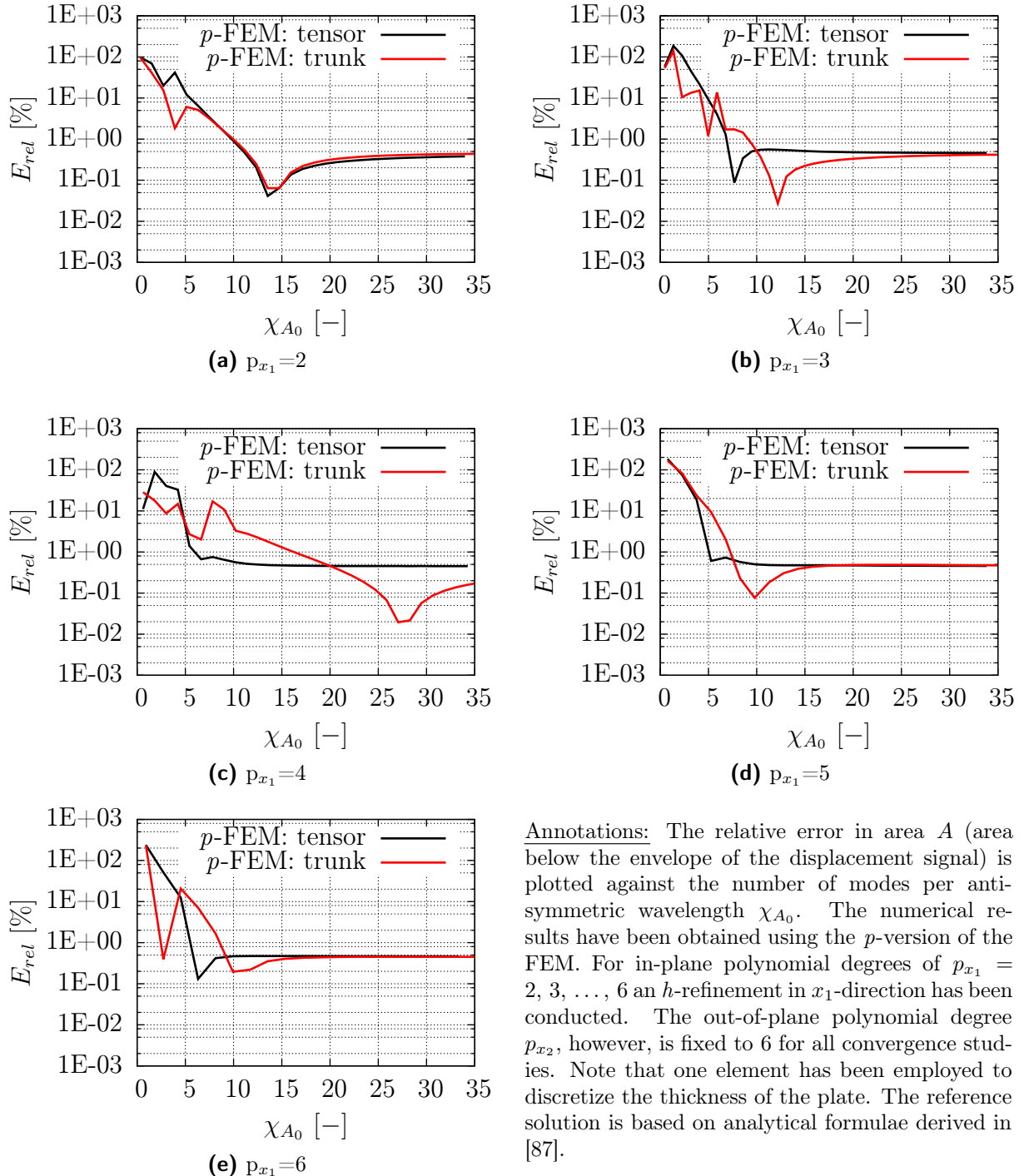


Figure 7.10: Convergence curves for the wave propagation analysis for the numerical model of a two-dimensional aluminum plate.

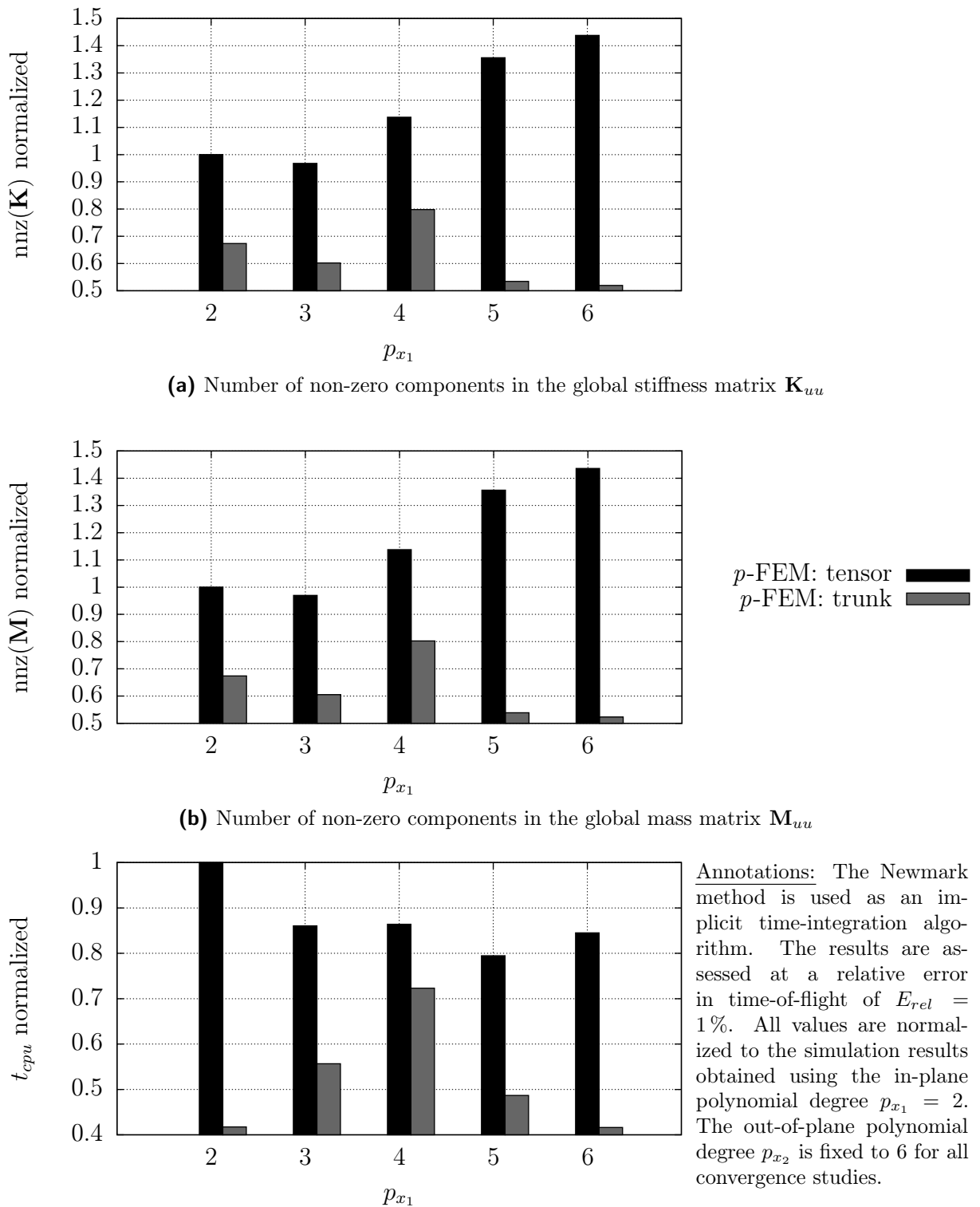


Figure 7.11: Comparison of the performance of different Ansatz spaces for the p -version of the FEM. The methods are evaluated concerning their memory requirements (number of non-zero components in the system matrices - nnz) and the computational time needed for the time-integration of equations of motion.

It can be noted, however, that the accuracy when reaching the constant error plateau is slightly improved compared to the SEM for this particular example. Yet, it can be generally expected that all polynomial-based *HO*-FE approaches deliver a similar accuracy.

Although the number of modes per wavelength (the term *modes* is used to replace the word *nodes* as the unknowns do not actually correspond to physical degrees-of-freedom) may be the same for the tensor product space and the trunk space, the number of degrees-of-freedom can be significantly different. The procedure outlined in the previous section will also serve to assess the performance of the different Ansatz spaces.

Fig. 7.11 summarizes the results for the memory requirements and the computational time. Depending on whether the computational time or the memory requirements seem more important, different optimal polynomial orders can be chosen for p -FEM. For the **trunk space**, the bar graphs (cf. Fig. 7.11) clearly indicate that $p_{x_1} = 6$ is the optimal in-plane polynomial degree for this particular wave propagation problem. For the **tensor product space**, however, there are two possible choices. In case a higher importance is ascribed to the memory requirement, the optimal polynomial order in the in-plane direction is $p_{x_1} = 3$. If, however, the computational time is seen as more important, $p_{x_1} = 5$ can be chosen for the tensor product space. Due to the fact that available physical memory tends to be limited, we decide to settle on $p_{x_1} = 3$.

Since less degrees-of-freedom are needed for the trunk space formulation, the computational time is shorter as well. Thus, we recommend to choose the **trunk space** instead of the tensor product space for the p -version of the FEM.

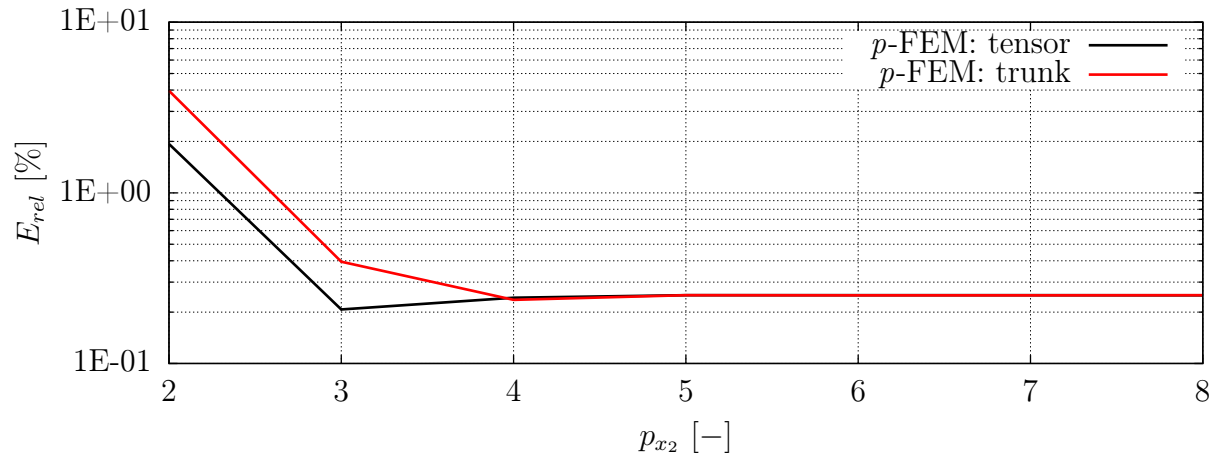
7.3.2 p -Refinement in x_2 -direction

As a next step, we conduct a p -refinement in order to determine the out-of-plane polynomial degree. Qualitatively the same behavior is seen - compare Figs. 7.8 and 7.12 - as already described in the previous section. The optimal polynomial order in out-of-plane direction can be chosen as $p_{x_2} = 3$ or $p_{x_2} = 4$. Simulations employing both values results in a relative error of less than 1%. However, as the error reaches a constant plateau at $p_{x_2} = 4$, the solution is deemed to be converged - which is why this value is chosen.

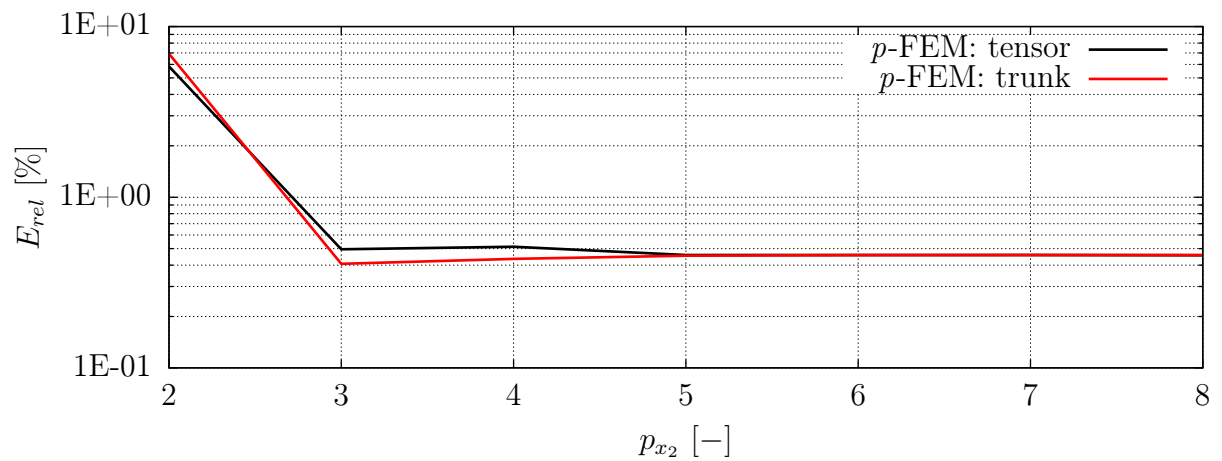
Accordingly, the following passage proposes a guideline on how to choose an appropriate discretization (for wave propagation analysis):

1. Choose the polynomial degree in the in-plane direction to be
 - a) $p_{x_1} = 3$ for the tensor product space version of the p -FEM.
 - b) $p_{x_1} = 6$ for the trunk space version of the p -FEM.
2. Choose the polynomial degree in out-of-plane direction to be $p_{x_2} = 4$ for both versions of p -FEM.
3. Choose the number of modes per wavelength to be:
 - a) $\chi_{A_0} = 6$ if an error threshold of 1% should be reached for the p -FEM deploying a tensor product space formulation.
 - b) $\chi_{A_0} = 5$ if an error threshold of 1% should be reached for the p -FEM deploying a trunk space formulation.

For calculations demanding a higher accuracy, the number of modes per wavelength can be adjusted accordingly, cf. Fig. 7.10.



(a) Error in time-of-flight t_c



(b) Error in area A

Figure 7.12: Convergence curves for the wave propagation analysis for the numerical model of a two-dimensional aluminum plate. The relative error in (a) time-of-flight t_c and (b) area A (area below the envelope of the displacement signal) is plotted against the out-of-plane polynomial degree p_{x_2} . The numerical results have been obtained using the p -version of the FEM. A p -refinement in x_2 -direction has been conducted. The in-plane polynomial degree p_{x_1} , however, is fixed to 8 for all convergence studies. A discretization employing $\chi_{A_0} > 35$ nodes per anti-symmetric wavelength is used in the in-plane direction. Note that one element has been employed to discretize the thickness of the plate. The reference solution is based on analytical formulae derived in [87].

7.4 Convergence behavior of the Fourier- p -version of the finite element method

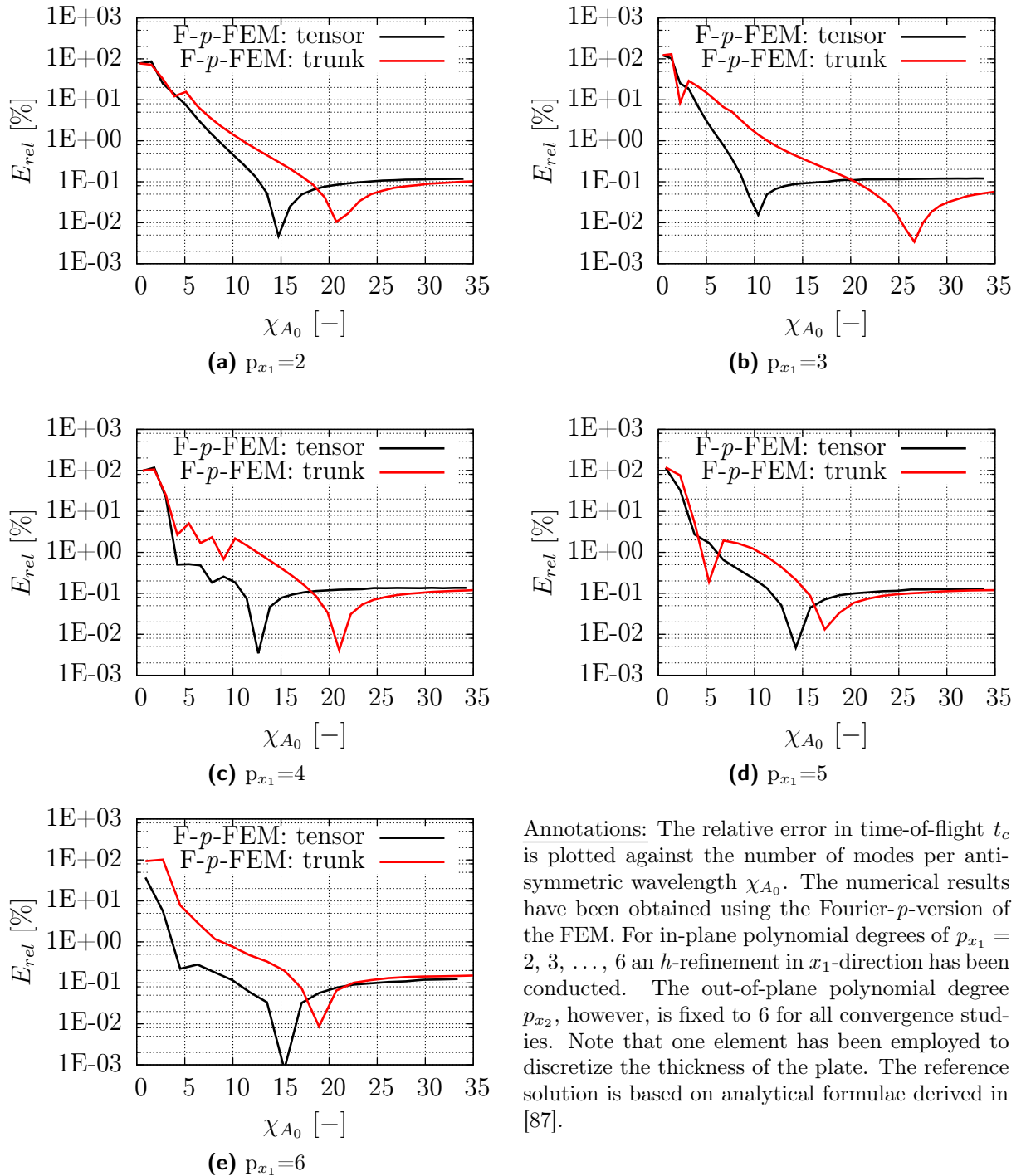


Figure 7.13: Convergence curves for the wave propagation analysis for the numerical model of a two-dimensional aluminum plate.

Concerning the Fourier- p -FEM we can also decide whether to employ the tensor product space or the trunk space. Accordingly, the convergence behavior of those two spaces is investigated in the following.

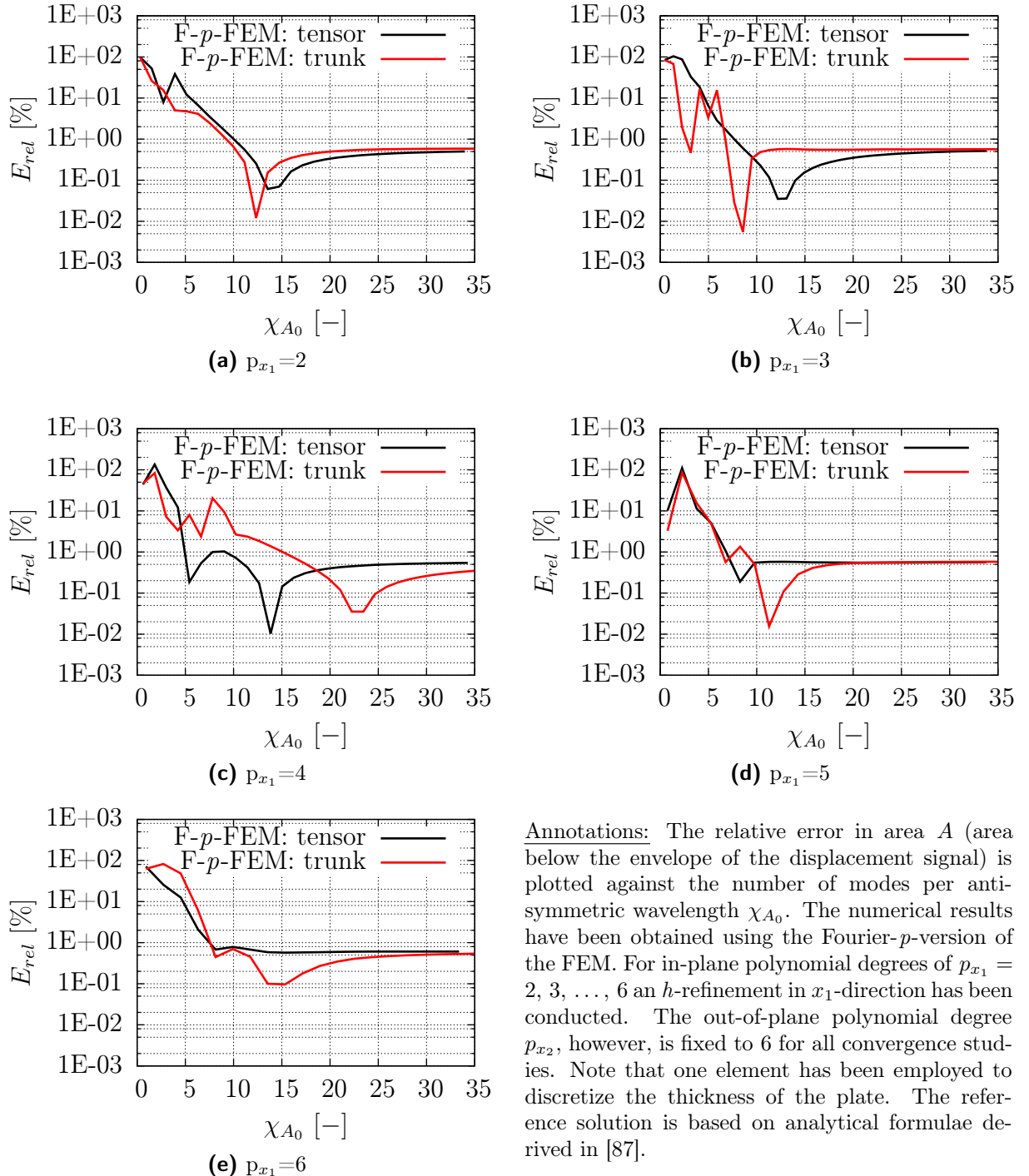
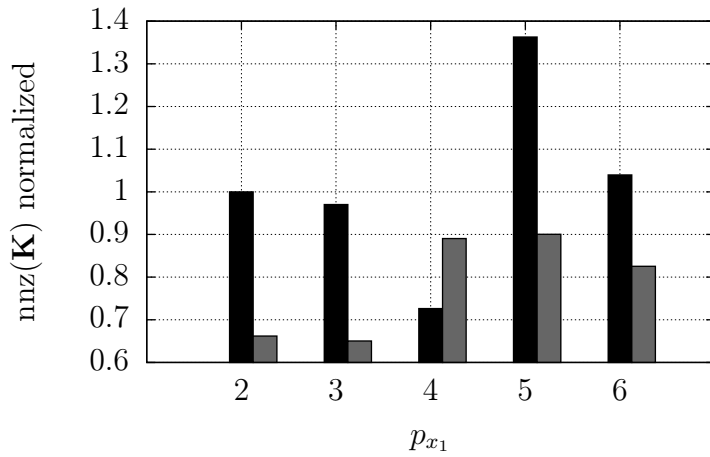
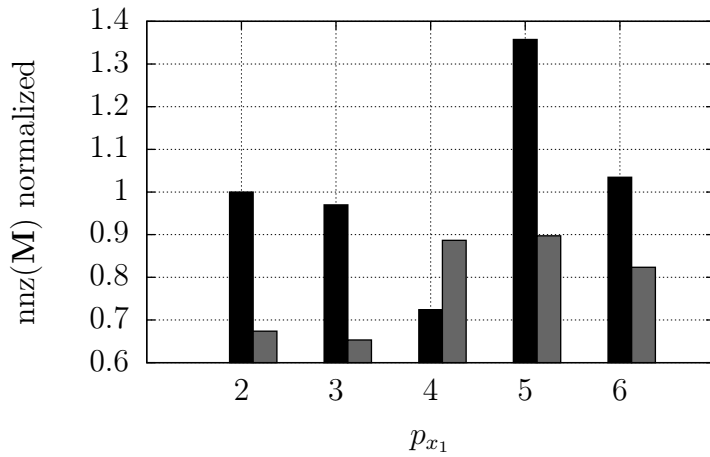


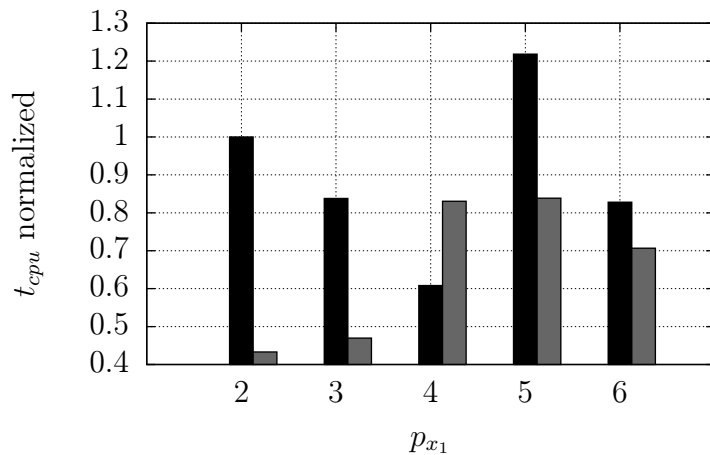
Figure 7.14: Convergence curves for the wave propagation analysis for the numerical model of a two-dimensional aluminum plate.



(a) Number of non-zero components in the global stiffness matrix \mathbf{K}_{uu}



(b) Number of non-zero components in the global mass matrix \mathbf{M}_{uu}



(c) Computational time for the solution of the equation of motion using the Newmark method

Annotations: The Newmark method is used as an implicit time-integration algorithm. The results are assessed at a relative error in time-of-flight of $E_{rel} = 1\%$. All values are normalized to the simulation results obtained using the in-plane polynomial degree $p_{x_1} = 2$. The out-of-plane polynomial degree p_{x_2} is fixed to 6 for all convergence studies.

Figure 7.15: Comparison of the performance of different Ansatz spaces for the Fourier- p -version of the FEM. The methods are evaluated concerning their memory requirements (number of non-zero components in the system matrices - nnz) and the computational time needed for the time-integration of equations of motion.

7.4.1 h -Refinement in x_1 -direction

Overall, the convergence behavior displays a similar tendency as discussed in the previous sections. It has to be mentioned however that the results obtained using the trigonometric shape functions yield the most accurate results of the tested sets of shape functions, cf. Figs. 7.13 and 7.14, at least for this particular example. The reason could be that sine-functions are natural solutions to wave equations. As discussed in Section 7.3 the trunk space offers advantages in terms of numerical efficiency.

We consult the bar graphs displayed in Fig.7.15 to determine the optimal polynomial order in the in-plane direction. There, the memory storage requirements and the computational time for the time-marching scheme are illustrated. Depending on whether the memory requirement or the computational time is seen as more important, the optimal polynomial degree in the in-plane direction is $p_{x_1} = 2$ or 3 when dealing with the **trunk space** formulation. Due to the fact that available physical memory tends to be limited, we decide to settle on $p_{x_1} = 3$. In case the **tensor product space** formulation is used, $p_{x_1} = 4$ is clearly advantageous. A comparison of the memory requirements and the computational time leads to the conclusion that that the trunk space formulation is more efficient, which is why the application of the **trunk space** is recommended for this example.

7.4.2 p -Refinement in x_2 -direction

The result of this p -refinement - to determine the out-of-plane polynomial order - is different to the ones depicted in the previous two sections. The optimal polynomial order in out-of-plane direction can be chosen as $p_{x_2} \geq 5$. Simulations employing these values results in a relative error of less than 1% in both the time-of-flight and in the area. At $p_{x_2} = 5$ the error, however, has reached a constant plateau for the time-of-flight, cf. Fig. 7.16a. This value is consequently chosen as optimal order in x_2 -direction.

Accordingly, the following passage proposes a guideline on how to choose an appropriate discretization (for wave propagation analysis):

1. Choose the polynomial degree in the in-plane direction to be:
 - a) $p_{x_1} = 4$ for the Fourier- p -FEM deploying a tensor product space formulation.
 - b) $p_{x_1} = 3$ for the Fourier- p -FEM method deploying a trunk space formulation.
2. Choose the polynomial degree in out-of-plane direction to be $p_{x_2} = 5$ for both approaches.
3. Choose the number of modes per wavelength to be:
 - a) $\chi_{A_0} = 4$ if an error threshold of 1% should be reached for the Fourier- p -FEM deploying a tensor product space formulation.
 - b) $\chi_{A_0} = 11$ if an error threshold of 1% should be reached for the Fourier- p -FEM deploying a trunk space formulation.

In case a lower threshold is desired, the number of modes per wavelength have to be adjusted according to results depicted in Fig. 7.13.

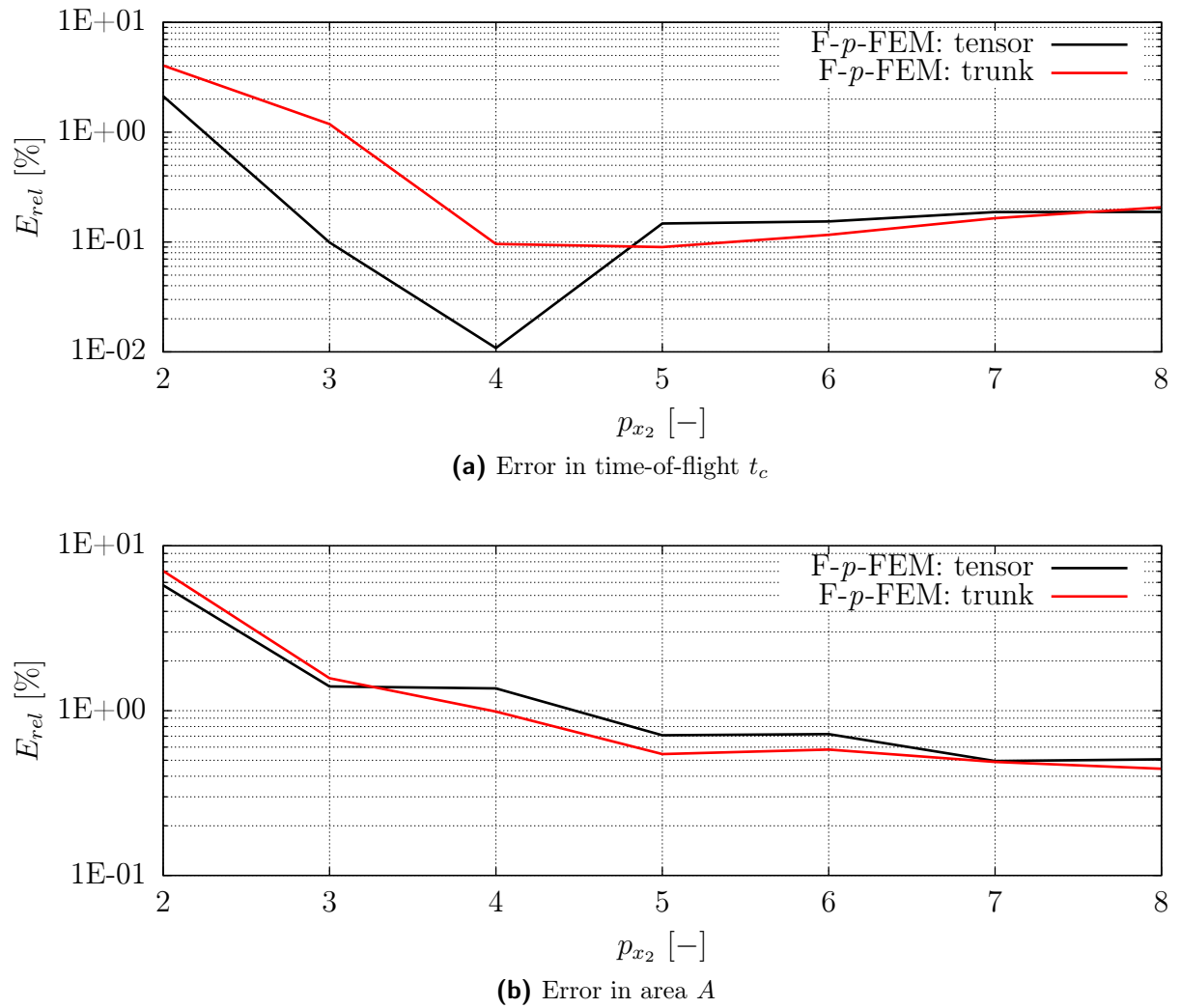


Figure 7.16: Convergence curves for the wave propagation analysis for the numerical model of a two-dimensional aluminum plate. The relative error in (a) time-of-flight t_c and (b) area A (area below the envelope of the displacement signal) is plotted against the out-of-plane polynomial degree p_{x_2} . The numerical results have been obtained using the Fourier- p -version of the FEM. A p -refinement in x_2 -direction has been conducted. The in-plane polynomial degree p_{x_1} , however, is fixed to 8 for all convergence studies. A discretization employing $\chi_{A_0} > 35$ nodes per anti-symmetric wavelength is used in the in-plane direction. Note that one element has been employed to discretize the thickness of the plate. The reference solution is based on analytical formulae derived in [87].

7.5 Comparison of different higher order finite element approaches

The polynomial degree templates for the different HO -FE approaches (Sections 7.2 to 7.4) are listed in Tab. 7.1. The most efficient representatives of each HO -FEM are highlighted in boldface font.

Table 7.1: Optimal polynomial degree templates for wave propagation analysis using different *HO*-FE schemes. The methods highlighted using a boldface font are the most efficient schemes for the different shape functions.

Higher order method	In-plane polynomial degree (p_{x_1})	Out-of-plane polynomial degree (p_{x_2})
SEM	3	4
SEM: GLL quadrature	2	4
SEM: Row-sum	2	4
SEM: HRZ	2	4
<i>p</i> -FEM: tensor	3	4
<i>p</i>-FEM: trunk	6	4
Fourier- <i>p</i> -FEM: tensor	4	5
Fourier-<i>p</i>-FEM: trunk	3	5

Regarding the SEM, we can infer from Fig. 7.7 that a lumped mass matrix formulation employing the GLL-quadrature rule is, at least for our example, the most efficient version. Both the memory storage requirement and the computational time are minimal.

Concerning the *p*-version of the FEM we recommend the trunk space formulation over the tensor product space one, cf. Fig. 7.11. In this particular case, the memory requirements as well as the computational time are minimized too. The same applies for the Fourier-*p*-FEM, cf. Fig. 7.15.

In the current section, these “optimal” approaches are compared with each other. The *h*-refinement methodology is therefore applied to the optimal polynomial degree templates listed in Tab. 7.1. Using this discretization, convergence curves are recorded and evaluated as described in the previous sections. The results serve as a basis of commendation concerning a suitable numerical tool for the simulation of ultrasonic guided waves.

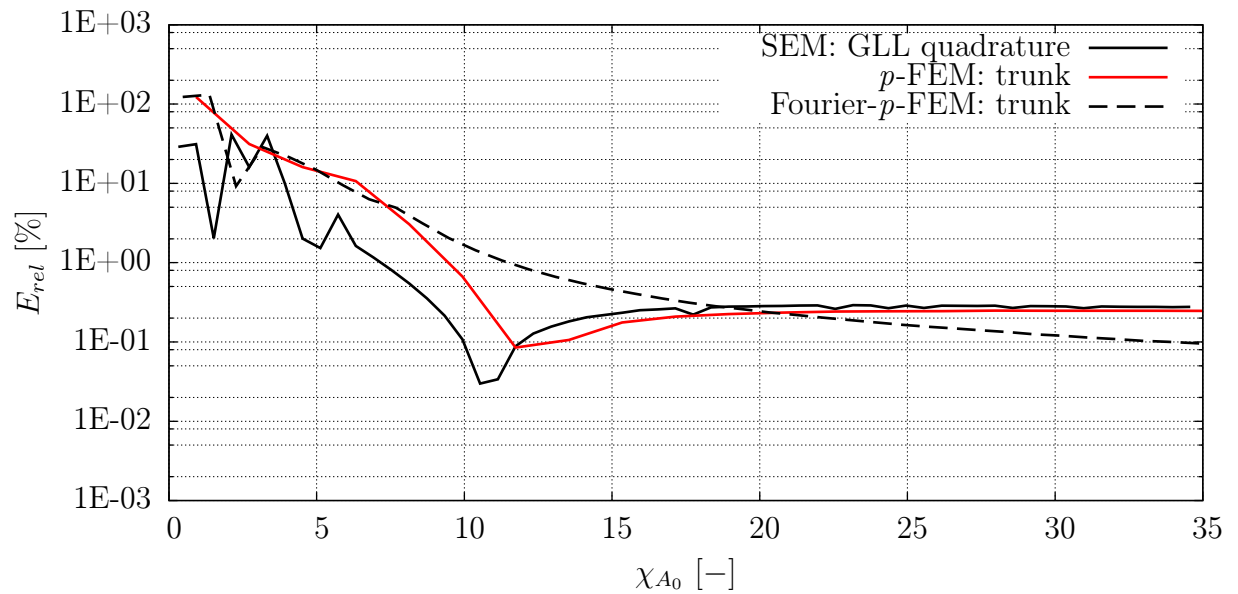
7.5.1 *h*-Refinement in x_1 -direction

The results of the convergence curves clearly indicate that the same level of accuracy can be reached with all different higher order schemes, cf. Figs. 7.17a and 7.17b. The differences in the convergence rates can be attributed to the different polynomial degree distributions. The elevated rate of the Fourier-*p*-FEM is a result of the increased polynomial degree in the out-of-plane direction in comparison to the other two approaches.

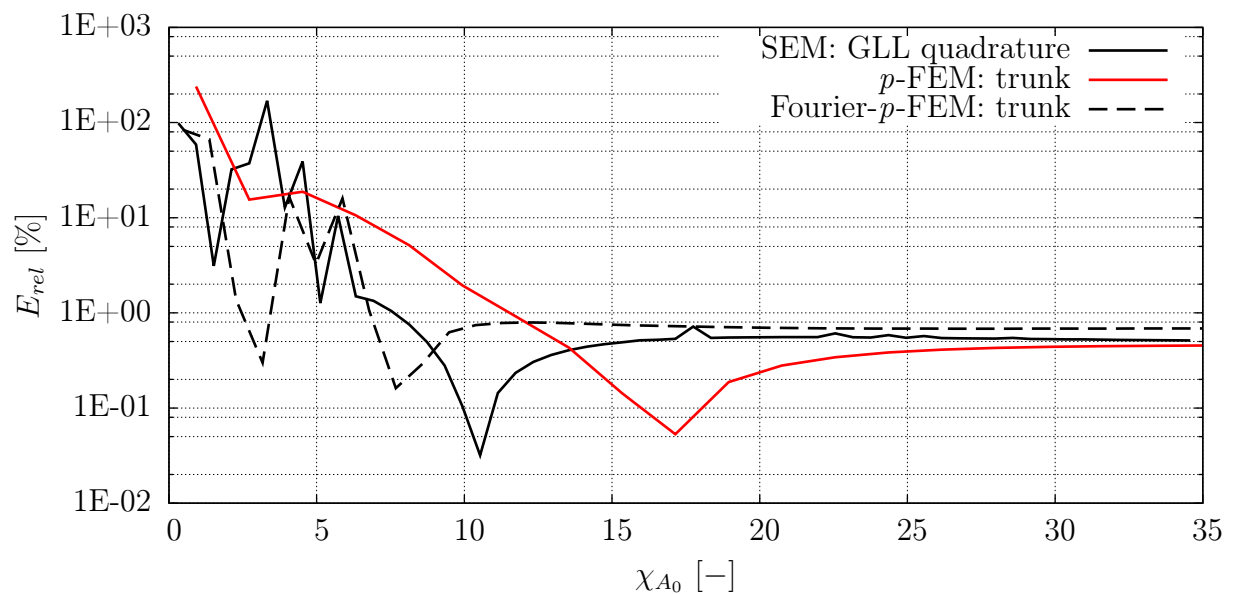
The error threshold of 1% is chosen again to assess the performance in terms of memory requirements and computational time. The results are illustrated in Fig. 7.18. Overall, we recommend the SEM in connection with a nodal GLL quadrature rule.

Due to the diagonal mass matrix, the memory requirements are similar for all three higher order schemes. The advantages in computational time are crucial. Keeping in mind that all simulations have been run using an implicit time-marching scheme, the displayed advantage of the SEM is much more significant in case the central difference algorithm is applied as time-integration algorithm. In summary, we infer from the presented results that the most efficient simulation regarding ultrasonic guided wave propagation problems is achieved by applying the SEM in conjunction with a Lobatto-integration. The optimal polynomial

degree distribution for this method has been found to be $p_{x_1} = 2$ (in-plane polynomial order) and $p_{x_2} = 4$ (out-of-plane polynomial order).



(a) Error in time-of-flight t_c



(b) Error in area A

Figure 7.17: Convergence curves for the wave propagation analysis for the numerical model of a two-dimensional aluminum plate. The relative error in (a) time-of-flight t_c and (b) area A (area below the envelope of the displacement signal) is plotted against the number of nodes/modes per anti-symmetric wavelength χ_{A_0} . The numerical results have been obtained using the different HO -FEMs deploying their respective optimal polynomial degree distribution, cf. Tab. 7.1. An h -refinement in x_1 -direction has been conducted. Note that one element has been employed to discretize the thickness of the plate. The reference solution is based on analytical formulae derived in [87].

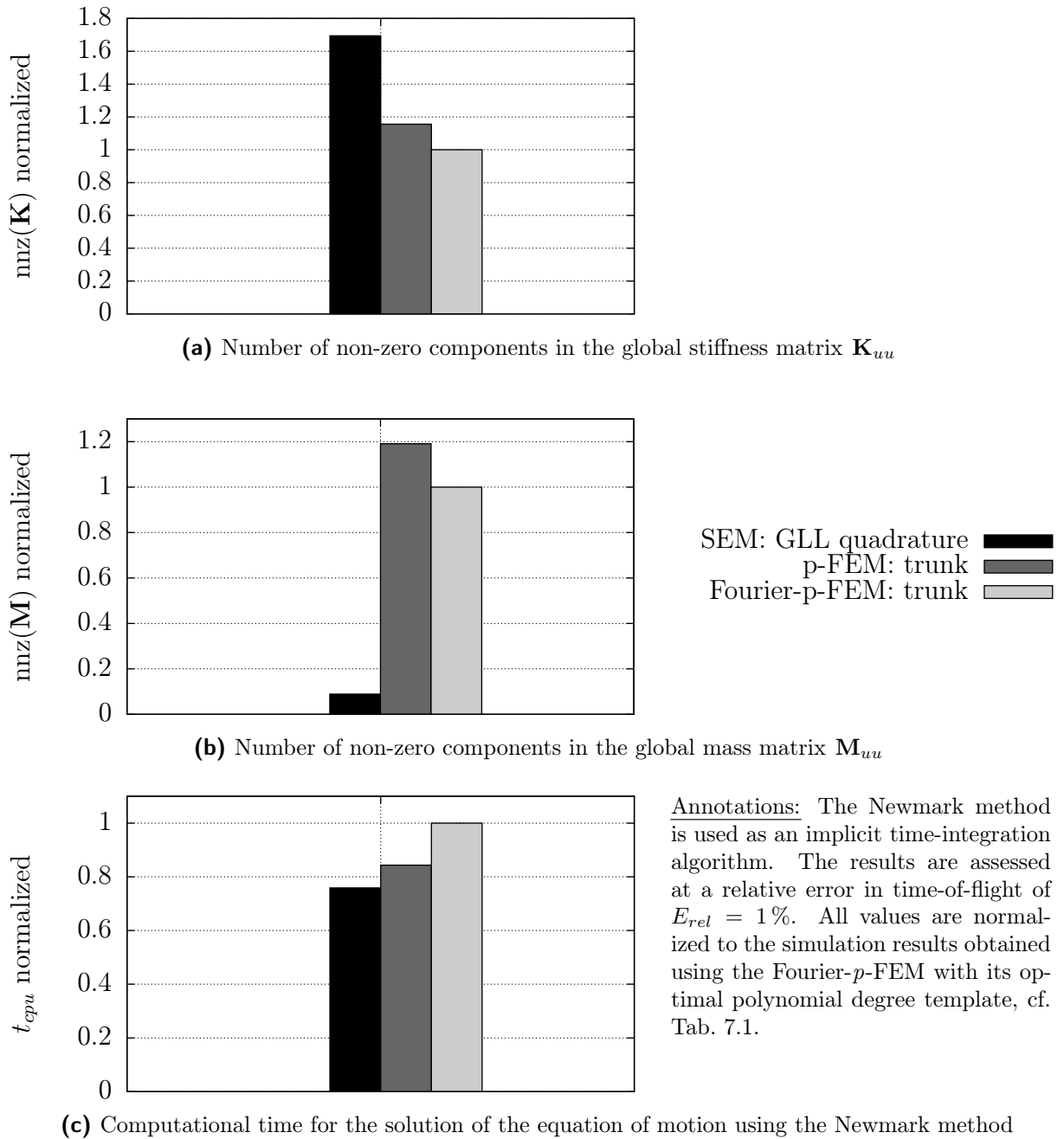


Figure 7.18: Comparison of the performance of the different HO -FE schemes. The methods are evaluated concerning their memory requirements (number of non-zero components in the system matrices - nnz) and the computational time needed for the time-integration of equations of motion.

Using the proposed discretization set-up will result in sufficiently accurate simulations with minimal RAM and computational time requirements. The peaks that can be observed in Fig. 7.17 are studied in detail in Section 7.8

7.6 Influence of the time-step width Δt

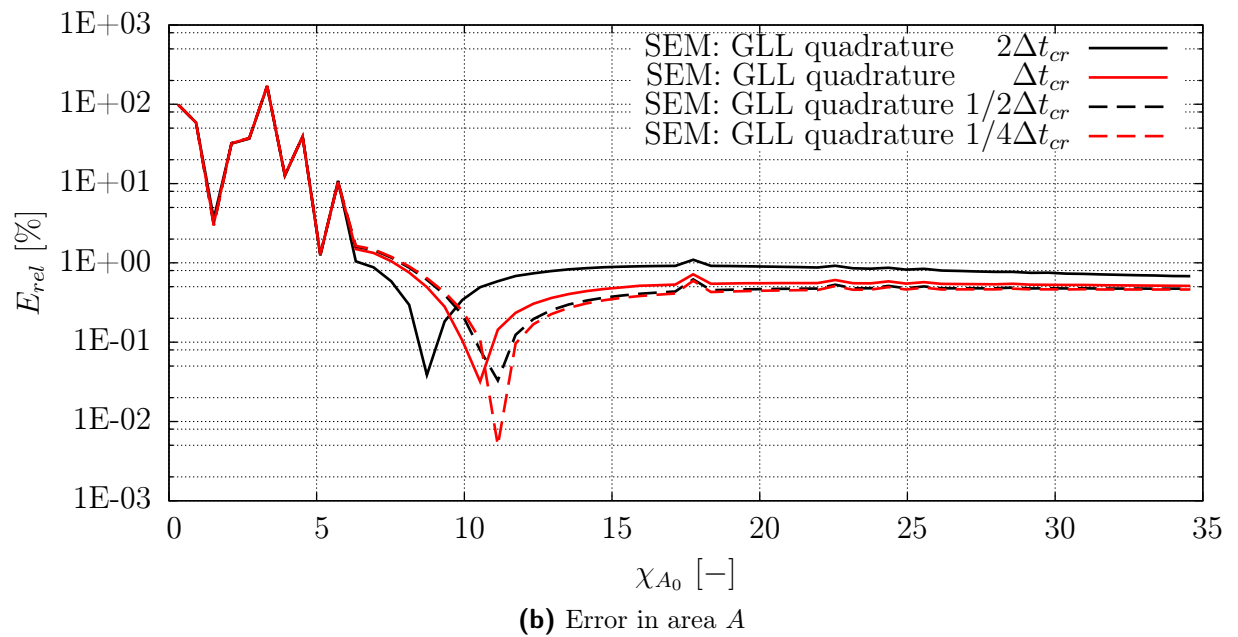
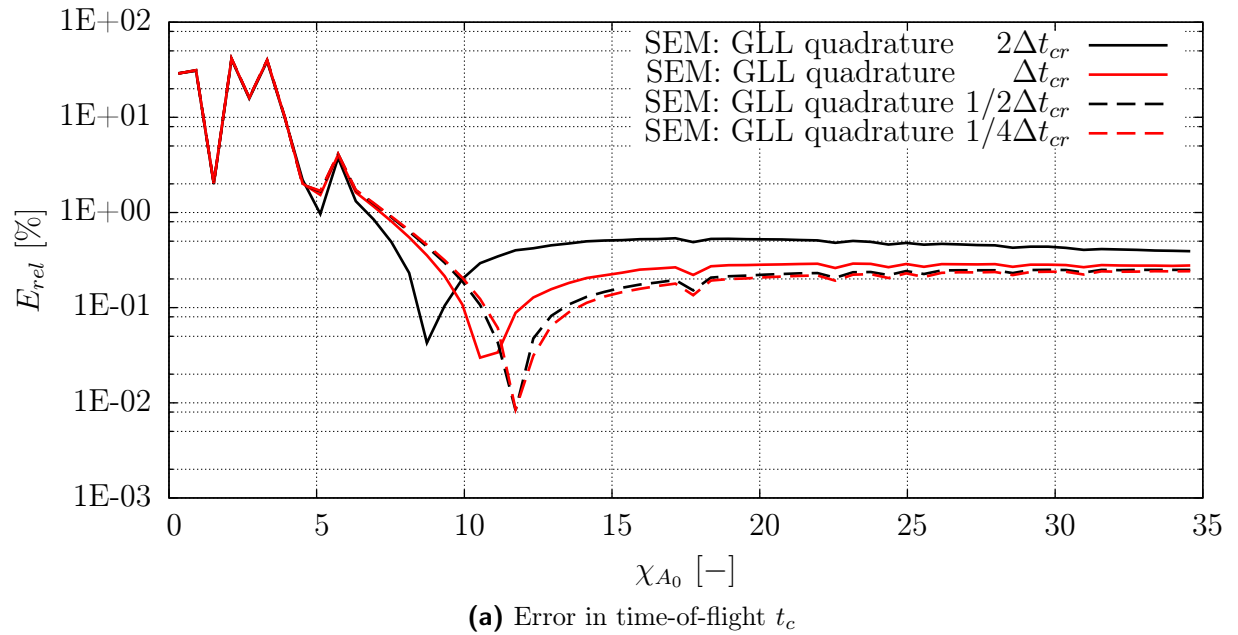


Figure 7.19: Convergence curves for the wave propagation analysis for the numerical model of a two-dimensional aluminum plate. The relative error in (a) time-of-flight t_c and (b) area A (area below the envelope of the displacement signal) is plotted against the number of nodes per anti-symmetric wavelength χ_{A_0} . The numerical results have been obtained using the SEM deploying its optimal polynomial degree distribution, cf. Tab. 7.1. An h -refinement in x_1 -direction has been conducted. Note that one element has been employed to discretize the thickness of the plate. The time-step of the time-integration scheme is varied to study its effect on the accuracy of the solution. The reference solution is based on analytical formulae derived in [87].

When unconditionally stable time-integration methods are used for the solution of the semi-discrete equations of motion, the time-step Δt plays an important role. Its significance is comparable to that of the element size for the spatial discretization. A closer look is therefore taken at Δt . In the present chapter, all simulation results have been obtained using the Newmark method (Section 4.3.3) as solver. This method is a representative of implicit, unconditionally stable time-stepping schemes. The time-step width has therefore been estimated using the critical time-step of the CDM (Section 4.3.2), cf. Eq. (4.77). For the sake of clarity, the expression to determine the critical time-step Δt_{cr} is given again at this point

$$\Delta t \leq \frac{2}{\omega_{max}} = \Delta t_{cr}.$$

To highlight the influence of Δt , we re-calculate the convergence curves for the SEM using the optimal polynomial degree template, a GLL quadrature rule and different time steps. We have to keep in mind, however, that the critical time-step is estimated for each simulation individually. For every new discretization, the system matrices are generated and the highest eigenfrequency of the system is estimated. This value is then used to determine the critical time-step size Δt_{cr} . Next, this time-step is multiplied by 2, 1, 1/2 and 1/4, respectively and simulations are conducted for each of these time-step sizes. Employing this methodology will serve to assess the influence of the time-step size.

Figs. 7.19a and 7.19b illustrate the evolution of the results depending on the time-step size Δt . The results clearly indicate that the time-step used in the present chapter ($\Delta t = \Delta t_{cr}$) is appropriate for an accurate simulation of wave propagation problems. Increasing the time-step beyond the stability limit of the central difference algorithm will result in a decreased accuracy of the displacement field. Nonetheless, the results still reach an acceptable level of accuracy. Decreasing the time-step size further does not lead to significant improvements in accuracy. It is therefore concluded that Δt based on Eq. (4.77) is an appropriate choice and provides the desired accuracy. Depending on the task, the results in Figs. 7.19a and 7.19b show that the time-step size can also be increased if a lower level of accuracy is acceptable.

7.7 Influence of the chosen signal processing method: Continuous wavelet transform

The main goal of any signal processing procedure is to extract specific information from a given function. To this end, the signal is transformed in a suitable manner in order to facilitate the acquisition of information. Which type of transform is used strongly depends on the investigated problem. In the thesis at hand, the Hilbert-transform has so far been deployed. In this section, we introduce the continuous wavelet transform (CWT) - to ensure that the results are not dependent on the applied method. The results of the CWT contain time-variant information of the received signal [39, 302].

The computation of the wavelet coefficients C is done by scaling and translating the basis function (mother wavelet) Ψ

$$C(a, b, f(t), \Psi(t)) = \int_{-\infty}^{\infty} f(t) \frac{1}{\sqrt{a}} \Psi^* \left(\frac{t-b}{a} \right) dt \quad (7.11)$$

where $()^*$ indicates the complex conjugate. The choice of the scale a , the position b and the wavelet Ψ affects the computation of the coefficients.

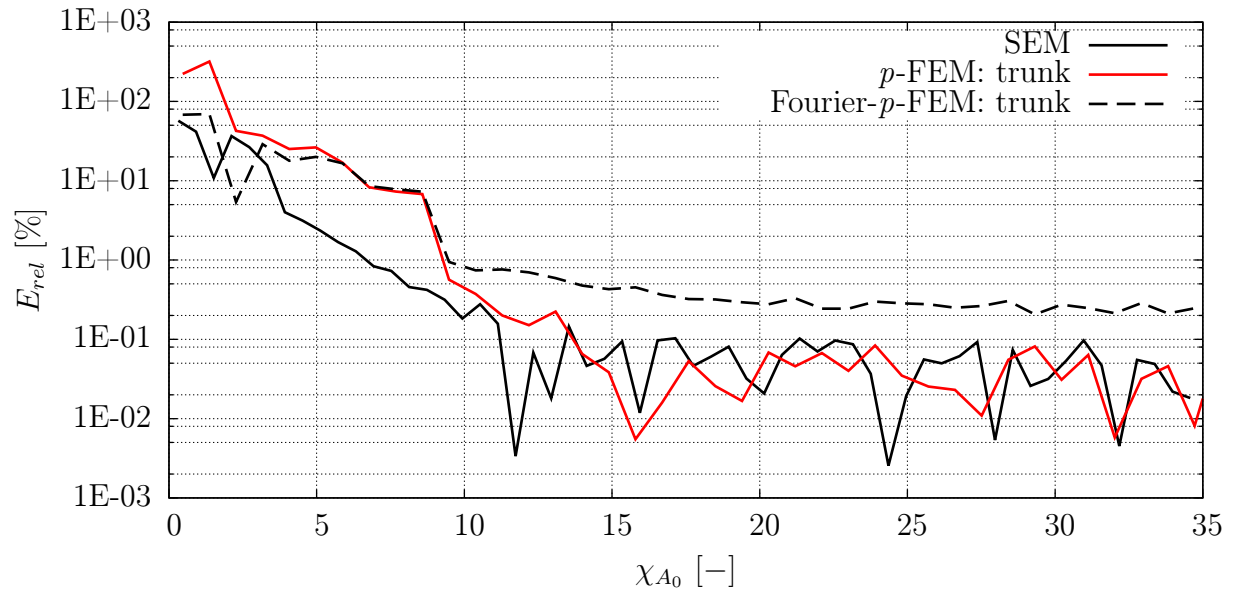


Figure 7.20: Convergence curves for the wave propagation analysis for the numerical model of a two-dimensional aluminum plate. The relative error in time-of-flight t_c is plotted against the number of nodes/modes per anti-symmetric wavelength χ_{A_0} . The numerical results have been obtained using the different *HO-FEMs* deploying their respective optimal polynomial degree distribution, cf. Tab. 7.1. An h -refinement in x_1 -direction has been conducted. Note that one element has been employed to discretize the thickness of the plate. The reference solution is based on analytical formulae derived in [87] - the continuous wavelet transform is applied.

The literature provides several admissible wavelets. Different basis functions will appear to be suitable, depending on the signal features that are to be extracted. Morlet or Daubechies wavelets are widely used in signal processing for wave propagation analysis [303–305]. The ‘db10’ wavelet was chosen for the subsequent signal analysis because recent publications found it to perform well regarding the measurement of the time-of-flight [306, 307].

The results of the convergence study concerning the optimal polynomial degree distribution (cf. Section 7.5) are re-computed using the continuous wavelet transform, cf. Fig. 7.20. This illustrates the fact that the convergence properties are independent of the method employed to evaluate the accuracy, if applied in a suitable manner.

The convergence characteristics are qualitatively similar to the results of the Hilbert-transform - and the accuracy is in the same range too. All conclusions drawn from the previous convergence studies are therefore still valid. The oscillatory trend of the graphs is due to the sampling rate. Since only 1000 time-steps are saved, small changes in the numerical time-of-flight can result in identifiable peaks.

7.8 Convergence disturbance

During the investigation of the convergence behavior of different *HO*-FEMs distinct peaks in the convergence curves have been observed, cf. Figs. 7.24a and 7.24b. Similar observations are also mentioned in articles in which the behavior of the S_0 - and A_0 -modes was studied separately [78, 308]. In the present section, we address the reasons for their occurrence in detail. By identifying the source of these anomalies in the results, measures to avoid their excitation can be taken [183, 309].

7.8.1 Numerical model

For the sake of simplicity, the two-dimensional plane strain model (described in Section 7.1) is adjusted in which a mono-modal excitation is favored. This technique allows us to study the properties and the behavior of symmetric and anti-symmetric Lamb waves separately. To this end, the excitation of the wave field is conducted using a pair of collocated point forces, cf. Fig. 7.21. This makes it easier to interpret the signal.

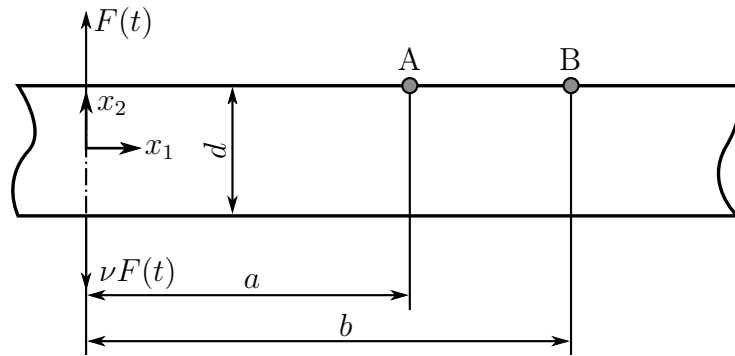


Figure 7.21: Two-dimensional (plane strain) model for wave propagation analysis. Due to an excitation using two collocated point forces only a single Lamb wave mode can be excited - either S_i - ($\nu = 1$; symmetric modes) or A_i -modes ($\nu = -1$; anti-symmetric modes).

Additional changes include the excitation function in order to demonstrate that this effect is not dependent on the frequency itself nor on the number of cycles within the signal. Based on this model, we propose a guideline on how to determine the element size according to the chosen polynomial degree distribution. The plate length is chosen in such a way that reflections from the right boundary do not interfere with the signals measured at the evaluation points A and B during the simulation time. The spatial discretization is characterized by the polynomial degree of the shape functions in propagation direction p_{x_1} , the polynomial degree in thickness direction p_{x_2} and the element width b_e . As before, the simulation results are evaluated using the procedure explained in Section 7.1.

For the sake of clarity, the dispersion diagram for aluminum is given at this point, cf. Fig. 7.23. The dashed vertical line marks the chosen excitation frequency $f_c = 477645$ Hz. Considering the fundamental symmetric Lamb mode (S_0), the excitation frequency is in a region where the dispersion is minimized. Additionally, a suitable number of cycles of the Hann function - cf. Eq. (7.1) - is chosen to provide for a narrow frequency bandwidth and thus to assure that the main part of the energy is concentrated around the center

frequency in the main lobe ($n = 32$). With this new set-up, an h -refinement as illustrated in Section 7.2 is conducted. Again the number of nodes/modes per wavelength (χ_{S_0/A_0}) is chosen as a dimensionless parameter to describe the discretization of the numerical model

$$\chi_{S_0/A_0} = \frac{p_{x_1}}{b_e} \lambda_{S_0/A_0}. \quad (7.12)$$

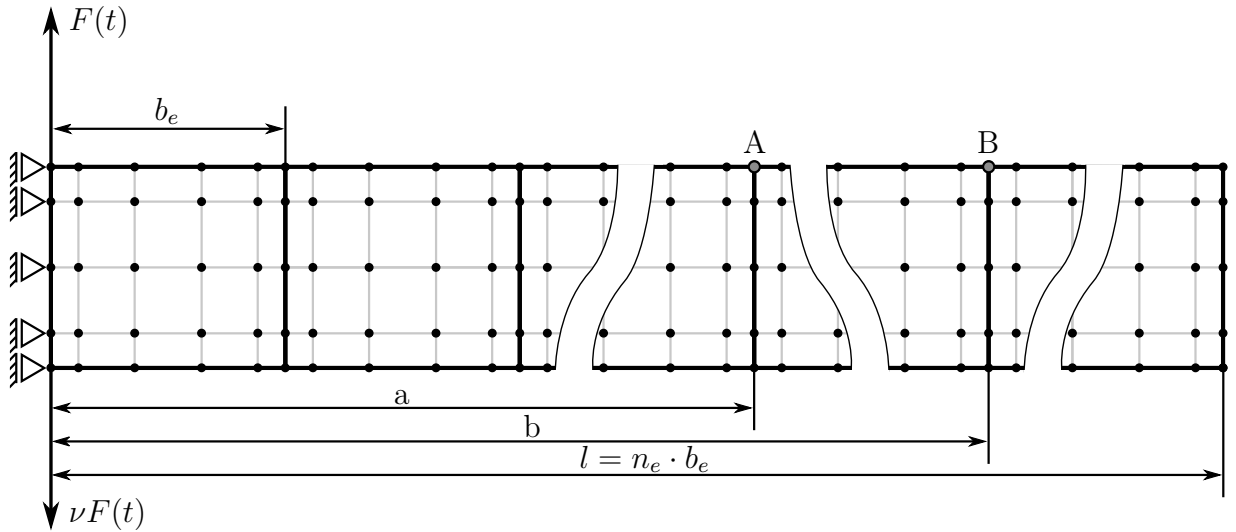


Figure 7.22: Numerical model of the two-dimensional (plane strain), illustrating the discretization employing the SEM. Geometrical dimensions: $a = 30$ mm, $b = 100$ mm, $d = 2$ mm (plate thickness). b_e denotes the element size.

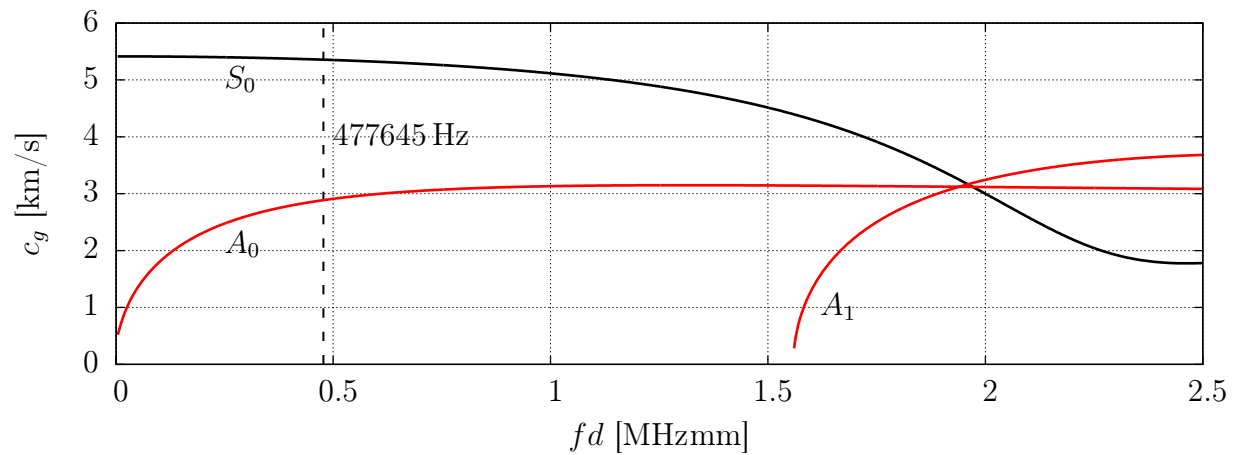


Figure 7.23: Group velocity dispersion diagram for aluminum (material properties: Tab. 2.1).

The group velocity of the fundamental symmetric and anti-symmetric Lamb wave mode can be taken from Fig. 7.23 ($c_{gS_0} = 5147.86$ m/s, $c_{gA_0} = 3129.99$ m/s). This information is used to limit the length of the plate and to make sure that no reflections are contained in the signal. The wavelength, however, is determined by computing the phase velocity. From Fig. 7.23 we infer c_p for 477.645 kHz ($c_{pS_0} = 5319.15$ m/s, $c_{pA_0} = 2299.57$ m/s). The relation between phase velocity and wavelength is given again at this point

$$c_{pS_0/A_0} = \lambda_{S_0/A_0} \cdot f_c. \quad (7.13)$$

The wavelengths of the fundamental modes are accordingly given as $\lambda_{S_0} = 11.14$ mm and $\lambda_{A_0} = 4.81$ mm. Time integration is performed with a Runge-Kutta algorithm of fourth/fifth (Matlab: ode45) order including an adaptive time-step control. At this point, a time-integration scheme from the Runge-Kutta family is deployed in order to demonstrate that the described effect occurs independent of the numerical time-marching algorithm. Note that the numerical quadrature of stiffness and mass matrices is exact - due to the fact that a regular mesh with undistorted rectangular elements is employed. Mass matrix diagonalization (lumping) methods are not applied in this investigation.

In the remainder of the present section, we only discuss the results with respect to the symmetric Lamb mode (S_0). The results of the convergence study for the SEM are depicted in Fig. 7.24a. As we can see, the convergence behavior is significantly disrupted at points where the amount of nodes per wavelength χ_{S_0} is a multiple of the shape function degree p_x . Similar observations are made by studying the anti-symmetric Lamb (A_0) wave mode, other polynomial degrees in thickness direction, or different excitation frequencies f_c , respectively. These statements also hold if the p -version of the FEM is employed to discretize the benchmark problem, cf. Fig. 7.24b. In reference [125], Willberg shows that these peaks can also be observed for C_0 -continuous IGEs. Thus, it is reasonable to assume that this problem is inherent to all C_0 -continuous FEs regardless of the chosen polynomial degree.

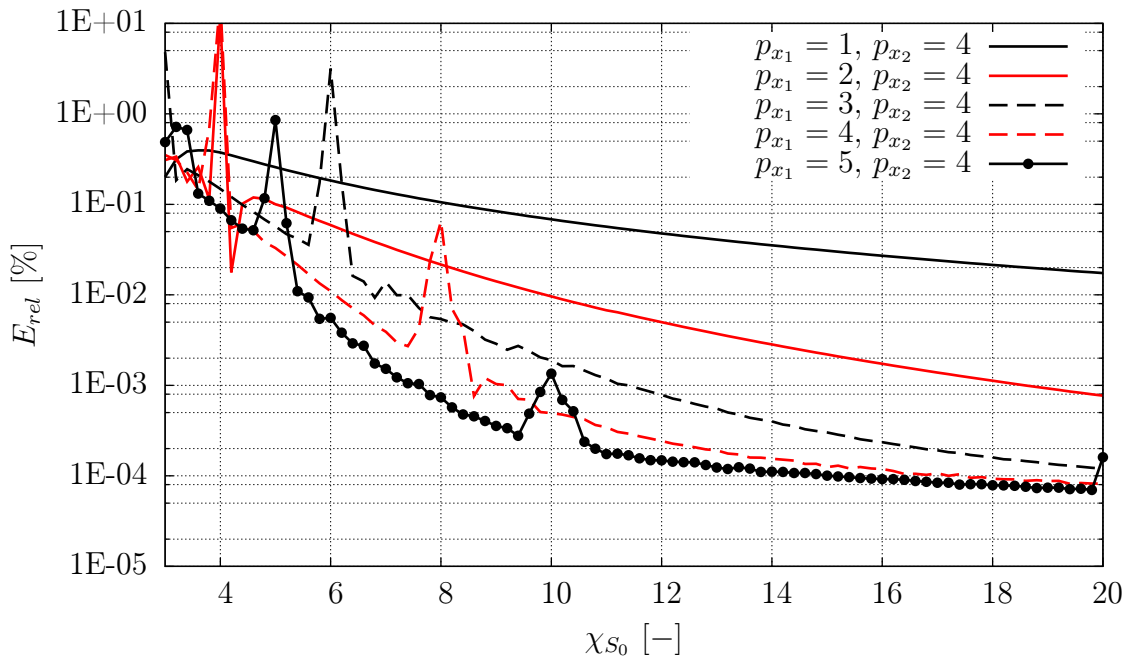
Fig. 7.25 illustrates the displacement history recorded at point A ($u_{x_1,A}$). The results are based on computations employing the SEM using the polynomial degree template $p_{x_1} = 3$, $p_{x_2} = 4$ and the different values of the number of nodes per wavelength $\chi_{S_0} = 5, 6$ and 7. Considering Figs. 7.24b and 7.24a the displacement signal at $\chi_{S_0} = 6$ is expected to be significantly distorted.

Studying the second diagram of Fig. 7.25 ($\chi_{S_0} = 6$), we observe stationary oscillations over time. That is to say, that point A experiences a standing wave similar to that familiar from a modal analysis. As the group velocity of the fundamental symmetric Lamb wave mode is known a priori, we can conclude that after $t = 7 \cdot 10^{-5}$ s no oscillations ought to occur at point A. This behavior can accordingly be described as non-physical. We would like to mention, however, that even simulations using a coarser grid $\chi_{S_0} = 5$ result in accurate displacement histories.

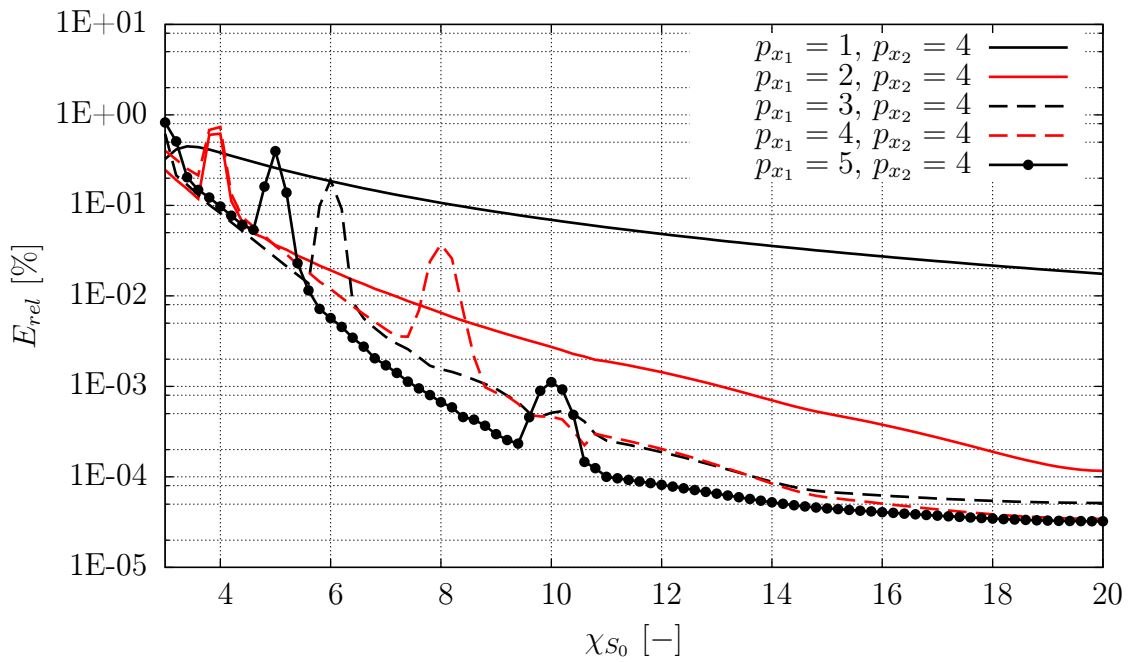
To sum up, if the discretization is refined or coarsened, accurate signals are computed. In principle, therefore, the shape functions are able to resolve the wave form correctly for all three meshes. Moreover, Fig. 7.25 suggests that the group velocity is not affected by the observed phenomenon. That is to say, the results of signal processing methods, such as the continuous wavelet transform (cf. Section 7.7), are not influenced by this effect. From a modelling point of view, however, it is interesting to investigate the source of these oscillations and to devise a remedy. In this way, the analyst can be sure that the results obtained are accurate and that there are no numerical artefacts to pollute the simulation results.

In order to identify the source of the described phenomenon, it is helpful to consider the mode shape of the remaining vibrations. Fig. 7.26 depicts a contour plot of the displacement field for $\chi_{S_0} = 6$. In view of the mode shape of the oscillations, the analyst might be reminded of the well-known hourglass phenomenon. This effect is usually seen in low order h -type FEs. In this case, efforts are made to avoid shear-locking by integrating special terms of the stiffness matrix deliberately using too few quadrature points. This procedure

is called under-integration and is itself another source of errors resulting in zero-energy modes or hourglass modes [241].



(a) The model has been discretized using SEs.



(b) The model has been discretized using p -version FEs.

Figure 7.24: Results of the convergence study for the fundamental symmetric Lamb wave mode are depicted. The relative error in group velocity is given by the number of modes per symmetric wavelength λ_{S_0} .

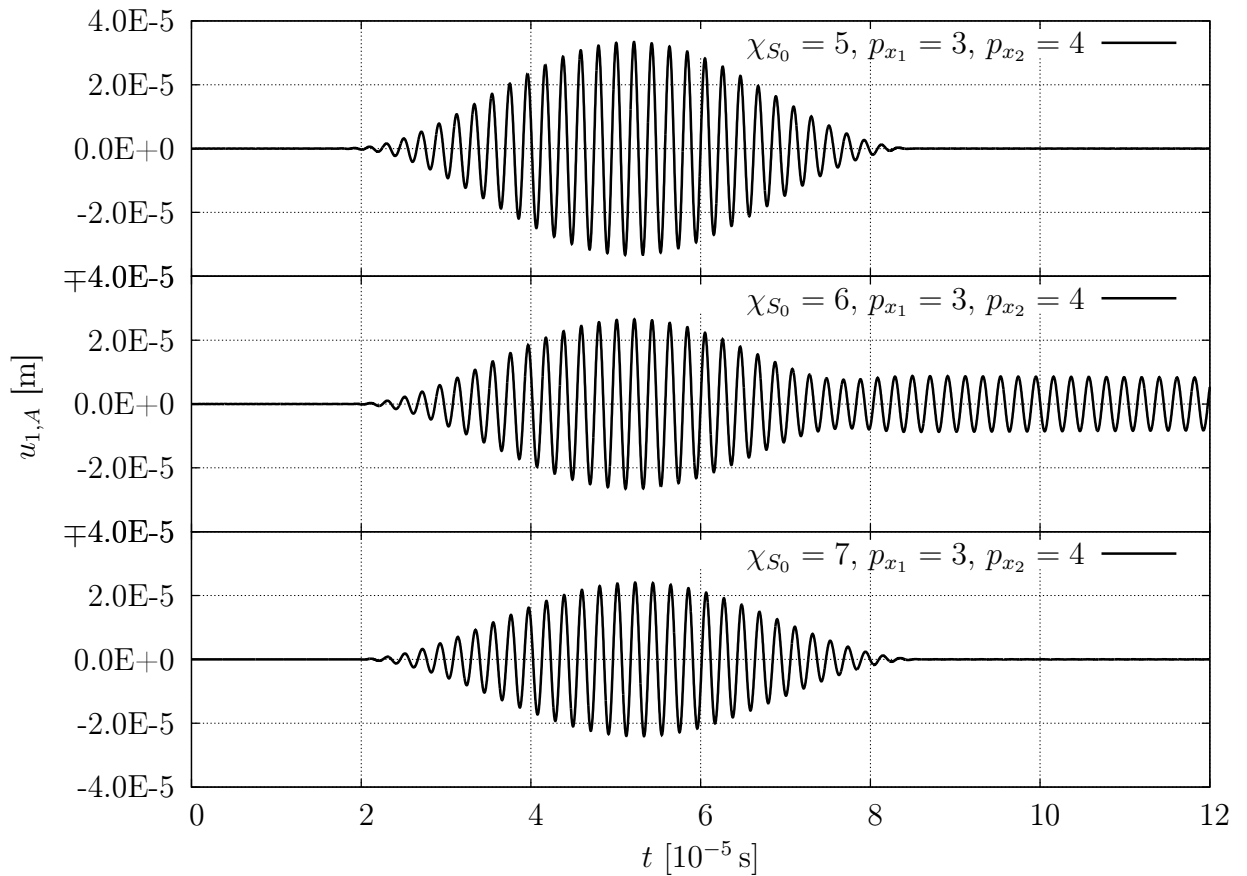


Figure 7.25: Displacement signal at point A. This depicts the in-plane displacement component u_1 . The results were obtained using the SEM with the following polynomial degree template: $p_{x_1} = 3$ and $p_{x_2} = 4$. Please note that if the amount of nodes per symmetric wavelength is chosen to be twice the polynomial degree in propagation direction, $\chi_{S_0} = 6$, the solution is evidently corrupted.

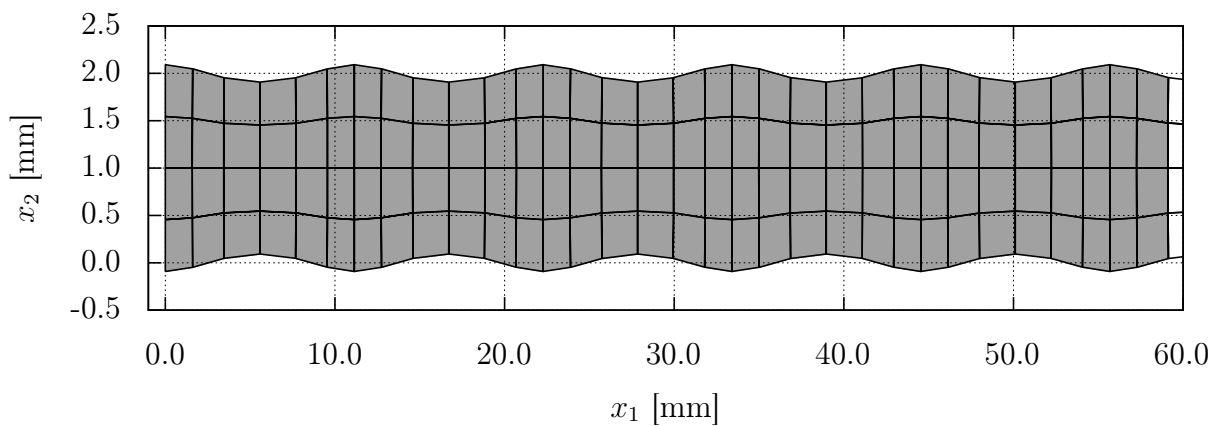


Figure 7.26: Snapshot of the spurious oscillation components remaining in the plate after the primary wave has already passed. The simulation was conducted using the SEM with $p_{x_1} = 3$, $p_{x_2} = 4$ and $\chi_{S_0} = 6$. Contour plot corresponding to the graph in the middle row of Fig. 7.25. The displacement field is scaled by the factor 25.

In other words, no energy is needed to achieve the deformed shape for different displacement configurations. As these oscillations are not suppressed by adding an artificial damping, we can conclude that zero-energy modes do not cause the described effect.

After ruling out hourglass modes as a possible source of these errors, a second obvious idea is that the modal dynamics of the numerical model might cause such vibrations. In order to prove this assumption, we conduct several modal analyses in the following subsections.

7.8.2 Modal analysis of a single finite element

As a next step in the investigation of this effect, we conduct a modal analysis of a single FE. It seems likely that elemental eigenfrequencies are excited. Owing to the fact that no physical damping is introduced and that the chosen time integration scheme does not add any numerical damping, the observed vibrations do not vanish. Taking the connection between adjacent FEs into account, we apply symmetry boundary conditions to its left-hand and right-hand side boundaries. All subsequent considerations are therefore based on the numerical model depicted in Fig. 7.27. It consists of one element with a variable element width b_e . The natural frequencies are calculated to solve the well-known linear eigenvalue problem

$$(\mathbf{K}_{uu} - \Omega \mathbf{M}_{uu}) \hat{\mathbf{v}} = \mathbf{0} \quad (7.14)$$

with $\hat{\mathbf{v}}$ describing the mode shape and Ω denoting the eigenvalue of the system. Ω is related to the natural frequency by

$$\Omega = \omega^2 = (2\pi f)^2. \quad (7.15)$$

The results presented in this section are obtained with the aid of the SEM. We wish to mention, however, that the same conclusions can be drawn in cases where the p -version of the FEM is used.

Fig. 7.28 depicts the first two symmetric mode shapes of an individual SE, using the polynomial degrees $p_{x_1} = 3$, $p_{x_2} = 4$ and an element size of $b_e = 5.568 \cdot 10^{-3}$ m corresponding to $\chi_{S_0} = 6$. A visual inspection of the results, in which the mode shapes are compared with the displacement field in Fig. 7.26, reveals a qualitative agreement between the first eigenvector and the vibrations. This can be taken as an initial clue to verify the stated assumption. Fig. 7.29 displays the first two asymmetric mode shapes. As they do not coincide with the oscillations, they are disregarded for the current investigation.

If, however, only an anti-symmetric Lamb wave mode is excited, these mode shapes are highly important. Since the present example focuses only symmetric waves excited to the middle plane of the plate, only the symmetric mode shapes are considered.

Fig. 7.30 plots the symmetric element eigenfrequencies $f_{r_{symi}}$ as a function of the element width b_e and the number of nodes per wavelength, respectively. For the sake of clarity, we give both abscissas although they can be easily converted, cf. Eq. (7.12). At the chosen excitation frequency of $f_D = 477$ kHz, a horizontal line is plotted in the diagram. The intersection of this line with the graphs of the symmetric element eigenfrequencies $f_{r_{symi}}(b_e)$ gives the critical element sizes at which non-physical vibrations are to be expected. The first critical element width is $b_e = 5.61$ mm ($\chi_{S_0} = 2.899$) and the second is $b_e = 11.53$ mm ($\chi_{S_0} = 5.956$). These points coincide with the locations of the peaks seen in Figs. 7.24a and 7.24b. Consequently, the discovered phenomenon is referred to as *the internal element eigenfrequency effect*.

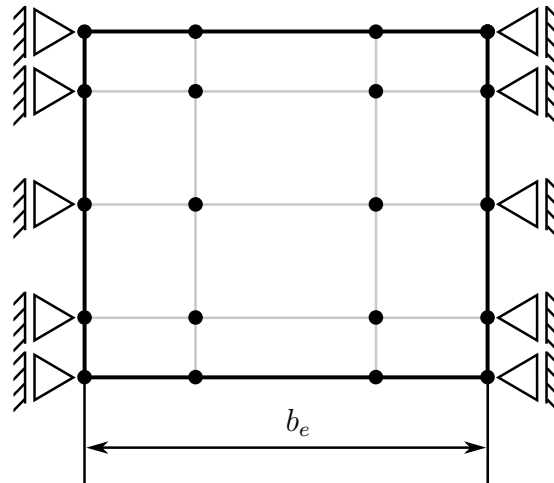


Figure 7.27: Model for the modal analysis: a single SE with symmetric boundary conditions.

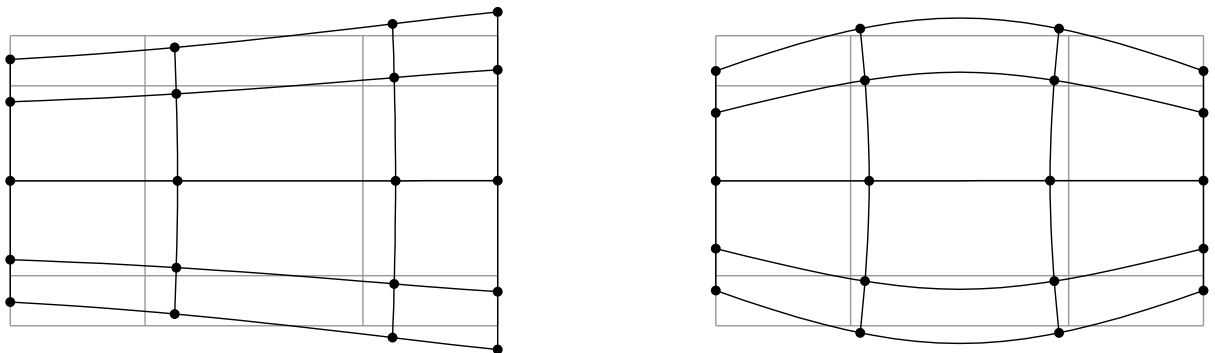


Figure 7.28: The first two symmetric mode shapes belonging to non-zero eigenvalues of one SE with symmetry boundary conditions, cf. Fig. 7.27. The polynomial degrees are chosen as: $p_{x_1} = 3$, $p_{x_2} = 4$. The element size is $b_e = 5.568 \cdot 10^{-3}$ m.

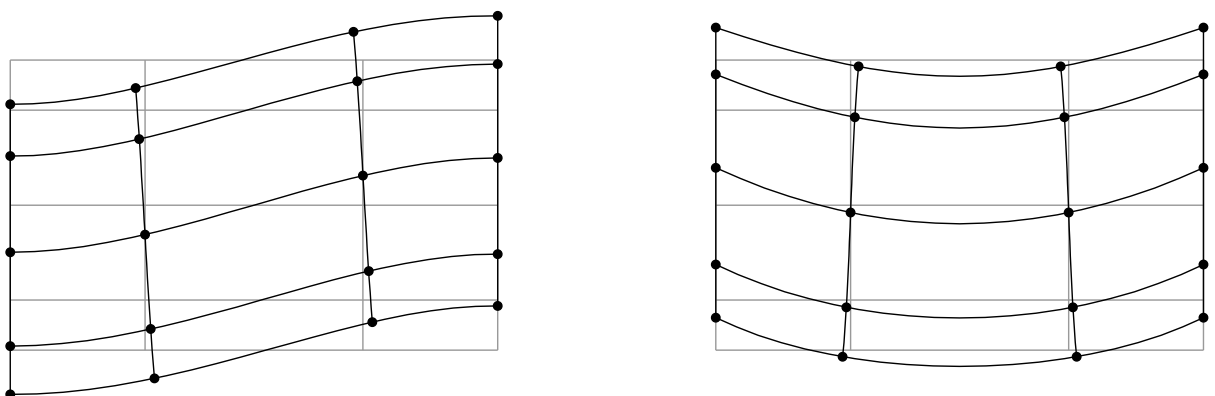


Figure 7.29: The first two asymmetric mode shapes belonging to non-zero eigenvalues of one SE with symmetry boundary conditions, cf. Fig. 7.27. The polynomial degrees are chosen as: $p_{x_1} = 3$, $p_{x_2} = 4$. The element size is $b_e = 5.568 \cdot 10^{-3}$ m.

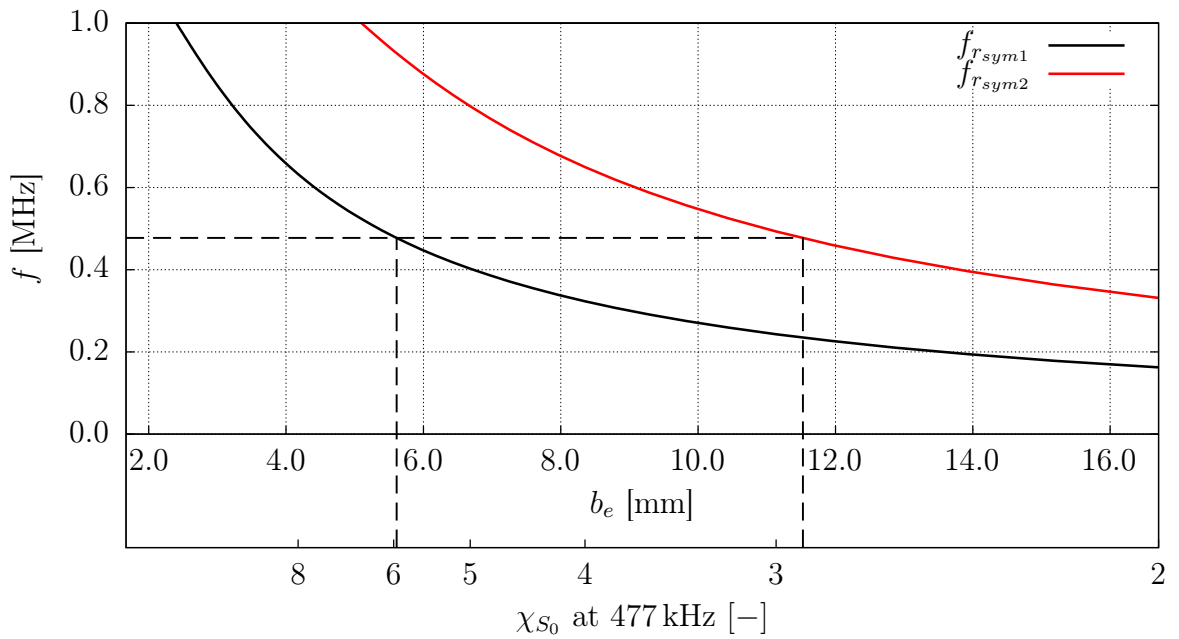


Figure 7.30: The relation between the first two symmetric element eigenfrequencies of a single SE and the element size is illustrated. The polynomial degree template is: $p_{x_1} = 3$ and $p_{x_2} = 4$.

7.8.3 Frequency dependency of the elemental eigenfrequency effect

In the following we investigate two different excitation frequencies. The wave is excited at $f_{D_1} = 4.77 \cdot 10^5$ Hz and $f_{D_2} = 1.59 \cdot 10^5$ Hz, respectively. The polynomial degrees are chosen as $p_{x_1} = 4$ and $p_{x_2} = 4$.

Figs. 7.31 and 7.32 depict the relative error in group speed for the chosen excitation frequencies and polynomial degree template. We conclude that $\chi_{S_0} = 3.9$ and $\chi_{S_0} = 8$ are critical discretization settings.

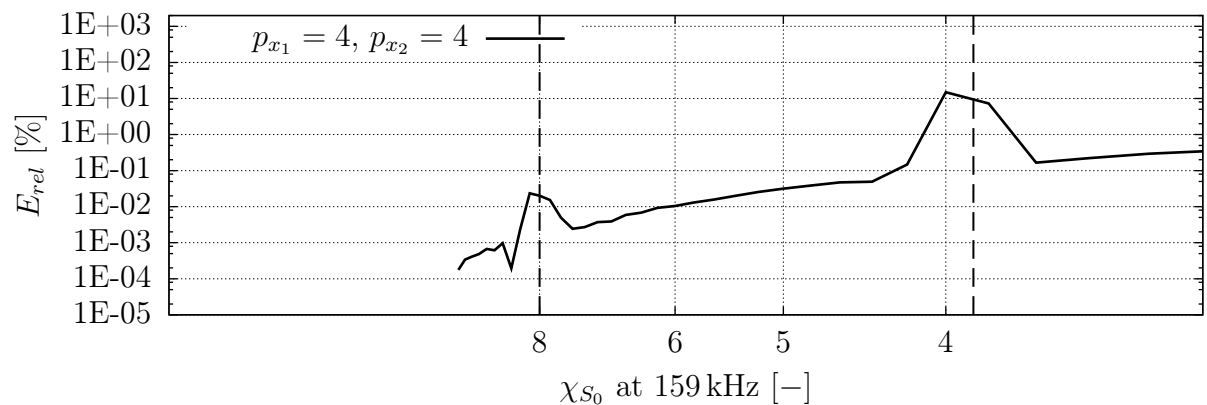


Figure 7.31: Convergence curve of the relative error in group velocity for the fundamental symmetric Lamb wave mode. The polynomial degree template is: $p_{x_1} = 4$, $p_{x_2} = 4$. The excitation frequency is $f_D = 1.59 \cdot 10^5$ Hz.

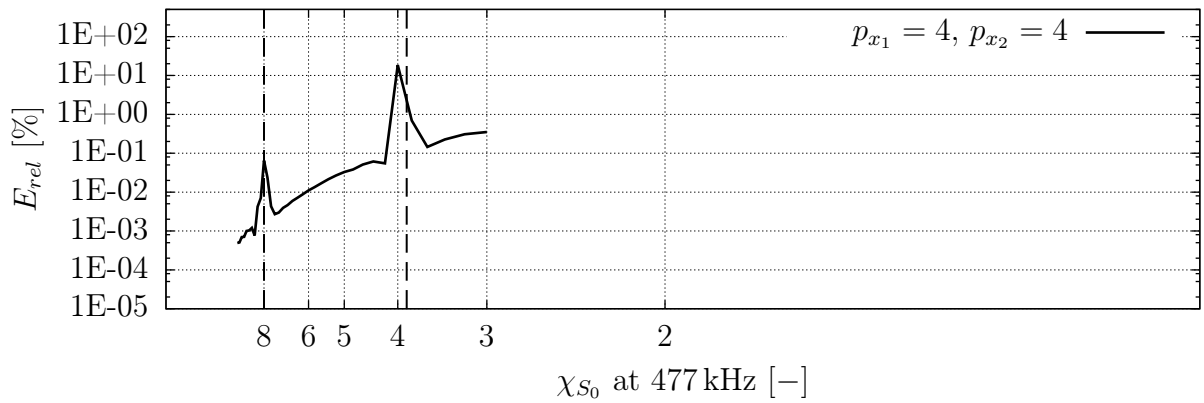


Figure 7.32: Convergence curve of the relative error in group velocity for the fundamental symmetric Lamb wave mode. The polynomial degree template is: $p_{x_1} = 4$, $p_{x_2} = 4$. The excitation frequency is $f_D = 4.77 \cdot 10^5$ Hz.

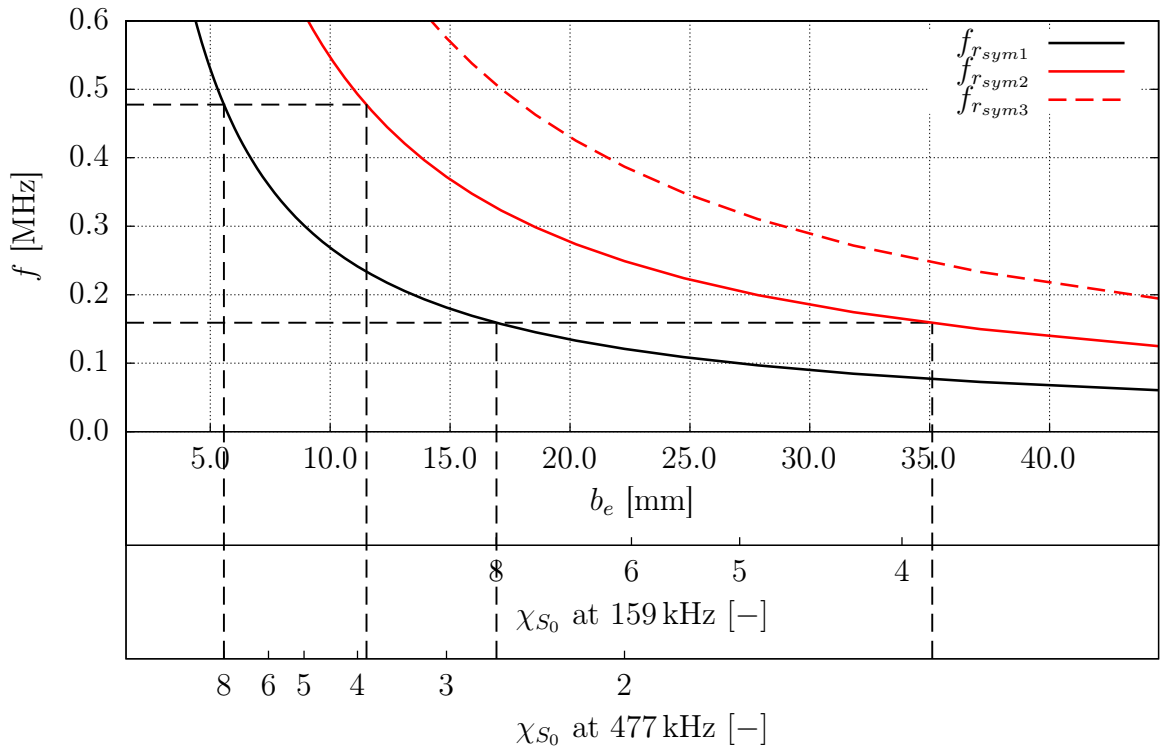


Figure 7.33: The relation between the first three symmetric element eigenfrequencies of a single SE and the element size is illustrated. The polynomial degree template is: $p_{x_1} = 3$ and $p_{x_2} = 4$. Where the eigenfrequencies correspond to the excitation frequency, distinct peaks in the convergence curves are observed, cf. Figs. 7.31 and Fig. 7.32.

It is surprising, however, that the excitation frequency does not seem to have any influence on the critical number of nodes per wavelength. Since the x_1 -direction is discretized with a shape function of polynomial order $p_{x_1} = 4$, the connection between the polynomial degree in wave propagation direction and the critical χ_{S_0} -value is again evident. For this reason, we introduce three abscissas that correspond to the element size b_e and χ_{S_0} for the

two excitation frequencies, cf. Fig. 7.33. Despite the change in the excitation frequency, the locations of the peaks are hardly influenced. Again, the locations of the peaks in the convergence plots for the group velocity are in excellent agreement with the predicted element size due to the elemental eigenfrequency effect.

7.8.4 Modal analysis of a group of finite elements

So far, it has been implicitly assumed that the structure under investigation is discretized using a regular, structured mesh - if possible a Cartesian grid. This can often be the case where thin-walled plate-like structures are concerned. To be applicable for a wider range of problem classes, however, it is necessary to add one last step to the current studies and to look at periodic meshes.

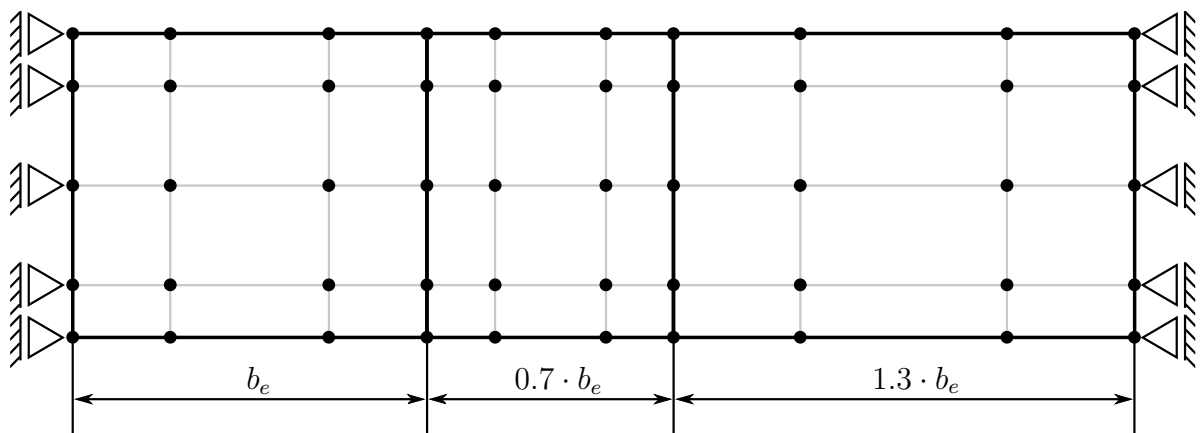


Figure 7.34: Numerical model for the modal analysis of a periodic sub-structure.

This means that adjacent SEs do not necessarily have to have the same element sizes. Nonetheless, it is possible to extract representative sub-structures from the model. To this end, we proceed to analyze the sub-model depicted in Fig. 7.34. This sub-structure consists of three SEs with varying dimensions $[1.0 \cdot b_e, 0.7 \cdot b_e, 1.3 \cdot b_e]$.

To facilitate the comparison between the results, we use the same mean number of nodes per wavelength as with the simulations discussed in the previous sections. The polynomial degrees are $p_{x_1} = 3$ and $p_{x_2} = 4$, cf. Fig. 7.34. As explained before, we begin by computing the symmetric eigenfrequencies of the sub-model as a function of the element width b_e . The results are illustrated in Fig. 7.35. The critical values of χ_{S_0} are determined to be 5.92, 8.98 and 18.00.

We then proceed to extend the sub-model periodically and study its convergence behavior. As predicted in the modal analysis, irregularities arise at $\chi_{S_0} = 5.92, 8.98$ and 18.00, cf. Fig. 7.36. We can therefore conclude that, even in cases where adjacent elements do not share the same dimensions, the wave propagation analysis can be corrupted. Consequently, the analyst also has to be aware of the eigenfrequency effect described above when employing a periodic mesh. This phenomenon is more pronounced if a coarse discretization is chosen in conjunction with a mono-frequent excitation.

Looking at Fig. 7.36, we notice that the effect of the disturbed convergence behavior is minimized for a fine spatial discretization. However, this is only the case in a nodes/modes per wavelength range that is of no interest to the practical engineer. The required dis-

cretization is too fine - and so the computational costs are too high. Usually, an accuracy of approximately 1% would seem sufficient from an engineering point of view. Thus, it is of particular importance to ensure that the external excitation frequency does not coincide with any internal eigenfrequency.

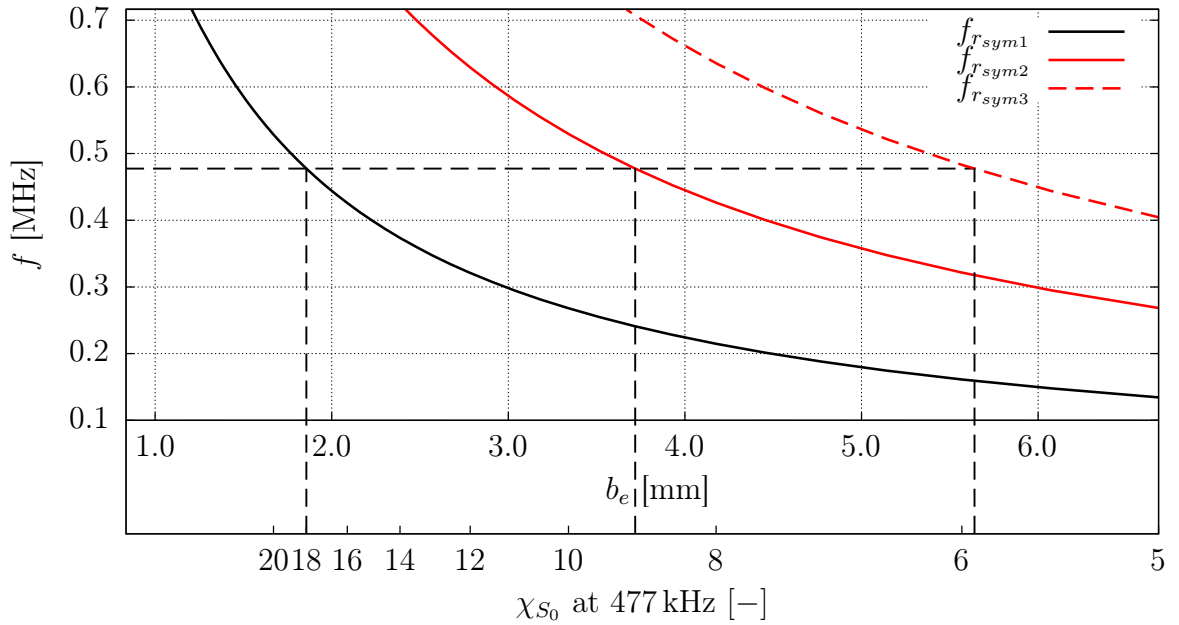


Figure 7.35: The relation between the first three symmetric element eigenfrequencies of a periodic SEM sub-model and the element size is illustrated. The polynomial degree template is: $p_{x_1} = 3$ and $p_{x_2} = 4$. Where the eigenfrequencies correspond to the excitation frequency, we observe distinct peaks in the convergence curves, cf. Fig. 7.36.

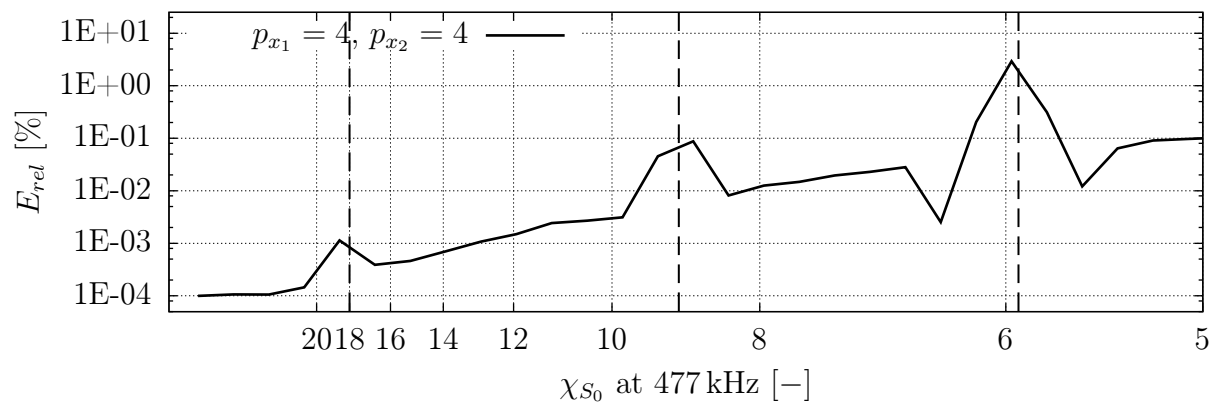


Figure 7.36: Convergence curve of the relative error in group velocity for the fundamental symmetric Lamb wave mode. The polynomial degree template is: $p_{x_1} = 4$, $p_{x_2} = 4$. The excitation frequency is $f_D = 4.77 \cdot 10^5$ Hz. A periodic sub-model is used.

The steps given below are designed to help analysts to avoid non-physical oscillations in wave propagation analyses:

1. Determine the size of a single *HO*-FE (structured grid) or the size of the smallest representative sub-structure.
2. Apply symmetry boundary conditions to the left-hand and right-hand boundaries.
3. Conduct a modal analysis of the representative sub-structure where the element size is an independent parameter.
4. Extract the symmetric eigenfrequencies.
5. Find the intersection of the excitation frequency with the first symmetric eigenfrequencies. This step determines the critical element sizes $b_{e,crit}$.
6. Ensure that the element dimensions b_e are not coincidental with the critical one.

The analyst can easily avoid the internal element eigenfrequency effect and achieve accurate simulations if he adheres to the proposed guideline.

If commercial mesh generators and unstructured discretizations are used, it is improbable that the observed effect will play a significant role. Concerning the quality of the simulations, it is nonetheless recommended to use FEs with low aspect ratios - which is why regular, structured grids (possibly even Cartesian grids) seem appropriate. The analyst consequently tries to partition the model under investigation in order to create regions where a structured, mapped mesh can be applied. It is therefore advised to adhere to the proposed guideline.

It could also be argued, however, that the peaks seen in the convergence curves are merely the results of an offset of the time signal envelope's centroid that was computed using the Hilbert-transform. The phenomenon under investigation has no effect on either the group and phase velocity or on the signal amplitudes. Although this statement is true and the eigenfrequency effect could indeed be suppressed by introducing different signal processing schemes, such as the CWT, this is not satisfactory from a numerical point of view. The time signal is nevertheless disrupted and thus, we deeply believe that such effects should be taken into account whenever conducting wave propagation analysis. Since the remedy for the eigenfrequency effect is fairly simple, every analyst should try to avoid such numerical disturbances (energy is lost in the process). Still, from our point of view it is essential to be aware of all the pitfalls one might come across dealing with the analysis of guided ultrasonic waves.

The present section concentrated on the behavior of the structure under symmetric excitation only - but similar observations can also be made if only anti-symmetric Lamb wave modes are excited. Here, asymmetric eigenshapes/eigenfrequencies (cf. Fig. 7.29) must be avoided. Apart from that, the methodology is identical to the one proposed in the present section.

Chapter 8

Numerical Results

In the present chapter, six benchmark examples are studied to evaluate the general performance of the proposed higher order methods, focusing on both academic and also more practice-oriented benchmark problems. The numerical examples are used to demonstrate the feasibility and the efficiency of the proposed approaches.

The numerical problems presented in the following sections are related to different aspects of numerical analysis. The first example is the modal analysis of a circular piezoelectric transducer (Section 8.1). Here, we will focus on computing eigenvalues and mode shapes of the transducer, verifying the results based on available analytical reference solutions. A two-dimensional plane strain model with an eccentrically located hole is investigated as a second example (Section 8.2). This problem involves the propagation of ultrasonic guided waves. Due to the location of the hole, we will be able to demonstrate important characteristics of Lamb waves, such as the mode conversion phenomenon. The third example continues to investigate the propagation of guided waves (Section 8.3). In the same line as before, a more complex geometry will serve to demonstrate the capabilities of the fictitious domain concept in conjunction with spectral shape functions and an explicit time-stepping scheme. So far, only the fundamental Lamb wave modes (A_0 , S_0) have been investigated in the numerical examples. In the fourth problem (Section 8.4) we therefore study the ability of the proposed higher order methods to capture higher order modes (A_1 -mode). Similar to the second benchmark problem, a three-dimensional plate with a conical hole is used as the fifth model (Section 8.5). This model is employed to study mode convergence in a three-dimensional setting. Here, collocated piezoelectric transducers are deployed to excite ultrasonic guided waves. Finally, we will compare the numerical results to the experimental data recorded for an aluminum plate (Section 8.6).

8.1 Modal analysis of a piezoelectric disc

The first problem deals with the modal analysis of a circular piezoelectric disc. As it investigates a piezoelectric transducer that can be bought off the shelf, this benchmark example is not limited to the scope of academic interest. This actuator is also used in Section 8.5 to excite ultrasonic guided waves.

As Pohl *et al.* showed in [310], the eigenmodes of piezoelectric actuators can have a significant effect on the wave field, which is why this section focuses on the eigenfrequencies and mode shapes of a piezoelectric circular disc made of PIC-151. Fig. 8.1 depicts both the geometry of the model and the boundary conditions, while Tab. 8.1 lists the material properties.

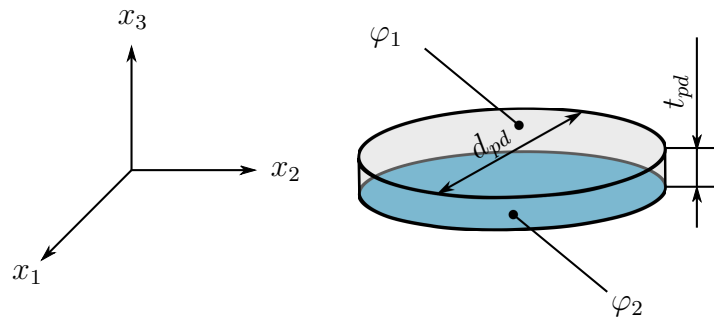


Figure 8.1: Geometry and boundary conditions of the circular piezoelectric disc transducer (index dp). The diameter of the disc is $d_{pd} = 0.03$ m and the thickness is $t_{pd} = 0.001$ m. Depending on the state of the transducer (open or short-circuited electrodes) the electrical boundary conditions φ_1 and φ_2 are specified on the bottom and the top surface of the actuator.

Table 8.1: Material properties for PIC-151. The poling direction of the material is the x_3 -direction. The vacuum permittivity (permittivity of free space) is given by $\kappa_0 = 8.8542 \cdot 10^{-12}$ As/Vm. The values of the non-zero components of the elasticity tensor \mathbf{C} , the piezoelectric coupling tensor \mathbf{e} , the dielectric tensor κ and the mass density ρ are given.

Mechanical properties		Electrical properties	
$C_{11} = C_{22}$	107.6 GPa	e_{31}	-9.6 N/Vm
C_{12}	63.12 GPa	e_{33}	15.1 N/Vm
$C_{13} = C_{23}$	63.85 GPa	e_{15}	12.0 N/Vm
C_{33}	100.4 GPa	κ_{11}^T / κ_0	1936
C_{44}	22.24 GPa	κ_{33}^T / κ_0	2109
$C_{55} = C_{66}$	19.62 GPa		
ρ	7760 kg/m ³		

Modal analysis of a piezoelectric transducer

Since the transducer's eigendynamic behavior is a matter of interest in the scope of SHM applications [193] a short excursion seems appropriate: A modal analysis for piezoelectric transducers can be conducted for two special cases of boundary conditions that are important for practice-oriented applications. The mechanical boundary conditions are chosen as free boundary conditions for the two simulations. This highlights the influence of the electro-mechanical coupling on the eigenfrequencies of the model. Here, the focus lies on examining the eigenvalues for (i) short-circuited and (ii) open electrodes. In the case of short-circuited electrodes, there is no coupling between the electrical and mechanical properties [205], so we can compare the results with the analytical solution for a free elastic circular plate [10, 311]. If we introduce a charge separation for the latter case (open electrodes), this will result in an electric field - which in turn shows that the plate's behavior is stiffer than in the purely elastic case. This is easily demonstrated by considering Eq. (4.33).

If the electric potential Φ is prescribed within the structure to model the short-circuited electrodes, the first row of Eq. (4.33) can be directly solved for the displacement field \mathbf{U}

$$\mathbf{M}_{uu}\ddot{\mathbf{U}} + \mathbf{K}_{uu}\mathbf{U} = \mathbf{f}_{uu} - \mathbf{K}_{u\varphi}\Phi. \quad (8.1)$$

The second term on the right-hand side of the equation accounts for the equivalent piezoelectric loads. Regarding Eq. (8.1), we can see that the modal analysis of a piezoelectric structure with prescribed electric potential is equal to the purely elastic case. This means that short-circuited electrodes ($\Phi = \mathbf{0}$) essentially resemble the elastic case. The eigenvalue problem for this case reads

$$(\mathbf{K}_{uu} - \omega^2\mathbf{M}_{uu})\mathbf{U} = \mathbf{0}, \quad \omega = 2\pi f. \quad (8.2)$$

In the present case, f represents the resonance frequency of the structure in question.

In the second case, the open electrodes, correspond to a zero charge boundary condition ($\mathbf{f}_{\varphi\varphi} = \mathbf{0}$). Thus, we need to rearrange the second row of the equation of motion of a piezoelectric body in the following manner

$$\Phi = \mathbf{K}_{\varphi\varphi}^{-1}\mathbf{K}_{\varphi u}\mathbf{U}. \quad (8.3)$$

We can now insert Eq. (8.3) into the equation of motion, yielding

$$\mathbf{M}_{uu}\ddot{\mathbf{U}} + (\mathbf{K}_{uu} + \mathbf{K}_{u\varphi}\mathbf{K}_{\varphi\varphi}^{-1}\mathbf{K}_{\varphi u})\mathbf{U} = \mathbf{f}_{uu}. \quad (8.4)$$

The eigenvalue problem for open electrodes can also be described as follows

$$(\mathbf{K}^* - \omega^2\mathbf{M}_{uu})\mathbf{U} = \mathbf{0}, \quad (8.5)$$

where

$$\mathbf{K}^* = \mathbf{K}_{uu} + \mathbf{K}_{u\varphi}\mathbf{K}_{\varphi\varphi}^{-1}\mathbf{K}_{\varphi u}. \quad (8.6)$$

Eq. (8.5) clearly indicates to what extent the electro-mechanical coupling influences the resonance frequencies and mode shapes. Clearly, this coupling effect increases the stiffness of the system, so that the natural frequencies are elevated as well.

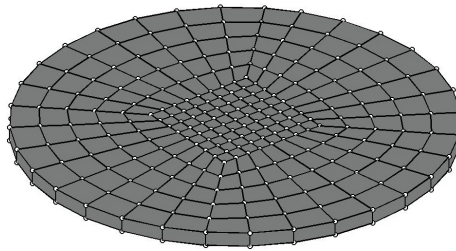


Figure 8.2: FE discretization of the piezoelectric disc. The domain contains 224 FEs (nodal points are indicated by white circles with black edges).

We compare the results of the FCM and the SCM with numerical solutions obtained by applying the p -version of the FEM in order to assess their performance. The geometry for p -FEM the model is described precisely by the blending function method proposed by Gordon [232]. Figs. 8.2 and 8.3 depict the FE and FC discretizations, respectively.

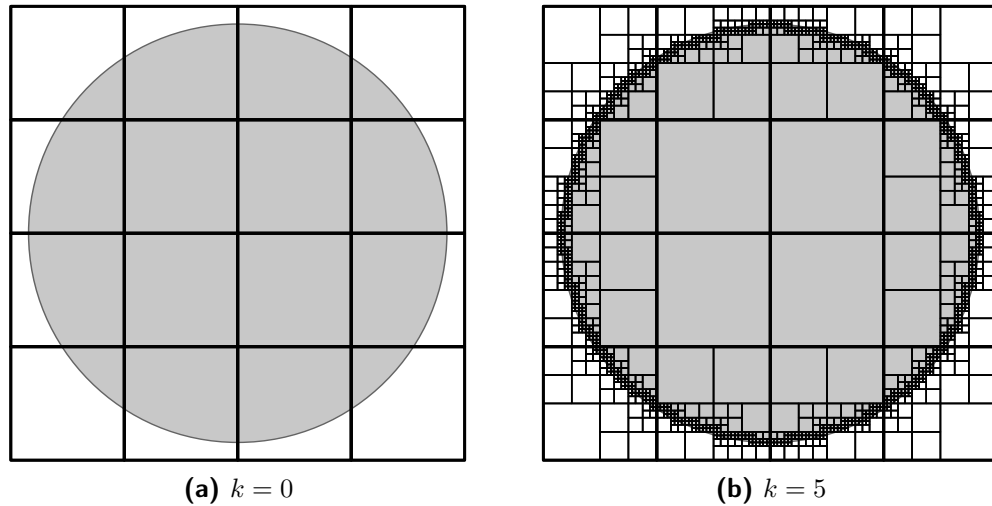


Figure 8.3: FC discretization of the piezoelectric disc and the sub-cell structure for the numerical integration of the system matrices and vectors. The domain contains 4×4 FEs and the integration grid has been refined 5 times ($k = 5$).

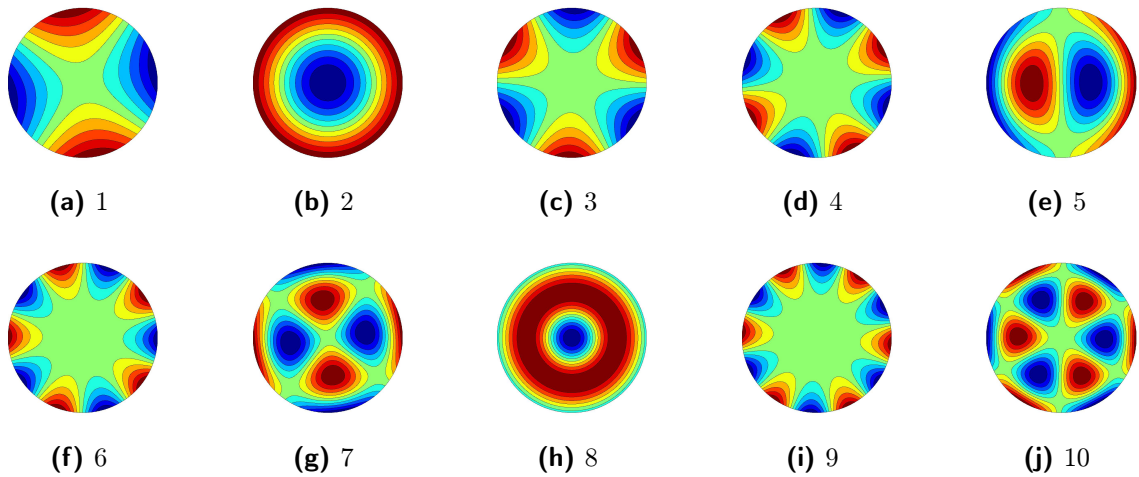


Figure 8.4: Mode shapes of the first 10 non-zero eigenfrequencies. The first 6 eigenvectors correspond to the rigid body motions of the free circular piezoelectric disc. Contour plots of the u_3 -component of the displacement field are depicted.

Each cut cell is adaptively refined several times ($k = 5$) to ensure a good accuracy when describing the geometry using the FCM approach. We accordingly assume that the influence of the geometry approximation on the numerical results is negligible (the relative error in the area is $\approx 10^{-9}$). The first 10 mode shapes of the circular piezoelectric disc are displayed in Fig. 8.4. It has to be kept in mind, however, that the deformation modes do not change, regardless of whether open or closed electrodes are assumed as boundary conditions.

Tab. 8.2 lists the eigenfrequency values, clearly showing that the results of the two different fictitious domain approaches - FCM/SCM - and those of the widely accepted p -version of the FEM agree well. Although the geometry is resolved exactly in the latter approach, the

eigenfrequencies are almost identical. The small deviations are due to the number of FCs used, resulting in only a third of the degrees-of-freedom. When comparing the eigenvalues for the two different cases of electrical boundary conditions, we should note that not all eigenfrequencies are influenced by the electro-mechanical coupling in the same way. The stiffening effect seems to apply to bending-dominated mode shapes in particular, whereas the resonance frequency remains almost unchanged if only the disc's boundary is deformed, cf. Fig. 8.4.

Table 8.2: Resonance frequencies for the piezoelectric circular disc with open and short-circuited electrodes (first 10 non-zero eigenfrequencies). The material properties are given in Tab. 8.1 and the geometry is depicted in Fig. 8.1. Results obtained using the p -version of FEM serve as a reference. Only the non-zero eigenvalues are compiled in this table (p -FEM: $p = 6$, $n_{dof} = 228508$, $n_e = 224$; FCM/SCM: $p = 4$, $n_{dof} = 5780$, $n_c = 16$).

Number	Open electrodes (unit [Hz])			Short-circuited electrodes (unit [Hz])		
	p -FEM	FCM	SCM	p -FEM	FCM	SCM
1	3159.279	3224.242	3222.950	3109.176	3172.648	3172.656
2	6248.338	6377.351	6357.027	5395.494	5503.186	5503.294
3	7365.543	7521.756	7516.886	7175.563	7325.055	7325.055
4	12921.62	13200.53	13192.93	12048.89	12292.53	12292.53
5	13662.00	13945.71	13860.77	12497.45	12760.30	12760.68
6	19743.22	20187.71	20174.90	18988.05	19403.89	19403.89
7	22909.19	23388.38	23200.96	20391.88	20809.84	20809.87
8	25298.34	25862.08	25708.77	22321.86	22809.57	22809.65
9	27745.19	28376.76	28358.74	26560.74	27144.99	27145.04
10	33709.19	34494.20	34134.73	30127.96	30824.55	30824.55

Huang *et al.* [311] also determined the eigenvalues and eigenvectors for the coupled case numerically, experimentally and analytically. The experimental results are based on measurements using a laser scanning Doppler vibrometer (LSDV) and on amplitude-fluctuation electronic speckle pattern interferometry (AF-ESPI). The numerical solutions are calculated using the h -version of the FEM. To compare the results of Huang *et al.* to our study, Tab. 8.3 lists the relative errors for the FCM and the SCM with respect to the analytical solution, since not all eigenvalues are calculated in [311]. The relative error in the resonance frequency is determined by

$$E_{rel} = \frac{f_{\text{numerical}} - f_{\text{analytical}}}{f_{\text{analytical}}} \cdot 100[\%] \quad (8.7)$$

with $f_{\text{analytical}}$ representing the analytical reference solution and $f_{\text{numerical}}$ the results of the numerical approach. The maximum difference is about 10.69%. This appears to be quite reasonable, considering the assumptions Huang *et al.* [311] made to derive the analytical solution (plate theory). Since our example mainly focuses on the bending-dominated modes, it can be concluded that the assumptions made by Huang do not strictly apply here.

To assess the accuracy of the solution in more detail, we compare the purely elastic case, corresponding to the short-circuited electrodes, with the analytical solution mentioned before. The results, which indicate an excellent agreement, are compiled in Tab. 8.4. The relative error is less than 2% for the first 40 eigenvalues.

Table 8.3: Comparison between analytically determined eigenfrequencies for a piezoelectric circular disc and numerical results obtained by means of the SCM. Eigenfrequency numbers $n_f = 1, 2, \dots, 8$ are compared - open electrodes.

Number	Analytical solution [Hz]	Numerical solution (SCM) [Hz]	Relative error [%]
1	3224	3224	0.033
2	7040	6357	9.701
3	7638	7517	1.586
4	13602	13193	3.007
5	15358	13861	9.749
6	21094	20175	4.357
7	25924	23201	10.50
8	28786	25709	10.69

Table 8.4: Comparison between analytically determined eigenfrequencies for an elastic circular disc and numerical results obtained by means of the SCM. Eigenfrequency numbers $n_f = 1, 2, \dots, 8$ are compared - short-circuited electrodes.

Number	Analytical solution [Hz]	Numerical solution (SCM) [Hz]	Relative error [%]
1	3130	3173	1.363
2	5400	5503	1.913
3	7300	7325	0.343
4	12230	12293	0.511
5	12840	12761	0.618
6	19700	19404	1.503
7	21020	20810	1.000
8	22970	22810	0.698

Up to this point, the comparison of the results is limited to the eigenvalues. In order to be able to compare the mode shapes as well, we employ the modal assurance criterion (MAC)

$$MAC = \frac{|\Phi_1^T \cdot \Phi_2|^2}{|\Phi_1^T \cdot \Phi_1| \cdot |\Phi_2^T \cdot \Phi_2|} \cdot [100\%]. \quad (8.8)$$

Φ_1 and Φ_2 are two eigenvectors from different models that are compared with one another, cf. Fig. 8.5. A MAC-value of 100% means that the vectors are identical, whereas 0% means that they are orthogonal. Typically, a MAC-value of over 90% is regarded as sufficient, representing a good agreement of the mode shapes. The eigenvectors of the p -FEM solution are compared to the SCM solution. Since the results based on the FCM and the SCM are practically identical, it suffices to calculate the MAC-matrix for this example.

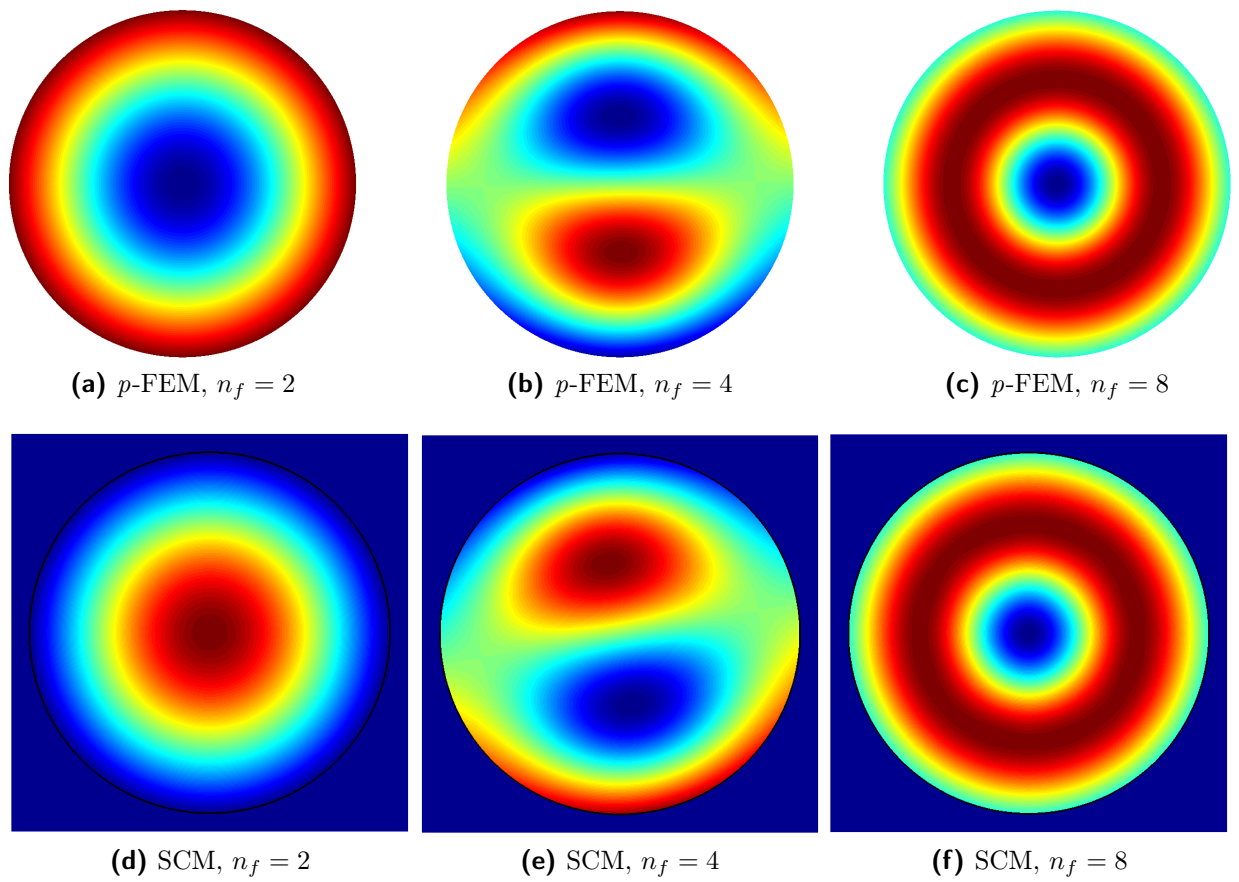


Figure 8.5: Comparison between selected mode shapes calculated with the help of the p -FEM and the SCM, respectively. Contour plots of the u_3 -component of the displacement field.

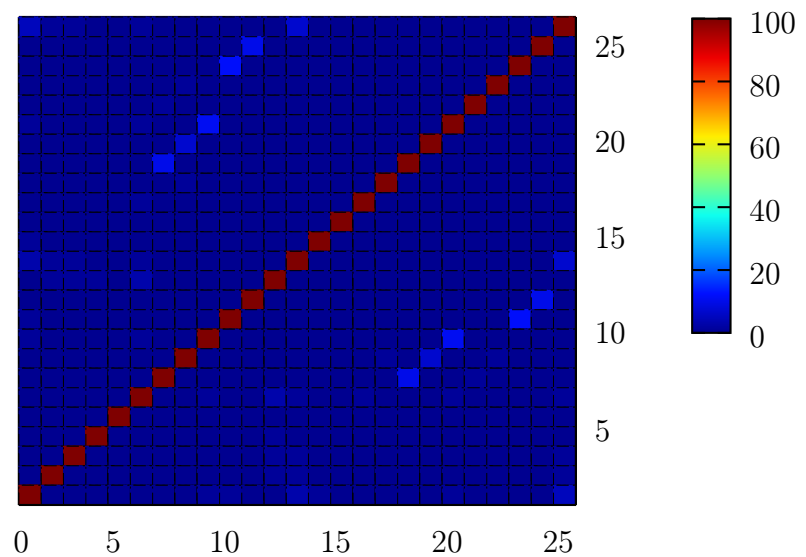


Figure 8.6: MAC matrix: Comparison between the mode shapes calculated using the p -FEM and the SCM.

As is already evident from Fig. 8.5, the mode shapes determined with both approaches are identical. This finding is also confirmed by Fig. 8.6. The MAC values along the main diagonal exceed 95%, indicating an excellent agreement not only in terms of the eigenvalues but also of the eigenvectors.

The modal analysis conducted in this section has shown that the proposed higher order fictitious domain approaches are capable of capturing the dynamic properties of electro-mechanically coupled structures.

The following sections will now approach the issue of wave propagation analysis. First, a “proof-of-concept” is conducted in Sections 8.2 and 8.3, highlighting the capabilities of FCM/SCM to model ultrasonic guided waves in heterogeneous materials. Second, higher order Lamb wave modes are addressed in Section 8.4. Thereafter, piezoelectrically excited ultrasonic guided waves in thin-walled structures are in the focus of Sections 8.5 and 8.6.

8.2 Two-dimensional perforated plate

The first simple transient benchmark problem demonstrating the capabilities of higher order fictitious domain methods with respect to wave propagation analysis is a two-dimensional plate with a circular hole. The hole is located eccentrically from the mid-plane of the structure, cf. Fig. 8.7. This geometric perturbation causes mode conversion and thus highlights an important characteristic of Lamb waves [15]. The following simulations are based on the tensor product space for both SEM and p -FEM.

The areas marked with a red (solid line) and a blue (dashed line) rectangle, respectively, indicate the position of the contour plots of the travelling wave depicted in Fig. 8.8. A pure S_0 -mode is excited on the left-hand boundary of the plate, cf. Fig. 8.8a. Some distance away from the local perturbation, we clearly see that a converted A_0 -mode occurred in addition to the transmitted S_0 -wave packet, cf. Fig. 8.8b. The location of the contour plot is chosen in such a way that the faster S_0 -mode is clearly separated from the A_0 -mode.

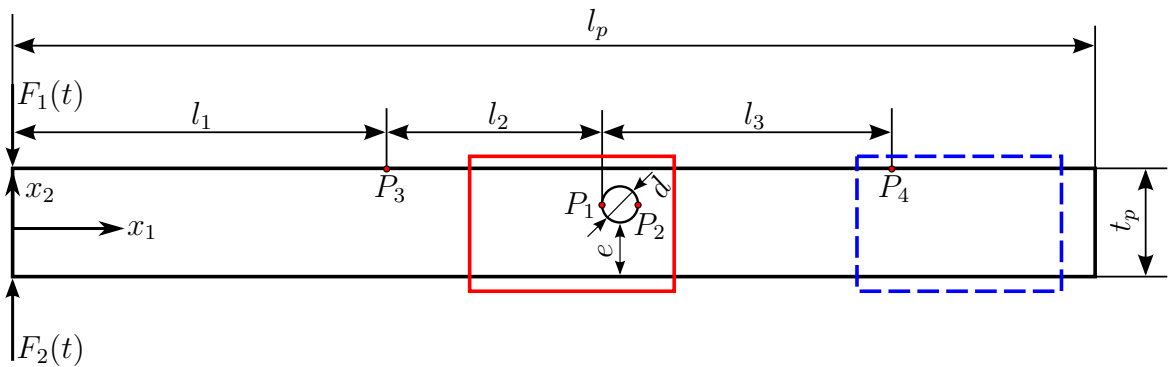


Figure 8.7: 2d aluminum plate (material properties: Tab. 2.1) with a circular hole (not to scale). Loads and boundary conditions are marked in the figure. Two point forces $F_1(t)$ and $F_2(t) = aF_1(t)$ are applied, with $a = 1$ for the excitation of a purely symmetric Lamb wave mode (S_0) and $a = -1$ if the anti-symmetric mode (A_0) is considered. The dimensions of the plate are: $l_1 = 100$ mm, $l_2 = 50$ mm, $l_3 = 152$ mm, $l_p = 600$ mm, $t_p = 5$ mm, $d = 2$ mm, $e = 2$ mm. The signal parameters are: $\hat{F} = 1$ N, $\omega = 2\pi f$, $f = 200$ kHz and $n = 5$ (Eq. (7.1)).

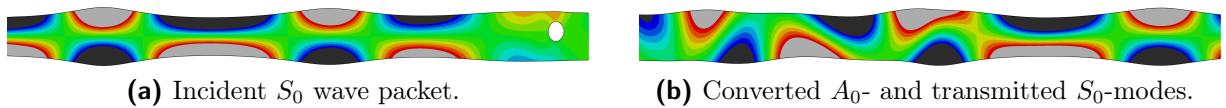


Figure 8.8: Contour plots of the u_2 -displacement of the travelling waves in an aluminum plate with a circular hole, highlighting the effect of mode conversion at asymmetrical perturbations of the structure under investigation.

Model For the sake of minimizing the numerical costs, we assume infinite dimensions in x_3 -direction and subsequently adopt the plane strain assumption. This poses no limitation to the results obtained, as all key features of guided wave propagation can be studied using the set-up described above. The boundary conditions, material properties as well as the dimensions of the plate are given in Fig. 8.7. The history of the displacement field is saved at the measurement points P_1 to P_4 . The results obtained using the FCM and the SCM are later compared to reference solutions attained by applying the p -version of the FEM. The ultrasonic guided waves are excited using a pair of collocated point forces on the top and the bottom surfaces of the plate, cf. Fig. 8.7. They act in the x_2 -direction and their time-dependent amplitudes follow a sine burst signal, cf. Eq. (7.1). This kind of pulse has the advantage that the frequency content is narrow-banded, thus keeping the physical dispersion of these waves to a minimum. The number of cycles within the signal n determines the width of the excited frequency band around the central frequency f_c (cf. Fig. 8.10b). For a narrow frequency bandwidth, it is necessary to select a relatively high value for n .

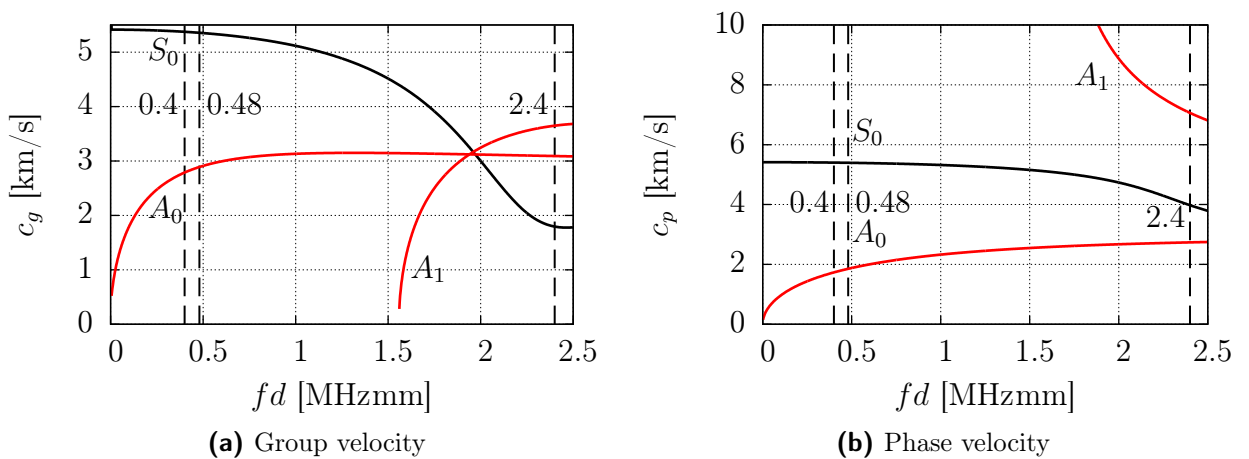


Figure 8.9: Dispersion diagram for aluminum (material properties: Tab. 2.1). The dashed vertical lines mark the fd -values that are used in the course of this chapter ($fd_1 = 0.4$ MHzmm, $fd_2 = 2.4$ MHzmm, $fd_3 = 0.48$ MHzmm).

Applying concentrated loads to the top and bottom surfaces allow us to exploit the advantages of a mono-modal excitation, which means that only a single mode is present at a time for $f \cdot t_p < 1.5$ MHzmm, cf. Fig. 8.9. In order to generate a signal containing only the A_0 -mode, both forces have to act in the same direction, meaning they have to be in-phase. If the two loads are out-of-phase, a pure S_0 -mode is generated.

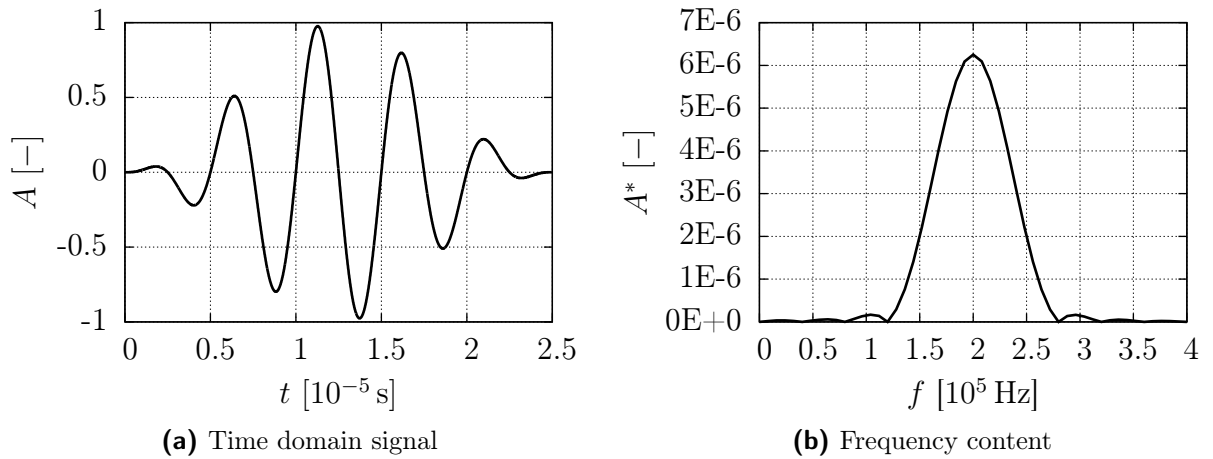


Figure 8.10: Sine-burst ($f_c = 200$ kHz, $n = 5$).

Discretization The rest of this section is dedicated to explaining how to choose the discretization parameter and how to determine appropriate values for the time-stepping scheme. The optimal discretization for this example follows the guidelines derived in Chapter 7 and published in Willberg *et al.* [78]. That is to say, we choose $p_{x_1} = 3$ as the polynomial degree in the direction of the travelling wave and $p_{x_2} = 4$ as the polynomial order in the thickness direction of the plate. In order to determine the necessary element size to achieve a relative error of less than 0.5% in the time-of-flight, we first need to look at the dispersion curves, cf. Fig. 8.9. From the phase velocity (c_p) of the A_0 -mode (shorter wavelength and consequently more demanding for the mesh density) at 1 MHzmm ($f_c = 200$ kHz, $t_p = 5$ mm) its wavelength can be calculated using

$$c_{pA_0/S_0} = \lambda_{A_0/S_0} \cdot f_c. \quad (8.9)$$

Here λ_{A_0/S_0} denotes the wavelength of the fundamental anti-symmetric and symmetric Lamb wave modes, while f_c is the excitation frequency. We read from Fig. 8.9b that the phase velocities for the A_0 - and S_0 -mode are

$$c_{pA_0} = 2327 \text{ m/s} \text{ and } c_{pS_0} = 5309 \text{ m/s}.$$

By substituting these values into Eq. (8.9) the wavelengths are calculated

$$\lambda_{A_0} = 0.0116 \text{ m} \text{ and } \lambda_{S_0} = 0.0265 \text{ m}.$$

Based on the wavelengths, the FE size (b_e) can be estimated based on Eq. (7.12) by

$$b_e = \frac{p_{x_1}}{\chi_{A_0}} \cdot \lambda_{A_0}. \quad (8.10)$$

The convergence curves, cf. Figs. 7.5b and 7.9b, are the last point to be taken into consideration. If the A_0 -mode is to be fully resolved, we have to ensure that the chosen mesh has at least 12 modes per wavelength ($\chi_{A_0} = 12$), cf. Fig. 7.17a, when using the p -version of the FEM for our simulations. By applying Eq. (8.10), we derive an element size of

$$b_e \leq 0.003 \text{ m}.$$

Time-integration A standard Newmark method is used for the numerical time-integration. An implicit method is employed to enable us to compare the results of the p -FEM, the FCM and the SCM. By choosing the same time-stepping scheme for all methods, we can disregard the effect of the time-integration on the numerical results. Since the unconditionally stable version of this method has been used, the time-step is bounded by the Shannon-Nyquist theorem. At least 2 points per period are required to avoid sampling errors. In order to achieve good quality results, however, considerably more points per period are generally recommended. From experience, we recommend to use at least 10 points. On the other hand, we conducted preliminary, unpublished studies suggesting that this number of sample points is not sufficient to achieve an effective and accurate time integration. We therefore propose that the chosen time-step Δt should not exceed a value of

$$\Delta t_{max} = \frac{1}{f \cdot n_{sample}} = 1 \cdot 10^{-7} \text{ s.}$$

n_{sample} denotes the number of sampling points per period. To ensure good results, we choose $n_{sample} = 50$. The experience with wave propagation analysis in the context of SHM leads us to also recommend the stability limit of a central difference time-integration scheme (CDM) as a suitable time-step [211] (cf. Section 7.6).

Since the group velocities of the A_0 - and S_0 -mode differ significantly ($c_{gA_0} \approx 3137 \text{ m/s}$, $c_{gS_0} \approx 5119 \text{ m/s}$) the simulation time can and should be adjusted. We determine the simulation time in such a way that the incident waves are able to reach the right boundary and are reflected from it ($l_p = 600 \text{ mm}$). Consequently, when exciting a pure A_0 - and a pure S_0 -mode respectively, the simulation times are

$$t_{A_0} \approx \frac{l_p}{c_{gA_0}} = 2 \cdot 10^{-4} \text{ s}$$

for the basic anti-symmetric (A_0) and

$$t_{S_0} \approx \frac{l_p}{c_{gS_0}} = 1.2 \cdot 10^{-4} \text{ s}$$

for the basic symmetric Lamb wave mode (S_0).

Results In order to provide a reference solution for evaluating the performance of the FCM and the SCM, we select the results obtained by applying the p -version of FEM ($n_e = 404$, $n_{dof} = 11288$, $b_e = 3 \text{ mm}$) with the optimal polynomial degree template and the corresponding FE size determined above. The geometrical features such as the circular hole are described exactly using the blending function method [115, 128, 232, 237, 239]. These blending elements have been proposed as a remedy to circumvent the geometrical approximation error. In this case, the corresponding mapping functions are based on sin- and cos-functions. Consequently, the error of the geometry representation is equal to zero. The FE discretization is depicted in Fig. 8.11.

Based on the FCM and the SCM, the mesh does not necessarily match the geometry, so mesh generation is straightforward. Here, the domain is simply discretized by using a Cartesian grid of cells, cf. Fig. 8.12. The current example is discretized using 400 quadrilateral higher order cells. The polynomial degrees are identical and the cell dimensions are

similar to the p -FEM grid. To account for the circular hole in the 4 cut cells (cells exhibiting a discontinuous integrand), we carry out an adaptive integration. Fig. 8.12 depicts the integration sub-cells of refinement level $k = 5$, that are used during the integration process. In order to judge the accuracy of the FCM and the SCM, they are compared to the reference solution (p -FEM) of the displacement time history at the points P_1 to P_4 , cf. Fig. 8.13. It is worth mentioning that, even though the cells do not resolve the circular hole geometrically, the FCM and the SCM are able to produce results with a similar accuracy as the p -FEM - even for points located on the perimeter of the hole, cf. Fig. 8.13a and 8.13b. Note, however, that the p -FEM requires slightly more degrees-of-freedom to resolve the hole.

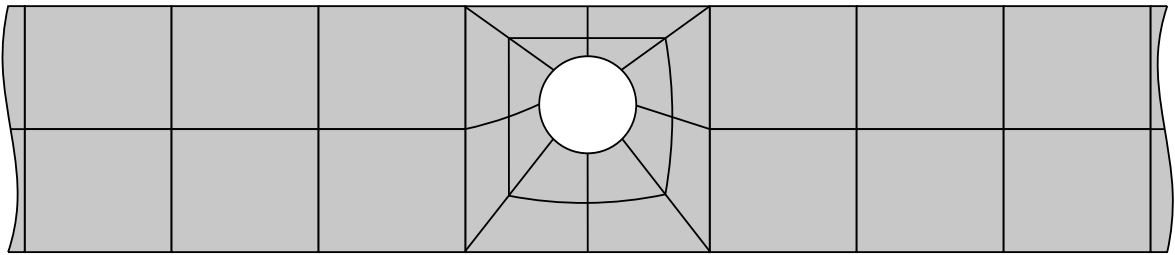


Figure 8.11: Blending elements used for the geometrically exact discretization.

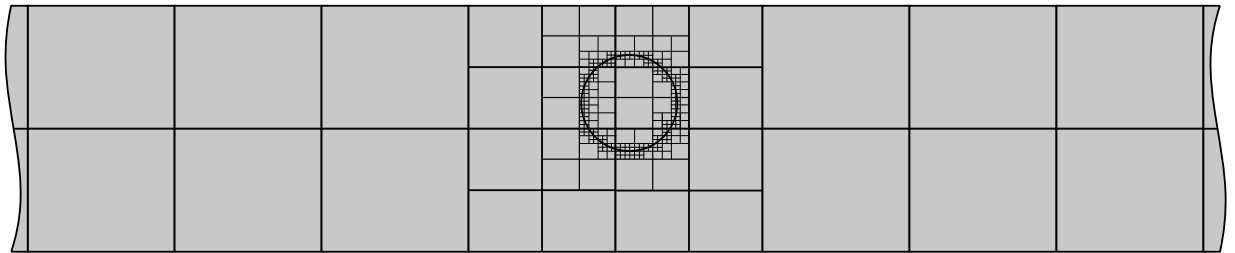
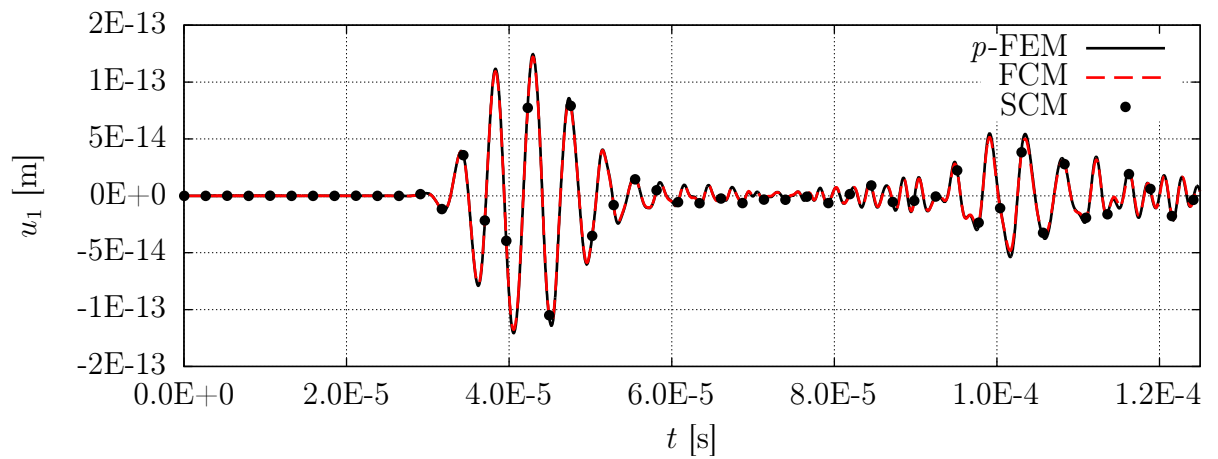


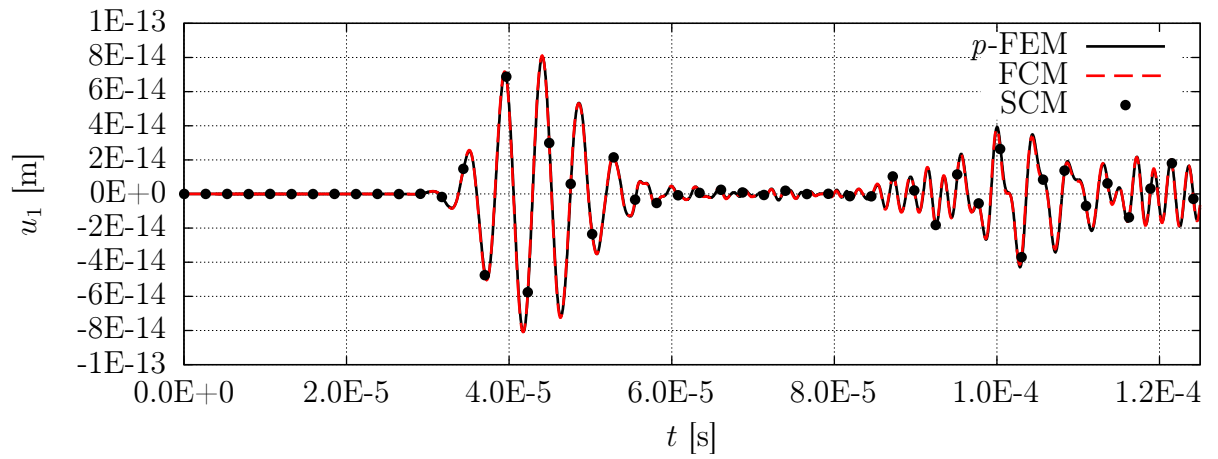
Figure 8.12: Sub-cells generated by the adaptive integration algorithm. The integration sub-cell refinement level is $k = 5$.

The different curves are virtually coincidental for all numerical approaches, thus emphasizing the applicability of fictitious domain methods to capture the discontinuity of the structure. As we can see, the reflections and mode conversion phenomena are well resolved. Only the displacements in x_1 -direction are depicted. As no new insights can be gained from the displacement field in x_2 -direction, the respective figures have been omitted.

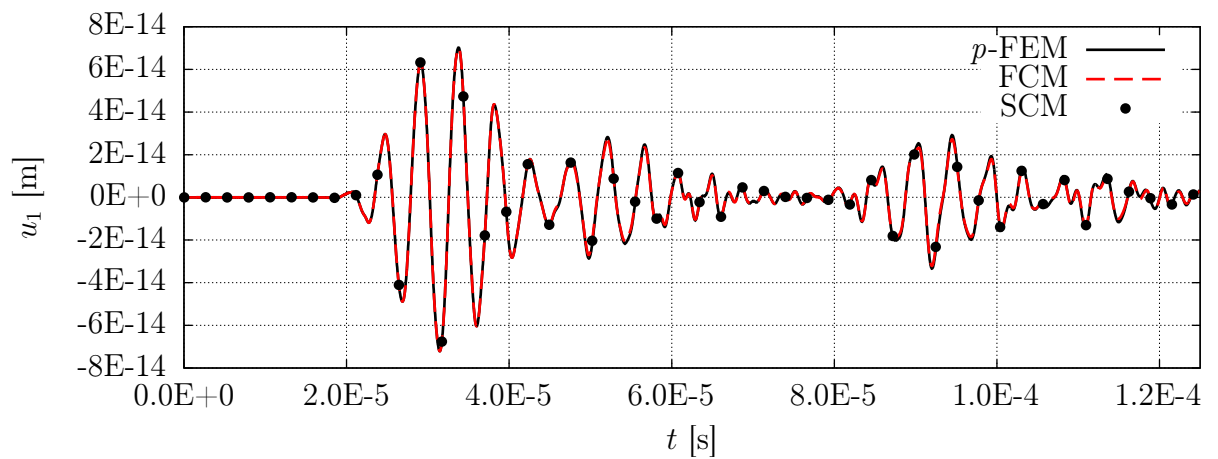
The extension of the higher order fictitious domain method to include the use of spectral shape functions entails the possibility to significantly speed up transient simulations. Because of the nodal character of Lagrange-type Ansatz functions the mass matrix can easily be diagonalized. Therefore, instead of deploying an implicit time-stepping scheme such as the Newmark method, another option would be to employ the CDM, one of the most widely-used explicit time-integration algorithms. By using this method, the numerical efficiency can be vastly improved making the SCM an appropriate tool for high-frequency wave propagation analysis.



(a) u_1 -displacement signal at P_1

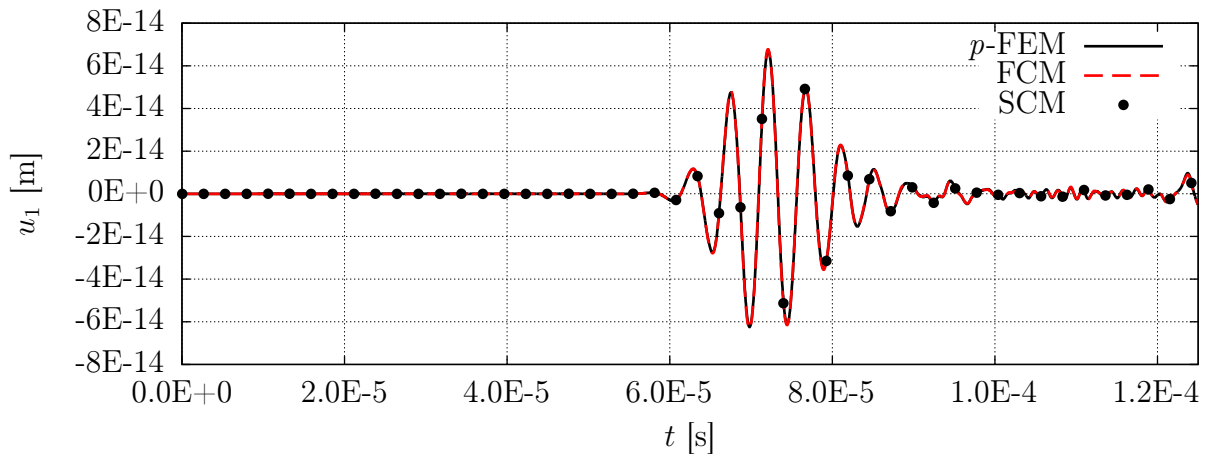


(b) u_1 -displacement signal at P_2



(c) u_1 -displacement signal at P_3

Figure 8.13: Comparison of the time history of the displacements for the different numerical approaches, namely the p -FEM, the FCM and the SCM. An excellent agreement of the numerical results is to be observed.



(d) u_1 -displacement signal at P_4

Figure 8.13: Comparison of the time history of the displacements for the different numerical approaches, namely the p -FEM, the FCM and the SCM. An excellent agreement of the numerical results is apparent.

In the present section, all results for the SCM are based on a consistent mass matrix, due to the fact that in the course of the presented research, we observed that the diagonalized mass matrix featured negative masses on the principal diagonal when relying on a simple row-sum lumping technique (Section 4.6.2). This leads to a divergence of the central difference time-stepping scheme. We have to bear in mind, however, that the negative masses are only connected to the cut cells of the geometry. If only a few cells are used to discretize the perturbation in the structure, the following approach can be suggested [177]:

All uncut cells can be numerically integrated by means of a GLL-quadrature lumping the elemental mass matrices. The cut cells however are integrated via a standard Gaussian quadrature, resulting in a consistent elemental mass matrix. The inversion of the assembled mass matrix is nonetheless numerically cheap and thus facilitates the use of an explicit time integration scheme. First studies show that the results of this practical approach are comparable to the fully consistent mass matrix approaches. In the next section, however, a different lumping scheme is introduced to take advantage of an explicit time-marching algorithm. Apart from introducing a proper, specific mass-lumping technique for the SCM, this also serves to further reduce the numerical effort.

In the following sections, we further focus on the possibility of mass-lumping in the context of the SCM and illustrate the achieved advantages.

8.3 Two-dimensional porous plate

According to the results published in reference [177] and the information gathered in the previous section, both a nodal quadrature (cf. Section 4.6.1) and a row-sum lumping technique (cf. Section 4.6.2) seem to be inappropriate for the diagonalization of the mass matrix of cut cells (cells that are intersected by the physical boundary). We therefore

propose to deploy the HRZ-lumping technique (cf. Section 4.6.3) [178]. This method yields positive entries on the diagonal of the lumped mass matrix while conserving the mass. The lumped mass matrix is computed directly from the consistent mass matrix. Consequently, the effects of the geometry of the cell and the distribution of the mass inside the cell are taken into account [178].

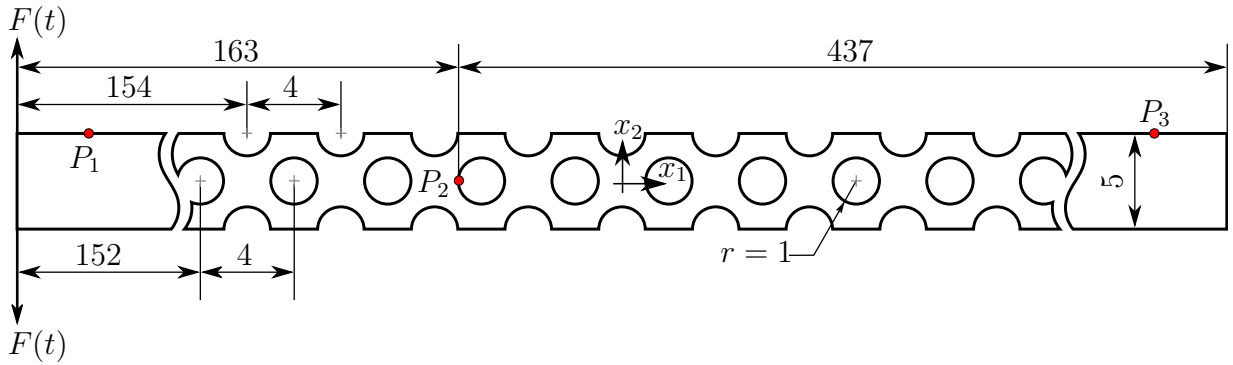


Figure 8.14: Porous plate with 13 circular holes in the middle and 12 semi-circular cut-outs on each side (top and bottom edge). The Neumann boundary (excitation forces) conditions are also illustrated. The coordinates of the three measurement points are: P_1 ($x_{1P_1} = 100$ mm, $x_{2P_1} = 2.5$ mm), P_2 ($x_{1P_2} = 163$ mm, $x_{2P_2} = 0$ mm), P_3 ($x_{1P_3} = 302$ mm, $x_{2P_3} = 2.5$ mm) [178].

A two-dimensional porous aluminum plate, as shown in Fig. 8.14, serves to demonstrate the capabilities of the suggested approach. The dimensions, material properties and boundary conditions are the same as in the previous section - so the element size is similar too. The discretization of the p -version of FEM and the FCM/SCM are illustrated in Fig. 8.15. The h -version uses isoparametric elements to describe the geometry, deploying linear or quadratic shape functions while the p -version draws on the blending function method (cf. Section 4.4.1). In contrast, the fictitious domain concept exploits the adaptive integration (cf. Section 5.2.2) in conjunction with an inside/outside test.

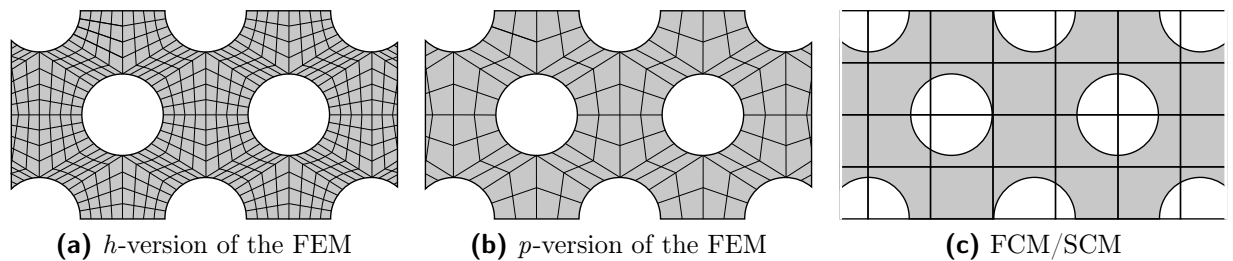
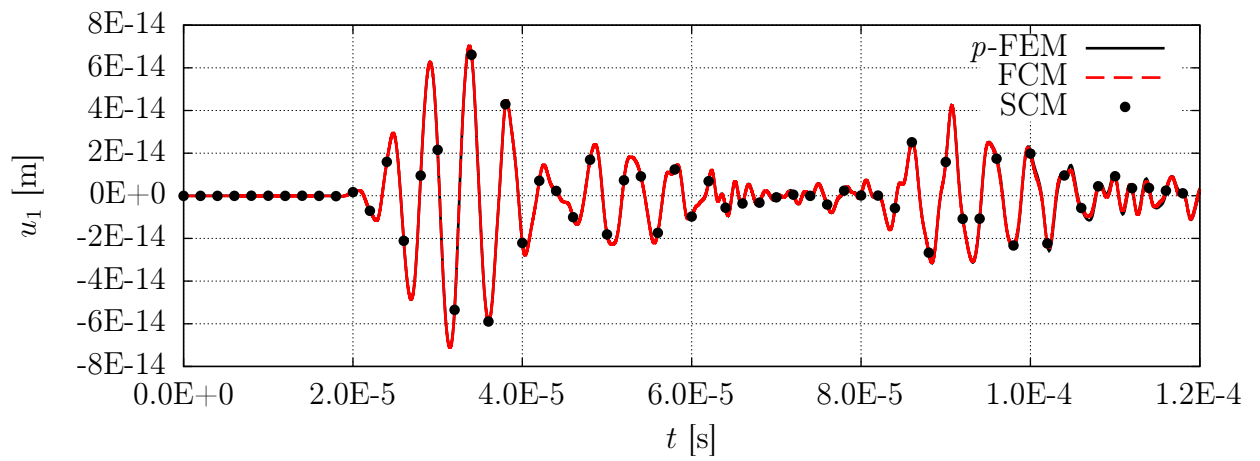


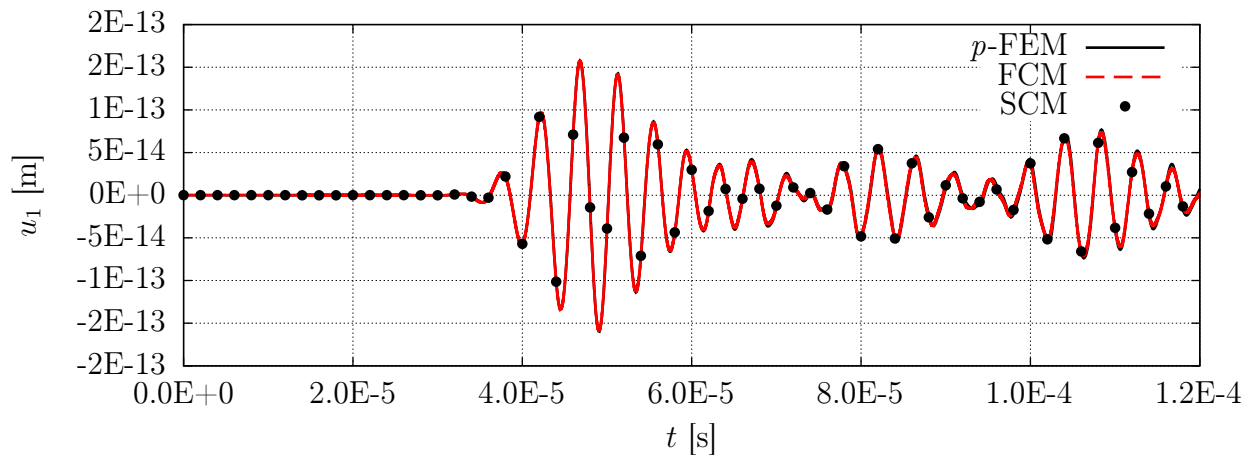
Figure 8.15: Discretization of the porous plate [178].

The simulation procedure is as follows. The mass matrices of those cells that are entirely within the physical domain (“full of material”) are lumped inherently by applying a GLL quadrature. On the other hand, cells that are intersected by the boundary of the domain are treated differently: Their mass and stiffness matrices are computed consistently by means of an adaptive integration technique, employing a quadtree refinement. Hereafter, the cell mass matrix is lumped using the HRZ-technique.

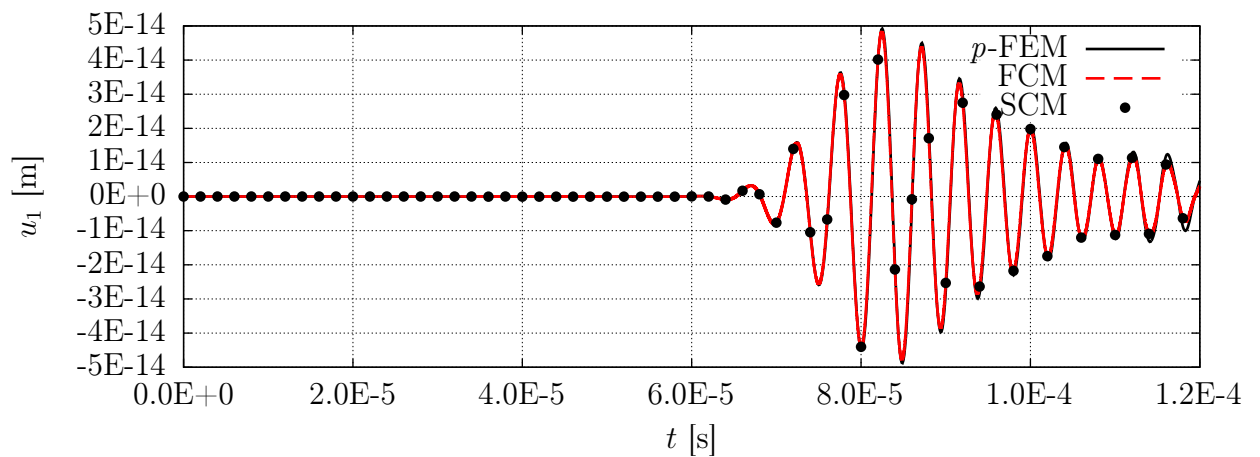


(a) u_1 -displacement signal at P_1

Figure 8.16: Displacement history at the measurement points.



(a) u_1 -displacement signal at P_2



(b) u_1 -displacement signal at P_3

Figure 8.17: Displacement history at the measurement points.

In order to assess the performance of the mass-lumping scheme, we focus on the the displacement history at points P_1 to P_3 . The reference solution derives from a case in which both the spatial and the temporal resolution are very fine (numerical “overkill” solution: $n_e = 4694$ (p -FEM), $p = 9$, $\Delta t = 10^{-9}$ s). Apart from some very small deviations at $t > 1 \cdot 10^{-4}$ s, the displacements are approximated accurately (cf. Fig. 8.17) and the proposed lumping technique seems to be effective and appropriate for nodal-based fictitious domain methods.

A more detailed analysis of different mass-lumping techniques and the accuracy of the proposed approach is published in reference [178]. Therein, the computational time is assessed and compared to other numerical approaches as well.

8.4 Two-dimensional plate: A_1 -mode

Although higher order Lamb waves modes (S_1 , A_1) are currently not widely used to detect damages, except in the field of non-linear acoustics [23–25], they could be of interest for further applications. So far, the literature features hardly any higher order modes captured by FE models. To demonstrate that HO -FE formulations are able to capture these modes, the excitation frequency is increased to $f_c = 1.2$ MHz. Here, the A_1 -mode is excited as well (cf. the dispersion diagrams Fig. 2.4). The model set-up is similar to the one described in Section 7.1 and depicted in Fig. 7.1, with the only difference that two collocated point forces are now applied at the top and the bottom surface to exploit a mono-modal excitation of the anti-symmetric modes. Therefore, the amplitudes exhibit a phase shift of 180° . The results for the symmetric Lamb wave mode are not displayed, for only the S_0 -mode exists at the chosen center frequency. Hence, no new insight can be gained. The group and phase velocities (wavelengths) of the A_0 - and A_1 -mode are read from the dispersion curves (cf. Fig. 8.9)

$$\begin{aligned} c_{g_{A_0}} &= 3100 \text{ m/s} & \text{and} & & \lambda_{A_0} &= 2.283 \text{ mm} \\ c_{g_{A_1}} &= 3652 \text{ m/s} & \text{and} & & \lambda_{A_1} &= 5.889 \text{ mm}. \end{aligned}$$

In order to observe two distinct wave packets without any reflections interfering with the signal, the dimensions of the plate are adjusted to the following values: $l_p = 700$ mm, $l_a = 100$ mm and $l_b = 400$ mm.

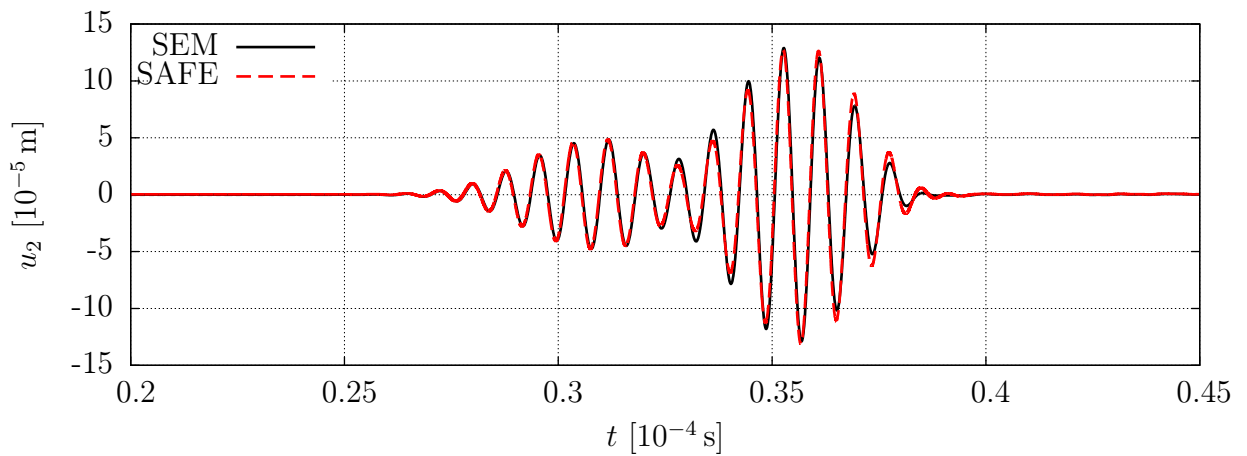
According to the results obtained in Section 7.5, the following discretization is proposed for the SEM (consistent mass matrix formulation):

- SEM: $p_{x_1} = 3$, $p_{x_2} = 3$, $p_{x_3} = 6$, $\chi_{A_0} = 8$ (cf. Fig. 7.5b).

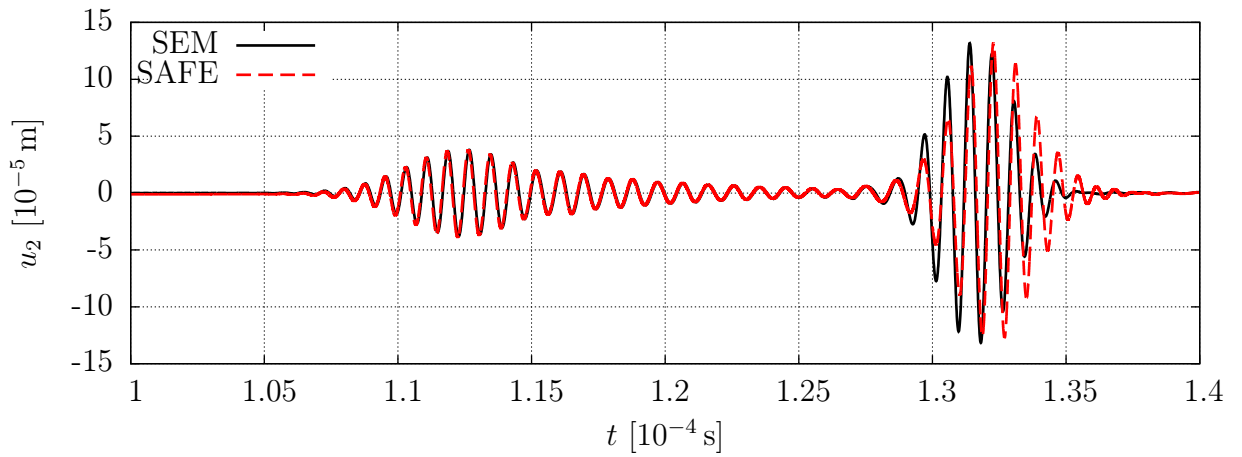
8 nodes per wavelength are chosen to ensure accurate results, since only the two basic modes were assessed by the convergence studies. The out-of-plane polynomial degree was increased in order to ensure a discretization of 8 nodes per wavelength in the out-of-plane direction. This is necessary as the wavelength of the A_0 -mode is almost equal to the plate thickness. A semi-analytical reference solution is chosen in order to evaluate the quality of the results. Fig. 8.18 displays the history plot saved at points A and B for the SAFE method [21] and the SEM. Evidently, the introduced guideline provides for a good agreement between the SEM and the SAFE method. Both the group velocity and the signal amplitudes are captured. As the p -FEM and the Fourier- p -FEM show the

same behavior, their results are not displayed. Considering the history plot at point B , the effects of dispersion are demonstrated clearly as well. In the chosen frequency range, the A_0 -mode is almost not dispersive - whereas the wave form of the A_1 -mode is notably distorted compared to the initially introduced excitation signal, cf. Fig. 2.4.

This example serves to demonstrate that even higher order Lamb wave modes can be captured if the discretization is chosen in accordance to the method proposed in Section 7.5. In contrast to the conventional lower order FEM, the various higher order approaches are an effective tool to address a frequency range containing more than the two fundamental guided wave modes.



(a) Point A .



(b) Point B .

Figure 8.18: Time history of the displacement field at the measurement points A and B in thickness direction (u_2). Comparison of the SEM and the SAFE method with respect to the resolution of the excited A_0 - and A_1 -mode.

8.5 Three-dimensional plate with a conical hole

To verify the results gained from the two-dimensional convergence studies conducted in Section 7.5, we will address the Lamb wave propagation in a three-dimensional plate with a conical hole. This model serves as an example of a more complex geometry, featuring reflections at the boundaries of the structure as well as a mode conversion at the defect. The more advanced test structure is to show that the guideline for an optimal discretization obtained in the previous Chapter 7 can easily be generalized even to three-dimensional problems involving geometrically more complex parts, like conical holes.

Numerical model A sketch of the model set-up is shown in Fig. 8.19. We use collocated actuators to exploit the advantages of a mono-modal excitation and excite the fundamental symmetric Lamb wave mode S_0 by driving the transducers in-phase. This gives a clear view of the mode conversion when encountering the conical hole.

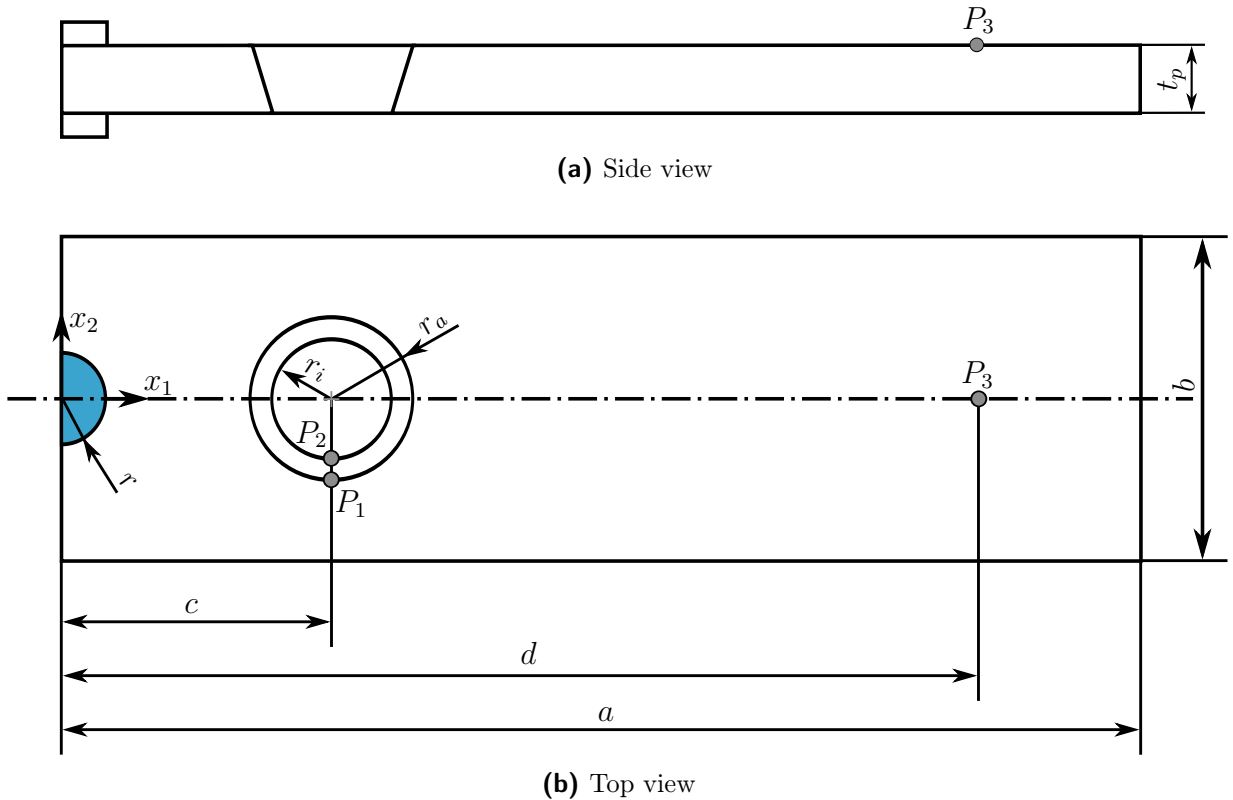
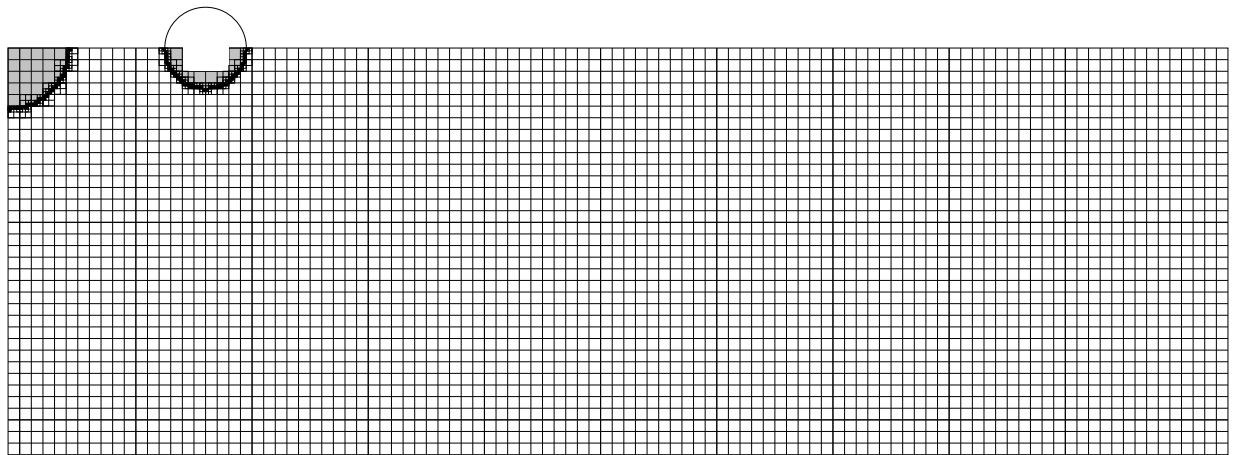
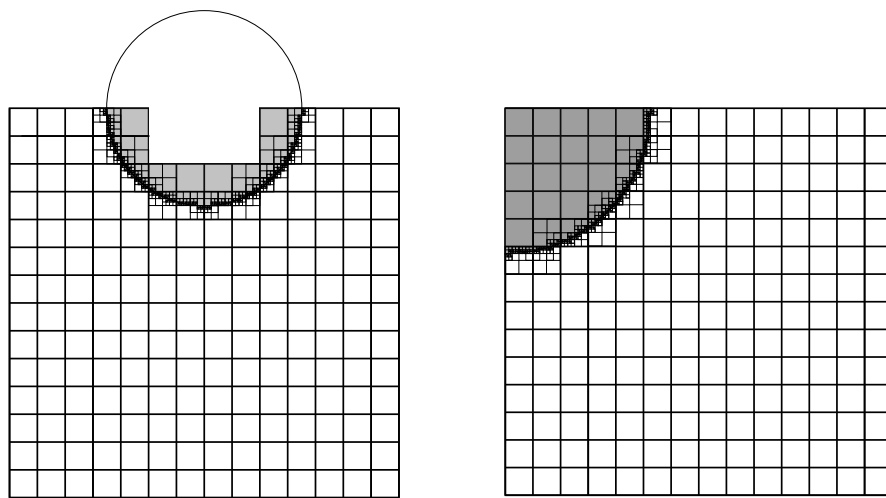


Figure 8.19: Aluminum plate with a conical hole. Dimensions: $a = 300$ mm, $b = 200$ mm, $c = 50$ mm, $d = 200$ mm, $r_a = 10$ mm, $r_i = 9$ mm, $h = 2$ mm (thickness of the plate); Material properties: Aluminum (cf. Tab. 2.1); Excitation: collocated transducers ($r = 15$ mm) at the origin of the coordinate system driven by a sine burst (cf. Eq. (7.1), $f_c = 175$ kHz, $n = 3$).

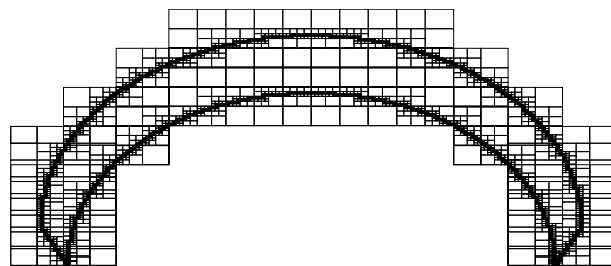
In reference [15], Ahmad and Gabbert showed that only an asymmetric perturbation of the wave field can cause a mode conversion. That is why, a conical hole has to be used and a cylindrical hole is not appropriate.



(a) FC discretization



(b) Detailed view of the adaptive refinement for the integration sub-cells: conical hole (left) and piezoelectric actuator (right).



(c) Detailed isometric view of the adaptive refinement for the integration sub-cells for the conical hole. Only cut cells are displayed.

Figure 8.20: FC and SC (spectral cell) discretization of the aluminum plate with a conical hole. The guided waves are excited by means of a piezoelectric transducer. Mode conversion occurs at the conical hole. Both the actuators and the conical hole are indicated in the figure by their sub-cell refinement and the grey shade.

The FC discretization and the integration sub-grid for the numerical quadrature are illustrated in Fig. 8.20. The size of the FCs matches the guidelines proposed in Section 7.5

and in Willberg *et al.* [78, 308], respectively. A detailed explanation of the methodology can be found in Sections 8.2 and 8.4.

The FC and the SC models use an anisotropic Ansatz space. That is to say, that the polynomial degree in the out-of-plane and in the in-plane direction are chosen differently. According to references [78, 308], the in-plane polynomial degrees are $p_{x_1} = p_{x_2} = 3$ and the out-of-plane polynomial order is $p_{x_3} = 4$.

To ensure accurate results, the element/cell size is $b_e = 0.2828$ mm. The FCM results are marched trough time using the Newmark method ($\Delta t = 5 \cdot 10^{-9}$ s), while the SCM draws on the CDM (Δt is determined according to Eq. (4.77); $\Delta t \approx 1 \cdot 10^{-9}$ s). Thus, a mode conversion can be detected visually by looking at the displacement field in the vicinity of the hole. The wave field is excited using the same piezoelectric transducers that have been thoroughly investigated in Section 8.1.

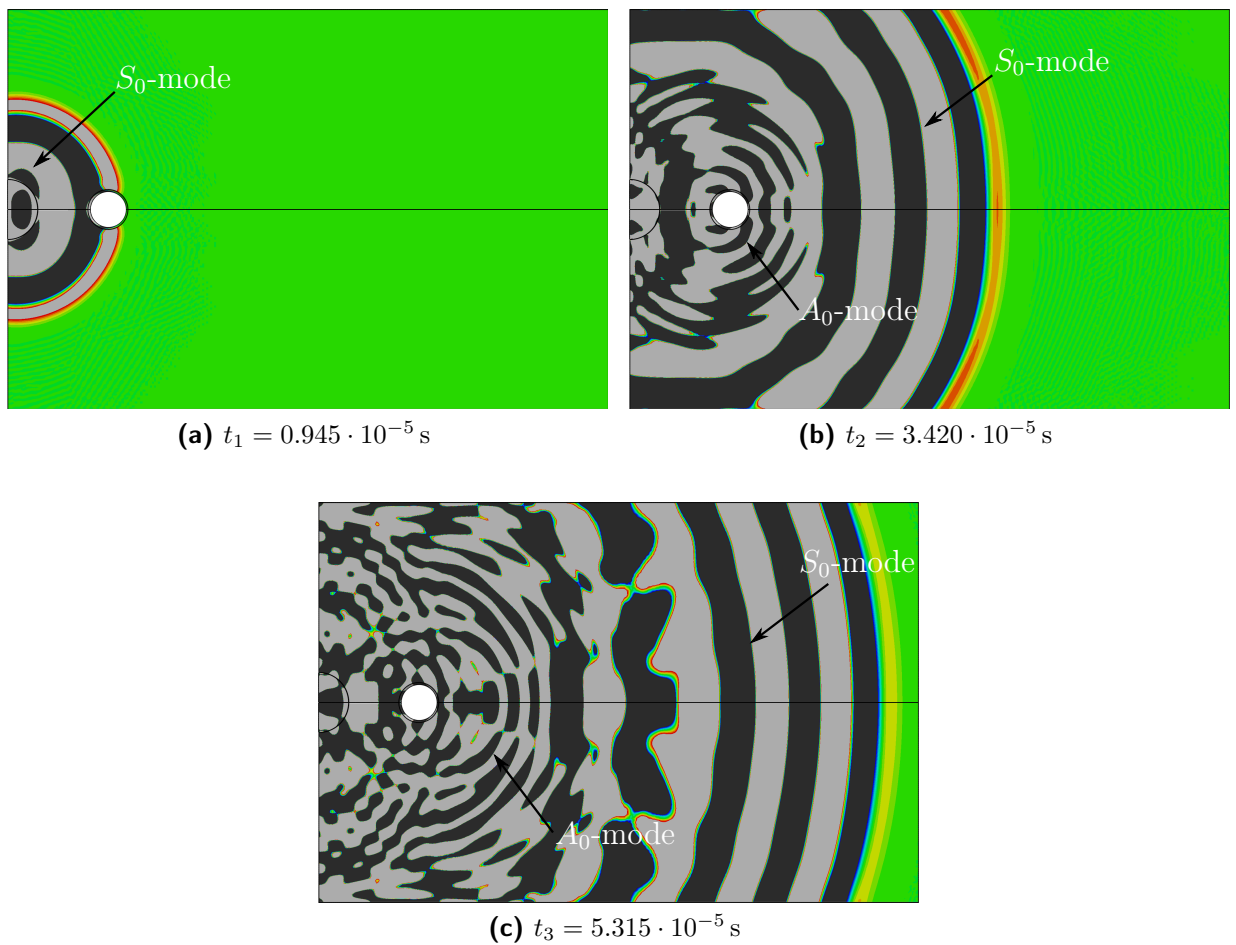
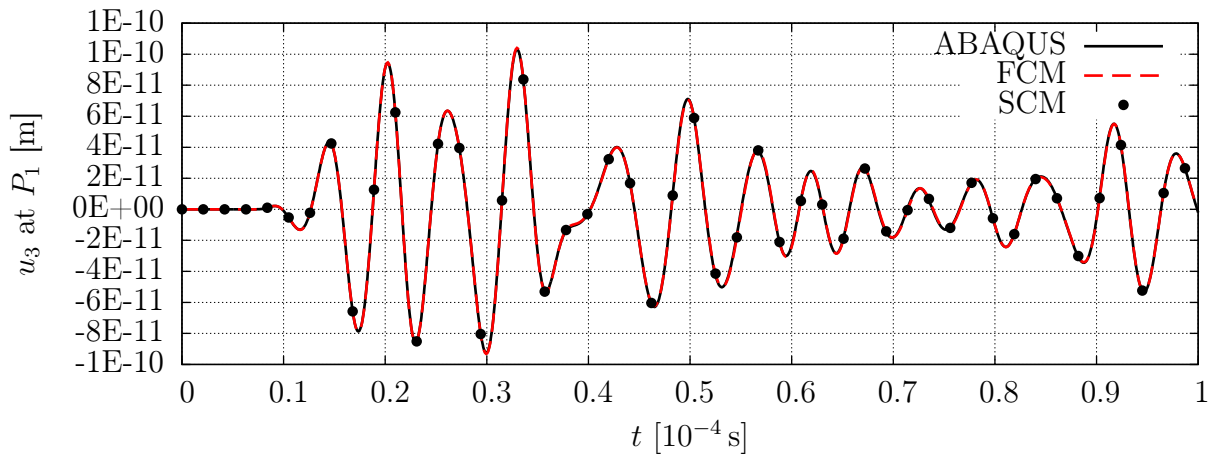
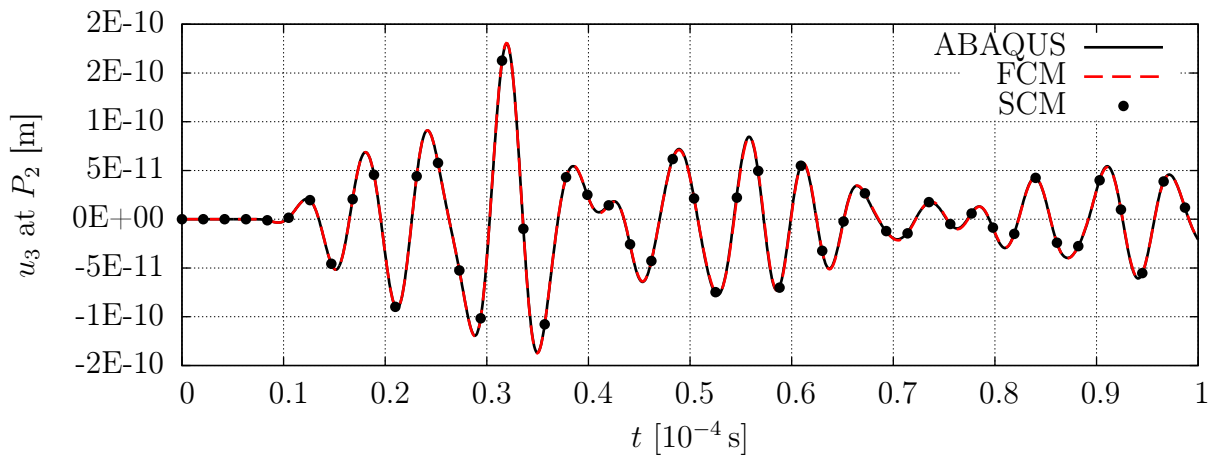


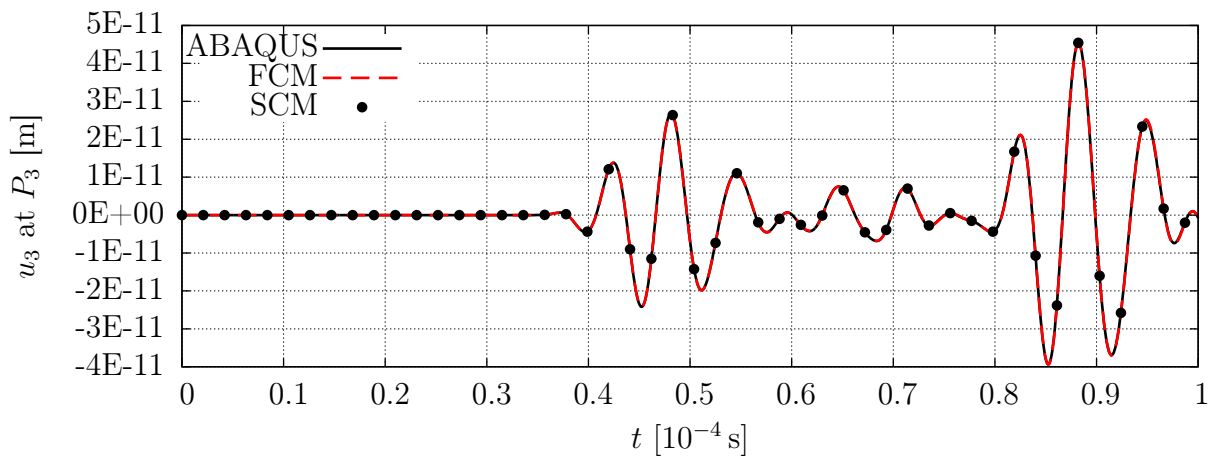
Figure 8.20: Contour plot of the displacement field in x_3 -direction. The propagating of the incident S_0 -wave packet is shown in part (a) of the figure. The complexity of the wave field is highlighted at two different time instances. Parts (b) and (c) show that - even in such a relatively simple structure - complex signals are generated due to mode conversion from the incident S_0 -mode to an A_0 -mode as well as a reflected and transmitted S_0 -mode. The additional reflections at the boundary and the discussed mode conversion at the perturbation of the plate-like structure clearly demonstrate the multi-modal behavior.



(a) Comparison of the ABAQUS reference solution at point P_1 to the FCM/SCM results, obtained using the optimal discretization.



(b) Comparison of the ABAQUS reference solution at point P_2 to the FCM/SCM results, obtained using the optimal discretization.



(c) Comparison of the ABAQUS reference solution at point P_3 to the FCM/SCM results, obtained using the optimal discretization.

Figure 8.21: Time history of the displacement field at the measurement points in thickness direction (u_3) - FCM/SCM.

Results Fig. 8.21a demonstrates the occurrence of the mode conversion phenomenon while highlighting the interaction between the travelling wave and the conical hole. Since no analytical solution is available for this benchmark problem, we compare the results of the different higher order FE approaches with an ABAQUS reference solution, deploying 20-node hexahedral FEs (C3D20) on a very fine grid ($n_{dof} \approx 1.5 \cdot 10^6$). This corresponds to more than 50 nodes per wavelength to ensure a converged solution with high accuracy. Please note that the symmetry of the structure is exploited to save numerical effort, so the model only depicts half of the plate. Fig. 8.21 plots the time history curves of the displacements at points P_1 to P_3 for the FCM and for the SCM, respectively.

The agreement between the proposed higher order fictitious domain methods and the commercial software ABAQUS is remarkable. The relative error in group velocity between the reference solution and the introduced methods is less than 0.1%. We consequently conclude that the FCM and the SCM are able to capture and resolve characteristic features of ultrasonic guided-wave propagation, such as mode conversion. Please refer to reference [178] for a thorough assessment of the convergence properties of the SCM.

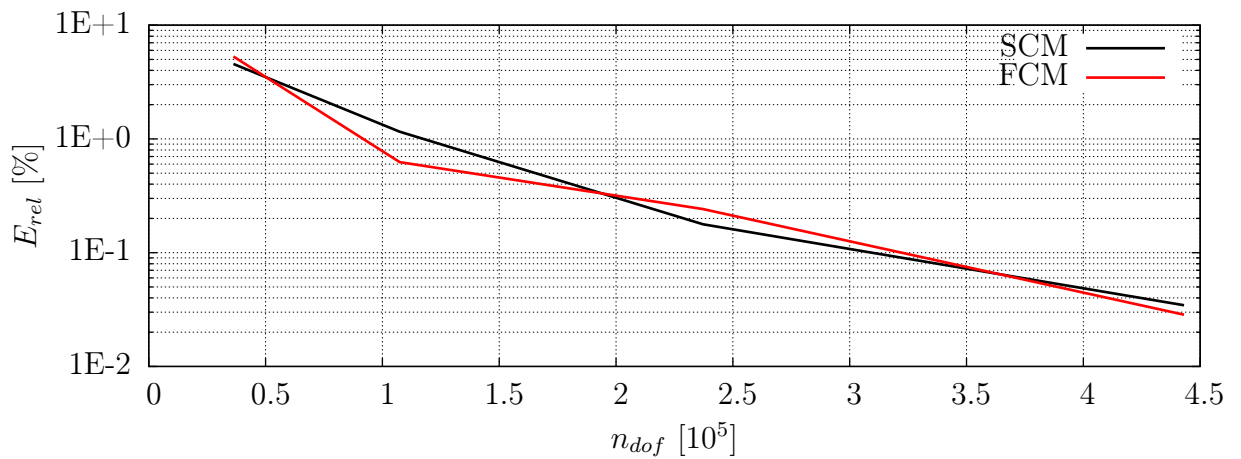
Error assessment and computational effort In order to provide an impression of the convergence properties of the SCM in comparison to the FCM, we conduct a convergence study based on a p -refinement. In this convergence study, the polynomial degree is successively increased from $p = 2$ to $p = 5$ (isotropic polynomial degree Ansatz). Both the relative error in the time-of-flight of the wave packets and the error in the L_2 -norm of the deflection are used to judge the accuracy of the solution. The L_2 -norm is defined as

$$e_{L_2} = \sqrt{\frac{\sum_{i=1}^{n_{step}} (u_{3,num}^i - u_{3,ref}^i)^2}{\sum_{i=1}^{n_{step}} (u_{3,ref}^i)^2}}, \quad (8.11)$$

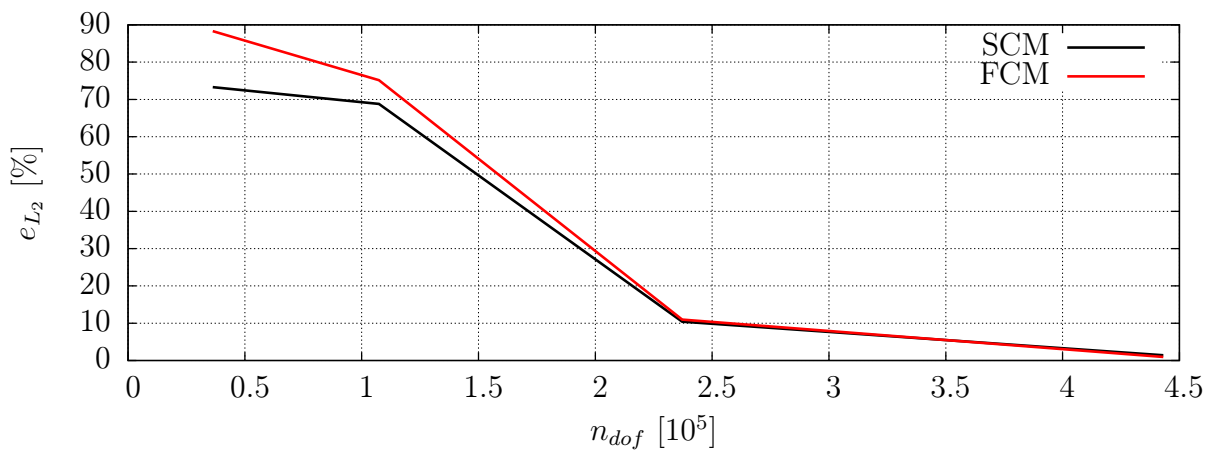
where n_{step} denotes the total number of time-steps of the solution, u_3^i is the out-of-plane displacement at the observation point (at point P_3), and the subscripts *num* and *ref* stand for numerical and reference solution, respectively. We also contemplate the computational time for the solution of the equation of motion in order to provide some preliminary statements regarding the efficiency of the algorithm.

Fig. 8.22a shows the convergence with respect to the time-of-flight t_c of the whole wave packet. We infer from the results that the convergence properties with respect to the time-of-flight are essentially similar for the proposed higher order methods. The same still holds when studying the error of the displacement signal in the L_2 -norm, cf. Fig. 8.22b. For polynomial degrees higher than 4, a plateau is reached in the L_2 -error. This can be attributed to the fact that the reference solution is not accurate enough, partly because of the geometry description of the cone and partly because of the insufficient refinement of the discretization. On the other hand, the emphasis of this example is placed on illustrating that the convergence properties of different higher order approaches are very similar, which is clearly apparent from Figs. 8.22a and 8.22b.

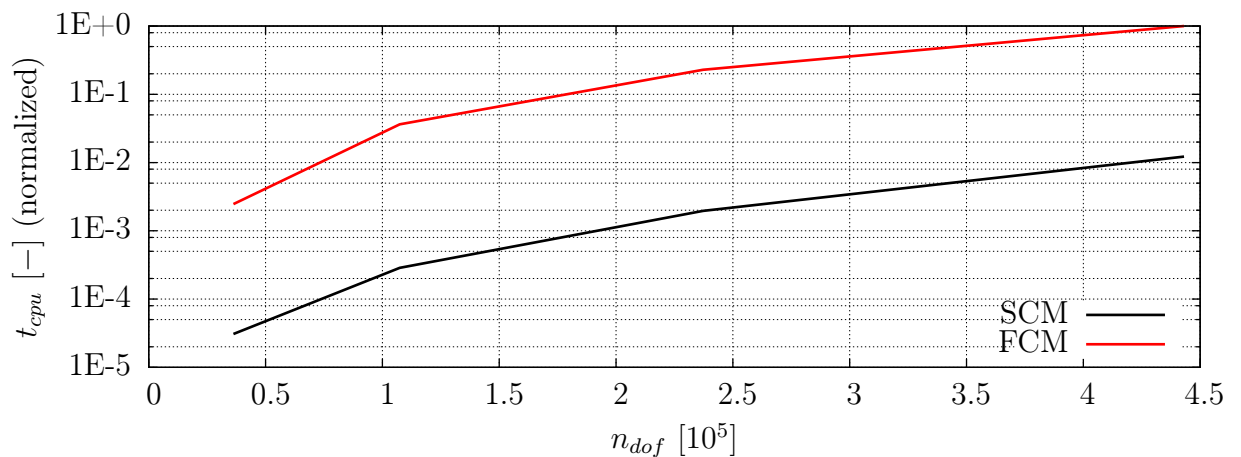
The development of the computational time t_{cpu} is illustrated in Fig. 8.22c. We have to bear in mind, however, that the time allotted for solving the equations of motion is taken into account. In the case of the SCM, a simple finite difference solver, namely the CDM, is used for the time-integration.



(a) Convergence curve for the relative error in time-of-flight



(b) Convergence curve for the relative error in the L_2 -norm



(c) Computational time (normalized with respect to FCM ($p = 5$); SCM (lumped mass matrix) is solved using the CDM (explicit time-integration); FCM (consistent mass matrix) is solved using the Newmark method (implicit time-integration)

Figure 8.22: Convergence graphs comparing the performance of the SCM and the FCM (tensor product space).

The mass matrix of the cut cells is lumped employing the HRZ-technique while the mass matrix of the uncut cells is inherently diagonal (GLL nodal quadrature). Mass-lumping is not an option when considering the FCM based on a tensor product space or trunk space formulation, so we employ a consistent mass matrix. As a result, we choose an implicit time-integration and integrate the equations of motion by means of the Newmark-method. The selected time-step is equal to the stability limit for the CDM, cf. Eq. (4.77). All results shown in Fig. 8.22c are normalized with respect to the computational time needed to solve the system of equations utilizing the FCM with the polynomial degree $p = 5$.

Based on the curves displayed in Fig. 8.22c, we conclude that the equations of motion can be solved efficiently relying on a combination of the SCM and the CDM. The computational time drops by over two orders of magnitude compared to solutions that are obtained using the FCM with a Newmark solver. It has to be born in mind, however, that the SCM requires hardly any manual input for discretizing the domain of interest, that is to say, generating the corresponding mesh is straightforward.

8.6 Validation - Aluminum plate with sensor network

This section focuses on a plate equipped with 8 piezoelectric transducers made of Sonox P5 (CeramTec). 4 transducers are operated as actuators (labeled with capital letters), while the others are operated as sensors (labeled with numbers).

Table 8.5: Material properties of Sonox P5. The poling direction of the material is the x_3 -direction. The vacuum permittivity (permittivity of free space) is given by $\kappa_0 = 8.8542 \cdot 10^{-12}$ As/Vm. The values of the non-zero components of the elasticity tensor \mathbf{C} , the piezoelectric coupling tensor \mathbf{e} , the dielectric tensor $\boldsymbol{\kappa}$ and the mass density ρ are given.

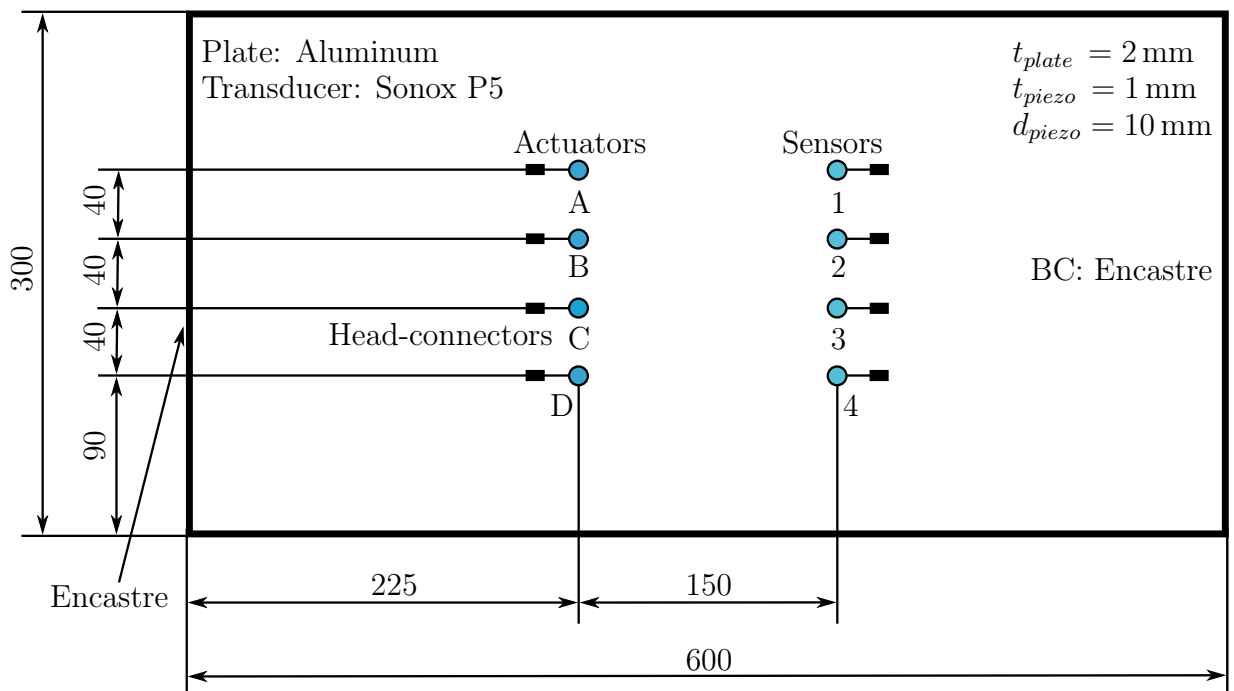
Mechanical properties		Electrical properties	
$C_{11} = C_{22}$	123.0 GPa	e_{31}	-2.2 N/Vm
C_{12}	81.00 GPa	e_{33}	16.3 N/Vm
$C_{13} = C_{23}$	77.00 GPa	e_{15}	18.0 N/Vm
C_{33}	110.0 GPa	κ_{11}^T / κ_0	1850
C_{44}	20.90 GPa	κ_{33}^T / κ_0	1850
$C_{55} = C_{66}$	28.10 GPa		
ρ	7650 kg/m ³		

Their location is given in Fig. 8.23. This set-up was originally used by Pavlopoulou et al. [20, 302] for the purpose of pattern recognition of Lamb waves in repaired structures. The experimental data to validate the numerical model was also provided by Dr. Pavlopoulou. The plate is fixed at the right-hand and left-hand side boundaries and its dimensions are given in Fig. 8.23. Tab. 8.6 shows the material properties of the piezoelectric transducers while the material data for the aluminum plate is listed in Tab. 2.1.

In the numerical study, actuator A is excited using a sine-burst modulated by a Hann-window (cf. previous section Fig. 8.19). The center frequency of the signal is $f_c = 240$ kHz and $n = 5$ periods, cf. Fig. 8.24.

As the model is again discretized following the guidelines published by Willberg *et al.* [78, 308], we employ the optimal anisotropic polynomial degree template, cf. Section 8.5. The FC size for the dimensions given for the plate and its material amounts to $b_e = 2.73$ mm.

Fig. 8.25 compares the experimental and numerical signals. The results of the electric potential are normalized (φ_{norm}) in order to compare the shape of the signals. On a global scale, a good agreement between both curves can be observed. The discrepancies are attributed to boundary conditions in the experiment which do not resemble an actual encastre. Accordingly, the numerical model employs stiffer boundary conditions. In addition, the ideal theoretical excitation signal used for the numerical model may comply completely with the experimental one, resulting in a modeling error that should not be disregarded.



(a) Geometry and dimensions of the aluminum plate.



(b) Photo of the experimental set-up.

Figure 8.23: Experimental setup and schematic graphic including the boundary conditions as well as the geometry for the aluminum plate.

Experiments have shown that, due to the ambient conditions, the “ideal” signal with which the transducer is driven is not always transmitted directly to the plate. For this reason, the plate’s response may differ slightly from the theoretically predicted signal. A third cause may possibly be attributed to the modeling of the head-connectors, which have been assumed to be made of aluminum, as well. Finally, the bonding conditions of both actuators and sensors in an experimental setup do not correspond to the model of a perfect bonding adopted in the FE model. The layer of adhesive cannot be regarded as negligible, since the plate was originally prepared for fatigue testing [20]. This might introduce additional errors that influence the simulated signal at the transducers. Considering the mentioned uncertainties, the results are promising and call for further research. We must also note that an optimal polynomial degree template with the suggested element size for this model results in approximately $5 \cdot 10^6$ degrees-of-freedom. Simulations such as the present one therefore require vast computational resources even for plates made of isotropic material (aluminum).

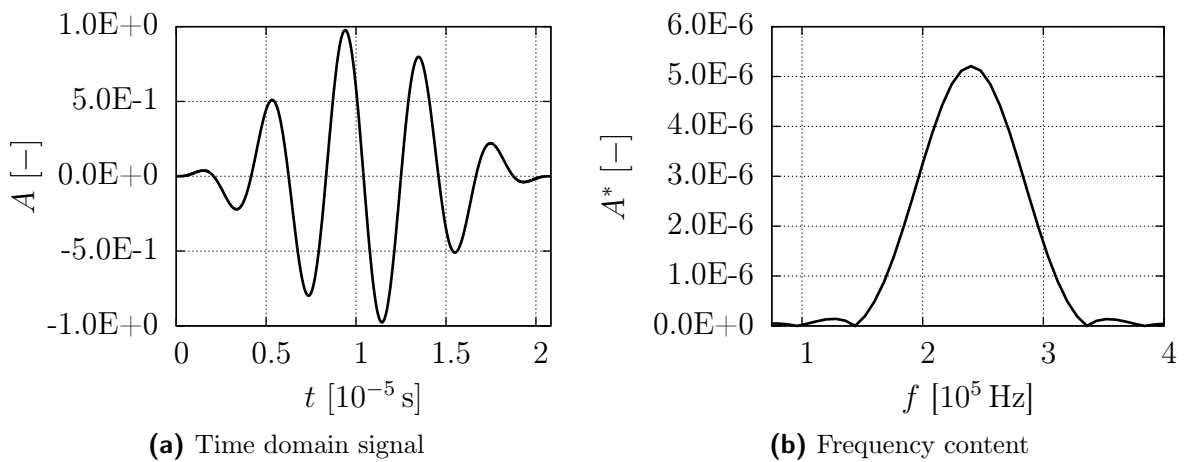


Figure 8.24: Loading function. Five-cycle ($n = 5$) sine burst modulated with a Hann-window. A center frequency of $f_c = 240$ kHz is chosen to excite the plate.

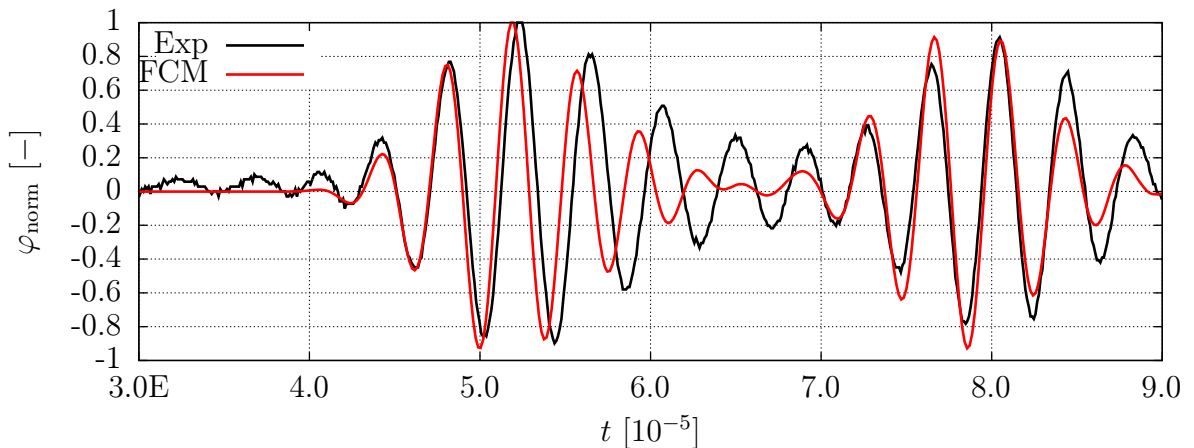


Figure 8.25: Comparison between numerical and experimental results. For this example actuator A was excited and the signal was measured at sensor 4, cf. Fig. 8.23a. The amplitude received at the sensor is normalized.

Spectral cell method - Summary Concerning spectral shape functions, the results found in the present and previous chapters indicate that mass-lumping techniques have only a negligible effect on the accuracy of wave propagation analysis. According to these findings we propose to combine the SEM with the FCM. Drawing on the GLL quadrature rule (cf. Section 4.6.1) for cells that are completely within the physical domain and on the HRZ-lumping technique (cf. Section 4.6.3) in conjunction with the adaptive integration scheme (cf. Section 5.2) for cut cells, we are able to diagonalize the mass matrix. For those reasons, we can fully exploit the computational advantages of an explicit time-integration method such as the CDM compared to implicit solvers, for example, the Newmark method. In analogy to the FE terminology we coined the term *spectral cell method* for the proposed method.

Chapter 9

Bandgaps

The focus of the present chapter is on wave propagation in inhomogeneous structures. In such systems, different phenomena can be observed. Here, a special emphasis is put on the so-called *bandgap effect*, starting with a brief introduction on the phenomenon. The basic principle is sketched in Fig. 9.1 [312]. Generally speaking, this effect occurs in waveguides consisting of at least two different materials with different material properties (elastic constants and density) and accordingly different wave velocities [313]. The set-up of the materials causes the waves to interact in such a way that there are frequency ranges in which no wave propagation occurs. To explain this phenomenon a periodic structure is taken as an example, cf. Fig. 9.1. The layout, however, does not need to be strictly periodic to observe a bandgap.

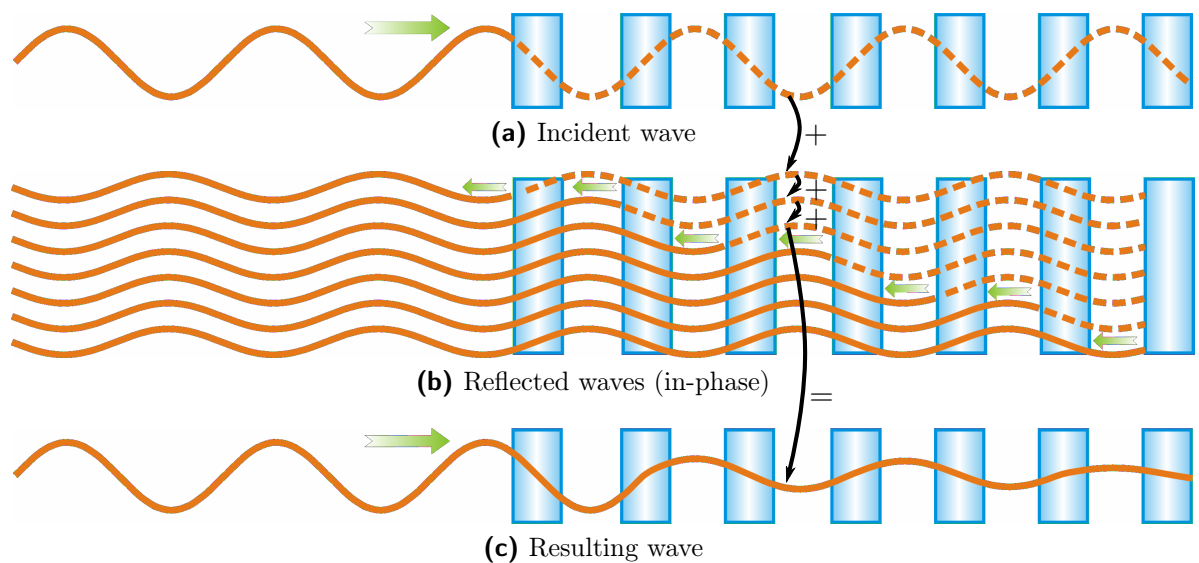


Figure 9.1: Schematic illustration of the wave propagation in a bandgap structure. The central frequency of the incident wave packet is within the bandgap frequency range; cf. [312].

In Fig. 9.1a the incident wave approaching a bandgap structure is shown. The dashed line indicates the wave propagation in an homogeneous material where the wave is neither reflected nor attenuated. In the periodic structure however the incident wave is partially reflected at each layer of the structure, cf. Fig. 9.1b. In part (b) we depict the reflected parts of the original wave as a solid line and its continuation as a dashed line. In case the center frequency (or to be exact a part of the frequency content) of the incident wave packet

is within the bandgap frequency range, the scattered waves are in-phase and consequently reinforce each other. If this bandgap condition is fulfilled, the amplitude of the transmitted wave decays exponentially with the number of inclusions. Considering an infinite number of inclusions the incoming wave will theoretically be totally reflected [314]. In Fig. 9.1c the transmitted wave is shown (at each obstacle a part of the energy is reflected). Here, also the amplitude decay is clearly visible. The incident and reflected waves consequently form a standing wave that cannot propagate through the structure [312].

Fig. 9.2 illustrates the behavior if the center frequency of the incident wave is outside the bandgap frequency range. Part (a) again shows the incident wave packet where the dashed line indicates the unperturbed wave propagation in a homogeneous material. At each obstacle the incident wave is naturally partly reflected. Due to the fact that the center frequency is outside the bandgap frequency range for this example the reflected waves are out-of-phase and therefore causing negative reinforcement (attenuation of the wave), cf. Fig. 9.2b. Accordingly, the wave is only slightly attenuated and can thus propagate through the material, cf. Fig. 9.2c [312].

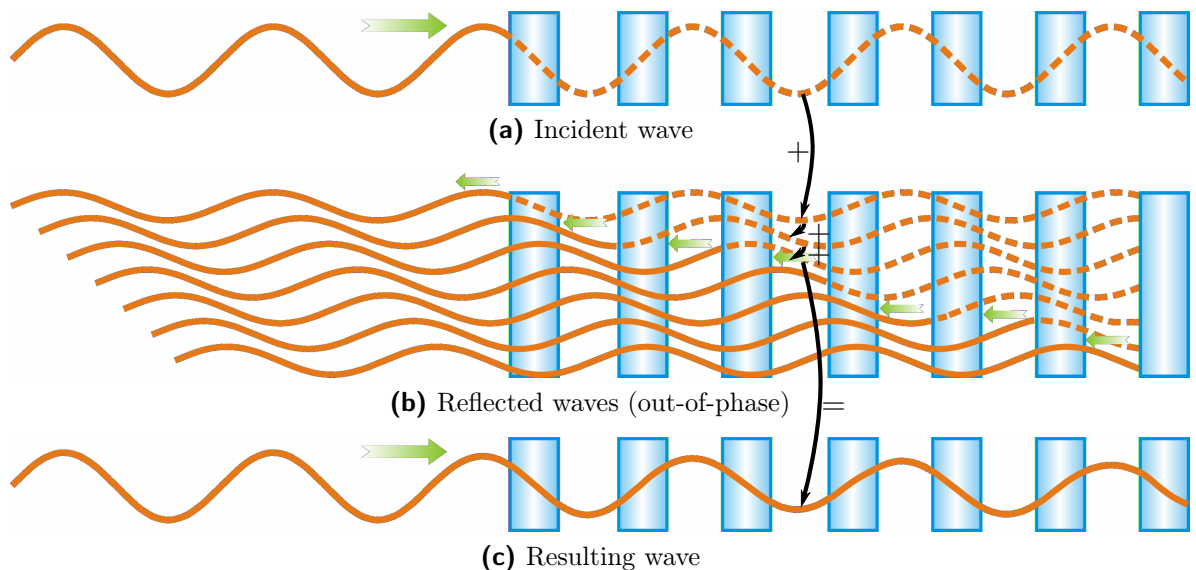


Figure 9.2: Schematic illustration of the wave propagation in a bandgap structure. The central frequency of the incident wave packet is not within the bandgap frequency range; cf. [312].

According to Jensen [314] the first published research concerning the bandgap phenomenon can be traced back to Rayleigh [315]. In certain materials, periodic structures waves may be totally reflected. A detailed overview of bandgaps can be found in [314] and the references cited within. Since the thesis at hand focuses on the propagation of elastic waves, phononic bandgaps are subject to further investigations. The term photonic simply refers to optical waves, pertaining to which the bandgap phenomenon has been extensively investigated [314, 316–319].

The structures under consideration in the present chapter are both numerically and experimentally investigated, highlighting the capabilities of higher order fictitious domain

approaches to model geometrically complex domains using an automated mesh generation procedure.

9.1 Bandgap structures

9.1.1 Fibonacci lattice

During the last century, research activities investigating phononic bandgap structures have been intensified [313, 314, 316, 320–324]. Recently, so-called Fibonacci super-lattices have been used in order to generate bandgap materials [323, 324]. A Fibonacci sequence consists of two different materials A and B , cf. Fig. 9.3. They are arranged in the following sequence starting with

$$S_0 = A \tag{9.1}$$

and

$$S_1 = B. \tag{9.2}$$

The first two sequences describe the homogeneous materials themselves. The n^{th} sequence can be generated by the recursive rule

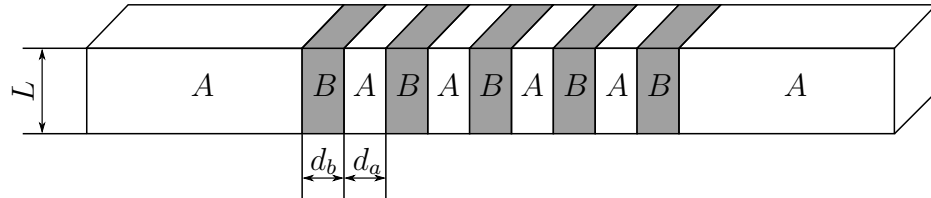
$$S_n = S_{n-1} \cdot S_{n-2} \quad \text{for } n \geq 2. \tag{9.3}$$

Therefore, the first Fibonacci sequences are

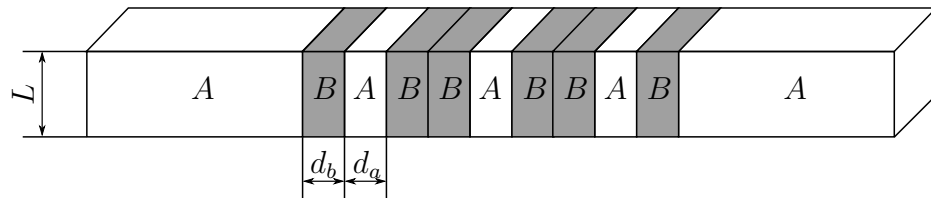
$$S_2 = BA \tag{9.4}$$

$$S_3 = BAB \tag{9.5}$$

$$S_4 = BABBA. \tag{9.6}$$



(a) Fibonacci sequence $S_2 = BA$ (five unit cells are exemplarily depicted)



(b) Fibonacci sequence $S_3 = BAB$ (three unit cells are exemplarily depicted)

Figure 9.3: Graphical representation of chosen Fibonacci sequences. The lattice is made of two different materials A and B arranged in a certain order.

Zhao *et al.* [324] found that for a material combination of tungsten and silicon one bandgap can be observed for the second Fibonacci sequence (S_2) at 1070 kHz to 1630 kHz. Furthermore, it is found that for higher order Fibonacci sequences the number of bandgaps increases.

9.1.2 Square hole arrangement

Zhang *et al.* [322] proposed a different type of phononic crystal by drilling a periodical array of holes in an aluminum plate, cf. Fig. 9.4. The mechanism that prevents the guided waves from travelling through the structure is the same as described in the previous section (cf. Fig. 9.1).

In general, bandgap structures become more efficient if a strong contrast in the elastic properties of the two materials is given. Typical applications of bandgap structures include sound filters [320, 322] and integrated optical circuits [314].

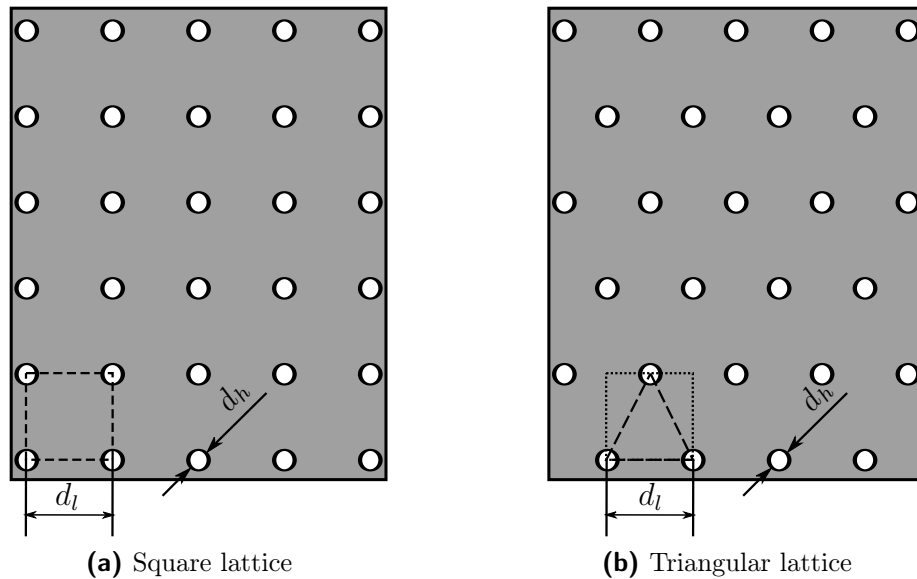


Figure 9.4: Illustration of the square and triangular layout of a lattice structure. The dashed lines indicate the unit cell of the material. The image indicates the alignment (array) of the holes that are crafted into the material.

In contrast to the periodic arrangement of materials, such as described above, also more complex layouts are possible. Due to the introduction of topology optimization to design bandgap structures [314, 318, 319], rather complex arrangements of mostly two materials have been proposed. The approach serves as a means to generate efficient waveguides [314]. Since topology optimization is out of the scope of the current thesis, we refer the interested reader to the thesis by Jensen [314] and the references cited therein.

9.2 Simulation results

In the current section, we briefly investigate the Fibonacci sequence S_3 (cf. Fig. 9.3b) and the square arrangement of holes (cf. Fig. 9.4a) in an aluminum plate. These two examples should highlight the feasibility of the proposed *HO*-FEMs and fictitious domain methods in the context of wave propagation analysis in heterogeneous media. Moreover, the current chapter introduces a new research field that is tailor-made for higher order fictitious domain approaches because of the geometrically complex shapes of bandgap structures and the possibility for topology optimization in order to generate structures with a desired behavior. The results that are obtained from the simulations are verified

and validated by means of numerical and experimental data which are available from the present literature.

9.2.1 Fibonacci lattice

Reference [324] lists results for different Fibonacci lattices. They employ the plane wave expansion method to compute the dispersion curves for the structure under investigation. Gao *et al.* [325], however, use the FEM to numerically determine bandgaps in periodic Fibonacci structures.

The periodic structure consists of a combination of tungsten (material B) and silicon (material A) whose material properties are given in Tab. 9.1. The width of the two materials is $d_a = d_b = 1$ mm and the plate thickness is $L = 1$ mm. We exemplarily choose the S_3 -Fibonacci sequence (cf. Eq. (9.5) and Fig. 9.5) to demonstrate the bandgap behavior of such periodic structures.

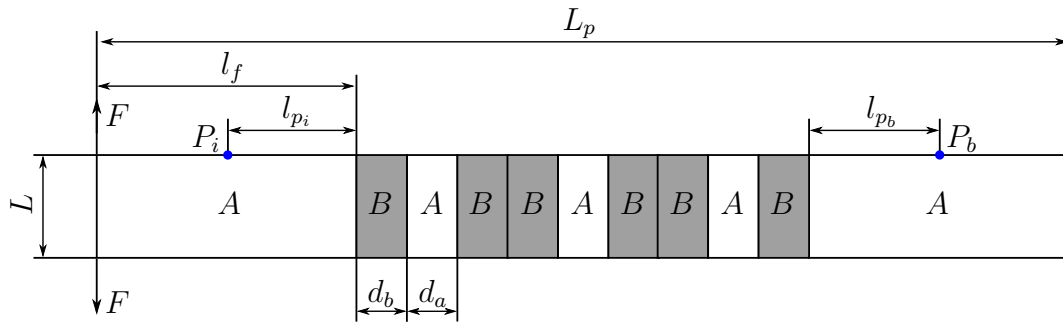
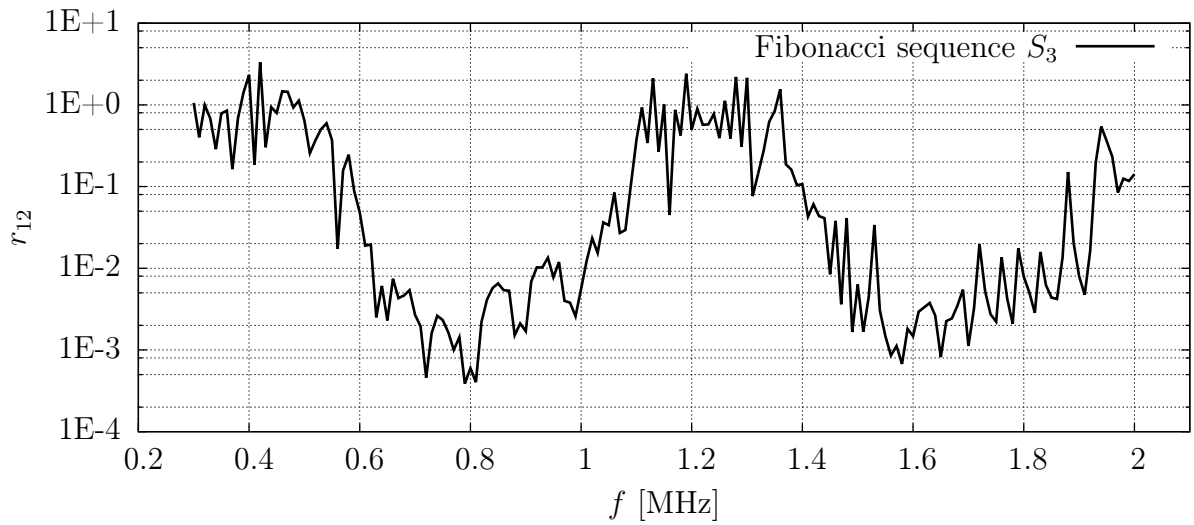


Figure 9.5: Two-dimensional model of the S_3 -Fibonacci sequence with loading conditions and dimensioning (three unit cells are exemplarily depicted).

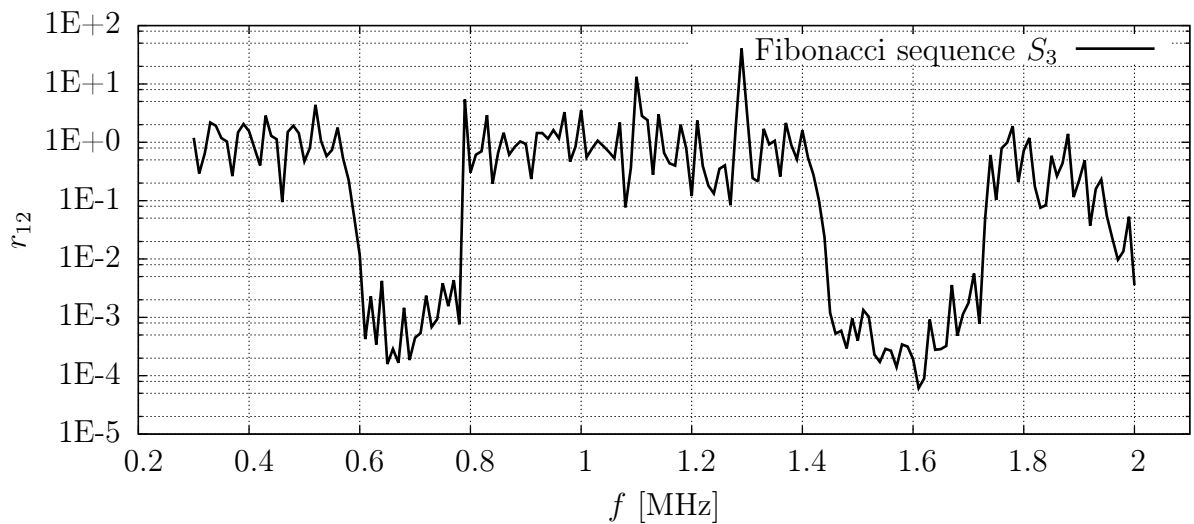
Table 9.1: Material properties of tungsten and silicon. Values of the non-zero components of the elasticity tensor \mathbf{C} and the mass density ρ are taken from [324].

Material	Tungsten	Silicon resin
C_{11}	502.0 GPa	165.7 GPa
C_{12}	199.0 GPa	63.90 GPa
C_{44}	152.0 GPa	79.56 GPa
ρ	19200 kg/m ³	2332 kg/m ³

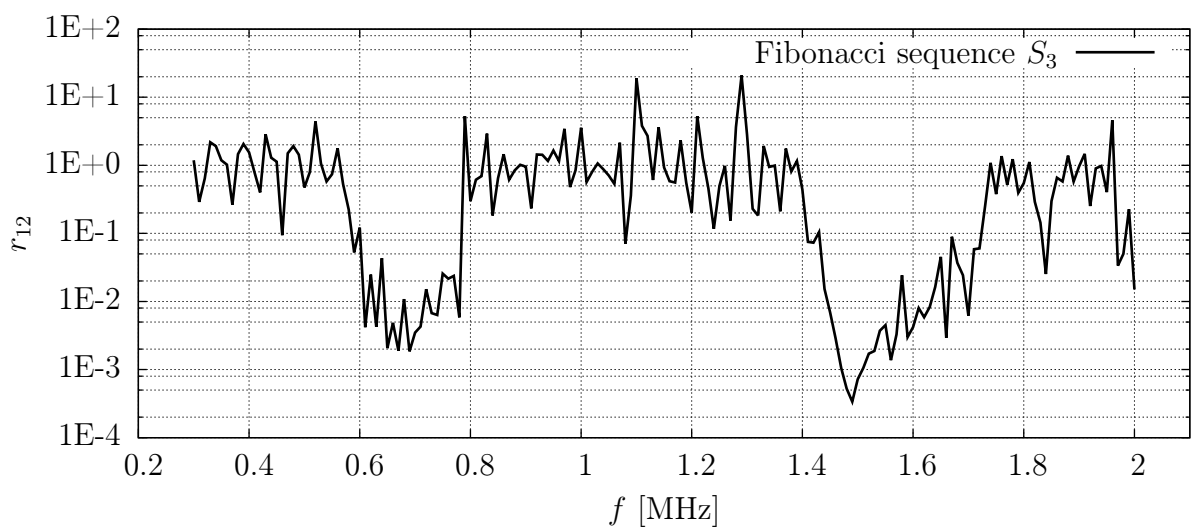
We record the displacement field one point in front of the Fibonacci sequence (P_i) and at a second point behind the Fibonacci lattice (P_b) to evaluate the structural behavior. The simulations are based on the p -version of the FEM with an isotropic polynomial degree of $p = 3$ and an element size of $b_e = 0.25$ mm. The evaluation points are located $l_p = 100$ mm in front and behind the Fibonacci lattice, respectively. The excitation force acts in a distance of $l_f = 200$ mm in front of the periodic array of silicon resin and tungsten. The length of the numerical model is therefore $L_p = 520$ mm. The fundamental layer of the Fibonacci sequence has been repeated $N = 40$ times. Again, a mono-modal excitation serves to separate the symmetric and anti-symmetric Lamb wave modes.



(a) Symmetric Lamb wave modes (excitation by two point forces in x_2 -direction - out-of-phase)



(b) Anti-symmetric Lamb wave modes (excitation by two point forces in x_1 -direction - out-of-phase)



(c) Symmetric and anti-symmetric Lamb wave modes (excitation by a single point forces in x_2 -direction)

Figure 9.6: Transmitted spectrum for the Fibonacci sequence S_3 .

The displacement signal is simulated in a frequency range between 30 kHz and 2 MHz. To this end, we increase the center frequency f_c of a Hann-window modulated sine-burst (cf. Eq. (7.1)) with $n = 5$ cycles by 10 kHz for every simulation.

In order to evaluate the obtained results, we address the ratio r_{bi} between the Fourier transforms of the displacement signals at points P_b and P_i . The displacement signals \mathbf{u}_b and \mathbf{u}_i are therefore subjected to a Fourier transform. The value of the Fourier transforms \mathcal{U}_b and \mathcal{U}_i at the center frequency f_c is then taken and evaluated

$$r_{bi}(f_c) = \frac{\mathcal{U}_b(f_c)}{\mathcal{U}_i(f_c)}. \quad (9.7)$$

The results for the transmitted spectra of the symmetric and anti-symmetric guided wave modes are illustrated in Fig. 9.6, showing two distinct stopbands between 570 kHz - 820 kHz and 1.5 MHz - 1.75 MHz are recognized. These are in good agreement with the results reported in reference [324]. Zhao *et al.* detected stopbands between 600 kHz - 775 kHz and 1.45 MHz - 1.72 MHz. It can be seen, however, that the behavior of the symmetric and anti-symmetric Lamb wave modes differs. This effect can be attributed to the different wavelengths of the individual modes.

Similar results for different Fibonacci lattices are to be found in reference [325] using the FEM to simulate the propagation of guided waves in periodic structures. The main advantage of using higher order FEMs is seen in the fast convergence and therefore a significantly reduced number of degrees-of-freedom.

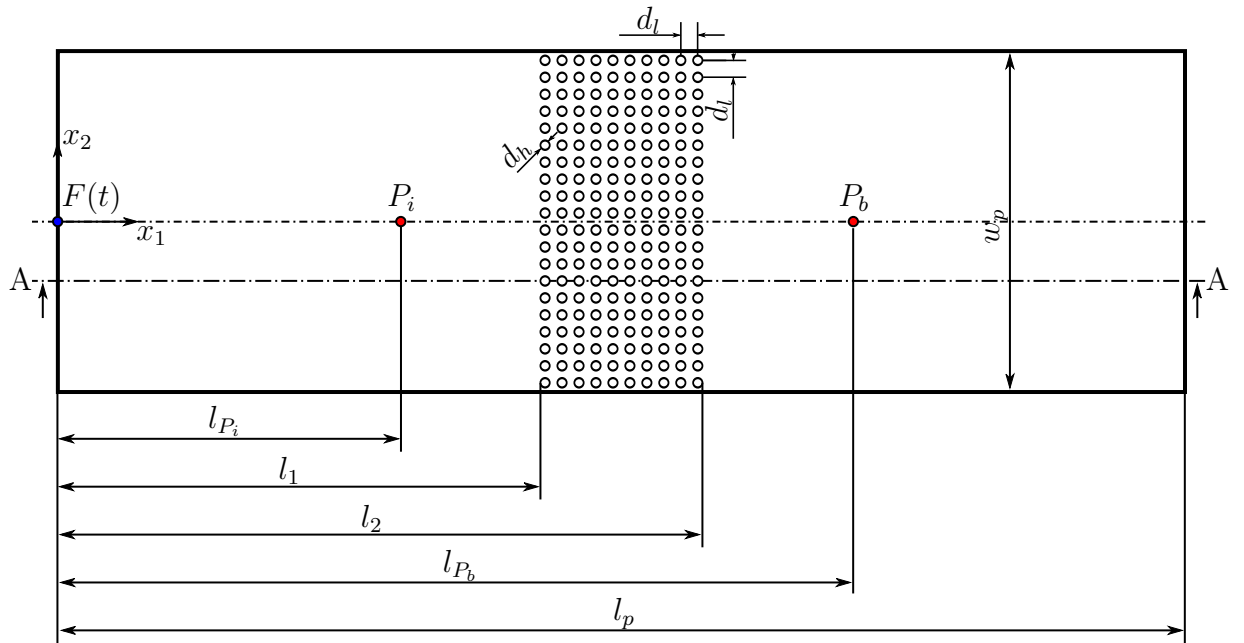
9.2.2 Square hole arrangement

In order to numerically verify the results presented by Zhang *et al.* [322], an aluminum plate (material data: Tab. 2.1) with a thickness of $t_p = 1.27$ mm is used, cf. Fig. 9.7. The following refers to a square arrangement of holes where the lattice spacing is $d_l = 1.077$ mm and the diameter of the holes is $d_h = 0.762$ mm. The “volume fraction” of air is accordingly 0.393.

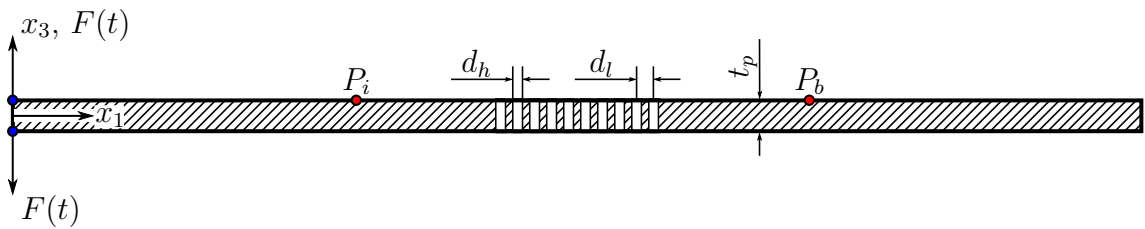
An array of 10×20 holes is investigated, based on the SCM - due to the symmetry only one half of the plate is modelled. The measurement points P_i and P_b are again located 100 mm away from the geometrically perturbed region. To separate the behavior of the symmetric and anti-symmetric modes, a mono-modal excitation is reached by applying two point loads similar to the previous example. Consequently, the simulated displacement signal lies in a frequency range between 0.3 MHz and 2 MHz. To this end, we increase the center frequency f_c of a Hann-window modulated sine-burst (cf. Eq. (7.1)) with $n = 5$ cycles by 10 kHz for every simulation.

The cell size for the current example corresponds to the lattice spacing and is therefore $b_e = 1.077$ mm. The polynomial degree template is again isotopic and chosen as $p = 4$. Figs. 9.7c - 9.7e depicts the FC discretization and the corresponding sub-cell grid for the numerical integration (refinement level: $k = 5$)

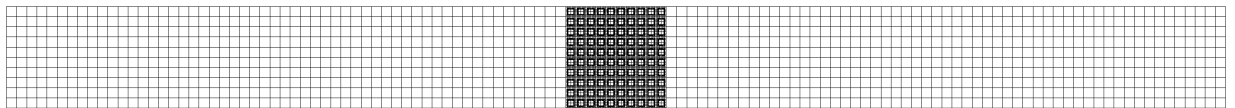
As discussed above, phononic materials can be created by choosing a two- or three-dimensional arrangement of two or more materials, exhibiting a strong contrast in their material properties. Reference [322] therefore suggests to use a square or a triangular arrangement of holes (filled with air) in an aluminum plate. In their study, Zhang *et al.* [322] reported on experimental results showing the existence of bandgaps in such structures.



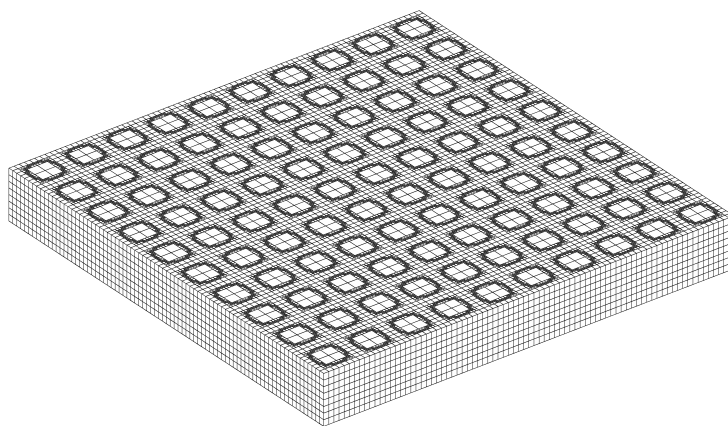
(a) Model of the square hole arrangement



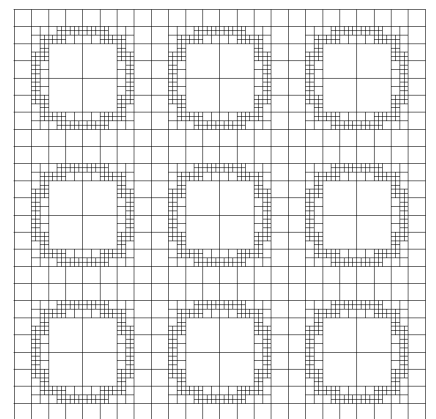
(b) Cross-section A-A



(c) FC discretization and integration sub-cells (refinement level: $k = 5$)



(d) 10×10 sub-cell grid



(e) Detail view

Figure 9.7: Three-dimensional model of the square hole arrangement bandgap structure and FC discretization. Geometric dimensions: $l_{P_i} = 50$ mm, $l_1 = 60.1575$ mm, $l_2 = 70.6125$ mm, $l_{P_b} = 80.77$ mm, $l_p = 103.77$ mm, $d_h = 0.762$ mm, $d_l = 1.077$ mm, $t_p = 1.27$ mm, $w_p = 21.54$ mm, $t_p = 1.27$ mm.

Zhang *et al.* [322] observed experimentally that the guided waves are significantly attenuated in a frequency range of 0.8 MHz to 1.5 MHz.

Figs. 9.8 and 9.9 therefore depict contour plots of the wavefields at different times and for two excitation frequencies. Fig. 9.8 shows the out-of-plane displacement field for an excitation frequency of $f_c = 300$ kHz. These contour plots illustrate the interaction of the wave packet with the square hole arrangement. Therefore, guided waves are hardly attenuated when excited at a frequency well below the stopband region. If the excitation frequency is increased to $f_c = 1.1$ MHz, however, a strong attenuation of the propagating wave packet can be observed in Fig. 9.9.

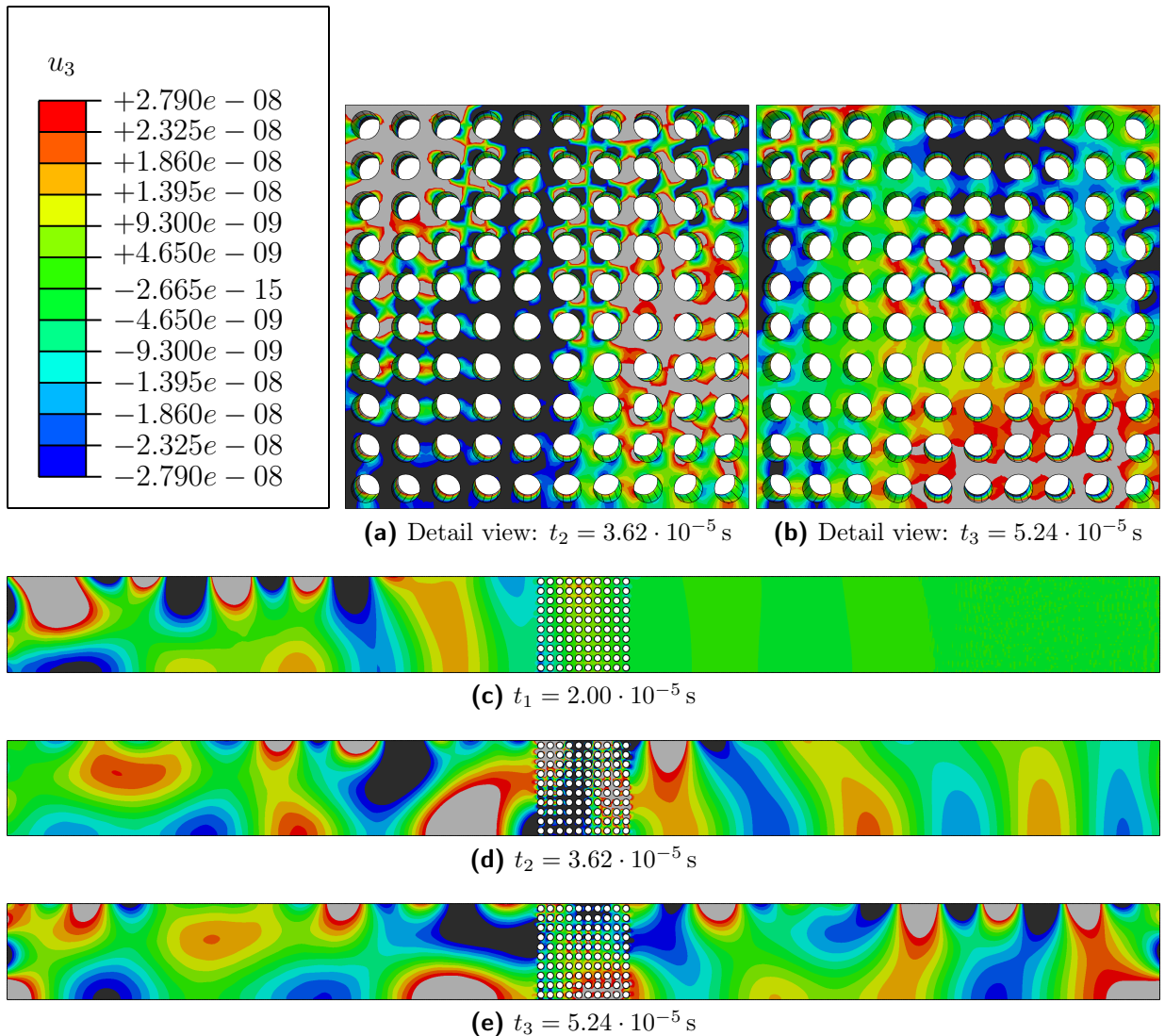


Figure 9.8: Snapshots of the displacement field (u_3) at different times for an excitation frequency of $f = 300$ kHz. A mono-modal excitation by two collocated forces is used to excite symmetric Lamb wave modes.

The simulation results are assessed according to the methodology described in the previous subsection given by Eq. (9.7). Fig. 9.10 depicts the transmitted spectra. A stopband in the frequency range from 0.75 MHz to 1.5 MHz can easily be observed. This is in good agreement to the experimental results observed by Zhang *et al.* [322]. They experimentally

found that the guided waves are significantly attenuated in a frequency range of 0.8 MHz to 1.5 MHz. Moreover, they also used the three-dimensional plane wave extension method to simulate the aluminum structure. There, they observed a stopband in a frequency range of 0.834 MHz to 1.42 MHz, agreeing well with the experimental data.

The reasons for the occurrence of such stopband regions still need to be investigated. There seems to be no obvious relation between the lattice spacing and the wavelengths (cf. Fig. 9.11) of the guided wave modes. We only observe that the wavelengths of both the fundamental symmetric and the fundamental anti-symmetric modes are larger than the lattice spacing and the hole diameter, respectively. Therefore, we can conclude that guided waves also interact with perturbations of the structure that are smaller than the excited wavelengths within the wave packet. It is only known that in a frequency range of approximately 0.8 MHz to 1.5 MHz the phononic structure prohibits the waves from propagating freely and that it consequently forms a stopband in this frequency range. For example, such materials could be used to develop sound filters or to effectively guide ultrasonic waves through the structure at a prescribed path.

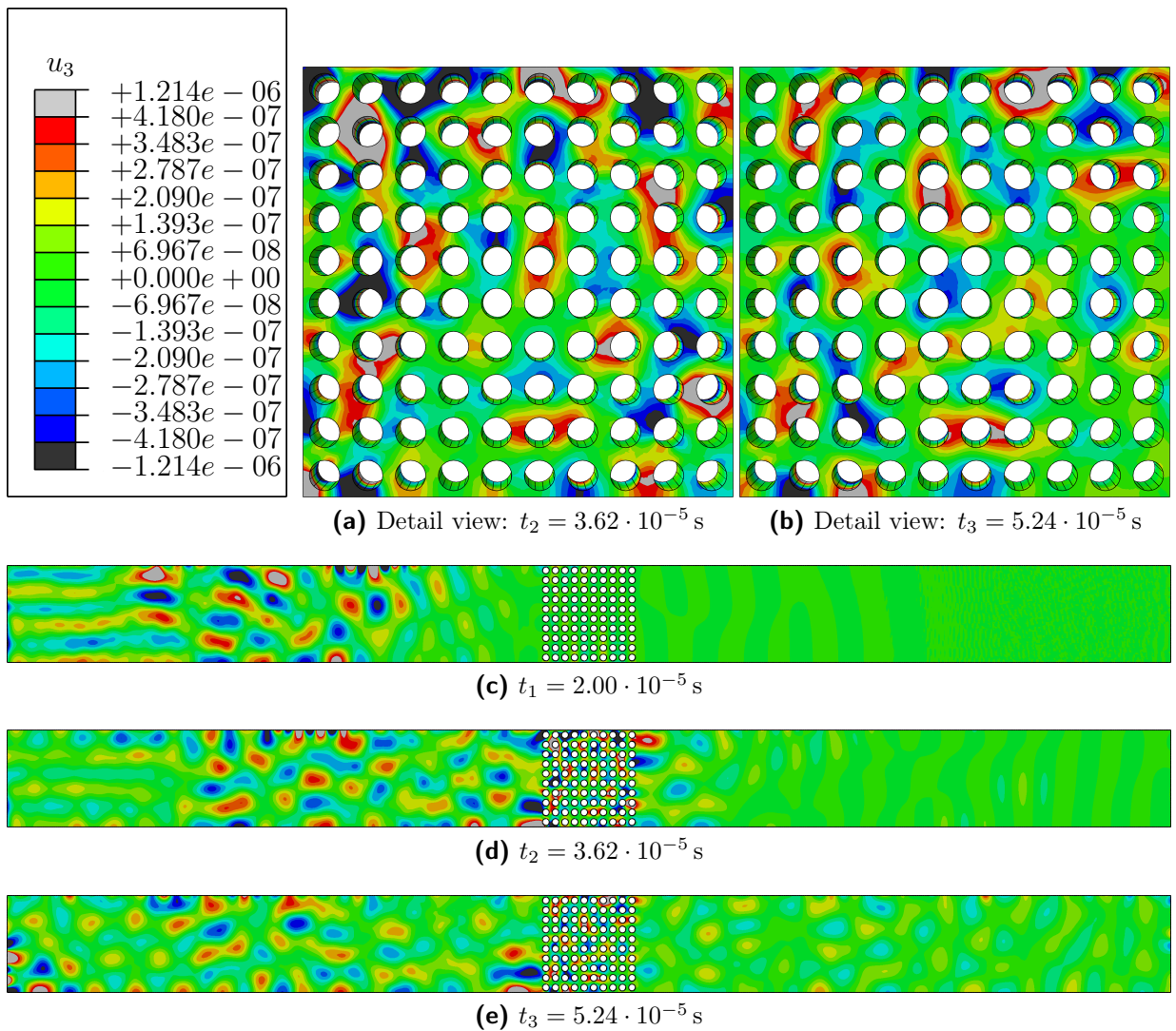
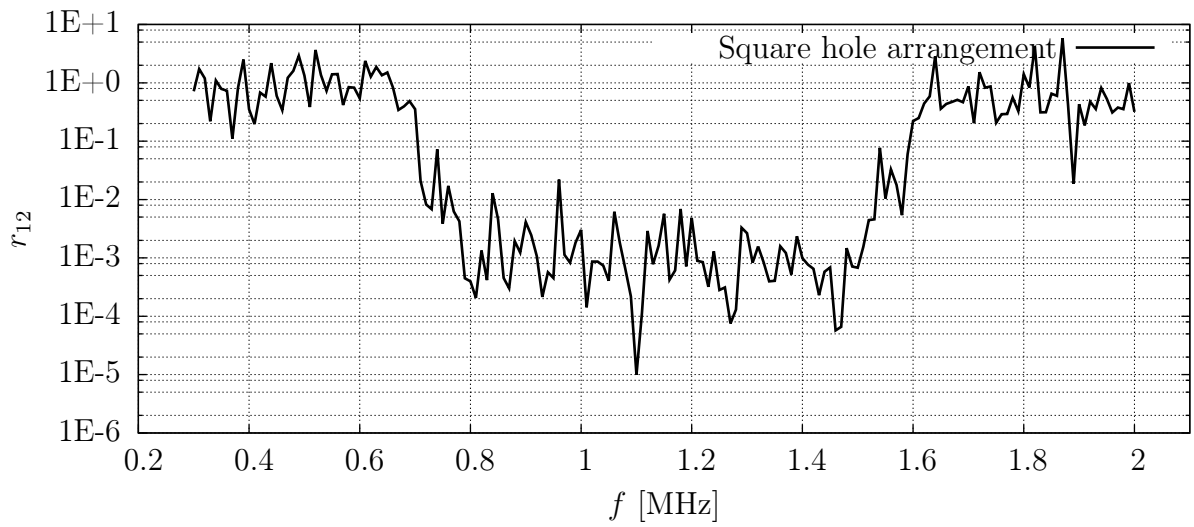
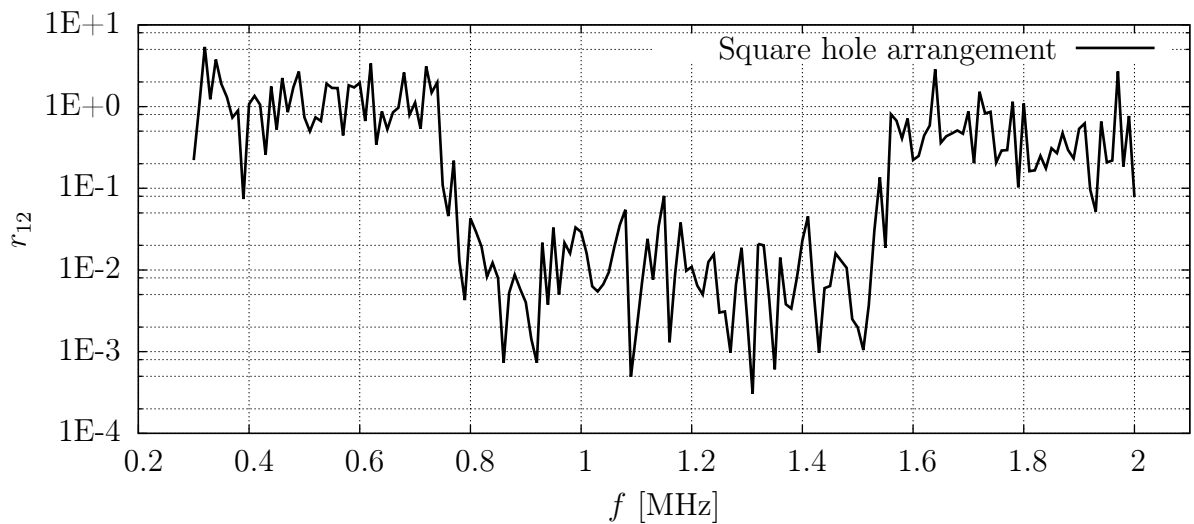


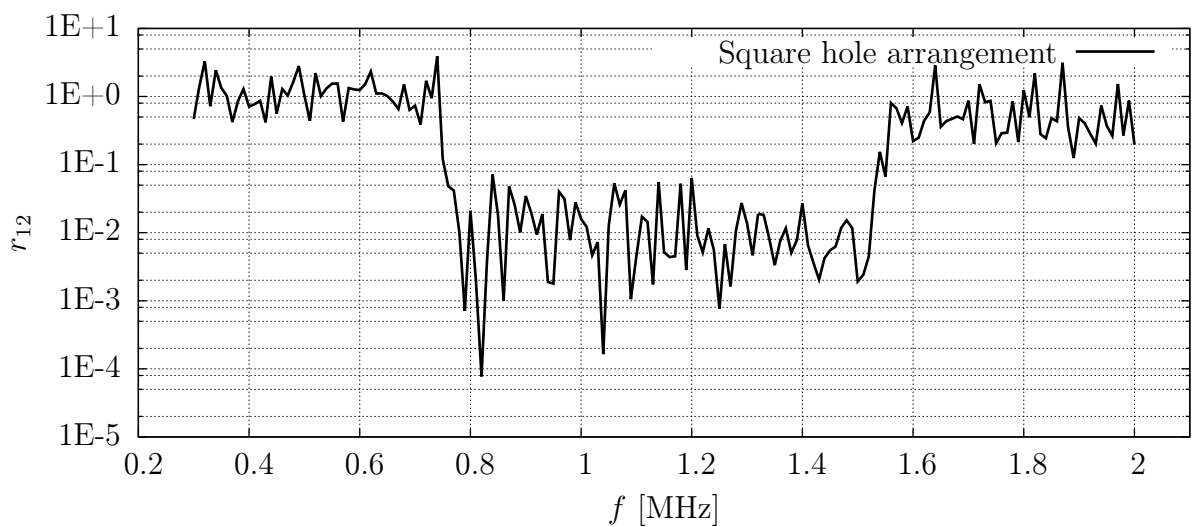
Figure 9.9: Snapshots of the displacement field (u_3) at different times for an excitation frequency of $f = 1.1$ MHz.



(a) Symmetric Lamb wave modes (excitation by two point forces in x_2 -direction - out-of-phase)



(b) Anti-symmetric Lamb wave modes (excitation by two point forces in x_2 -direction - in-phase)



(c) Symmetric and anti-symmetric Lamb wave modes (excitation by a single point forces in x_2 -direction)

Figure 9.10: Transmitted spectrum for the square hole arrangement.

The present chapter briefly touches an interesting research topic which has a number of practical applications. It is demonstrated that the proposed higher order methods are a suitable tool to numerically study the bandgap phenomenon. It is especially the second example that highlights the capabilities of the fictitious domain concept in conjunction with higher order Ansatz functions.

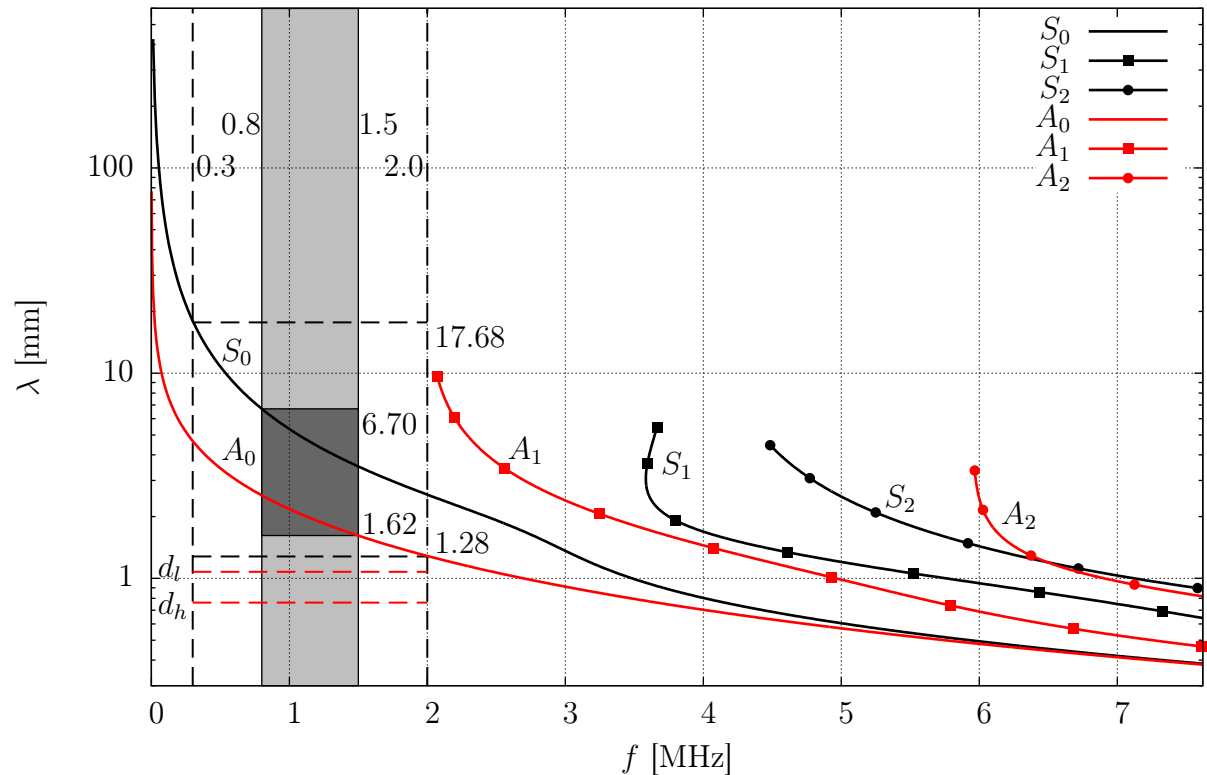


Figure 9.11: Dispersion curves for a 1.27 mm thick aluminum plate. The wavelength λ is plotted against the frequency f .

Open questions that still need to be investigated are such as: (i) What influence does the diameter of the hole have?, (ii) What is the influence of the lattice spacing?, (iii) What is the influence of the shape of the hole (conical, cylindrical, elliptical, etc.)? and many more.

Considering the questions posed above, we reckon that the FCM and the SCM are particularly suited to provide answers. The numerical treatment of wave propagation phenomena in complex, heterogeneous domains is especially easy if a higher order fictitious domain approach is employed. The mesh can be generated automatically and the simulations can be executed fast and efficiently in conjunction with appropriate mass-lumping techniques. The proposed numerical methods are therefore seen as suitable tools to analyze the propagation of elastic guided waves in complex, real-life structures.

Chapter 10

Conclusion & Outlook

The present thesis intends to contribute to a more efficient methodology for the simulation of ultrasonic guided wave propagation problems. In this context, the main objective was to extend different *HO*-FEMs and fictitious domain methods to structural dynamics - including multi-physics applications.

In the framework of *HO*-FE approaches, the SEM was investigated in conjunction with various mass-lumping - with the result that the most efficient option for wave propagation analysis is to be seen in the SEM deploying a GLL quadrature rule. Due to the diagonalized mass matrix, the memory requirements are minimized and an explicit time-marching scheme, such as the CDM, can be used as an efficient approach. The latter fact offers significant advantages in terms of computational time compared to a formulation based on a consistent mass matrix.

The *p*-version and the Fourier-*p*-version of the FEM were studied with regards to hierarchic shape functions. The objective was to analyze whether the tensor product space or the trunk space are to be recommended. The results of the convergence studies revealed that, even for wave propagation analysis, the trunk space offers advantages with respect to the numerical efficiency.

In the framework of higher order fictitious domain methods, the SCM and Fourier-*p*-version of the FCM were introduced and applied to the simulation of ultrasonic guided waves. To this end, the standard version of the FCM was extended by introducing two new sets of shape functions.

First, Lagrange polynomials defined on a Gauß-Lobatto-Legendre nodal distribution were proposed as possible nodal-based shape functions. In accordance with the terminology accepted by the numerical mechanics community, we coined the term *spectral cell method*. To exploit the advantages of an explicit time-integration method it is essential to have access to an efficient mass-lumping technique. It is evident that only uncut cells can be lumped using a GLL-quadrature. Because of the composed numerical integration based on a quadtree/octree-refinement, the integration points do not coincide with the nodal points defining the Ansatz functions. A standard GLL-quadrature accordingly does not result in a diagonalized mass matrix. In consequence, different procedures are required for cut cells. The first idea to be implemented was to compute the consistent mass matrix for cut cells and to use the row-sum technique to diagonalize the cell's mass matrix. Here, it was found that negative components arise on the main diagonal of the mass matrix, preventing the convergence of the explicit time integration algorithm. A different approach was to employ the HRZ-lumping technique that is known to produce only positive mass matrix components. In the present thesis, benchmark simulations served to illustrate the feasibility of this procedure.

Second, the Fourier- p -version of the FCM was introduced. Drawing on the results of the HO -FE calculations, the trunk space was found to be a favorable option for the analysis of different engineering problems. Due to the fact that, at least to the our knowledge, no lumping schemes are available for hierarchic sets of shape functions, it is recommended to rely on the SCM - as discussed in the previous paragraph is recommended.

As a first important conclusion, we are convinced that **spectral methods** are the method of choice if wave propagation analysis is in the focus of the investigations - which is (only) due to the fact that there are elegant lumping techniques to facilitate the use of explicit time-stepping algorithms such as the CDM.

The fundamental concepts of Lamb waves and piezo-electro-elasticity were introduced in Chapters 2 and 3. As this can be seen as state-of-the-art, no new insights were presented.

Chapter 4 establishes the HO -FEM, a concept that is not dependent on a specific set of higher order basis functions. All important techniques, including special lumping methods for nodal-based formulations, are discussed in detail. A similar path was followed in Chapter 5, concerning the explanation of higher order fictitious domain methods.

In Chapter 6, the proposed shape functions were specified. The Lagrange polynomials based on a GLL grid or an equispaced nodal distribution, the normalized integrals of the Legendre polynomials and trigonometric functions were compared to each other, concluding that the hierarchic and the nodal based Ansatz functions offer different advantages in terms of local adaptability, ensuring C_0 -continuity and the condition number of the matrices. It was clearly demonstrated that deploying a hierarchic basis provides significant advantages with respect to a local adaptivity (local p -refinement) while Ansatz functions based on Lagrange polynomials defined on a GLL grid offer the lowest condition numbers for the system matrices (three-dimensional case). To ensure a continuous approximation between adjacent FEs different measures regarding the orientation of the local and global element coordinate systems have to be taken (Section 6.4).

Chapter 7 provided a deeper insight in the convergence characteristics of the proposed HO -FEMs. We proposed a guideline on how to discretize the investigated structure for each different set of shape functions. We also determined the respective element size for the optimal polynomial degree distribution, depending on the central frequency of the excited wave packet and the desired accuracy. In this context, an interesting phenomenon was observed that is referred to as *the internal element eigenfrequency effect*. A detailed investigation of this phenomenon was motivated by undefineable peaks in the convergence curves. A thorough analysis revealed that these peaks are related to stationary oscillations occurring at elemental eigenfrequencies. If the center frequency of the propagating wave packet coincides with the first or second element resonant frequency, the element vibrates infinitely - presumed that there is no physical damping. An analyst must to be aware of such effects in order to avoid them. To this end, another guideline was established to elucidate how to circumvent this eigenfrequency effect.

In Chapter 8, several static and dynamic benchmark problems were computed. These simulations highlight the great potential of HO -FEMs and fictitious domain methods. Lamb wave based problems can be efficiently computed by deploying higher order multi-physics FEs/FCs. Since the implementation of the numerical approaches is based on a hexahedral element/cell formulation, complex structures can be readily discretized and simulated. A

special focus was placed on SHM applications. Based on a closer examination of different wave propagation problems, it was found that the proposed approaches are superior to the state-of-the-art in commercially available software packages, as both memory requirements and computational time can be reduced significantly. Concerning heterogeneous materials, we advocate to deploy the fictitious domain concept, as it seems to be the only available option to automatically resolve complex boundaries. Therefore, the SCM is recommended for wave propagation analysis in cellular media (sandwich panels etc.) that show a microstructure the wave packet can interact with.

Chapter 9 is used to introduce the bandgap phenomenon. The basic principles causing such behavior are discussed and initial studies regarding two phononic bandgap structures are conducted. There, it is shown that both a Fibonacci sequence consisting of two materials and a periodical arrangement of holes exhibit frequency ranges in which the propagating guided waves are significantly attenuated. This chapter can be understood as an introduction to further research. In this context the source for the bandgap phenomenon still needs to be investigated in detail.

Despite these promising results there are still several questions that need to be addressed in future studies; first and foremost, the development of suitable time-integration schemes for methods based on a hierarchic set of shape functions. Adapted time-stepping algorithms will hopefully help to improve the efficiency of the p -version and the Fourier- p -version of the FEM, in order to be competitive with the SEM. In the same line as the previous argument, advanced mass-lumping algorithms are required for modal based Ansatz functions.

Regarding the fictitious domain methods, a detailed investigation concerning the impact of the geometry approximation on the wave front should be conducted. To this end, the defect should be approximately one order of magnitude larger than the wavelength of Lamb mode interrogating the structure. In this case a relation between the geometry approximation of the boundary, the wavelength of the guided wave and the numerical error can be established. This would be an important step towards a thorough validation of the immersed boundary concept for high-frequency wave propagation simulations.

Another idea would be to extend the coupling of HO -FEMs with analytical solutions also to the fictitious domain method. Basically, the algorithms are the same. Special care only needs to be taken concerning the boundary between the analytical solution and the fictitious domain.

In the context of SHM, lightweight materials such as carbon and glass fiber reinforced plastics are in the focus of current developments. As it is known that these types of material exhibit a high degree of material damping, suitable damping models should be implemented. With regard to CFRP/GFRP composites, there is currently no computational tool to accurately and efficiently model ultrasonic wave propagation. Unfortunately, it is computationally prohibitive to use one higher order element per layer of the laminated composite, which is why it is common to draw on an average stiffness. This procedure is, however, not appropriate - due to the fact that it tends to result in potentially wrong simulation data [326]. The idea of a layered FE can therefore be seized [327]. The fundamentals of this approach can be adopted to the fictitious domain concept. This seems to be a viable option to further enhance the capabilities of higher order fictitious domain methods.

Finally, ambient conditions such as temperature, moisture and air pressure need to be taken into account as well. To date, there are only very few publications that deal with such topics (especially temperature variations) from a numerical point of view [83, 99]. In the existing works, no fully coupled model has yet been developed. Instead, the influence of temperature variations was included implicitly by running several simulations based on different dimensions (effect of thermal expansion) and different (time-dependent) material properties. Therefore, it is to be expected that a fully-coupled three-dimensional model would lead to valuable new insight.

Appendix A

Piezoelectric constitutive matrices

Recall the constitutive equations of linear piezoelectricity

$$\boldsymbol{\sigma} = \mathbf{C}\boldsymbol{\varepsilon} - \mathbf{e}^T \mathbf{E}, \quad (\text{A-1})$$

$$\mathbf{D} = \mathbf{e}\boldsymbol{\varepsilon} + \boldsymbol{\kappa}\mathbf{E}. \quad (\text{A-2})$$

Rearranging Eq. (A-1) and substituting it into Eq. (A-2) yields

$$\mathbf{D} = \mathbf{e}(\mathbf{S}^E \boldsymbol{\sigma} + \mathbf{d}^T \mathbf{E}) + \boldsymbol{\kappa}\mathbf{E} \quad (\text{A-3})$$

with $\mathbf{S}^E = \mathbf{C}^{-1}$ and $\mathbf{d} = \mathbf{e}\mathbf{S}^E$.

$$\mathbf{D} = \mathbf{e}\mathbf{S}^E \boldsymbol{\sigma} + \mathbf{e}\mathbf{d}^T \mathbf{E} + \boldsymbol{\kappa}\mathbf{E} \quad (\text{A-4})$$

$$\mathbf{D} = \mathbf{d}\boldsymbol{\sigma} + \boldsymbol{\kappa}^{(\sigma)} \mathbf{E} \quad (\text{A-5})$$

$$\boldsymbol{\kappa}^{(\sigma)} = \mathbf{e}\mathbf{S}^E \mathbf{e}^T + \boldsymbol{\kappa} \quad (\text{A-6})$$

Assuming transversely isotropic material properties, the constitutive Eq. (A-1) can be written as:

Three-dimensional problem

Poling direction coincides with the global x_1 -direction

$$\left\{ \begin{array}{l} \sigma_{11} \\ \sigma_{22} \\ \sigma_{33} \\ \tau_{12} \\ \tau_{23} \\ \tau_{13} \\ D_1 \\ D_2 \\ D_3 \end{array} \right\} \left[\begin{array}{cccccccccc} C_{33} & C_{13} & C_{13} & 0 & 0 & 0 & -e_{33} & 0 & 0 & 0 \\ C_{13} & C_{11} & C_{12} & 0 & 0 & 0 & -e_{31} & 0 & 0 & 0 \\ C_{13} & C_{12} & C_{11} & 0 & 0 & 0 & -e_{31} & 0 & 0 & 0 \\ 0 & 0 & 0 & C_{44} & 0 & 0 & 0 & -e_{15} & 0 & 0 \\ 0 & 0 & 0 & 0 & C_{66} & 0 & 0 & 0 & 0 & 0 \\ 0 & 0 & 0 & 0 & 0 & C_{44} & 0 & 0 & 0 & -e_{15} \\ e_{33} & e_{31} & e_{31} & 0 & 0 & 0 & \kappa_{33} & 0 & 0 & 0 \\ 0 & 0 & 0 & e_{15} & 0 & 0 & 0 & \kappa_{11} & 0 & 0 \\ 0 & 0 & 0 & 0 & 0 & e_{15} & 0 & 0 & 0 & \kappa_{11} \end{array} \right] \left\{ \begin{array}{l} \epsilon_{11} \\ \epsilon_{22} \\ \epsilon_{33} \\ \gamma_{12} \\ \gamma_{23} \\ \gamma_{13} \\ E_1 \\ E_2 \\ E_3 \end{array} \right\} \quad (\text{A-7})$$

Poling direction coincides with the global x_2 -direction

$$\left\{ \begin{array}{l} \sigma_{11} \\ \sigma_{22} \\ \sigma_{33} \\ \tau_{12} \\ \tau_{23} \\ \tau_{13} \\ D_1 \\ D_2 \\ D_3 \end{array} \right\} \left[\begin{array}{cccccccccc} C_{11} & C_{13} & C_{12} & 0 & 0 & 0 & 0 & -e_{31} & 0 & 0 \\ C_{13} & C_{33} & C_{13} & 0 & 0 & 0 & 0 & -e_{33} & 0 & 0 \\ C_{12} & C_{13} & C_{11} & 0 & 0 & 0 & 0 & -e_{31} & 0 & 0 \\ 0 & 0 & 0 & C_{44} & 0 & 0 & -e_{15} & 0 & 0 & 0 \\ 0 & 0 & 0 & 0 & C_{44} & 0 & 0 & 0 & 0 & -e_{15} \\ 0 & 0 & 0 & 0 & 0 & C_{66} & 0 & 0 & 0 & 0 \\ 0 & 0 & 0 & e_{15} & 0 & 0 & \kappa_{11} & 0 & 0 & 0 \\ e_{31} & e_{33} & e_{31} & 0 & 0 & 0 & 0 & \kappa_{33} & 0 & 0 \\ 0 & 0 & 0 & 0 & e_{15} & 0 & 0 & 0 & 0 & \kappa_{11} \end{array} \right] \left\{ \begin{array}{l} \epsilon_{11} \\ \epsilon_{22} \\ \epsilon_{33} \\ \gamma_{12} \\ \gamma_{23} \\ \gamma_{13} \\ E_1 \\ E_2 \\ E_3 \end{array} \right\} \quad (\text{A-8})$$

Poling direction coincides with the global x_3 -direction

$$\left\{ \begin{array}{l} \sigma_{11} \\ \sigma_{22} \\ \sigma_{33} \\ \tau_{12} \\ \tau_{23} \\ \tau_{13} \\ D_1 \\ D_2 \\ D_3 \end{array} \right\} \left[\begin{array}{cccccccccc} C_{11} & C_{12} & C_{13} & 0 & 0 & 0 & 0 & 0 & -e_{31} & 0 \\ C_{12} & C_{11} & C_{13} & 0 & 0 & 0 & 0 & 0 & -e_{31} & 0 \\ C_{13} & C_{13} & C_{33} & 0 & 0 & 0 & 0 & 0 & -e_{33} & 0 \\ 0 & 0 & 0 & C_{66} & 0 & 0 & 0 & 0 & 0 & 0 \\ 0 & 0 & 0 & 0 & C_{44} & 0 & 0 & -e_{15} & 0 & 0 \\ 0 & 0 & 0 & 0 & 0 & C_{44} & -e_{15} & 0 & 0 & 0 \\ 0 & 0 & 0 & 0 & 0 & e_{15} & \kappa_{11} & 0 & 0 & 0 \\ 0 & 0 & 0 & 0 & e_{15} & 0 & 0 & \kappa_{11} & 0 & 0 \\ e_{31} & e_{31} & e_{33} & 0 & 0 & 0 & 0 & 0 & 0 & \kappa_{33} \end{array} \right] \left\{ \begin{array}{l} \epsilon_{11} \\ \epsilon_{22} \\ \epsilon_{33} \\ \gamma_{12} \\ \gamma_{23} \\ \gamma_{13} \\ E_1 \\ E_2 \\ E_3 \end{array} \right\} \quad (\text{A-9})$$

Two-dimensional problem: Plane strain assumption

The constitutive equations

$$\begin{aligned} \boldsymbol{\sigma} &= \mathbf{C}\boldsymbol{\epsilon} - \mathbf{e}^T \mathbf{E}, \\ \mathbf{D} &= \mathbf{e}\boldsymbol{\epsilon} + \boldsymbol{\kappa} \mathbf{E} \end{aligned}$$

are modified utilizing the plane strain assumption $\epsilon_{33} = \gamma_{13} = \gamma_{23} = E_3 = 0$.
Poling direction coincides with the global x_1 -direction

$$\left\{ \begin{array}{l} \sigma_{11} \\ \sigma_{22} \\ \tau_{12} \\ D_1 \\ D_2 \end{array} \right\} \left[\begin{array}{ccccc} C_{33} & C_{13} & 0 & -e_{33} & 0 \\ C_{13} & C_{11} & 0 & -e_{31} & 0 \\ 0 & 0 & C_{44} & 0 & -e_{15} \\ e_{33} & e_{31} & 0 & \kappa_{33} & 0 \\ 0 & 0 & e_{15} & 0 & \kappa_{11} \end{array} \right] \left\{ \begin{array}{l} \epsilon_{11} \\ \epsilon_{22} \\ \gamma_{12} \\ E_1 \\ E_2 \end{array} \right\} \quad (\text{A-10})$$

Poling direction coincides with the global x_2 -direction

$$\left\{ \begin{array}{l} \sigma_{11} \\ \sigma_{22} \\ \tau_{12} \\ D_1 \\ D_2 \end{array} \right\} \left[\begin{array}{ccccc} C_{11} & C_{13} & 0 & 0 & -e_{31} \\ C_{13} & C_{33} & 0 & 0 & -e_{33} \\ 0 & 0 & C_{44} & -e_{15} & 0 \\ 0 & 0 & e_{15} & \kappa_{11} & 0 \\ e_{31} & e_{33} & 0 & 0 & \kappa_{33} \end{array} \right] \left\{ \begin{array}{l} \epsilon_{11} \\ \epsilon_{22} \\ \gamma_{12} \\ E_1 \\ E_2 \end{array} \right\} \quad (\text{A-11})$$

Two-dimensional problem: Plane stress assumption

The constitutive equations

$$\begin{aligned} \boldsymbol{\epsilon} &= \mathbf{S}^E \boldsymbol{\sigma} + \mathbf{d}^T \mathbf{E}, \\ \mathbf{D} &= \mathbf{d}\boldsymbol{\sigma} + \boldsymbol{\kappa}^{(\sigma)} \mathbf{E} \end{aligned}$$

are modified utilizing the plane stress assumption $\sigma_{33} = \tau_{13} = \tau_{23} = E_3 = 0$.
Poling direction coincides with the global x_1 -direction

$$\left\{ \begin{array}{l} \epsilon_{11} \\ \epsilon_{22} \\ \gamma_{12} \\ D_1 \\ D_2 \end{array} \right\} \left[\begin{array}{ccccc} S_{33} & S_{13} & 0 & d_{33} & 0 \\ S_{13} & S_{11} & 0 & d_{31} & 0 \\ 0 & 0 & S_{44} & 0 & d_{15} \\ d_{33} & d_{31} & 0 & \kappa_{33}^{(\sigma)} & 0 \\ 0 & 0 & d_{15} & 0 & \kappa_{11}^{(\sigma)} \end{array} \right] \left\{ \begin{array}{l} \sigma_{11} \\ \sigma_{22} \\ \tau_{12} \\ E_1 \\ E_2 \end{array} \right\} \quad (\text{A-12})$$

Poling direction coincides with the global x_2 -direction

$$\begin{Bmatrix} \sigma_{11} \\ \sigma_{22} \\ \tau_{12} \\ D_1 \\ D_2 \end{Bmatrix} = \begin{bmatrix} S_{11} & S_{13} & 0 & 0 & d_{31} \\ S_{13} & S_{33} & 0 & 0 & d_{33} \\ 0 & 0 & S_{44} & d_{15} & 0 \\ 0 & 0 & d_{15} & \kappa_{11}^{(\sigma)} & 0 \\ d_{31} & d_{33} & 0 & 0 & \kappa_{33}^{(\sigma)} \end{bmatrix} \begin{Bmatrix} \epsilon_{11} \\ \epsilon_{22} \\ \gamma_{12} \\ E_1 \\ E_2 \end{Bmatrix} \quad (\text{A-13})$$

Appendix B

3D shape functions: p -FEM

Considering hierarchic shape functions based on the normalized polynomials of the Legendre polynomials, four distinct groups of shape functions can be classified

1. Nodal modes,
2. Edge modes,
3. Face modes,
4. Internal modes.

Principally, it is possible to define separate polynomial degrees for each edge, face (for each of the two local directions) and the internal shape functions (for each of the three local directions). This is, however, only possible for hierarchic Ansatz functions. Accordingly, for every finite element there are three vectors containing the edge polynomial degrees, the face polynomial degrees and the internal polynomial order.

$$\mathbf{p}_{\text{edge}} = \{p_{E_1} \ p_{E_2} \ \dots \ p_{E_{12}}\}^T, \quad (\text{B-1})$$

$$\mathbf{p}_{\text{face}} = \{\mathbf{p}_{F_1} \ \mathbf{p}_{F_2} \ \dots \ \mathbf{p}_{F_6}\}^T, \quad (\text{B-2})$$

$$\mathbf{p}_{\text{internal}} = \{p_{\xi} \ p_{\eta} \ p_{\zeta}\}^T. \quad (\text{B-3})$$

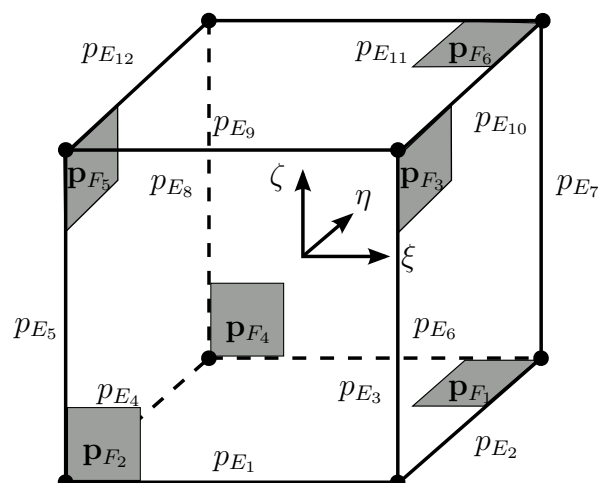


Figure B-1: Hexahedral reference element ($-1 \leq \xi \leq 1$, $-1 \leq \eta \leq 1$, $-1 \leq \zeta \leq 1$) with the definitions of the polynomial degree distributions.

The implementation is based on the reference element depicted in Fig. 4.2. There are eight **nodal modes**. These are the same trilinear Ansatz functions used for the well-known 8-node isoparametric hexahedral element in h -version FEM computer programs

$$N_{(1,1,1)}^{N_i}(\xi, \eta, \zeta) = \frac{1}{8} (1 + \xi_i \xi) (1 + \eta_i \eta) (1 + \zeta_i \zeta), \quad i = 1, 2, \dots, 8. \quad (\text{B-4})$$

(ξ_i, η_i, ζ_i) denote the local coordinates of the i -th node. The nodal mode for node 5 is shown in Fig. B-2 exemplarily.

There are $4((p_\xi + 1) + (p_\eta + 1) + (p_\zeta + 1))$ **edge modes**. These modes are associated with the sides of the finite element ($p_\xi, p_\eta, p_\zeta \geq 2$). They are defined separately for each individual edge and vanish at all other edges,

$$N_{(i,1,1)}^{E_1}(\xi, \eta, \zeta) = N_{i+1}^{p\text{-FEM}}(\xi) \cdot N_1^{p\text{-FEM}}(\eta) \cdot N_1^{p\text{-FEM}}(\zeta), \quad i = 2, 3, \dots, p_\xi, \quad (\text{B-5a})$$

$$N_{(1,j,1)}^{E_2}(\xi, \eta, \zeta) = N_2^{p\text{-FEM}}(\xi) \cdot N_{j+1}^{p\text{-FEM}}(\eta) \cdot N_1^{p\text{-FEM}}(\zeta), \quad j = 2, 3, \dots, p_\eta, \quad (\text{B-5b})$$

$$N_{(i,1,1)}^{E_3}(\xi, \eta, \zeta) = N_{i+1}^{p\text{-FEM}}(\xi) \cdot N_2^{p\text{-FEM}}(\eta) \cdot N_1^{p\text{-FEM}}(\zeta), \quad i = 2, 3, \dots, p_\xi, \quad (\text{B-5c})$$

$$N_{(1,j,1)}^{E_4}(\xi, \eta, \zeta) = N_1^{p\text{-FEM}}(\xi) \cdot N_{j+1}^{p\text{-FEM}}(\eta) \cdot N_1^{p\text{-FEM}}(\zeta), \quad j = 2, 3, \dots, p_\eta, \quad (\text{B-5d})$$

$$N_{(1,1,k)}^{E_5}(\xi, \eta, \zeta) = N_1^{p\text{-FEM}}(\xi) \cdot N_1^{p\text{-FEM}}(\eta) \cdot N_{k+1}^{p\text{-FEM}}(\zeta), \quad k = 2, 3, \dots, p_\zeta, \quad (\text{B-5e})$$

$$N_{(1,1,k)}^{E_6}(\xi, \eta, \zeta) = N_2^{p\text{-FEM}}(\xi) \cdot N_1^{p\text{-FEM}}(\eta) \cdot N_{k+1}^{p\text{-FEM}}(\zeta), \quad k = 2, 3, \dots, p_\zeta, \quad (\text{B-5f})$$

$$N_{(1,1,k)}^{E_7}(\xi, \eta, \zeta) = N_2^{p\text{-FEM}}(\xi) \cdot N_2^{p\text{-FEM}}(\eta) \cdot N_{k+1}^{p\text{-FEM}}(\zeta), \quad k = 2, 3, \dots, p_\zeta, \quad (\text{B-5g})$$

$$N_{(1,1,k)}^{E_8}(\xi, \eta, \zeta) = N_1^{p\text{-FEM}}(\xi) \cdot N_2^{p\text{-FEM}}(\eta) \cdot N_{k+1}^{p\text{-FEM}}(\zeta), \quad k = 2, 3, \dots, p_\zeta, \quad (\text{B-5h})$$

$$N_{(i,1,1)}^{E_9}(\xi, \eta, \zeta) = N_{i+1}^{p\text{-FEM}}(\xi) \cdot N_1^{p\text{-FEM}}(\eta) \cdot N_2^{p\text{-FEM}}(\zeta), \quad i = 2, 3, \dots, p_\xi, \quad (\text{B-5i})$$

$$N_{(1,j,1)}^{E_{10}}(\xi, \eta, \zeta) = N_2^{p\text{-FEM}}(\xi) \cdot N_{j+1}^{p\text{-FEM}}(\eta) \cdot N_2^{p\text{-FEM}}(\zeta), \quad j = 2, 3, \dots, p_\eta, \quad (\text{B-5j})$$

$$N_{(i,1,1)}^{E_{11}}(\xi, \eta, \zeta) = N_{i+1}^{p\text{-FEM}}(\xi) \cdot N_2^{p\text{-FEM}}(\eta) \cdot N_2^{p\text{-FEM}}(\zeta), \quad i = 2, 3, \dots, p_\xi, \quad (\text{B-5k})$$

$$N_{(1,j,1)}^{E_{12}}(\xi, \eta, \zeta) = N_1^{p\text{-FEM}}(\xi) \cdot N_{j+1}^{p\text{-FEM}}(\eta) \cdot N_2^{p\text{-FEM}}(\zeta), \quad j = 2, 3, \dots, p_\eta. \quad (\text{B-5l})$$

The edge modes for edge 9 with a polynomial order of $p_\xi = 2$ and $p_\zeta = 4$ ($i = 2, 4$) are illustrated in Fig. B-3 exemplarily.

Face modes are associated with the faces of the finite element ($p_\xi, p_\eta, p_\zeta \geq 2$, tensor product space). They are similar to the internal modes of a two-dimensional quadrilateral element. Face modes are generated separately for each face and vanish at all other faces

$$N_{(i,j,1)}^{F_1}(\xi, \eta, \zeta) = N_{i+1}^{p\text{-FEM}}(\xi) \cdot N_{j+1}^{p\text{-FEM}}(\eta) \cdot N_1^{p\text{-FEM}}(\zeta), \quad i = 2, 3, \dots, p_\xi, \quad j = 2, 3, \dots, p_\eta, \quad (\text{B-6a})$$

$$N_{(i,1,k)}^{F_2}(\xi, \eta, \zeta) = N_{i+1}^{p\text{-FEM}}(\xi) \cdot N_1^{p\text{-FEM}}(\eta) \cdot N_{k+1}^{p\text{-FEM}}(\zeta), \quad i = 2, 3, \dots, p_\xi, \quad k = 2, 3, \dots, p_\zeta, \quad (\text{B-6b})$$

$$N_{(1,j,k)}^{F_3}(\xi, \eta, \zeta) = N_2^{p\text{-FEM}}(\xi) \cdot N_{j+1}^{p\text{-FEM}}(\eta) \cdot N_{k+1}^{p\text{-FEM}}(\zeta), \quad j = 2, 3, \dots, p_\eta, \quad k = 2, 3, \dots, p_\zeta, \quad (\text{B-6c})$$

$$N_{(i,1,k)}^{F_4}(\xi, \eta, \zeta) = N_{i+1}^{p\text{-FEM}}(\xi) \cdot N_2^{p\text{-FEM}}(\eta) \cdot N_{k+1}^{p\text{-FEM}}(\zeta), \quad i = 2, 3, \dots, p_\xi, \quad k = 2, 3, \dots, p_\zeta, \quad (\text{B-6d})$$

$$N_{(1,j,k)}^{F_5}(\xi, \eta, \zeta) = N_1^{p\text{-FEM}}(\xi) \cdot N_{j+1}^{p\text{-FEM}}(\eta) \cdot N_{k+1}^{p\text{-FEM}}(\zeta), \quad j = 2, 3, \dots, p_\eta, \quad k = 2, 3, \dots, p_\zeta, \quad (\text{B-6e})$$

$$N_{(i,j,1)}^{F_6}(\xi, \eta, \zeta) = N_{i+1}^{p\text{-FEM}}(\xi) \cdot N_{j+1}^{p\text{-FEM}}(\eta) \cdot N_2^{p\text{-FEM}}(\zeta), \quad i = 2, 3, \dots, p_\xi, \quad j = 2, 3, \dots, p_\eta. \quad (\text{B-6f})$$

The face modes for face 6 with a polynomial order of $p_\xi = 2, p_\eta = 2$ and $p_\xi = 5, p_\eta = 3$ ($i = 2, 5, j = 2, 3$) are shown in Fig. B-4 exemplarily.

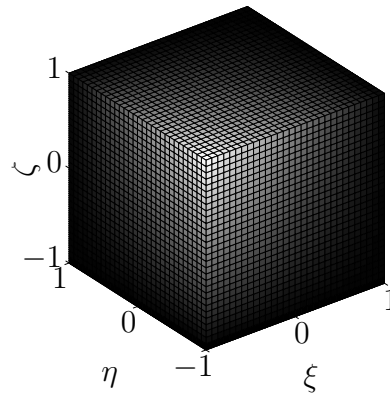


Figure B-2: Nodal modes of a three-dimensional hexahedral finite element: Node 5, $p_\xi = 1, p_\eta = 1, p_\zeta = 1$ (p -FEM).

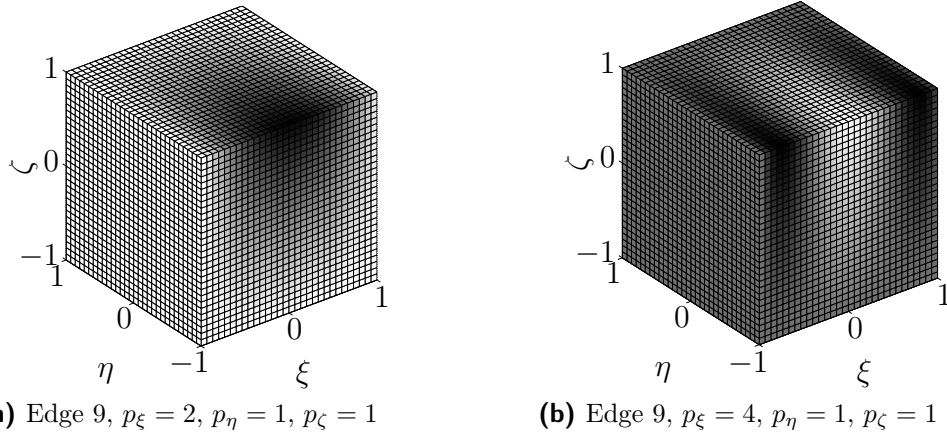


Figure B-3: Edge modes of a three-dimensional hexahedral finite element (p -FEM).

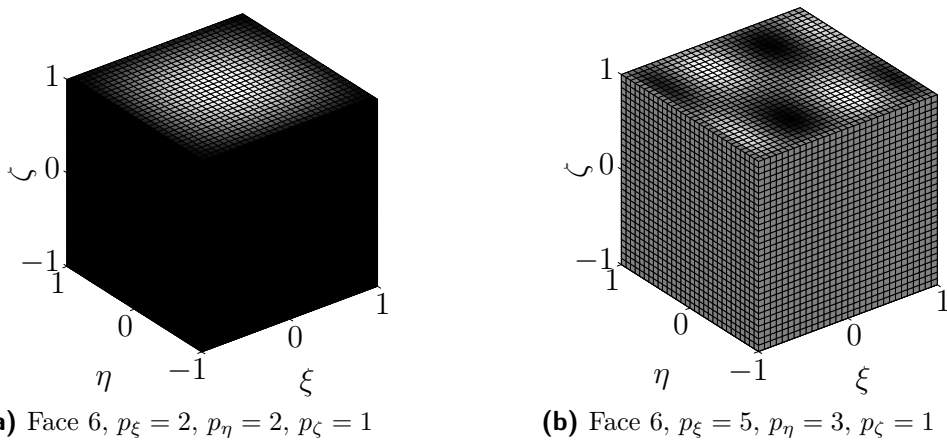


Figure B-4: Face modes of a three-dimensional hexahedral finite element (p -FEM).

The **internal modes** ($p_\xi, p_\eta, p_\zeta \geq 2$, tensor product space) are purely local and vanish at all nodes, edges and faces of the hexahedral finite element.

$$N_{(i,j,k)}^{int}(\xi, \eta, \zeta) = N_{i+1}^{p\text{-FEM}}(\xi)N_{j+1}^{p\text{-FEM}}(\eta)N_{k+1}^{p\text{-FEM}}(\zeta), \quad (\text{B-7})$$

$$i = 2, 3, \dots, p_\xi, \quad j = 2, 3, \dots, p_\eta, \quad k = 2, 3, \dots, p_\zeta$$

The internal modes with a polynomial order of $p_\xi = 2, p_\eta = 2$ and $p_\zeta = 2$ ($i = 2, j = 2, k = 2$) and $p_\xi = 5, p_\eta = 2$ and $p_\zeta = 4$ ($i = 5, j = 2, k = 4$) are displayed in Fig. B-5 exemplarily.

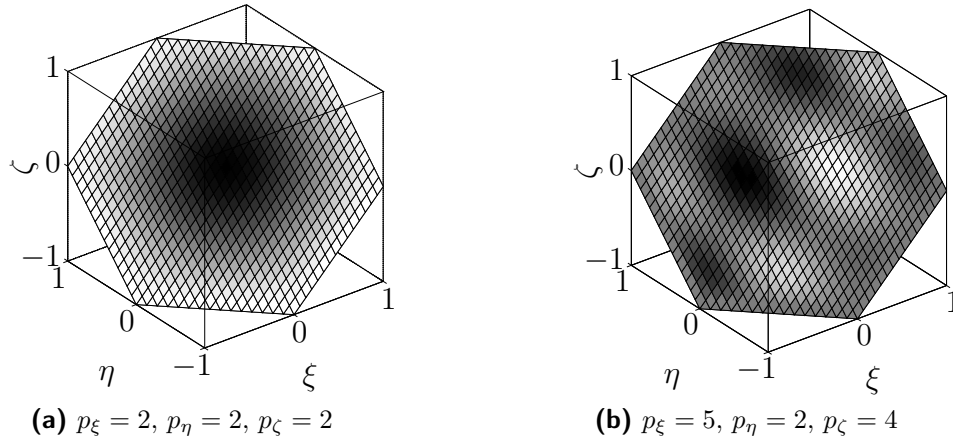


Figure B-5: Internal modes of a three-dimensional hexahedral finite element (p -FEM).

Appendix C

Ansatz spaces for higher order finite elements - hierarchic set based on the Legendre polynomials

$$le_n(x) = \frac{1}{2^n n!} \frac{d^n}{dx^n} [(x^2 - 1)^n], \quad n = 1, 2, \dots \quad -1 \leq x \leq 1 \quad (\text{C-1})$$

$$N_1^{p\text{-FEM}}(\xi) = \frac{1}{2} (1 - \xi) \quad (\text{C-2a})$$

$$N_2^{p\text{-FEM}}(\xi) = \frac{1}{2} (1 + \xi) \quad (\text{C-2b})$$

$$N_n^{p\text{-FEM}}(\xi) = \frac{1}{\|le_{n-2}\|} \int_{x=-1}^{\xi} le_{n-2}(x) dx, \quad n = 3, 4, \dots, p+1 \quad (\text{C-3})$$

$$\|le_{n-2}\| = \sqrt{\frac{2}{2n-3}} \quad (\text{C-4})$$

C.1 The trunk space for two-dimensional quadrilateral finite elements

4 nodal modes

$$N_{(1,1)}^{N_i}(\xi, \eta) = \frac{1}{4} (1 + \xi_i \xi) (1 + \eta_i \eta), \quad i = 1, \dots, 4 \quad (\text{C-5})$$

$2[(p_\xi - 1) + (p_\eta - 1)]$ edge modes

$2(p_\xi - 1)$ edge modes in ξ -direction

$$N_{(i,1)}^{E_1}(\xi, \eta) = N_{i+1}^{p\text{-FEM}}(\xi) \cdot N_1^{p\text{-FEM}}(\eta), \quad i = 2, 3, \dots, p_\xi \quad (\text{C-6a})$$

$$N_{(i,1)}^{E_3}(\xi, \eta) = N_{i+1}^{p\text{-FEM}}(\xi) \cdot N_2^{p\text{-FEM}}(\eta), \quad i = 2, 3, \dots, p_\xi \quad (\text{C-6b})$$

$2(p_\eta - 1)$ edge modes in η -direction

$$N_{(1,j)}^{E_2}(\xi, \eta) = N_2^{p\text{-FEM}}(\xi) \cdot N_{j+1}^{p\text{-FEM}}(\eta), \quad j = 2, 3, \dots, p_\eta \quad (\text{C-7a})$$

$$N_{(1,j)}^{E_4}(\xi, \eta) = N_1^{p\text{-FEM}}(\xi) \cdot N_{j+1}^{p\text{-FEM}}(\eta), \quad j = 2, 3, \dots, p_\eta \quad (\text{C-7b})$$

internal modes

$$N_{(i,j)}^{int}(\xi, \eta) = N_{i+1}^{p\text{-FEM}}(\xi) \cdot N_{j+1}^{p\text{-FEM}}(\eta), \quad i = 2, 3, \dots, p_\xi - 2, \quad j = 2, 3, \dots, p_\eta - 2, \quad (C-8)$$

$$i + j = 4, 5, \dots, \max(p_\xi, p_\eta)$$

C.2 The tensor product space for two-dimensional quadrilateral finite elements

The tensor product space only influences the internal modes. Nodal and edge modes stay unchanged.

 $[(p_\xi - 1) \cdot (p_\eta - 1)]$ internal modes

$$N_{(i,j)}^{int}(\xi, \eta) = N_{i+1}^{p\text{-FEM}}(\xi) \cdot N_{j+1}^{p\text{-FEM}}(\eta), \quad i = 2, 3, \dots, p_\xi, \quad j = 2, 3, \dots, p_\eta \quad (C-9)$$

C.3 The trunk space for three-dimensional hexahedral finite elements**8 nodal modes**

$$N_{(1,1,1)}^{N_i}(\xi, \eta, \zeta) = \frac{1}{8} (1 + \xi_i \xi) (1 + \eta_i \eta) (1 + \zeta_i \zeta), \quad i = 1, 2, \dots, 8 \quad (C-10)$$

 $4[(p_\xi - 1) + (p_\eta - 1) + (p_\zeta - 1)]$ edge modes **$4(p_\xi - 1)$ edge modes in ξ -direction**

$$N_{(i,1,1)}^{E_1}(\xi, \eta, \zeta) = N_{i+1}^{p\text{-FEM}}(\xi) \cdot N_1^{p\text{-FEM}}(\eta) \cdot N_1^{p\text{-FEM}}(\zeta), \quad i = 2, 3, \dots, p_\xi \quad (C-11a)$$

$$N_{(i,1,1)}^{E_3}(\xi, \eta, \zeta) = N_{i+1}^{p\text{-FEM}}(\xi) \cdot N_2^{p\text{-FEM}}(\eta) \cdot N_1^{p\text{-FEM}}(\zeta), \quad i = 2, 3, \dots, p_\xi \quad (C-11b)$$

$$N_{(i,1,1)}^{E_9}(\xi, \eta, \zeta) = N_{i+1}^{p\text{-FEM}}(\xi) \cdot N_1^{p\text{-FEM}}(\eta) \cdot N_2^{p\text{-FEM}}(\zeta), \quad i = 2, 3, \dots, p_\xi \quad (C-11c)$$

$$N_{(i,1,1)}^{E_{11}}(\xi, \eta, \zeta) = N_{i+1}^{p\text{-FEM}}(\xi) \cdot N_2^{p\text{-FEM}}(\eta) \cdot N_2^{p\text{-FEM}}(\zeta), \quad i = 2, 3, \dots, p_\xi \quad (C-11d)$$

 $4(p_\eta - 1)$ edge modes in η -direction

$$N_{(1,j,1)}^{E_2}(\xi, \eta, \zeta) = N_2^{p\text{-FEM}}(\xi) \cdot N_{j+1}^{p\text{-FEM}}(\eta) \cdot N_1^{p\text{-FEM}}(\zeta), \quad j = 2, 3, \dots, p_\eta \quad (C-12a)$$

$$N_{(1,j,1)}^{E_4}(\xi, \eta, \zeta) = N_1^{p\text{-FEM}}(\xi) \cdot N_{j+1}^{p\text{-FEM}}(\eta) \cdot N_1^{p\text{-FEM}}(\zeta), \quad j = 2, 3, \dots, p_\eta \quad (C-12b)$$

$$N_{(1,j,1)}^{E_{10}}(\xi, \eta, \zeta) = N_2^{p\text{-FEM}}(\xi) \cdot N_{j+1}^{p\text{-FEM}}(\eta) \cdot N_2^{p\text{-FEM}}(\zeta), \quad j = 2, 3, \dots, p_\eta \quad (C-12c)$$

$$N_{(1,j,1)}^{E_{12}}(\xi, \eta, \zeta) = N_1^{p\text{-FEM}}(\xi) \cdot N_{j+1}^{p\text{-FEM}}(\eta) \cdot N_2^{p\text{-FEM}}(\zeta), \quad j = 2, 3, \dots, p_\eta \quad (C-12d)$$

 $4(p_\zeta - 1)$ edge modes in ζ -direction

$$N_{(1,1,k)}^{E_5}(\xi, \eta, \zeta) = N_1^{p\text{-FEM}}(\xi) \cdot N_1^{p\text{-FEM}}(\eta) \cdot N_{k+1}^{p\text{-FEM}}(\zeta), \quad k = 2, 3, \dots, p_\zeta \quad (C-13a)$$

$$N_{(1,1,k)}^{E_6}(\xi, \eta, \zeta) = N_2^{p\text{-FEM}}(\xi) \cdot N_1^{p\text{-FEM}}(\eta) \cdot N_{k+1}^{p\text{-FEM}}(\zeta), \quad k = 2, 3, \dots, p_\zeta \quad (C-13b)$$

$$N_{(1,1,k)}^{E_7}(\xi, \eta, \zeta) = N_2^{p\text{-FEM}}(\xi) \cdot N_2^{p\text{-FEM}}(\eta) \cdot N_{k+1}^{p\text{-FEM}}(\zeta), \quad k = 2, 3, \dots, p_\zeta \quad (C-13c)$$

$$N_{(1,1,k)}^{E_8}(\xi, \eta, \zeta) = N_1^{p\text{-FEM}}(\xi) \cdot N_2^{p\text{-FEM}}(\eta) \cdot N_{k+1}^{p\text{-FEM}}(\zeta), \quad k = 2, 3, \dots, p_\zeta \quad (C-13d)$$

face modes $\xi - \eta$ -plane

$$N_{(i,j,1)}^{F_1}(\xi, \eta, \zeta) = N_{i+1}^{p\text{-FEM}}(\xi) \cdot N_{j+1}^{p\text{-FEM}}(\eta) \cdot N_1^{p\text{-FEM}}(\zeta), \quad i = 2, 3, \dots, p_\xi - 2, \quad (C-14a)$$

$$j = 2, 3, \dots, p_\eta - 2, \quad i + j = 4, 5, \dots, \max(p_\xi, p_\eta)$$

$$N_{(i,j,1)}^{F_6}(\xi, \eta, \zeta) = N_{i+1}^{p\text{-FEM}}(\xi) \cdot N_{j+1}^{p\text{-FEM}}(\eta) \cdot N_2^{p\text{-FEM}}(\zeta), \quad i = 2, 3, \dots, p_\xi - 2, \quad (C-14b)$$

$$j = 2, 3, \dots, p_\eta - 2, \quad i + j = 4, 5, \dots, \max(p_\xi, p_\eta)$$

 $\xi - \zeta$ -plane

$$N_{(i,1,k)}^{F_2}(\xi, \eta, \zeta) = N_{i+1}^{p\text{-FEM}}(\xi) \cdot N_1^{p\text{-FEM}}(\eta) \cdot N_{k+1}^{p\text{-FEM}}(\zeta), \quad i = 2, 3, \dots, p_\xi - 2, \quad (C-15a)$$

$$k = 2, 3, \dots, p_\zeta - 2, \quad i + k = 4, 5, \dots, \max(p_\xi, p_\zeta)$$

$$N_{(i,1,k)}^{F_4}(\xi, \eta, \zeta) = N_{i+1}^{p\text{-FEM}}(\xi) \cdot N_2^{p\text{-FEM}}(\eta) \cdot N_{k+1}^{p\text{-FEM}}(\zeta), \quad i = 2, 3, \dots, p_\xi - 2, \quad (C-15b)$$

$$k = 2, 3, \dots, p_\zeta - 2, \quad i + k = 4, 5, \dots, \max(p_\xi, p_\zeta)$$

 $\eta - \zeta$ -plane

$$N_{(1,j,k)}^{F_3}(\xi, \eta, \zeta) = N_2^{p\text{-FEM}}(\xi) \cdot N_{j+1}^{p\text{-FEM}}(\eta) \cdot N_{k+1}^{p\text{-FEM}}(\zeta), \quad j = 2, 3, \dots, p_\eta - 2, \quad (C-16a)$$

$$k = 2, 3, \dots, p_\zeta - 2, \quad j + k = 4, 5, \dots, \max(p_\eta, p_\zeta)$$

$$N_{(1,j,k)}^{F_5}(\xi, \eta, \zeta) = N_1^{p\text{-FEM}}(\xi) \cdot N_{j+1}^{p\text{-FEM}}(\eta) \cdot N_{k+1}^{p\text{-FEM}}(\zeta), \quad j = 2, 3, \dots, p_\eta - 2, \quad (C-16b)$$

$$k = 2, 3, \dots, p_\zeta - 2, \quad j + k = 4, 5, \dots, \max(p_\eta, p_\zeta)$$

internal modes

$$N_{(i,j,k)}^{int}(\xi, \eta, \zeta) = N_{i+1}^{p\text{-FEM}}(\xi) \cdot N_{j+1}^{p\text{-FEM}}(\eta) \cdot N_{k+1}^{p\text{-FEM}}(\zeta), \quad i = 2, 3, \dots, p_\xi - 4, \quad (C-17)$$

$$j = 2, 3, \dots, p_\eta - 4, \quad k = 2, 3, \dots, p_\zeta - 4,$$

$$i + j + k = 6, 7, \dots, \max(p_\xi, p_\eta, p_\zeta)$$

C.4 The tensor product space for three-dimensional hexahedral finite elements

The tensor product space only influences the face and internal modes. Nodal and edge modes stay unchanged.

$2[(p_\eta - 1) \cdot (p_\zeta - 1) + (p_\eta - 1) \cdot (p_\zeta - 1) + (p_\eta - 1) \cdot (p_\zeta - 1)]$ **face modes**

$2[(p_\xi - 1) \cdot (p_\eta - 1)]$ $\xi - \eta$ -plane

$$N_{(i,j,1)}^{F_1}(\xi, \eta, \zeta) = N_{i+1}^{p\text{-FEM}}(\xi) \cdot N_{j+1}^{p\text{-FEM}}(\eta) \cdot N_1^{p\text{-FEM}}(\zeta), \quad i = 2, 3, \dots, p_\xi, \quad (C-18a)$$

$$j = 2, 3, \dots, p_\eta$$

$$N_{(i,j,1)}^{F_6}(\xi, \eta, \zeta) = N_{i+1}^{p\text{-FEM}}(\xi) \cdot N_{j+1}^{p\text{-FEM}}(\eta) \cdot N_2^{p\text{-FEM}}(\zeta), \quad i = 2, 3, \dots, p_\xi, \quad (C-18b)$$

$$j = 2, 3, \dots, p_\eta$$

$2[(p_\xi - 1) \cdot (p_\zeta - 1)]$ $\xi - \zeta$ -plane

$$N_{(i,1,k)}^{F_2}(\xi, \eta, \zeta) = N_{i+1}^{p\text{-FEM}}(\xi) \cdot N_1^{p\text{-FEM}}(\eta) \cdot N_{k+1}^{p\text{-FEM}}(\zeta), \quad i = 2, 3, \dots, p_\xi, \\ k = 2, 3, \dots, p_\zeta, \quad (\text{C-19a})$$

$$N_{(i,1,k)}^{F_4}(\xi, \eta, \zeta) = N_{i+1}^{p\text{-FEM}}(\xi) \cdot N_2^{p\text{-FEM}}(\eta) \cdot N_{k+1}^{p\text{-FEM}}(\zeta), \quad i = 2, 3, \dots, p_\xi, \\ k = 2, 3, \dots, p_\zeta \quad (\text{C-19b})$$

$2[(p_\eta - 1) \cdot (p_\zeta - 1)]$ $\eta - \zeta$ -plane

$$N_{(1,j,k)}^{F_3}(\xi, \eta, \zeta) = N_2^{p\text{-FEM}}(\xi) \cdot N_{j+1}^{p\text{-FEM}}(\eta) \cdot N_{k+1}^{p\text{-FEM}}(\zeta), \quad j = 2, 3, \dots, p_\eta, \\ k = 2, 3, \dots, p_\zeta \quad (\text{C-20a})$$

$$N_{(1,j,k)}^{F_5}(\xi, \eta, \zeta) = N_1^{p\text{-FEM}}(\xi) \cdot N_{j+1}^{p\text{-FEM}}(\eta) \cdot N_{k+1}^{p\text{-FEM}}(\zeta), \quad j = 2, 3, \dots, p_\eta, \\ k = 2, 3, \dots, p_\zeta \quad (\text{C-20b})$$

$[(p_\xi - 1) \cdot (p_\eta - 1) \cdot (p_\zeta - 1)]$ **internal modes**

$$N_{(i,j,k)}^{int}(\xi, \eta, \zeta) = N_{i+1}^{p\text{-FEM}}(\xi) \cdot N_{j+1}^{p\text{-FEM}}(\eta) \cdot N_{k+1}^{p\text{-FEM}}(\zeta), \quad i = 2, 3, \dots, p_\xi, \\ j = 2, 3, \dots, p_\eta, \quad k = 2, 3, \dots, p_\zeta \quad (\text{C-21})$$

Appendix D

Numerical Quadrature - points and weights

D.1 Gauß-Legendre quadrature

The points ξ_i and weights w_i used for the Gauß-Legendre quadrature are compiled in the following tables up to polynomial order $p = 9$.

Table D-1: 2-point Gauß-Legendre quadrature.

$\pm\xi_i$	w_i
0.57735 02691 89626	1.00000 00000 00000

Table D-2: 3-point Gauß-Legendre quadrature.

$\pm\xi_i$	w_i
0.00000 00000 00000	0.88888 88888 88889
0.77459 66692 41483	0.55555 55555 55555

Table D-3: 4-point Gauß-Legendre quadrature.

$\pm\xi_i$	w_i
0.33998 10435 84856	0.65214 51548 62546
0.86113 63115 94053	0.34785 48451 37454

Table D-4: 5-point Gauß-Legendre quadrature.

$\pm\xi_i$	w_i
0.00000 00000 00000	0.56888 88888 88889
0.53846 93101 05683	0.47862 86704 99366
0.90617 98459 38663	0.34785 48451 37454

Table D-5: 6-point Gauß-Legendre quadrature.

$\pm\xi_i$	w_i
0.23861 91860 83196	0.46791 39345 72691
0.66120 93864 66264	0.36076 15730 48138
0.93246 95142 03152	0.17132 44923 79170

Table D-6: 7-point Gauß-Legendre quadrature.

$\pm\xi_i$	w_i
0.00000 00000 00000	0.41795 91836 73469
0.40584 51513 77397	0.38183 00505 05118
0.74153 11855 99394	0.27970 53914 89276
0.94910 79123 42758	0.12948 49661 68869

Table D-7: 8-point Gauß-Legendre quadrature.

$\pm\xi_i$	w_i
0.18343 46424 95649	0.36268 37833 78361
0.52553 24099 16328	0.31370 66458 77887
0.79666 64774 13626	0.22238 10344 53374
0.96028 98564 97536	0.10122 85362 90376

Table D-8: 9-point Gauß-Legendre quadrature.

$\pm\xi_i$	w_i
0.00000 00000 00000	0.33023 93550 01259
0.32425 34234 03808	0.31234 70770 40002
0.61337 14327 00590	0.26061 06964 02935
0.83603 11073 26635	0.18064 81606 94857
0.96816 02395 07626	0.08127 43883 61574

Table D-9: 10-point Gauß-Legendre quadrature.

$\pm\xi_i$	w_i
0.14887 43389 81631	0.29552 42247 14752
0.43339 53941 29247	0.26926 67193 09996
0.67940 95682 99024	0.21908 63625 15982
0.86506 33666 88984	0.14945 13491 50580
0.97390 65285 17171	0.06667 13443 08688

D.2 Gauß-Lobatto quadrature

The points ξ_i and weights w_i used for the Gauß-Lobatto quadrature are compiled in the following tables up to polynomial order $p = 9$.

Table D-10: 3-point Gauß-Lobatto quadrature.

$\pm\xi_i$	w_i
0.00000 00000 00000	1.33333 33333 33333
1.00000 00000 00000	0.33333 33333 33333

Table D-11: 4-point Gauß-Lobatto quadrature.

$\pm\xi_i$	w_i
0.44721 35954 99958	0.83333 33333 33333
1.00000 00000 00000	0.16666 66666 66667

Table D-12: 5-point Gauß-Lobatto quadrature.

$\pm\xi_i$	w_i
0.00000 00000 00000	0.71111 11111 11111
0.65465 36707 07977	0.54444 44444 44444
1.00000 00000 00000	0.10000 00000 00000

Table D-13: 6-point Gauß-Lobatto quadrature.

$\pm\xi_i$	w_i
0.28523 15164 80645	0.55485 83770 35486
0.76505 53239 29465	0.37847 49562 97847
1.00000 00000 00000	0.06666 66666 66667

Table D-14: 7-point Gauß-Lobatto quadrature.

$\pm\xi_i$	w_i
0.00000 00000 00000	0.48761 90476 19048
0.46884 87934 70714	0.43174 53812 09863
0.83022 38962 78567	0.27682 60473 61566
1.00000 00000 00000	0.04761 90476 19048

Table D-15: 8-point Gauß-Lobatto quadrature.

$\pm\xi_i$	w_i
0.20929 92179 02479	0.41245 87946 58704
0.59170 01814 33142	0.34112 26924 83504
0.87174 01485 09607	0.21070 42271 43506
1.00000 00000 00000	0.03571 42857 14286

Table D-16: 9-point Gauß-Lobatto quadrature.

$\pm\xi_i$	w_i
0.00000 00000 00000	0.37151 92743 76417
0.36311 74638 26178	0.34642 85109 73046
0.67718 62795 10738	0.27453 87125 00162
0.89975 79954 11460	0.16549 53615 60806
1.00000 00000 00000	0.02777 77777 77778

Table D-17: 10-point Gauß-Lobatto quadrature.

$\pm\xi_i$	w_i
0.16527 89576 66387	0.32753 97611 83897
0.47792 49498 10445	0.29204 26836 79684
0.73877 38651 05505	0.22488 93420 63126
0.91953 39081 66459	0.13330 59908 51070
1.00000 00000 00000	0.02222 22222 22222

References

- [1] C. Boller, *Encyclopedia of Structural Health Monitoring*. John Wiley & Sons, 2009.
- [2] K. Diamanti and C. Soutis, “Structural health monitoring techniques for aircraft composite structures,” *Progress in Aerospace Sciences*, vol. 46, pp. 342–352, 2010.
- [3] C. Boller, “Ways and options for aircraft structural health management,” *Smart Materials and Structures*, vol. 10, pp. 432–440, 2001.
- [4] V. Giurgiutiu, J. M. Redmond, D. P. Roach, and K. Rackow, “Active sensors for health monitoring of aging aerospace structures,” in *Proceedings of SPIE*, 2000.
- [5] W. J. Staszewski, *Health Monitoring for Aerospace Structures*. John Wiley & Sons, 2003.
- [6] W. J. Staszewski, S. Mahzan, and R. Traynor, “Health monitoring of aerospace composite structures - active and passive approach,” *Composite Science and Technology*, vol. 69, pp. 1678–1685, 2009.
- [7] S. Doebling, C. Farrar, M. Prime, and W. Daniel, “Damage identification and health monitoring of structural and mechanical systems from changes in their vibration characteristics: A literature review,” tech. rep., Los Alamos National Laboratory Report LA-13070-MS, 1996.
- [8] A. Raghavan and C. E. S. Cesnik, *Damage Prognosis: For Aerospace, Civil and Mechanical Systems*, ch. 11, pp. 235–258. John Wiley and Sons, 2005.
- [9] A. Raghavan and C. E. S. Cesnik, “Review of guided-wave structural health monitoring,” *The Shock and Vibration Digest*, vol. 39, pp. 91–114, 2007.
- [10] V. Giurgiutiu, *Structural Health Monitoring with Piezoelectric Active Wafer Sensors: Fundamentals and Applications*. Elsevier, 2008.
- [11] V. Giurgiutiu, M. Gresil, B. Lin, A. Cuc, Y. Shen, and C. Roman, “Predictive modeling of piezoelectric wafer active sensors interaction with high-frequency structural waves and vibration,” *Acta Mechanica*, vol. 223, pp. 1681–1691, 2012.
- [12] H. Lamb, “On waves in an elastic plate,” *Proceedings of the Royal Society of London. Series A*, vol. 93, no. 648, pp. 114–128, 1917.
- [13] I. A. Viktorov, *Rayleigh and Lamb Waves*. Plenum Press., 1967.
- [14] A. Żak, M. Radziński, M. Krawczuk, and W. Ostachowicz, “Damage detection strategies based on propagation of guided elastic waves,” *Smart Materials and Structures*, vol. 21, pp. 1–18, 2012.

- [15] Z. A. B. Ahmad and U. Gabbert, "Simulation of Lamb wave reflections at plate edges using the semi-analytical finite element method," *Ultrasonics*, vol. 52, pp. 815–820, 2012.
- [16] H. Cho and C. J. Lissenden, "Structural health monitoring of fatigue crack growth in plate structures with ultrasonic guided waves," *Structural Health Monitoring*, vol. 11, pp. 393–404, 2012.
- [17] F. Ciampa, M. Meo, and E. Barbieri, "Impact localization in composite structures of arbitrary cross section," *Structural Health Monitoring*, vol. 11, pp. 643–655, 2012.
- [18] J. C. Dodson and D. J. Inman, "Thermal sensitivity of Lamb waves for structural health monitoring applications," *Ultrasonics*, 2012.
- [19] S. Pavlopoulou, C. Soutis, and W. J. Staszewski, "Cure monitoring through time-frequency analysis of guided ultrasonic waves," *Plastics, Rubber and Composites*, vol. 41, pp. 180–186, 2012.
- [20] S. Pavlopoulou, C. Soutis, and G. Manson, "Non-destructive inspection of adhesively bonded patch repairs using Lamb waves," *Plastics, Rubber and Composites*, vol. 41, pp. 61–68, 2012.
- [21] Z. A. B. Ahmad, *Numerical Simulation of Lamb Waves in Plates Using a Semi-Analytical Finite Element Method*. VDI Fortschritt-Berichte Reihe 20 Nr. 437, 2011.
- [22] W. Li, Y. Cho, and J. D. Achenbach, "Detection of thermal fatigue in composites by second order harmonic Lamb waves," *Smart Materials and Structures*, vol. 21, p. 8pp., 2012.
- [23] C. Pruell, J.-Y. Kim, J. Qu, and L. J. Jacobs, "Evaluation of plasticity driven material damage using Lamb waves," *Applied Physics Letters*, vol. 91, p. 3pp., 2007.
- [24] C. Pruell, J.-Y. Kim, J. Qu, and L. J. Jacobs, "Evaluation of fatigue damage using nonlinear guided waves," *Smart Materials and Structures*, vol. 18, p. 7pp., 2009.
- [25] C. Pruell, J.-Y. Kim, J. Qu, and L. J. Jacobs, "A nonlinear-guided wave technique for evaluating plasticity-driven material damage in a metal plate," *NDT & E International*, vol. 42, pp. 199–203, 2009.
- [26] F. Aymerich and W. J. Staszewski, "Impact damage detection in composite laminates using nonlinear acoustics," *Composites: Part A*, vol. 41, pp. 1084–1092, 2010.
- [27] Z. Parsons and W. J. Staszewski, "Nonlinear acoustics with low-profile piezoceramic excitation for crack detection in metallic structures," *Smart Materials and Structures*, vol. 15, pp. 1110–1118, 2006.
- [28] Z. Su, L. Ye, and X. Bu, "A damage identification technique for CF/EP composite laminates using distributed piezoelectric transducers," *Composite Structures*, vol. 57, pp. 465–471, 2002.

- [29] Z. Su, X. Wang, Z. Chen, L. Ye, and D. Wang, "A built-in active sensor network for health monitoring of composite structures," *Smart Materials and Structures*, vol. 15, pp. 1939–1949, 2006.
- [30] J. Hou, K. R. Leonard, and M. K. Hinders, "Automatic multi-mode Lamb wave arrival time extraction for improved tomographic reconstruction," *Inverse Problems*, vol. 20, pp. 1873–1888, 2004.
- [31] T. R. Hay, R. L. Royer, H. Gao, X. Zhao, and J. L. Rose, "A comparison of embedded sensor Lamb wave ultrasonic tomography approaches for material loss detection," *Smart Materials and Structures*, vol. 15, pp. 946–951, 2006.
- [32] B. V. Soma Sekhar, K. Balasubramaniam, C. V. Krishnamurthy, and B. Maxfield, "Algorithm for health monitoring of anisotropic plates using flexible ultrasonic patches," *Review of Quantitative Nondestructive Evaluation*, vol. 26, pp. 1501–1508, 2007.
- [33] A. H. Rohde, M. Veidt, L. R. F. Rose, and J. Homer, "A computer simulation study of imaging flexural inhomogeneities using plate-wave diffraction tomography," *Ultrasonics*, vol. 48, pp. 6–15, 2008.
- [34] C. T. Ng and M. Veidt, "A Lamb-wave-based technique for damage detection in composite laminates," *Smart Materials and Structures*, vol. 18, pp. 1–12, 2009.
- [35] C. H. Wang, J. T. Rose, and F.-K. Chang, "A computerized time-reversal method for structural health monitoring," in *Proceedings of SPIE*, 2007.
- [36] Z. Su and L. Ye, "A fast damage locating approach using digital damage fingerprints extracted from Lamb wave signals," *Smart Materials and Structures*, vol. 14, pp. 1047–1054, 2005.
- [37] N. Pan, Z. Su, L. Ye, L. M. Zhou, and Y. Lu, "A quantitative identification approach for delamination in laminated composite beams using digital damage fingerprints," *Composite Structures*, vol. 75, pp. 559–570, 2006.
- [38] Z. Su, C. Yang, N. Pan, L. Ye, and L. M. Zhou, "Assessment of delamination in composite beams using shear horizontal (SH) wave mode," *Composite Science and Technology*, vol. 67, pp. 244–251, 2007.
- [39] A. Ungethüm, *Migrationsbasierte Lokalisierung von Schadensereignissen und Schäden in flächigen anisotropen Strukturen*. PhD thesis, Helmut Schmidt University Hamburg, 2011.
- [40] R. Weber, S. M. H. Hosseini, and U. Gabbert, "Numerical simulation of the guided Lamb wave propagation in particle reinforced composites," *Composite Structures*, vol. 94, pp. 3064–3071, 2012.
- [41] S. M. H. Hosseini, A. Kharaghani, C. Kirsch, and U. Gabbert, "Numerical simulation of Lamb wave propagation in metallic foam sandwich structures: A parametric study," *Composite Structures*, vol. 97, pp. 387–400, 2013.

- [42] S. M. H. Hosseini and U. Gabbert, “Numerical simulation of the Lamb wave propagation in honeycomb sandwich panels: A parametric study,” *Composite Structures*, vol. 97, pp. 189–201, 2013.
- [43] T. Monnier, “Lamb wave-based impact damage monitoring of a stiffened aircraft panel using piezoelectric transducers,” *Journal of Intelligent Material Systems and Structures*, vol. 17, pp. 411–421, 2006.
- [44] M. D. Rogge and C. A. C. Leckey, “Characterization of impact damage in composite laminates using guided wavefield imaging and local wavenumber domain analysis,” *Ultrasonics*, vol. 53, pp. 1217–1226, 2013.
- [45] C. Ramadas, K. Balasubramaniam, M. Joshi, and C. V. Krishnamurthy, “Interaction of the primary anti-symmetric Lamb mode (A_0) with delaminations: Numerical and experimental studies,” *Smart Materials and Structures*, vol. 18, pp. 1–7, 2009.
- [46] K. S. Tan, N. Guo, B. S. Wong, and C. G. Tui, “Experimental evaluation of delaminations in composite plates by the use of Lamb waves,” *Composite Science and Technology*, vol. 53, pp. 77–84, 1995.
- [47] N. Toyama and J. Tkatsubo, “Lamb wave method for quick inspection of impact-induced delaminations in composite laminates,” *Composite Science and Technology*, vol. 64, pp. 1293–1300, 2004.
- [48] H. Duffo, B. Morvan, and J.-L. Izbicki, “Interaction of Lamb waves on bonded composite plates with defects,” *Composite Structures*, vol. 79, pp. 229–233, 2007.
- [49] J. Moll, R. T. Schulte, B. Hartmann, C.-P. Fritzen, and O. Nelles, “Multi-site damage localization in anisotropic plate-like structures using an active guided wave structural health monitoring system,” *Smart Materials and Structures*, vol. 19, no. 4, p. 15pp., 2010.
- [50] A. Shelke, T. Kundu, U. Amjad, K. Hahn, and W. Grill, “Mode-selective excitation and detection of ultrasonic guided waves for delamination detection in laminated aluminum plates,” *IEEE Transactions on Ultrasonics, Ferroelectrics and Frequency Control*, vol. 58, pp. 567–577, 2011.
- [51] Z. Su, L. Ye, and Y. Lu, “Guided Lamb waves for identification of damage in composite structures: A review,” *Journal of Sound and Vibration*, vol. 295, pp. 753–780, 2006.
- [52] Z. Su and L. Ye, *Lecture Notes in Applied and Computational Mechanics: Volume 48 Identification of Damage Using Lamb Waves*. Springer Verlag, 2009.
- [53] A. J. Croxford, J. Moll, P. D. Wilcox, and J. E. Michaels, “Efficient temperature compensation strategies for guided wave structural health monitoring,” *Ultrasonics*, vol. 50, pp. 517–528, 2010.
- [54] Y. Lu and J. E. Michaels, “A methodology for structural health monitoring with diffuse ultrasonic waves in the presence of temperature variations,” *Ultrasonics*, vol. 43, pp. 717–731, 2005.

- [55] K. J. Schubert and A. S. Herrmann, "On the influence of moisture absorption on Lamb wave propagation and measurements in viscoelastic CFRP using surface applied piezoelectric sensors," *Composite Structures*, vol. 94, pp. 3635–3643, 2012.
- [56] T. Clarke, *Guided Wave Health Monitoring of Complex Structures*. PhD thesis, Imperial College London, 2009.
- [57] L. Schubert, *Zustandsüberwachung an luftfahrttechnischen Faserverbundwerkstoffen durch Impakterkennung mittels geführter Wellen*. PhD thesis, Technical University Dresden, 2011.
- [58] J. Moll and C.-P. Fritzen, "Guided waves for autonomous online identification of structural defects under ambient temperature variations," *Journal of Sound and Vibration*, vol. 331, pp. 4587–4597, 2012.
- [59] J. Moll, *Strukturdiagnose mit Ultraschallwellen durch Verwendung von piezoelektrischen Sensoren und Aktoren*. PhD thesis, University of Siegen, 2011.
- [60] O. Putkis and A. J. Croxford, "Continuous baseline growth and monitoring for guided wave SHM," *Smart Materials and Structures*, vol. 22, p. 10pp., 2013.
- [61] T. H. Miller, T. Kundu, J. Huang, and J. Y. Grill, "A new guided wave-based technique for corrosion monitoring in reinforced concrete," *Structural Health Monitoring*, vol. 12, pp. 35–47, 2012.
- [62] T. H. T. Chan, L. Yu, H. Y. Tam, Y. Q. Ni, S. Y. Liu, W. H. Chung, and L. K. Cheng, "Fiber Bragg grating sensors for structural health monitoring of Tsing Ma Bridge: Background and experimental observation," *Engineering Structures*, vol. 28, pp. 648–659, 2006.
- [63] W. J. Staszewski, B. C. Lee, L. Mallet, and F. Scarpa, "Structural health monitoring monitoring using scanning laser vibrometry: I. Lamb wave sensing," *Smart Materials and Structures*, vol. 13, pp. 251–260, 2004.
- [64] L. Mallet, B. C. Lee, W. J. Staszewski, and F. Scalea, "Structural health monitoring monitoring using scanning laser vibrometry: II. Lamb waves for damage detection," *Smart Materials and Structures*, vol. 13, pp. 261–269, 2004.
- [65] W. H. Leong, B. C. Lee, W. J. Staszewski, and F. Scalea, "Structural health monitoring monitoring using scanning laser vibrometry: III. Lamb waves for fatigue crack detection," *Smart Materials and Structures*, vol. 14, pp. 1387–1395, 2005.
- [66] W. Hillger, "Lamb-Wellen zur Schadensanzeige in faserverstärkten Kunststoffen," in *DGZfP-Jahrestagung*, 2005.
- [67] W. Hillger, "Structural health monitoring using Lamb waves and visualization of their propagation in composites," in *EU Project Meeting on Aircraft Integrated Structural Health Assessment (AISHA)*, 2007.
- [68] R. Lammering, "Observation of piezoelectrically induced Lamb wave propagation in thin plates by use of speckle interferometry," *Experimental Mechanics*, vol. 50, pp. 377–387, 2010.

- [69] J. S. Ahn, P. K. Basu, and K. S. Woo, "Analysis of cracked aluminum plates with one-sided patch repair using p -convergent layered model," *Finite Elements in Analysis and Design*, vol. 46, pp. 438–448, 2010.
- [70] S. Pavlopoulou, C. Soutis, and K. Worden, "Application of pattern recognition for damage classification in scarf repairs," in *ISMA '12*, 2012.
- [71] S. Pavlopoulou, C. Soutis, and W. J. Staszewski, "Structural health monitoring of composite scarf repairs with guided waves," *Key Engineering Materials*, vol. 518, pp. 328–337, 2012.
- [72] M. A. Caminero, S. Pavlopoulou, M. Lopez-Pedrosa, B. G. Nicolaisson, C. Pinna, and C. Soutis, "Analysis of adhesively bonded repairs in composites: Damage detection and prognosis," *Composite Structures*, vol. 95, pp. 500–517, 2013.
- [73] M. H. Abedinmasab and M. I. Hussein, "Wave dispersion under finite deformation," *Wave Motion*, vol. 50, pp. 374–388, 2013.
- [74] M. S. Jensen, "High convergence order finite elements with lumped mass matrix," *International Journal for Numerical Methods in Engineering*, vol. 39, pp. 1879–1888, 1996.
- [75] C. E. Shannon, "Communication in the presence of noise," in *Proceedings of the Institute of Radio Engineers 37 (1949), 10-21*, 1949.
- [76] I. Bartoli, F. Scalea, M. Fateh, and E. Viola, "Modeling guided wave propagation with application to the long-range defect detection in railroad tracks," *NDT & E*, vol. 38, pp. 325–334, 2005.
- [77] F. Moser, J. J. Laurence, and J. Qu, "Modeling elastic wave propagation in waveguides with finite element method," *NDT & E*, vol. 32, pp. 225–234, 1999.
- [78] C. Willberg, S. Duczek, J. M. Vivar-Perez, D. Schmicker, and U. Gabbert, "Comparison of different higher order finite element schemes for the simulation of Lamb waves," *Computer Methods in Applied Mechanics and Engineering*, vol. 241-244, pp. 246–261, 2012.
- [79] O. Diligent, T. Grahn, A. Bostrom, P. Cawley, and M. J. S. Lowe, "The low frequency reflection and scattering of the s_0 lamb mode for a circular through-thickness hole in a plate: Finite element, analytical and experimental studies," *Journal of the Acoustical Society of America*, vol. 112, pp. 2589–2601, 2002.
- [80] H. Gao, *Ultrasonic Guided Wave Mechanics for Composite Material Structural Health Monitoring*. PhD thesis, Pennsylvania State University, 2007.
- [81] B. R. Mace and E. Manconi, "Modelling wave propagation in two-dimensional structures using finite element analysis," *Journal of Sound and Vibration*, vol. 318, pp. 884–902, 2008.
- [82] W. J. Zhou and M. N. Ichchou, "Wave propagation in mechanical waveguides with curved members using wave finite element solution," *Computer Methods in Applied Mechanics and Engineering*, vol. 199, pp. 2099–2109, 2010.

- [83] A. Marzani and S. Salamone, “Numerical prediction and experimental verification of temperature effect on plate waves generated and received by piezoceramic sensors,” *Mechanical Systems and Signal Processing*, vol. 30, pp. 204–217, 2012.
- [84] E. Manconi and S. Sorokin, “On the effect of damping on dispersion curves in plates,” *International Journal of Solids and Structures*, vol. 50, pp. 1966–1973, 2013.
- [85] S. Duczek, J. M. Vivar-Perez, and U. Gabbert, “Coupling of analytical and higher order finite element approaches for an efficient simulation of ultrasonic guided waves,” in *10th World Congress on Computational Mechanics*, 2012.
- [86] J. M. Vivar Perez, S. Duczek, and U. Gabbert, “Coupling of analytical and higher order finite element approaches for an efficient simulation of ultrasonic guided waves I: Two-dimensional analysis,” *Smart Structures and Systems*, vol. accepted for publication, p. 22pp., 2014.
- [87] J. M. Vivar-Perez, *Analytical and Spectral Methods for the Simulation of Elastic Waves in Thin Plates*. VDI Fortschritt-Berichte Reihe 20 Nr. 441, 2012.
- [88] M. Mazzotti, I. Bartoli, A. Marzani, and E. Viola, “A coupled SAFE-2.5D BEM approach for the dispersion analysis of damped leaky guided waves in embedded waveguides for arbitrary cross-section,” *Ultrasonics*, vol. 53, pp. 1227–1241, 2013.
- [89] M. Mazzotti, I. Bartoli, A. Marzani, and E. Viola, “A 2.5D boundary element formulation for modeling damped waves in arbitrary cross-section waveguides and cavities,” *Journal of Computational Physics*, vol. 248, pp. 363–382, 2013.
- [90] J.-M. Mencik, “On the low- and mid-frequency forced response of elastic structures using wave finite elements with one-dimensional propagation,” *Computers and Structures*, vol. 88, pp. 674–689, 2010.
- [91] J.-M. Mencik, “Model reduction and perturbation analysis of wave finite element formulations for computing the forced response of coupled elastic systems involving junctions with uncertain eigenfrequencies,” *Computer Methods in Applied Mechanics and Engineering*, vol. 200, pp. 3051–3065, 2011.
- [92] S. Gopalakrishnan, A. Chakraborty, and D. Mahapatra, *Spectral Finite Element Method*. Springer Verlag, 2007.
- [93] S. Gopalakrishnan and M. Mitra, *Wavelet Methods for Dynamical Problems*. CRC Press, 2010.
- [94] S. Gopalakrishnan, M. Ruzzene, and S. Hanagud, *Computational Techniques for Structural Health Monitoring*. Springer Verlag, 2011.
- [95] J. F. Doyle, *Wave Propagation in Structures*. Springer Verlag, 1997.
- [96] B. C. Lee and W. J. Staszewski, “Lamb wave propagation modelling for damage detection: I. two-dimensional analysis,” *Smart Materials and Structures*, vol. 16, pp. 249–259, 2007.

- [97] B. C. Lee and W. J. Staszewski, "Lamb wave propagation modelling for damage detection: II. Damage monitoring strategy," *Smart Materials and Structures*, vol. 16, pp. 260–274, 2007.
- [98] P. Paćko, T. Bielak, A. B. Spencer, W. J. Staszewski, T. Uhl, and K. Worden, "Lamb wave propagation modelling and simulation using parallel processing architecture and graphical cards," *Smart Materials and Structures*, vol. 21, pp. 1–13, 2012.
- [99] P. Kijanka, R. Radecki, P. Paćko, W. J. Staszewski, and T. Uhl, "GPU-based local interaction simulation approach for simplified temperature effect modelling in Lamb wave propagation used for damage detection," *Smart Materials and Structures*, vol. 22, p. 16pp., 2013.
- [100] H. Yim and Y. Sohn, "Simulation of ultrasonic waves in various types of elastic media using the mass-spring lattice model," *Materials Evaluation*, vol. 58, pp. 889–896, 2000.
- [101] P. Kluska, W. J. Staszewski, M. J. Leamy, and T. Uhl, "Cellular automata for Lamb wave propagation modelling in smart structures," *Smart Materials and Structures*, vol. 22, no. 8, p. 13pp., 2013.
- [102] P. Kudela, A. Żak, M. Krawczuk, and W. Ostachowicz, "Modelling of wave propagation in composite plates using the time domain spectral element method," *Journal of Sound and Vibration*, vol. 302, pp. 728–745, 2007.
- [103] P. Kudela and W. Ostachowicz, "Wave propagation modelling in composite plates," *Journal of Physics: Conference Series*, vol. 9, pp. 89–104, 2008.
- [104] P. Kudela, W. Ostachowicz, and A. Żak, "Damage detection in composite plates with embedded PZT transducers," *Mechanical Systems and Signal Processing*, vol. 22, pp. 1327–1335, 2008.
- [105] A. Żak, "A novel formulation of a spectral plate element for wave propagation in isotropic structures," *Finite Elements in Analysis and Design*, vol. 45, pp. 650–658, 2009.
- [106] W. Ostachowicz, P. Kudela, M. Krawczuk, and A. Żak, *Guided Waves in Structures for SHM: The Time-Domain Spectral Element Method*. John Wiley & Sons, 2011.
- [107] A. Żak, M. Krawczuk, and W. Ostachowicz, "Spectral finite element method for propagation of guided elastic waves in wind turbine blades for SHM purposes," in *In Proceedings of the 6th European Workshop on Structural Health Monitoring*, 2012.
- [108] R. T. Schulte, C.-P. Fritzen, and J. Moll, "Spectral element modelling of wave propagation in isotropic and anisotropic shell-structures including different types of damage," *IOP Conference Series: Materials Science and Engineering*, vol. 10, pp. 1–10, 2010.
- [109] R. T. Schulte and C.-P. Fritzen, "Simulation of wave propagation in damped composite structures with piezoelectric coupling," *Journal of Theoretical and Applied Mechanics*, vol. 49, pp. 879–903, 2011.

- [110] C.-P. Fritzen, R. T. Schulte, and H. Jung, “A modelling approach for virtual development of wave based shm systems,” *Journal of Physics: Conference Series*, vol. 305, pp. 1–10, 2011.
- [111] P. Kudela and W. Ostachowicz, “3d time-domain spectral elements for stress waves modelling,” *Journal of Physics: Conference Series*, vol. 181, pp. 1–8, 2009.
- [112] A. T. Patera, “A spectral element method for fluid dynamics: Laminar flow in a channel expansion,” *Journal of Computational Physics*, vol. 54, pp. 468–488, 1984.
- [113] H. Peng, G. Meng, and F. Li, “Modeling of wave propagation in plate structures using three-dimensional spectral element method for damage detection,” *Journal of Sound and Vibration*, vol. 320, pp. 942–954, 2009.
- [114] W. Ostachowicz and P. Kudela, “Wave propagation numerical models in damage detection based on the time domain spectral element method,” *IOP Conference Series: Materials Science and Engineering*, vol. 10, pp. 1–8, 2010.
- [115] B. Szabó and I. Babuška, *Finite Element Analysis*. John Wiley and Sons, 1991.
- [116] A. Düster, *High Order Finite Elements for Three-Dimensional, Thin-Walled Nonlinear Continua*. PhD thesis, Technical University Munich, 2002.
- [117] P. Solin, K. Segeth, and I. Dolezel, *Higher-Order Finite Element Methods*. Chapman and Hall, 2004.
- [118] L. Demkowicz, *Computing with hp-Adaptive Finite Elements: Volume 1: One and Two Dimensional Elliptic and Maxwell Problems*. Chapman and Hall, 2006.
- [119] L. Demkowicz, J. Kurtz, D. Pardo, M. Paszynski, W. Rachowicz, and A. Zdunek, *Computing with hp-Adaptive Finite Elements: Volume 2 Frontiers: Three Dimensional Elliptic and Maxwell Problems with Applications*. Chapman and Hall, 2008.
- [120] B. Szabó and I. Babuška, *Introduction to Finite Element Analysis: Formulation, Verification and Validation*. John Wiley and Sons, 2011.
- [121] T. J. R. Hughes, J. A. Cottrell, and Y. Bazilevs, “Isogeometric analysis: CAD, finite elements, NURBS, exact geometry and mesh refinement,” *Computer Methods in Applied Mechanics and Engineering*, vol. 194, pp. 4135–4195, 2005.
- [122] T. J. R. Hughes, A. Reali, and G. Sangalli, “Duality and unified analysis of discrete approximations in structural dynamics and wave propagation: Comparison of p -method finite elements with k -method NURBS,” *Computer Methods in Applied Mechanics and Engineering*, vol. 197, pp. 4104–4124, 2008.
- [123] J. A. Cottrell, T. J. R. Hughes, and Y. Bazilevs, *Isogeometric Analysis: Toward Integration of CAD and FEA*. John Wiley & Sons, 2009.
- [124] C. Willberg and U. Gabbert, “Development of a three-dimensional piezoelectric isogeometric finite element for smart structure applications,” *Acta Mechanica*, vol. 223, pp. 1837–1850, 2012.

- [125] C. Willberg, *Development of a New Isogeometric Finite Element and its Application for Lamb Wave Based Structural Health Monitoring*. VDI Fortschritt-Berichte Reihe 20 Nr. 446, 2013.
- [126] W. Dornisch, S. Klinkel, and B. Simeon, “Isogeometric Reissner-Mindlin shell analysis with exactly calculated director vectors,” *Computer Methods in Applied Mechanics and Engineering*, vol. 253, pp. 491–504, 2013.
- [127] A. Houmat, “A sector Fourier p -element applied to free vibration analysis of sectorial plates,” *Journal of Sound and Vibration*, vol. 243, pp. 269–282, 2000.
- [128] A. Düster, H. Bröker, and E. Rank, “The p -version of the finite element method for three-dimensional curved thin walled structures,” *International Journal for Numerical Methods in Engineering*, vol. 52, pp. 673–703, 2001.
- [129] D. Schillinger, L. Dede, M. A. Scott, J. A. Evans, M. J. Borden, E. Rank, and T. J. R. Hughes, “An isogeometric design-through-analysis methodology based on adaptive hierarchical refinement of NURBS, immersed boundary methods, and T-spline CAD surfaces,” *Computer Methods in Applied Mechanics and Engineering*, vol. 249-252, pp. 116–150, 2012.
- [130] Z. Yosibash, “ p -FEMs in biomechanics: Bones and arteries,” *Computer Methods in Applied Mechanics and Engineering*, vol. 249-252, pp. 169–184, 2012.
- [131] K. S. Woo, C. H. Hong, and P. K. Basu, “Materially and geometrically nonlinear analysis of laminated anisotropic plates by p -version of FEM,” *Computers & Structures*, vol. 81, pp. 1653–1662, 2003.
- [132] A. Düster and E. Rank, “The p -version of the finite element method compared to an adaptive h -version for the deformation theory of plasticity,” *Computer Methods in Applied Mechanics and Engineering*, vol. 190, pp. 1925–1935, 2001.
- [133] S. M. Holzer and Z. Yosibash, “The p -version of the finite element method in incremental elasto-plastic analysis,” *International Journal for Numerical Methods in Engineering*, vol. 39, pp. 1859–1878, 1996.
- [134] R. Krause, R. Mücke, and E. Rank, “ hp -version finite elements for geometrically nonlinear problems,” *Communications in Numerical Methods in Engineering*, vol. 11, pp. 887–897, 1995.
- [135] Y. Bazilevs, M.-C. Hsu, and M. A. Scott, “Isogeometric fluid-structure interaction analysis with emphasis on non-matching discretizations, and with application to wind turbines,” *Computer Methods in Applied Mechanics and Engineering*, vol. 249-252, pp. 28–41, 2012.
- [136] S. Geller, J. Tölke, and M. Krafczyk, “Lattice Boltzmann methods on quadtree-type grids for fluid-structure interaction,” *Fluid-Structure Interaction, Modelling, Simulation and Optimization*, vol. 53 Lecture Notes in Computational Sciences and Engineering, pp. 270–293, 2006.

- [137] S. Kollmannsberger, S. Geller, A. Düster, J. Tölke, C. Sorger, M. Krafczyk, and E. Rank, “Fixed-grid fluid-structure interaction in two dimensions based on a partitioned lattice Boltzmann and p-FEM approach,” *International Journal for Numerical Methods in Engineering*, vol. 79, pp. 817–845, 2009.
- [138] D. Scholz, S. Kollmannsberger, A. Düster, and E. Rank, “Thin solids for fluid-structure interaction,” *Fluid-Structure Interaction, Modelling, Simulation and Optimization*, vol. 53 Lecture Notes in Computational Sciences and Engineering, pp. 294–335, 2006.
- [139] G. Seriani, “Double-grid Chebyshev spectral elements for acoustic wave modeling,” *Wave Motion*, vol. 39, pp. 351–360, 2004.
- [140] G. Seriani and C. Su, “Wave propagation modeling in highly heterogeneous media by a poly-grid Chebyshev spectral element method,” *Journal of Computational Acoustics*, vol. 20, pp. 1–19, 2012.
- [141] G. Seriani and E. Priolo, “Spectral element method for acoustic wave simulation in heterogeneous media,” *Finite Elements in Analysis and Design*, vol. 16, pp. 337–348, 1994.
- [142] F. Li, H. Peng, X. Sun, J. Wang, and G. Meng, “Wave propagation analysis in composite laminates containing a delamination using a three-dimensional spectral element method,” *Mathematical Problems in Engineering*, vol. 1, pp. 1–19, 2012.
- [143] H. Peng, L. Ye, G. Meng, K. Sun, and F. Li, “Characteristics of elastic wave propagation in thick beams - when guided waves prevail?,” *Journal of Theoretical and Applied Mechanics*, vol. 49, pp. 807–823, 2011.
- [144] H. Peng, L. Ye, G. Meng, S. Mustapha, and F. Li, “Concise analysis of wave propagation using the spectral element method and identification of delamination in cf/ep composite beams,” *Smart Materials and Structures*, vol. 19, pp. 1–11, 2010.
- [145] D. Komatitsch and J. P. Vilotte, “The spectral-element method: An efficient tool to simulate the seismic response of 2d and 3d geological structures,” *Bulletin of the Seismological Society of America*, vol. 88, pp. 368–392, 1998.
- [146] D. Komatitsch and J. Tromp, “Spectral-element simulations of global seismic wave propagation I. - Validation,” *International Journal of Geophysics*, vol. 149, pp. 390–412, 2002.
- [147] D. Komatitsch and J. Tromp, “Spectral-element simulations of global seismic wave propagation II. - Three-dimensional models, oceans, rotation and self-gravitation,” *International Journal of Geophysics*, vol. 150, pp. 303–318, 2002.
- [148] S. Ha and F.-K. Chang, “Optimizing a spectral element for modeling PZT-induced Lamb wave propagation in thin plates,” *Smart Materials and Structures*, vol. 19, pp. 1–11, 2010.
- [149] S. Ha and F.-K. Chang, “Adhesive interface layer effects in PZT-induced Lamb wave propagation,” *Smart Materials and Structures*, vol. 19, pp. 1–9, 2010.

- [150] S. Ha, *Modeling Lamb Wave Propagation Induced by Adhesively Bonded PZTs on Thin Plates*. PhD thesis, Stanford University, 2009.
- [151] W. Dauksher and A. F. Emery, “An evaluation of the cost effectiveness of Chebyshev spectral and p -finite element solutions to the scalar wave equation,” *International Journal for Numerical Methods in Engineering*, vol. 45, pp. 1099–1113, 1999.
- [152] W. Dauksher and A. F. Emery, “Accuracy in modeling the acoustic wave equation with Chebyshev spectral finite elements,” *Finite Elements in Analysis and Design*, vol. 26, pp. 115–128, 1997.
- [153] W. Dauksher and A. F. Emery, “The solution of elastostatic and elastodynamic problems with Chebyshev spectral finite elements,” *Computer Methods in Applied Mechanics and Engineering*, vol. 188, pp. 217–233, 2000.
- [154] G. Seriani, “3-d large-scale wave propagation modeling by spectral element method on Cray T3E multiprocessor,” *Computer Methods in Applied Mechanics and Engineering*, vol. 164, pp. 235–247, 1998.
- [155] G. Seriani and S. P. Oliveira, “DFT modal analysis of spectral element methods for acoustic wave propagation,” *Journal of Computational Acoustics*, vol. 16, pp. 531–561, 2008.
- [156] R. Sridhar, A. Chakraborty, and S. Gopalakrishnan, “Wave propagation analysis in anisotropic and inhomogeneous uncracked and cracked structures using pseudospectral finite element method,” *International Journal of Solids and Structures*, vol. 43, pp. 4997–5031, 2006.
- [157] F. Ihlenburg and I. Babuška, “Dispersion analysis and error estimation of Galerkin finite element methods for the numerical computation of waves,” *International Journal for Numerical Methods in Engineering*, vol. 38, pp. 3745–3774, 1995.
- [158] F. Ihlenburg and I. Babuška, “Reliability of finite element methods for the numerical computation of waves,” *Advances in Engineering Software*, vol. 28, pp. 417–424, 1997.
- [159] M. Ainsworth and H. A. Wajid, “Dispersive and dissipative behavior of the spectral element method,” *SIAM Journal on Numerical Analysis*, vol. 47, pp. 3910–3937, 2010.
- [160] M. A. Christon, “The influence of the mass matrix on the dispersive nature of the semi-discrete, second-order wave equation,” *Computer Methods in Applied Mechanics and Engineering*, vol. 173, pp. 147–166, 1999.
- [161] M. Ainsworth and H. A. Wajid, “Optimally blended spectral-finite element scheme for wave propagation and nonstandard reduced integration,” *SIAM Journal on Numerical Analysis*, vol. 48, pp. 346–371, 2010.
- [162] J. Parvizian, A. Düster, and E. Rank, “Finite cell method: h - and p -extension for embedded domain problems in solid mechanics,” *Computational Mechanics*, vol. 41, pp. 121–133, 2007.

- [163] D. Schillinger, M. Ruess, N. Zander, Y. Bazilevs, A. Düster, and E. Rank, “Small and large deformation analysis with the p - and B-spline versions of the finite cell method,” *Computational Mechanics*, vol. 50, pp. 445–478, 2012.
- [164] A. Düster, H.-G. Sehlhorst, and E. Rank, “Numerical homogenization of heterogeneous and cellular materials utilizing the finite cell method,” *Computational Mechanics*, vol. 1, pp. 1–19, 2012.
- [165] E. Rank, S. Kollmannsberger, C. Sorger, and A. Düster, “Shell finite cell method: A high order fictitious domain approach for thin-walled structures,” *Computer Methods in Applied Mechanics and Engineering*, vol. 200, pp. 3200–3209, 2011.
- [166] A. Düster, J. Parvizian, Z. Yang, and E. Rank, “The finite cell method for three-dimensional problems of solid mechanics,” *Computer Methods in Applied Mechanics and Engineering*, vol. 197, pp. 3768–3782, 2008.
- [167] D. Schillinger, A. Düster, and E. Rank, “The hp - d -adaptive finite cell method for geometrically nonlinear problems of solid mechanics,” *International Journal for Numerical Methods in Engineering*, vol. 89, pp. 1171–1202, 2012.
- [168] A. Abedian, J. Parvizian, A. Düster, and E. Rank, “The finite cell method for the J_2 flow theory of plasticity,” *Finite Elements in Analysis and Design*, vol. 69, pp. 37–47, 2013.
- [169] A. Abedian, J. Parvizian, A. Düster, and E. Rank, “The FCM compared to the h -version FEM for elasto-plastic problems,” *Applied Mathematics and Mechanics*, vol. accepted for publication, 2014.
- [170] J. Parvizian, A. Düster, and E. Rank, “Topology optimization using the finite cell method,” *Optimization and Engineering*, vol. 13, pp. 57–78, 2012.
- [171] M. Joulaian and A. Düster, “Local enrichment of the finite cell method for problems with material interfaces,” *Computational Mechanics*, vol. 52, pp. 741–762, 2013.
- [172] N. Zander, S. Kollmannsberger, M. Ruess, Z. Yosibash, and E. Rank, “The finite cell method for linear thermoelasticity,” *Computers and Mathematics with Applications*, vol. 64, pp. 3527–3541, 2012.
- [173] S. Duczek, S. Liefold, and U. Gabbert, “The finite and spectral cell method for smart structure applications: Transient analysis,” *Acta Mechanica*, vol. under review, 2014.
- [174] A. N. Bugrov and S. Smagulov, “Fictitious domain method for Navier-Stokes equation,” *Mathematical Model of Fluid Flow*, vol. 1, pp. 79–90, 1978.
- [175] C. S. Peskin, “The fluid dynamics of heart valves: Experimental, theoretical and computational methods,” *Annual Review of Fluid Mechanics*, vol. 14, pp. 235–259, 1981.
- [176] S. Duczek, M. Joulaian, A. Düster, and U. Gabbert, “Simulation of Lamb waves using the spectral cell method,” in *Proceedings of SPIE Smart Structures/NDE (8695)*, 2013.

- [177] S. Duczek, M. Joulaian, A. Düster, and U. Gabbert, “Numerical analysis of Lamb waves using the finite and spectral cell methods,” *International Journal for Numerical Methods in Engineering*, vol. 99, pp. 26–53, 2014.
- [178] M. Joulaian, S. Duczek, U. Gabbert, and A. Düster, “Finite and spectral cell method for wave propagation in heterogeneous materials,” *Computational Mechanics*, vol. on-line available, p. 15pp., 2014.
- [179] K. F. Graff, *Wave Motion in Elastic Solids*. Oxford University Press, 1975.
- [180] J. D. Achenbach, *Applied Mathematics and Mechanics: Volume 16 Wave Propagation in Elastic Solids*. North-Holland Publishing Company, 1987.
- [181] J. L. Rose, *Ultrasonic Waves in Solid Media*. Cambridge University Press, 1999.
- [182] S. von Ende, *Transient angeregte Lamb-Wellen in elastischen und viskoelastischen Platten: Berechnung und experimentelle Verifikation*. PhD thesis, Helmut-Schmidt-University Hamburg, 2008.
- [183] D. Schmicker, “Development and testing of higher order finite elements based on lagrange polynomials for the analysis of guided ultrasonic waves in thin-walled structures,” Master’s thesis, Otto-von-Guericke-University Magdeburg, 2011.
- [184] M. Calomfirescu, *Lamb Waves for Structural Health Monitoring in Viscoelastic Materials*. PhD thesis, University of Bremen, 2008.
- [185] J. Pohl, *Zerstörungsfreie Charakterisierung adaptiver CFK-Piezokeramik-Verbunde: Konventionelle Verfahren und Health Monitoring*. PhD thesis, Otto-von-Guericke-University Magdeburg, 2003.
- [186] X. Zhao, H. Gao, G. Zhang, B. Ayhan, F. Yan, C. Kwan, and J. L. Rose, “Active health monitoring of an aircraft wing with embedded piezoelectric sensor/actuator network. I. Defect detection, localization and growth monitoring,” *Smart Materials and Structures*, vol. 16, pp. 1208–1217, 2007.
- [187] X. Zhao, T. Qian, G. Mei, C. Kwan, R. Zane, C. Walsh, T. Paing, and Z. Popovic, “Active health monitoring of an aircraft wing with embedded piezoelectric sensor/actuator network. II. Wireless approach,” *Smart Materials and Structures*, vol. 16, pp. 1218–1225, 2007.
- [188] W. H. Prosser, K. E. Jackson, S. Kellas, B. T. Smith, J. McKeon, and A. Friedman, “Advanced, waveform based acoustic emission detection of matrix cracking in composites,” *Materials Evaluation*, vol. 9, pp. 1052–1058, 1995.
- [189] L. de Marchi, A. Marzani, N. Speciale, and E. Viola, “A passive monitoring technique based on dispersion compensation to locate impacts in plate-like structures,” *Smart Materials and Structures*, vol. 20, p. 9pp., 2011.
- [190] MEAS-SPEC, “Piezo sensor - dt series lead attachments.” url: http://www.meas-spec.com/product/t_product.aspx?id=2480&terms=DT%20Series%20Lead%20Attachments*, accessed: 2014-05-01.

- [191] Gizmag, “Kyocera - wafer-thin piezo film speaker.” url: <http://www.gizmag.com/piezo-film-speaker-smart-sonic-sound/28866/>, accessed: 2014-05-01.
- [192] V. Giurgiutiu, “Lamb wave generation with piezoelectric wafer active sensors for structural health monitoring,” *SPIE*, vol. 10, pp. 1–12, 2002.
- [193] H. Huang, T. Pamphile, and M. Derriso, “The effect of actuator bending on Lamb wave displacement fields generated by a piezoelectric patch,” *Smart Materials and Structures*, vol. 17, pp. 13–25, 2008.
- [194] X. Wang, Y. Lu, and J. Tang, “Damage detection using piezoelectric transducers and the Lamb wave approach: I. System analysis,” *Smart Materials and Structures*, vol. 17, p. 15pp., 2008.
- [195] Y. Lu, X. Wang, L. Tang, and Y. Ding, “Damage detection using piezoelectric transducers and the Lamb wave approach: II. Robust and quantitative decision making,” *Smart Materials and Structures*, vol. 17, p. 13pp., 2008.
- [196] M. S. Azzouz, C. Mei, J. S. Bevan, and J. J. Ro, “Finite element modeling of MFC/AFC actuators and performance of MFC,” *Journal of Intelligent Material Systems and Structures*, vol. 12, pp. 601–612, 2001.
- [197] R. B. Williams, G. Park, D. J. Inman, and W. K. Wilkie, “An overview of composite actuators with piezoceramic fibers,” in *Proceedings of SPIE*, 2002.
- [198] E. K. Akdogan, M. Allahverdi, and A. Safari, “Piezoelectric composites for sensor and actuator applications,” *IEEE Transactions on Ultrasonics, Ferroelectrics and Frequency Control*, vol. 52, pp. 746–775, 2005.
- [199] A. Benjeddou, “Advances in piezoelectric finite element modeling of adaptive structural elements: A survey,” *Computers & Structures*, vol. 76, pp. 347–363, 2000.
- [200] A. Görnandt, *Einbeziehung der Temperatur in die Modellbildung und Berechnung von aktiven Strukturen mit piezokeramischen Aktuatoren und Sensoren*. PhD thesis, Otto-von-Guericke-University Magdeburg, 2002.
- [201] T. Ikeda, *Fundamentals of Piezoelectricity*. Oxford Science Publications, 1990.
- [202] K. Uchino, *Ferroelectric Devices*. Marcel Dekker, Inc., 2000.
- [203] H. F. Tiersten, *Linear Piezoelectric Plate Vibrations: Elements of the Linear Theory of Piezoelectricity and the Vibrations of Piezoelectric Plates*. Plenum Press., 1969.
- [204] S. Katzir, *The Beginnings of Piezoelectricity*. Springer Verlag, 2006.
- [205] V. Piefort, *Finite Element Modelling of Piezoelectric Active Structures*. PhD thesis, University of Brussels, 2001.
- [206] C. Zwick Rosen, B. V. Hiremath, and R. Newnham, *Piezoelectricity*. American Institute of Physics, 1992.

- [207] D. Marinkovic, *A New Finite Composite Shell Element for Piezoelectric Active Structures*. PhD thesis, Otto-von-Guericke-University Magdeburg, 2007.
- [208] T. H. Brockmann, *Theory of Adaptive Fiber Composites: From Piezoelectric Material Behavior to Dynamics of Rotating Structures*. Springer Verlag, 2009.
- [209] H. F. Tiersten, “Nonlinear electroelastic equations cubic in the small field variables,” *Journal of the Acoustical Society of America*, vol. 57, pp. 660–666, 1975.
- [210] van Randeraat, *Piezoelectric Ceramics*. Mullard Ltd., 1974.
- [211] K. J. Bathe, *Finite-Elemente-Methoden*. Springer Verlag, 2002.
- [212] T. J. R. Hughes, *The Finite Element Method: Linear Static and Dynamic Finite Element Analysis*. Prentice-Hall, 1987.
- [213] J. N. Reddy, *An Introduction to Nonlinear Finite Element Analysis*. Oxford Science Publications, 2004.
- [214] K. Weinberg, *Ein Finite-Elemente-Konzept zur lokalen Netzverdichtung und seine Anwendung auf Koppel- und Kontaktprobleme*. PhD thesis, Otto-von-Guericke-University Magdeburg, 1996.
- [215] C. Becker, *Finite Elemente Methoden zur räumlichen Diskretisierung von Mehrfeldproblemen der Strukturmechanik unter Berücksichtigung diskreter Risse*. PhD thesis, Ruhr-University Bochum, 2007.
- [216] H. Allik and T. J. R. Hughes, “Finite element method for piezoelectric vibration,” *International Journal for Numerical Methods in Engineering*, vol. 2, pp. 151–157, 1970.
- [217] F. Seeger, *Simulation und Optimierung adaptiver Schalenstrukturen*. PhD thesis, Otto-von-Guericke-University Magdeburg, 2003.
- [218] J. Lefèvre, *Finite-Elemente-Simulation adaptiver Leichtbaustrukturen zur Untersuchung der Schwingungs- und Schallreduktion*. PhD thesis, Otto-von-Guericke-University Magdeburg, 2007.
- [219] S. Ringwelski, *Numerische Modelle für die aktive Schwingungs- und Schallreduktion und deren Verifikation*. PhD thesis, Otto-von-Guericke-University Magdeburg, 2011.
- [220] S. Duczek and U. Gabbert, “Anisotropic hierarchic finite elements for the simulation of piezoelectric smart structures,” *Engineering Computations*, vol. 30 (5), pp. 682–706, 2013.
- [221] A. Benjeddou and J.-F. Deü, “A two-dimensional closed-form solution for the free-vibrations analysis of piezoelectric sandwich plates,” *International Journal of Solids and Structures*, vol. 39, pp. 1463–1486, 2002.
- [222] J. W. S. Rayleigh, *The Theory of Sound*. Dover Publications, 1894.

- [223] K. C. Park and P. G. Underwood, "A variable-step central difference method for structural dynamics analysis - part 1. Theoretical aspects," *Computer Methods in Applied Mechanics and Engineering*, vol. 22, pp. 241–258, 1980.
- [224] K. C. Park and P. G. Underwood, "A variable-step central difference method for structural dynamics analysis - part 2. Implementation and performance evaluation," *Computer Methods in Applied Mechanics and Engineering*, vol. 23, pp. 259–279, 1980.
- [225] R. R. Craig and A. J. Kurdila, *Fundamentals of Structural Dynamics*. John Wiley & Sons, 2006.
- [226] H. M. Hilber and T. J. R. Hughes, "Collocation, dissipation and 'overshoot' for time integration schemes in structural dynamics," *Earthquake Engineering and Structural Dynamics*, vol. 6, pp. 99–117, 1978.
- [227] N. M. Newmark, "A method of computation for structural dynamics," *ASCE Journal of the Engineering Mechanics Division*, vol. 85, pp. 2067 – 2094, 1959.
- [228] N. M. Newmark, "Computation of dynamic structural response in the range approaching failure," in *Proceedings of the Symposium on Earthquake and Blast Effects on Structures*, 1952.
- [229] J. Stoer and R. Bulirsch, *Stoer/Bulirsch: Numerische Mathematik 2*. Springer Verlag, 2005.
- [230] I. Ergatoudis, B. M. Irons, and O. C. Zienkiewicz, "Curved isoparametric 'quadrilateral' elements for finite element analysis," *International Journal of Solids Structures*, vol. 4, pp. 31–42, 1968.
- [231] O. C. Zienkiewicz, B. M. Irons, I. Ergatoudis, S. Ahmad, and F. Scott, *Finite Element Methods in Stress Analysis*, ch. Isoparametric and Associate Finite Element Families for Two- and Three-Dimensional Analysis. Tapir, Technical University of Norway, Trondheim, 1969.
- [232] W. J. Gordon, "Blending-function methods of bivariate and multivariate interpolation and approximation," *SIAM Journal on Numerical Analysis*, vol. 8, pp. 158–177, 1971.
- [233] W. J. Gordon and C. A. Hall, "Construction of curvilinear co-ordinate systems and applications to mesh generation," *International Journal for Numerical Methods in Engineering*, vol. 7, pp. 461–477, 1973.
- [234] W. J. Gordon and C. A. Hall, "Transfinite element methods: Blending-function interpolation over arbitrary curved element domains," *Numerische Mathematik*, vol. 21, pp. 109–129, 1973.
- [235] W. J. Gordon and L. C. Thiel, *Transfinite Mappings and their Application to Grid Generation*. Elsevier Science Publishing, 1982.

- [236] K.-U. Bletzinger, *Formoptimierung von Flächentragwerken*. PhD thesis, Technical University Stuttgart, 1990.
- [237] G. Királyfalvi and B. Szabó, “Quasi-regional mapping for the p -version of the finite element method,” *Finite Elements in Analysis and Design*, vol. 27, pp. 85–97, 1997.
- [238] S. Dey, *Geometry-Based Three-Dimensional hp-Finite Element Modelling and Computations*. PhD thesis, Rensselaer Polytechnic Institute Troy, 1997.
- [239] H. Bröker, *Integration von geometrischer Modellierung und Berechnung nach der p -Version der FEM*. PhD thesis, Technical University Munich, 2001.
- [240] U. Heisserer, *High-Order Finite Elements for Material and Geometric Nonlinear Finite Strain Problems*. PhD thesis, Technical University Munich, 2008.
- [241] O. C. Zienkiewicz and R. L. Taylor, *The Finite Element Method: Volume 1 The Basis*. Butterworth Heinemann, 2000.
- [242] D. P. Bertsekas, *Constrained Optimization and Lagrange Multiplier Methods*. Athena Scientific, 1996.
- [243] N. Zander, “The finite cell method for linear thermoelasticity,” Master’s thesis, Technical University Munich, 2011.
- [244] J. Nitsche, “Über ein Variationsprinzip zur Lösung von Dirichlet-Problemen bei Verwendung von Teilräumen, die keinen Randbedingungen unterworfen sind,” tech. rep., *Abhandlungen aus dem Mathematischen Seminar der Universität Hamburg*, 1970.
- [245] M. Ainsworth, “Essential boundary conditions and multi-point constraints in finite element analysis,” *Computer Methods in Applied Mechanics and Engineering*, vol. 190, pp. 6323–6339, 2001.
- [246] M. Ruess, D. Tal, N. Trabelsi, Z. Yosibash, and E. Rank, “The finite cell method for bone simulations: Verification and validation,” *Biomechanics and Modeling in Mechanobiology*, vol. 11, pp. 425–437, 2012.
- [247] M. Ruess, Y. Bazilevs, D. Schillinger, N. Zander, and E. Rank, “Weakly enforced boundary conditions for the NURBS-based finite cell method,” in *Proceedings of the European Congress on Computational Methods in Applied Sciences and Engineering*, 2012.
- [248] P. Hansbo, “Nitsche’s method for interface problems in computational mechanics,” *GAMM Mitteilungen*, vol. 28, pp. 183–206, 2005.
- [249] N. Zander, T. Bog, R. Elhaddad, M. Espinoza, H. H., A. Joly, C. Wu, P. Zerbe, A. Düster, S. Kollmannsberger, J. Parvizian, M. Ruess, D. Schillinger, and E. Rank, “FCMLab: A finite cell research toolbox for MATLAB,” *Advances in Engineering Software*, vol. 74, pp. 49–63, 2014.
- [250] D. N. Arnold, F. Brezzi, B. Cockburn, and L. D. Marini, “Unified analysis of discontinuous Galerkin methods for elliptic problems,” *SIAM Journal on Numerical Analysis*, vol. 39, pp. 1749–1779, 2002.

- [251] S. Fernández-Méndez and A. Huerta, “Imposing essential boundary conditions in mesh-free methods,” *Computer Methods in Applied Mechanics and Engineering*, vol. 193, pp. 1257–1275, 2004.
- [252] Y. Bazilevs and T. J. R. Hughes, “Weak imposition of Dirichlet boundary conditions in fluid mechanics,” *Computers & Fluids*, vol. 36, pp. 12–26, 2007.
- [253] A. Embar, J. Dolbow., and I. Harari, “Imposing Dirichlet boundary conditions with Nitsche’s method and spline-based finite elements,” *International Journal for Numerical Methods in Engineering*, vol. 83, pp. 877–898, 2010.
- [254] M. Ruess, D. Schillinger, Y. Bazilevs, V. Varduhn, and E. Rank, “Weakly enforced essential boundary conditions for NURBS-embedded and trimmed NURBS geometries on the basis of the finite cell method,” *International Journal for Numerical Methods in Engineering*, vol. 95, pp. 811–846, 2013.
- [255] I. N. Bronstein, K. A. Semendjajew, G. Musiol, and H. Mühlig, *Taschenbuch der Mathematik*. Harri Deutsch, 2008.
- [256] E. Hinton, T. Rock, and O. C. Zienkiewicz, “A note on mass lumping and related processes in the finite element method,” *Earthquake Engineering and Structural Dynamics*, vol. 4, pp. 245–249, 1976.
- [257] D. Schillinger, *The p- and B-Spline Versions of the Geometrically Nonlinear Finite Cell Method and Hierarchical Refinement Strategies for Adaptive Isogeometric and Embedded Domain Analysis*. PhD thesis, Technical University Munich, 2012.
- [258] D. Schillinger and M. Ruess, “The finite cell method: A review in the context of high-order structural analysis of CAD and image-based geometric models,” *Archives of Computational Methods in Engineering*, vol. online available, p. 65pp., 2014.
- [259] E. Rank, M. Ruess, S. Kollmannsberger, D. Schillinger, and A. Düster, “Geometric modeling, isogeometric analysis and the finite cell method,” *Computer Methods in Applied Mechanics and Engineering*, vol. 249-252, pp. 104–115, 2012.
- [260] V. K. Saul’ev, “A method for automatization of the solution of boundary value problems on high performance computers,” *Doklady Akademii Nauk SSSR 144 (1962), 497-500 (in Russian)*. *English translation in Soviet Mathematics Doklady*, vol. 3, pp. 763–766, 1963.
- [261] V. K. Saul’ev, “On solution of some boundary value problems on high performance computers by fictitious domain method,” *Siberian Mathematical Journal*, vol. 4, pp. 912–925, 1963.
- [262] P. Neittaanmäki and D. Tiba, “An embedding of domains approach in free boundary problems and optimal design,” *SIAM Journal on Control and Optimization*, vol. 33, pp. 1587–1602, 1995.
- [263] A. Abedian, J. Parvizian, A. Düster, H. Khademyzadeh, and E. Rank, “Performance of different integration schemes in facing discontinuities in the finite cell method,” *International Journal of Computational Methods*, vol. 10, p. 24pp., 2013.

- [264] R. W. Freund and R. H. W. Hoppe, *Stoer/Bulirsch: Numerische Mathematik 1*. Springer Verlag, 2007.
- [265] Z. Yang, *The Finite Cell Method for Geometry-Based Structural Simulation*. PhD thesis, Technical University Munich, 2011.
- [266] Z. Yang, S. Kollmannsberger, A. Düster, M. Ruess, E. Grande Garcia, R. Burgkart, and E. Rank, “Non-standard bone simulation: Interactive numerical analysis by computational steering,” *Computing and Visualization in Science*, vol. 14, pp. 207–216, 2011.
- [267] Z. Yang, M. Ruess, S. Kollmannsberger, A. Düster, and E. Rank, “An efficient integration technique for the voxel-based finite cell method,” *International Journal for Numerical Methods in Engineering*, vol. 91, pp. 457–471, 2012.
- [268] C. Vinci, “Application of Dirichlet boundary conditions in the finite cell method,” Master’s thesis, Technical University Munich, 2009.
- [269] J. M. Melenk, K. Gerde, and C. Schwab, “Fully discrete hp -finite elements: Fast quadrature,” *Computer Methods in Applied Mechanics and Engineering*, vol. 190, pp. 4339–4364, 2001.
- [270] H. E. Hinnant, “A fast method of numerical quadrature for p -version finite element matrices,” *International Journal for Numerical Methods in Engineering*, vol. 37, pp. 3723–3750, 1994.
- [271] S. A. Orszag, “Spectral methods for problems in complex geometries,” *Journal of Computational Physics*, vol. 37, pp. 70–92, 1980.
- [272] V. Nübel, “Eine effiziente Methode zur numerischen Integration von Elementmatrizen bei der p -Version der Finite-Elemente-Methode,” Master’s thesis, Technical University Munich, 1999.
- [273] V. Nübel, A. Düster, and E. Rank, “Die Methode Vektorintegration bei der p -Version der Finite-Elemente-Methode,” tech. rep., Technical University Munich, 2000.
- [274] V. Nübel, A. Düster, and E. Rank, “Adaptive vector integration as an efficient quadrature scheme for p -version finite element matrices,” in *Proceedings of the European Conference on Computational Mechanics*, 2001.
- [275] V. Nübel, *Die adaptive rp-Methode für elastoplastische Probleme*. PhD thesis, Technical University Munich, 2005.
- [276] L. L. Thompson and P. M. Pinsky, “Complex wavenumber Fourier analysis of the p -version finite element method,” *Computational Mechanics*, vol. 13, pp. 255–275, 1994.
- [277] M. G. Milsted and J. R. Hutchinson, “Use of trigonometric terms in the finite element method with application to vibrating membranes,” *Journal of Sound and Vibration*, vol. 32, pp. 327–346, 1973.

- [278] O. Beslin and J. Nicolas, “A hierarchical functions set for predicting very high order plate bending modes with any boundary conditions,” *Journal of Sound and Vibrations*, vol. 202, pp. 633–655, 1996.
- [279] J. B. Gunda, A. P. Singh, P. S. Chhabra, and R. Ganguli, “Free vibration analysis of rotating tapered blades using Fourier- p superelement,” *Structural Engineering and Mechanics*, vol. 27, pp. 1–15, 2007.
- [280] A. Houmat, “Hierarchical finite element analysis of the vibration of membranes,” *Journal of Sound and Vibration*, vol. 201, pp. 465–472, 1996.
- [281] A. Houmat, “An alternative hierarchical finite element formulation applied to plate vibrations,” *Journal of Sound and Vibration*, vol. 206, pp. 201–215, 1997.
- [282] A. Y. T. Leung and J. K. W. Chan, “Fourier p -element for the analysis of beams and plates,” *Journal of Sound and Vibration*, vol. 212, pp. 179–185, 1997.
- [283] A. Y. T. Leung and B. Zhu, “Hexahedral Fourier p -elements for vibration of prismatic solids,” *International Journal of Structural Stability and Dynamics*, vol. 4, pp. 125–138, 2003.
- [284] L. Yongqiang and L. Jian, “Free vibration analysis of circular and annular sectorial thin plates using curve strip Fourier p -element,” *Journal of Sound and Vibration*, vol. 305, pp. 457–466, 2007.
- [285] Z. Bin, *p-Version Finite Elements and Applications in Structural Impact and Damage Detection*. PhD thesis, City University Hong Kong, 2005.
- [286] F. Jie, *p-Version Finite Elements in Structural Dynamics and Stability*. PhD thesis, City University Hong Kong, 2010.
- [287] L. J. West, N. S. Bardell, J. M. Dunsdon, and P. M. Loasby, “Some limitations associated with the use of k -orthogonal polynomials in hierarchical versions of the finite element method,” in *Structural Dynamics: Recent Advances. Proceedings of the 6th International Conference. Volume 1*, 1997.
- [288] W. Betz, I. Papaioannou, and D. Straub, “Numerical methods for the discretization of random fields by means of the Karhunen-Loève expansion,” *Computer Methods in Applied Mechanics and Engineering*, vol. 271, pp. 109–129, 2014.
- [289] R. Krause and E. Rank, “Multiscale computations with a combination of the h - and p -versions of the finite-element method,” *Computer Methods in Applied Mechanics and Engineering*, vol. 192, pp. 3959–3983, 2003.
- [290] D. Gottlieb and S. A. Orzag, *Numerical Analysis of Spectral Methods: Theory and Applications*. Society for Industrial and Applied Mathematics, 1987.
- [291] L. N. Trefethen, *Spectral Methods in Matlab*. Siam, 2000.
- [292] J. P. Boyd, *Chebyshev and Fourier Spectral Methods*. Dover Publications, 2000.

- [293] C. Pozrikidis, *Introduction to Finite and Spectral Methods using MATLAB*. Chapman and Hall, 2005.
- [294] J. Dankert and D. H., *Technische Mechanik: Statik, Festigkeitslehre, Kinematik/Kinetik*. Vieweg Teubner, 2010.
- [295] J. Stoer and R. Bulirsch, *Numerische Mathematik 1*. Springer Verlag, 2007.
- [296] A. Düster, *High Order FEM*. University of Technology Hamburg-Harburg, 2010.
- [297] U. Heisserer, *AdhoC⁴ - Technical Guided*. Technical University Munich.
- [298] F. W. King, *Hilbert Transforms Volume 1*. Cambridge University Press, 2009.
- [299] F. W. King, *Hilbert Transforms Volume 2*. Cambridge University Press, 2009.
- [300] B. Xu, L. Yu, and V. Giurgiutiu, “Advanced methods for time-of-flight estimation with application to lamb wave structural health monitoring,” in *The 7th International Workshop on Structural Health Monitoring*, 2009.
- [301] R. Courant, K. Friedrichs, and H. Levy, “Über die partiellen Differenzgleichungen der mathematischen Physik,” *Mathematische Annalen*, vol. 100, pp. 32–74, 1928.
- [302] S. Pavlopoulou, *On Structural Health Monitoring of Aircraft Adhesively Bonded Repairs*. PhD thesis, University of Sheffield, 2013.
- [303] S.-S. Lih and A. K. Mal, “On the accuracy of approximate plate theories for wave filed calculations in composite laminates,” *Wave Motion*, vol. 21, pp. 17–34, 1995.
- [304] W. J. Staszewski, “Wavelet based compression and feature selection for vibration analysis,” *Journal of Sound and Vibration*, vol. 211, pp. 734–760, 1998.
- [305] M. Meo, G. Zumpano, M. Piggott, and G. Marengo, “Impact identification on a sandwich plate from wave propagation responses,” *Composite Structures*, vol. 71, no. 3-4, pp. 302–306, 2005.
- [306] S. M. H. Hosseini, S. Duczek, and U. Gabbert, “Non-reflecting boundary condition for Lamb wave propagation problems in honeycomb and CFRP plates using dashpot elements,” *Composites: Part B: Engineering*, vol. 54, pp. 1–10, 2013.
- [307] S. M. H. Hosseini, S. Duczek, and U. Gabbert, “Damage localization in plates using mode conversion characteristics of ultrasonic guided waves,” *Journal of Nondestructive Evaluation*, vol. 33, pp. 152–165, 2014.
- [308] S. Duczek, C. Willberg, D. Schmicker, and U. Gabbert, “Development, validation and comparison of higher order finite element approaches to compute the propagation of Lamb waves efficiently,” *Key Engineering Materials*, vol. 518, pp. 95–105, 2012.
- [309] D. Schmicker, S. Duczek, S. Liefold, and U. Gabbert, “Wave propagation analysis using high-order finite element methods: Spurious oscillations excited by internal element eigenfrequencies,” *Technische Mechanik*, vol. 34, pp. 51–71, 2014.

- [310] J. Pohl, C. Willberg, U. Gabbert, and G. Mook, "Experimental and theoretical analysis of Lamb wave generation by piezoceramic actuators for structural health monitoring," *Experimental Mechanics*, vol. 52, pp. 429–438, 2012.
- [311] C.-h. Huang, Y.-c. Lin, and C.-c. Ma, "Theoretical analysis and experimental measurement for resonant vibration of," *IEEE Transactions on Ultrasonics, Ferroelectrics, and Frequency Control*, vol. 51, no. 1, pp. 12–24, 2004.
- [312] E. Yablonovitch, "Photonic crystals: Semiconductors of light," *Scientific American*, vol. 285, pp. 47–55, 2001.
- [313] C. J. Rupp, A. Evgrafov, K. Maute, and M. L. Dunn, "Design of phononic materials/structures for surface wave devices using topology optimization," *Structural and Multidisciplinary Optimization*, vol. 34, pp. 111–121, 2007.
- [314] J. S. Jensen, *Waves and Vibrations in Inhomogeneous Structures: Bandgaps and Optimal Designs*. PhD thesis, Technical University of Denmark, 2011.
- [315] J. W. S. Rayleigh, "On the maintenance of vibrations by forces of double frequency, and on the propagation of waves through a medium endowed with a periodic structure," *Philosophical Magazine*, vol. 24, pp. 145–159, 1887.
- [316] Y. El Hassouani, H. Aynaou, E. H. El Boudouti, B. Djafari-Rouhani, A. Akjouj, and V. R. Velasco, "Surface electromagnetic waves in Fibonacci superlattices: Theoretical and experimental results," *Physical Review B*, vol. 74, p. 11pp., 2006.
- [317] J. S. Jensen, "Space-time topology optimization for one-dimensional wave propagation," *Computer Methods in Applied Mechanics and Engineering*, vol. 198, pp. 705–715, 2009.
- [318] R. Matzen, *Topology Optimization for Transient Wave Propagation Problems*. PhD thesis, Technical University of Denmark, 2011.
- [319] F. Wang, *Systematic Design of Slow Light Waveguides*. PhD thesis, Technical University of Denmark, 2012.
- [320] M. S. Kushwaha, "Stop-bands for periodic metallic rods: Sculptures that can filter noise," *Applied Physics Letters*, vol. 70, p. 3pp., 1997.
- [321] X. Zhang, T. Jackson, and E. Lafond, "Noncontact determination of elastic moduli by two-dimensional Fourier transformation and laser ultrasonic technique," *Review of Scientific Instruments*, vol. 76, p. 3pp., 2005.
- [322] G. Zhang, T. Jackson, E. Lafond, P. Deymier, and J. Vasseur, "Evidence of surface acoustic wave band gaps in the phononic crystals created on thin plates," *Applied Physics Letters*, vol. 88, p. 3pp., 2006.
- [323] J.-J. Chen, K.-W. Zhang, J. Gao, and J.-C. Cheng, "Stopbands for lower-order Lamb waves in one-dimensional composite thin plates," *Physical Review B*, vol. 73, p. 4pp., 2006.

-
- [324] M. Zhao, Y.-Z. Xie, X.-G. Zhang, and J. Gao, “Band gaps of Lamb waves propagating in one-dimensional periodic and nesting Fibonacci superlattices thin plates,” *Thin Solid Films*, vol. 546, pp. 439–442, 2013.
- [325] J. Gao, J.-C. Cheng, and B. Li, “Propagation of Lamb waves in one-dimensional quasiperiodic composite thin plates: A split of phonon band gap,” *Applied Physics Letters*, vol. 90, p. 3pp., 2007.
- [326] K. Lonkar and F.-K. Chang, “Modeling of piezo-induced ultrasonic wave propagation in composite structures using layered solid spectral element,” *Structural Health Monitoring*, vol. 13, pp. 50–67, 2014.
- [327] H. Köppe, U. Gabbert, and H. S. Tzou, *On Three-Dimensional Layered Piezoelectric Shell Elements for Design Simulation of Adaptive Structures*, ch. 13, pp. 125–136. VDI, 1998.